CHAPTER 1

INTRODUCTION

'The number of different forms of atoms is finite.'
Lucretius, De Rerum Natura.

High energy physics is the science which seeks to understand the world at its most fundamental level. As such, it is a manifestation of one of the most basic impulses of human behavior. One particular aspect of this behavior is that the worldviews of different peoples can be quite disparate given the same basic experience, and, in addition, these 'models' are historically derived. Before proceeding to the physics collectively known as the 'top quark', and because it relates directly to science in this field, it will be helpful to elaborate on this behavior.

1. Worldviews

Regardless of where or how people have lived, they have pondered the essence of their world. In order to prosper they have looked to their environs with a discriminating eye in search of patterns. For human cultures, the process of understanding the world is a gradual one in which views are developed, then retained or replaced with new ones according to their utility. The worldview arising from this process can be quite different for different cultures and the 'understanding' that this gives them will influence their subsequent thought about the world.

An example of a case where a culture's worldview is strongly affected by the historical consequence of their previous experience can be found in the society of ancient Greece. It has been noted that, in contrast to many of the world's cultures, the Greek religious outlook had attained the quality that the gods in their religion ceased to serve the role of upholding and explaining the world[1]. Partly as a reaction to this, a trait of one prominent strain of Greek thought was to denigrate the divine as a source of explanation of the world's events[2]. Instead, some turned to everyday phenomena and a rationalistic approach. This emphasis inevitably led to attempts to understand the world at its most basic level in materialistic terms. One tenet which arose from this effort was 'atomism' (Gr. *atomos* = indivisible; *a*- = not + *temnein* = to cut), the concept that all material in the world is comprised of tiny unbreakable particles. As the Roman Lucretius has it, this conclusion rests on the fundamental changelessness of animate and inanimate species, as well as the obvious longevity of individual objects in retaining their nature[3].

This process of worldview building can give rise to dramatically different models. A striking example of this is found with the Hopi of the American Southwest. Unlike the Greeks and Romans (and ourselves), whose Indo-European languages elevate noun concepts to preeminence in their metaphysical outlook, the worldview of the Hopi is mostly contained in verbs[4]. In addition to this, an important basic physical concept in Western culture is dealt with quite differently within their language. There is no reference to time in the language, no concept of things flowing continuously from past through present into the future. For the Hopi, verbs are divided into two main groups: those in which an event has become 'part of the record', and those events which are 'unmanifest'(4). The first class includes our events of the past and physical present. The second class includes our future as well as the mental and emotional realm of experience.

Within the field of classical physics, we can also see systems of thought which carry perspectives which shape further scientific inquiry. As part of the effort to sever the connection between divine and mundane which continues from the ancient Greeks, determinism has been used in combination with the concepts of particles and forces to form a mechanistic view of nature. By further removing a supernatural role in the ongoing evolution of the world, this view has profoundly affected our worldviews even to this day.

As another example, in the contemporary scientific view one encounters a linguistic limitation in our debate on waves and particles. On the one hand, the particle paradigm follows from the atomic hypothesis -- the particle being the 'tiny part' making up macroscopic bodies we see. On the other hand, waves connote implicitly the periodic, extended, travelling waves on water. The observation of both aspects in light presents difficulty since they are seemingly conflicting ideas. In contrast, one who speaks a markedly different language (ie. has a very different worldview) may not have this limitation. In terms of conceptual tools, for instance, it has been suggested that the Hopi may be better able to understand this apparent dichotomy[4].

2. Advent of Modern Physics

By the late 19th Century, the world was viewed as being composed of fundamental, massive atoms in approximately 100 elemental types. These were thought to interact with each other deterministically via two forces: gravity and electromagnetism. Some physicists were claiming that all that remained was to measure the world to more decimal places. In the last 100 years a profound transformation has occurred in our fundamental understanding of the world and little of these views remain today.

The structurelessness of the atom was first refuted by Rutherford in 1911 when he used α and β particles to study the atomic structure of gold atoms. The low mass β particles passed through atoms almost unimpaired which indicated that atoms were mostly empty. The more massive α particles were occasionally deflected with large scattering angles. This led to the understanding that atoms, approximately 10^{-10}m in size, were mostly composed of a nucleus 10^{-15}m in diameter. Later, this nucleus was itself found to be composed of still smaller parts called protons and neutrons.

The advent of quantum mechanics early this century brought a 'paradigm shift'[5] which our language still has difficulty accommodating. In order to account for the basic stability of matter, physics has relinquished a strictly deterministic view. This condition manifests itself through a fundamental limitation in our ability to measure events by the uncertainty principle $\Delta p \Delta x \geq \hbar/2$. The resultant frustration arising from this situation is perhaps best indicated by Einstein's famous dictum 'God does not throw dice.' Additionally, the paradigm of quantum mechanics calls the very idea of a particle into question, and we are left with indeterminate fluctuations of mass fields out of a vacuum.

3. High Energy Physics

In time, the fundamentalness of protons and neutrons was undermined by several measurements which ultimately led to discussion of yet another level of structure. Ongoing experiments found a proliferation of hadronic states which possessed many patterns in terms of their quantum numbers. This led to the SU(3) flavor model[6] in 1964 in which these particles were anticipated to be composed of still smaller particles called 'quarks'. Another observation in favor of hadron substructure came from experiments performed at SLAC in the 1960's in which electrons were collided with nucleons. The large momentum transfer interactions that occurred were more frequent than anticipated and this led to the view that there were localized scattering centers within the nucleon *a la* Rutherford. This progression from atom to nucleus to nucleon/hadron to quark may have no end. In fact a major effort at the DØ experiment at Fermilab is to probe for quark substructure by looking for an excess of very high energy jets at wide angles with respect to the collision axis.

The current picture we have of the fundamental behavior of matter thus involves a small number of particles (quarks, leptons, guage bosons) interacting via four forces (strong, electromagnetic, weak, gravity). Two of these interactions have been unified into the electroweak theory of Salam and Weinberg. This theoretical framework has had some remarkable successes in the last 30 years and provides strong indirect motivation for the existence of an additional fundamental particle -- the top quark. In fact, the case for the top quark is so strong and the successes of the model are so profound that some would consider top found even before the experimental observation which came in 1995, of which the analysis in this thesis is a part. However, the theory requires several parameters as input from experiment, and the experimental discovery of the top quark is in fact a crucial test of the model.

4. Thesis Scope and Organization

Because the existence of the top quark is such an incisive test of the electroweak model, we have conducted a search for evidence of its production at the Fermilab Tevatron using the DØ detector. In this thesis we will review the so-called 'Minimal Standard Model' of high energy physics and those of its aspects which indicate the existence of the top quark (Chapter II). We will describe the subsequent experimental evidence and limits for a high mass top search. A description of the expected production and decay mechanisms and their implications for this search concludes this section.

Next, the subsystems of the DØ detector relevant to this analysis are discussed in detail along with supporting information about the Fermilab Accelerator. Calorimetry is emphasized because it dictates the nature of our search. Following this in Chapter 4 is a discussion of the integrity of the data selected in triggering and streaming, and various issues related to the data reconstruction and particle identification. Chapter 5 provides explanations of various calorimeter corrections for the effects of the Main Ring.

In an experiment such as DØ, the detector is a complex assembly of many disparate components. The ability to make significant measurements of physical processes of interest relies on our ability to understand the both the physics of the detector, and that of the processes we ultimately wish to study. As a result, considerable time will be spent in Chapter 6 describing the determination of the jet energy scale using direct photon events. Then the event selection for the dielectron top search is presented in Chapter 7 along with an itemization of the signal and background for our chosen cuts. Chapter 8 summarizes the results of this search as well as some thoughts for the future.

CHAPTER 2

EXPERIMENTAL AND THEORETICAL MOTIVATION

'What is swifter than the wind?
Thought.
What is sharper than the sword?
Understanding.'
Irish Anon., 5th century

1. Local Gauge Theories of Fundamental Interactions

The formalism used to describe interactions between fermions (spin 1/2 particles) is that of 'local gauge' theories. In such theories, one requires that an interaction be unchanged under a phase or 'gauge' transformation, even if that transformation is position-dependent (ie. 'local gauge invariance'). The general requirement of gauge invariance results in conservation of some property such as charge in electromagnetism. Making this a local gauge invariance necessitates the inclusion of an interaction carried by massless gauge bosons (spin 1 particles), and it restricts the form of the coupling between these bosons and matter. If the model is 'non-Abelian', then the gauge bosons can interact with one another.

a. Electroweak Interactions

One such theory is the Salam-Weinberg $SU(2) \times U(1)$ theory of electroweak interactions which represents a unification of electromagnetism and the weak nuclear interaction. Electroweak interactions are mediated by four gauge bosons: the $W^{\pm}$ which mediate charge changing weak currents for left-handed fermions, and the Z/γ which propagate the neutral current. The unification is achieved through a process in which a symmetry in the theory's Lagrangian is broken in the ground state of the system. This is accomplished by the introduction of a spin 0 Higgs SU(2) doublet in the model. This symmetry breaking gives mass to the SU(2) vector bosons, W^{α} (α=1,2,3), and to the U(1) boson, B, which are rewritten in terms of physical states as

$$\begin{aligned} W^{\pm} &= (W^1 \mp iW^2)/\sqrt{2} \\ Z &= W^3 \cos\theta_w - B\sin\theta_w \\ \gamma &= W^3 \sin\theta_w + B\cos\theta_w \end{aligned} \qquad \textbf{Eq. 2.1}.$$

The properties of the observed states are given in Table 2.1 where Q denotes the electric charge of the particle and C denotes the color charge (discussed in next subsection). Note that the photon mass has been measured to be very tiny at most and is assumed to be zero. As a result, the electroweak model had to be constructed in a way that one neutral linear combination in Equation 2.1 remains massless. Unlike the W but like the γ, the Z couples to right-handed fermions due to mixing with B.

The unification of electromagnetism and the weak interaction is incomplete depending on one's perspective. There are still two fundamental coupling constants with different strengths in the theory. However, there is unification in the sense that the two interactions are two specific mixtures of these two coupling constants and are therefore inextricably linked by the theory. One triumph of the electroweak model, in fact, rests with the near-equality of these parameters when the observable strengths of the electromagnetic and weak forces are several orders of magnitude different. The main reason for this difference is now understood to be the result of the enormous masses of the W and Z gauge bosons.

Table 2.1. Mass and charge of fundamental bosons of the electroweak and strong interactions.

boson	mass	Q
γ	$< 4.5 \times 10^{-16}$ eV/c^2	0
W	80.33 ± 0.15 GeV/c^2	± 1
Z	91.118 ± 0.022 GeV/c^2	0
g	0	0

b. Strong Color Interactions

For strong interactions, the currently accepted model is the non-Abelian SU(3) theory of color interactions, quantum chromodynamics (QCD). This interaction is mediated by eight massless gauge bosons called 'gluons'. Because they carry color they can interact with one another and change the color of quarks they interact with. One characteristic of this interaction is 'confinement' in which the potential energy between colored objects (partons) increases with their distance from one another. Thus infinite energy is required to separate them. A complimentary feature of the theory is 'asymptotic freedom' in which the strength of the interaction decreases as the energy of the collision increases.

One feature of the strong interaction as predicted by QCD is the 'color coherence' process. In the model, the coherent nature of gluon radiation results in regions where the final state particle density is enhanced or depleted. This phenomenon can be modeled in such a way that radiation from a parent parton proceeds at smaller and smaller angles with respect to that parton as the process evolves. This approximation is referred to as 'angular ordering' of the gluon radiation and is valid at leading order in N_c, the number of colors. It has a significant effect on the evolution of jets in high energy events.

One of the central difficulties of QCD is the magnitude of the strong coupling constant which precludes perturbative calculations at low energy. This has significantly limited our understanding of the evolution of colored systems. For instance, because of the confinement property of the strong interaction, no colored objects can be observed in the final state. This is believed to cause color fields to 'fragment' into hadrons as two partons recede from each other. As the potential energy increases between them, $q\bar{q}$ pairs are pulled out of the vacuum producing a 'jet' of colorless hadrons. This process is not calculable with perturbative QCD so that one must employ one of the prevailing phenomenological descriptions of the process.

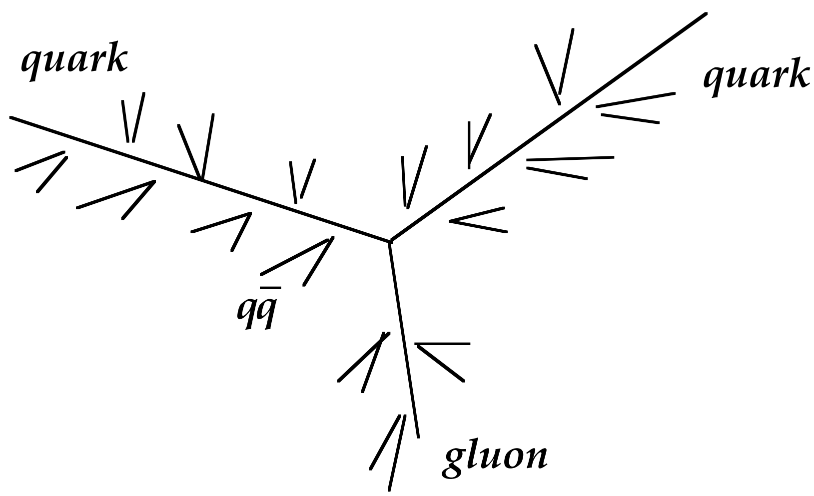

Figure 2.1: Schematic of evolution of a three jet event according to Field-Feynman independent fragmentation.

In the Field-Feynman model[7], the efforts of strong interactions to reorder colored partons into colorless hadrons are treated as being local to a particular parton. This is motivated by the consideration that the parton is moving rapidly away from other partons in the event. This results in a fragmentation which proceeds independently of these other partons. If we consider a quark, at some point along its motion a $q\bar{q}$ pair will appear out of the vacuum leaving the initial quark with some reduced momentum. This branching iterates until the quark's momentum passes below a chosen cutoff as shown in Figure 2.1. The rate of production of different types of hadrons in a jet is dictated by the flavor content of the hadron. Those with strange quarks, for instance, are less frequent due to the higher mass of s relative to u and d.

The cluster fragmentation[8] considers mostly just phase space issues. Here, gluons calculated perturbatively are split into $q\bar{q}$ pairs. To neutralize color, these quarks are ordered into colorless clusters which are then either decayed into lower mass clusters or hadrons themselves.

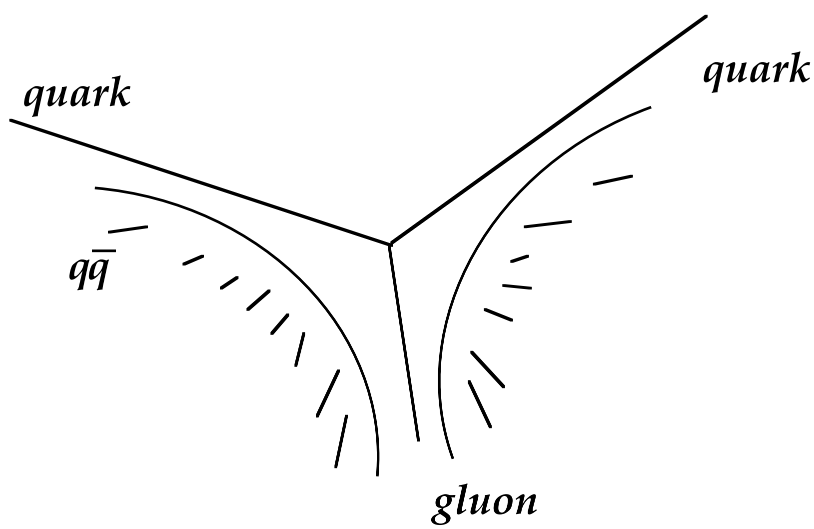

Figure 2.2: Schematic of evolution of three jet event according to Lund string fragmentation. Note lack of activity opposite the gluon jet.

In the string fragmentation model[9], two colored partons can be connected to each other via a narrow tube or 'string' of force lines. The two particles oscillate on this string until a $q\bar{q}$ is created along the string. The new particles cut the string and terminate its ends such that there are now two strings. The quarks at the ends of these new strings also oscillate and their string can likewise break. This process continues until the invariant mass is small at which point we have a hadron. One aspect of this model is the expectation of significant energy along lines of color connection in an event, and a deficit of energy where there are no color connections, such as shown in Figure 2.2.

2. Fermion Structure of the Theory

It is currently believed that all matter is made of fundamental fermion mass fields of two general types: leptons and quarks. These have been found to be point-like on a scale of 10^{-18} m. Only the quarks interact via the strong force. They are grouped into weak isospin doublets which have several observable effects. In the quark sector of the theory, it has been observed that the electroweak eigenstates are a mixture of the mass eigenstates. Also, there are no flavor changing neutral currents for any interactions. We now enumerate these properties.

a. Quark Mixing and Weak Isospin

The flavor SU(3) model reduced all baryons and mesons to particular combinations of u and d quarks forming an isospin doublet, an s quark forming a singlet, and their antiparticles. Because the weak charged current couples particular left-handed fermion states, we should only observe charge currents between d and u *weak* eigenstates. Since the transition $K^+ \rightarrow \mu^+\nu$ occurs, we know a weak current also couples s and u. In the most general situation, there is no reason for the weak and mass eigenstates to be the same and there will then be some transformation between them. Because the weak interaction is non-Abelian, there is only one coupling constant and the transformation matrix must be unitary. Quantum mechanical considerations further specify that the weak states will be linear superpositions of the mass states. Therefore, we can describe these interactions by one additional parameter, the Cabibbo angle or θ_c, such that

$$\begin{pmatrix} d' \\ s' \end{pmatrix} = \begin{pmatrix} \cos\theta_c & \sin\theta_c \\ -\sin\theta_c & \cos\theta_c \end{pmatrix} \begin{pmatrix} d \\ s \end{pmatrix} = U_C \begin{pmatrix} d \\ s \end{pmatrix}.$$

We then expect a neutral current of the form

$$\begin{aligned} J'_{nc} &= (u\ d')\gamma^{\mu}(1-\gamma_5)(u\ d') \\ &= g\,(u\gamma^{\mu}(1-\gamma_5)u + d\gamma^{\mu}(1-\gamma_5)d\cos^2\theta_C + s\gamma^{\mu}(1-\gamma_5)s\sin^2\theta_C \\ &\qquad + (d\gamma^{\mu}(1-\gamma_5)s + s\gamma^{\mu}(1-\gamma_5)d)\cos\theta_C\sin\theta_C) \end{aligned}$$

This neutral current, which allows transitions from *s-d* and is not balanced in *u-u*, *d-d*, or *s-s* currents, is not supported by experiment. A mechanism[10] was proposed in 1970 to overcome this discrepancy by suggesting a weak isospin partner to the strange quark, called charm, giving a current of the form

$$\begin{aligned} J''_{nc} &= (c\ s')\gamma^{\mu}(1-\gamma_5)(c\ s') \\ &= g\,(c\gamma^{\mu}(1-\gamma_5)c + d\gamma^{\mu}(1-\gamma_5)d\sin^2\theta_C + s\gamma^{\mu}(1-\gamma_5)s\cos^2\theta_C. \\ &\qquad - (d\gamma^{\mu}(1-\gamma_5)s + s\gamma^{\mu}(1-\gamma_5)d)\cos\theta_C\sin\theta_C) \end{aligned}$$

This cancels the flavor changing terms and gives a total neutral current of the form

$$\begin{aligned} J_{nc} = J'_{nc} + J''_{nc} &= g(\bar{u}\gamma^{\mu}(1-\gamma_5)u + \bar{c}\gamma^{\mu}(1-\gamma_5)c \\ &\qquad + \bar{d}\gamma^{\mu}(1-\gamma_5)d + \bar{s}\gamma^{\mu}(1-\gamma_5)s) \end{aligned}$$

which is also balanced in the different flavors. The charged current in this situation is then,

$$J_{cc} = \begin{pmatrix} u & c \end{pmatrix}\gamma^{\mu}(1-\gamma_5)U_C \begin{pmatrix} d \\ s \end{pmatrix}$$

This model is able to account for the measured charged and neutral current processes although θ_c is not predicted by the theory and must be determined experimentally. Narrow dilepton resonances were observed at 3.1 GeV/c^2 in November, 1974 at the SLAC e^+e^- collider[11] and also at the Brookhaven AGS using 28 GeV protons on a Be target[12]. These states were eventually interpreted as $c\bar{c}$ bound states.

b. Generations

In the theory, fermions interact with one another via exchange of gauge bosons. The fermions are grouped into quark and lepton weak isospin doublets when left-handed, while right-handed fermions are singlets which do not participate in the weak interaction charged current. The families of fermions are grouped into generations as indicated in Table 2.2. Limited by baryon number conservation and the conservation of electron, muon and tau number, only the first, lowest mass, generation is composed of stable particles.

The number of generations is not constrained by the electroweak theory. Varied experimental evidence, however, points to the existence of three generations of fermions. Data from e^+e^- collisions at LEP and SLAC will only allow a fourth generation if the neutrino mass is > 30 GeV/c^2 for that generation. The central value for the number of light neutrinos from LEP measurements is 2.991 ± 0.015[13], which is strong evidence for three generations.

Components of the third generation were first seen twenty years ago beginning with the discovery of the tau lepton in 1975[14]. At FNAL in 1977, narrow meson resonances were produced in 400 GeV proton-nucleus collisions in the mass range 9.5 - 10.5 GeV/c^2[15]. This family was given the name Y ('upsilon') and is composed of a new b-quark, called beauty or bottom, and its antiquark. The properties of all fundamental fermions are given in Table 2.2 including the third component of the weak isospin, $\tau_{3L,R}$, for the the left and right-handed fermions.

Table 2.2. Weak isospin and charge of fundamental fermions. The right-handed fermions are weak isospin singlets.

fermion	τ_{3L}	τ_{3R}	Q
$\nu_i = \nu_e, \nu_\mu, \nu_\tau$	1/2	---	0
$l_i = e, \mu, \tau$	-1/2	0	-1
$q_i = d, s, b$	-1/2	0	-1/3
$q'_i = u, c, t$	1/2	0	+2/3

c. Kobayashi-Maskawa Matrix:

Although the existence of the third generation of fundamental fermions was unknown at the time, Kobayashi and Maskawa generalized the Cabibbo matrix by adding a third quark generation. In general, there can be mixing of the u-type quarks into u'-type quarks as well as mixing of d-type quarks into d'-type quarks. The generalized charged current interactions can be written,

$$J_{cc} = \begin{pmatrix} u & c & t \end{pmatrix} \gamma^\mu (1 - \gamma_5) U_{KM} \begin{pmatrix} d \\ s \\ b \end{pmatrix}$$

where the Kobayashi-Maskawa matrix, U_{KM}, is the product of the mixing matrices for the u-type and d-type quarks. This matrix is required to be a unitary 3x3 matrix with three mixing angles and one nontrivial complex phase. It can be expressed by the various quark coupling probabilities

$$U_{KM} = \begin{pmatrix} U_{ud} & U_{us} & U_{ub} \\ U_{cd} & U_{cs} & U_{cb} \\ U_{td} & U_{ts} & U_{tb} \end{pmatrix} \cong \begin{pmatrix} 1-\frac{1}{2}\lambda^2 & \lambda & A\lambda^3(\rho - i\eta) \\ -\lambda & 1-\frac{1}{2}\lambda^2 - iA^2\lambda^4\eta & A\lambda^2 \\ A\lambda^3(1-\rho-i\eta) & -A\lambda^2 & 1 \end{pmatrix}$$
$$= \begin{pmatrix} 0.975* & 0.22* & 0.01* \\ 0.22* & 0.974* & 0.04* \\ 0.01 & 0.04 & 0.999 \end{pmatrix}$$

where the second part is the parametrization of Wolfenstein[16]. The third expression gives the approximate numerical values of each matrix element with an * indicating which ones have been experimentally measured. Unitarity is assumed to estimate the as yet unmeasured elements.

Interestingly, the complex phase allows a potential venue for CP violation to enter the theory via the third generation. Since Hamiltonians with complex numbers violate time reversal invariance, we can get CP violation because quantum field theories are assumed to be CPT invariant. The experimental observation of CP violation in the K meson system[17] might then have been the first indication of a third generation. We do not know, however, if this transformation is actually the source of CP violation because we cannot calculate the matrix *a priori* from the electroweak theory.

3. Arguments Favoring a Top Quark

The top quark is expected within the standard model on three grounds. First, chiral anomalies in theoretical calculations suggest that there is another colored fermion which will complete the third generation. Second, flavor changing neutral current interactions do not occur suggesting that, like charm for the strange quark, there is a weak isospin partner to bottom. Third, the weak isospin of the b-quark has been measured to be -1/2 which implies the existence of a partner which is by definition the top quark.

a. Chiral Anomalies:

We can look within the theory to see that it favors complete generations. Ultimately without a top quark we run into 'chiral anomalies'. One of the requirements of the theory, like renormalizability, is that it not have anomalies. An anomaly arises when an invariance of the classical Lagrangian is not upheld in the quantum corrections[18]. Considering loop diagrams of a fermion coupling to vector and axial vector currents, for the Salam-Weinberg model to be anomaly free requires that the net charge in each generation must be 0. Since the charged tau leptons give -1, the tau neutrino gives 0, and the *b*-quark in three colors give -1, we need a top quark in three colors (= $+^2/_3$ x 3 = +2) to complete the generation. Also, this tells us that the existence of the τ alone motivates a search for the quarks since this requirement of no anomalies means the number of lepton generations should equal the number of quark generations.

b. Flavor Changing Neutral Currents:

The strongest indirect evidence for the top quark has come from measurements of hadrons with *b* content. As in the two generation case, the presence of the *b*-quark as a weak isospin singlet would allow flavor-changing neutral current interactions such as $b \to d$ or $b \to s$. As a result, the processes $b \to s \to sl^+l^-$ and $b \to s \to cl\nu$ should occur[19] such that

$$\frac{BR(b \to sl^+l^-)}{BR(b \to cl\nu)} \geq 0.12.$$

If we invoke lepton universality, however, the experimental limit on the inclusive semileptonic decay of B mesons[20]:

$$\frac{BR(B \to \mu^+\mu^- X)}{BR(B \to \mu\nu X)} < 5 \times 10^{-4}.$$

This is several orders of magnitude lower, suggesting that b is not a weak isosinglet.

c. $B^\circ - \overline{B}^\circ$ Mixing

Figure 2.3: Box diagrams leading to mixing of neutral B mesons.

The charged current allows box diagrams to contribute processes with large changes in flavor content, such that particles can transform into their antiparticles. One of these processes, $B^\circ - \overline{B}^\circ$ mixing, allows us to discern the strength of the U_{td} and U_{ts} matrix elements. The processes are shown in Figure 2.3. The level of measured mixing[21,22] suggests that U_{td} and U_{ts} are non-zero, although there are non-standard explanations for the observed rate[23].

d. Weak Isospin of the b-quark:

The above issues are suggestive of the top quark but are not conclusive because one can manipulate the parameters such that the b-quark is in a weak isospin singlet as in the model of E. Ma[24]. A measurement of the weak isospin of the b-quark partially addresses this limitation. One method to measure the b-quark isospin is from the charge asymmetry for the process $e^+e^- \to b\overline{b}$. This is because the process occurs through both Z and γ channels and the Z contribution gives an asymmetric charge distribution relative to the plane perpendicular to the incoming e^+e^- beams. This asymmetry is a function of the coupling between the b-quark and the Z which theoretically is $\propto \tau_{3L}^b + \frac{1}{3}\sin^2\theta_w$. This asymmetry has been measured experimentally[25] and, given the current measured value of $\sin^2\theta_w$, this indicates that $\tau_{3b} = -\,^1/_2$ which necessitates the existence of a weak isospin partner with $\tau_{3b} = +\,^1/_2$. A measurement of $\Gamma(Z \to bb)$ also depends on the coupling strength of b to the Z boson, and may therefore be useful to measure the weak isospin of the b-quark. The width has been measured to be 378 MeV[26] which again suggests from measurement that $\tau_{3b} = -\,^1/_2$. It should be noted that this evidence, being defined essentially by the theoretical model which currently holds sway, is confined to that model. The measurements in both cases require significant theoretical edifice to extract a value of the weak isospin. Also, one should note that the model of Ma is able to reproduce the charge asymmetry measurement and is only refuted by the measurement of the absolute width of the Z to $b\bar{b}$ or $\tau^+\tau^-$.

4. Previous Experimental Constraints:

Having seen that a search for top is strongly motivated in the electroweak model, we now turn to some experimental contraints.

a. Mass Limits:

If we only consider standard model processes then measurements of M_W and M_Z provide an upper mass limit of $m_{top} < 211$ GeV/c^2 at the 95% c.l.[27]. Fits using all electroweak data from LEP, $p\bar{p}$, and $\sin^2\theta_w$ from νN scattering give a mass estimate of $178\ \mathrm{GeV}/c^2 \pm 11\ \mathrm{GeV}/c^2\,{}^{+18\ \mathrm{GeV}/c^2}_{-11\ \mathrm{GeV}/c^2}$ [28]. Unfortunately, these theoretical estimates have had a strong tendency over the last 15 years to migrate upward as lower masses were experimentally ruled out.

b. Direct Searches:

The direct search for top has proceeded for several years and the experimental lower mass limit at the outset of this dissertation experiment was m_{top} > 91GeV/c^2 at the 95% c.l.[29]. This mass limit comes from assuming that $|U_{tb}|$ = 1.0. A more general limit comes from searches in e^+e^- collisions which gives m_{top} > 46 GeV/c^2 independent of decay modes[30].[31] In hadron colliders, the width of the W allows a higher model-independent limit of 62 GeV/c^2[32].

5. Hadroproduction and Evolution of $t\bar{t}$ States:

It would appear then that we expect top to be in the mass range 90 GeV/c^2 to 210 GeV/c^2. Our next consideration should then be how top is produced in high energy proton-antiproton collisions.

a. Production

The top quark is expected to be produced mostly via $p\bar{p} \rightarrow t\bar{t} + X$[33] at center-of-momentum energies of 1.8 TeV (see Figure 2.4).

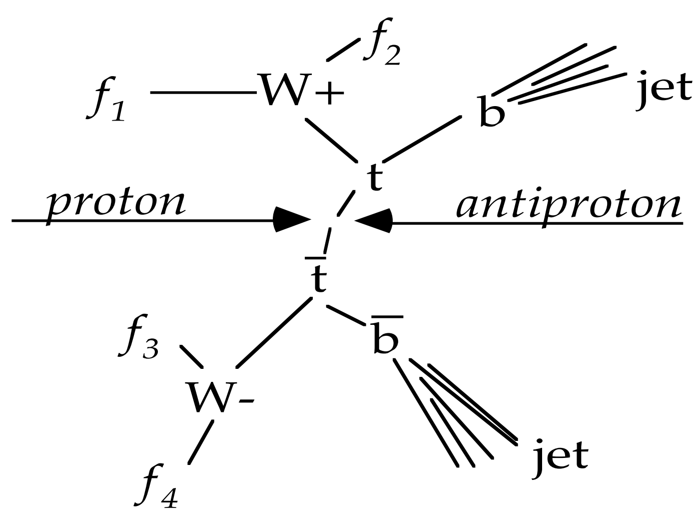

Figure 2.4: Scheme of evolution of $t\bar{t}$ system. The final state fermions, f_i, can be either leptons or quarks.

In the frame in which the proton and antiproton are rapidly moving, the hard interaction between constituent partons is fast relative to the time for partons to interact. As a result, we can factorize the above process into a parton collision weighted by parton *distribution functions* or *structure functions, $F_i(x)$*, which give the momentum fraction x carried by parton i relative to the parent hadron. If we know these structure functions, which are experimentally determined, we can calculate the top cross section as

$$\sigma(p_1\bar{p}_2 \to t\bar{t} + X) = \sum_{i,j} \int dx_1 dx_2 \\ \times F_i(x_1,\mu) F_j(x_2,\mu)\, \hat{\sigma}_{ij}(x_1 x_2 S, m^2, \mu^2)$$

where the sum runs over gluons and all relevant light quarks in the colliding proton and antiproton, μ is the QCD renormalization scale, and $\hat{\sigma}_{ij}$ is the cross section for partons i and j to interact. The calculation is performed in perturbative next-to-leading order QCD and the leading processes ($O(\alpha_s^2)$) are diagrammed in Figure 2.5.

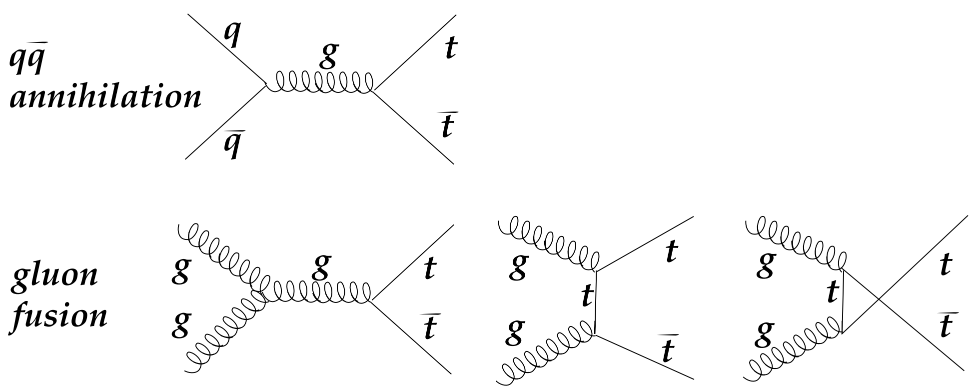

Figure 2.5: Leading order Feynman diagrams for top production.

Due to the large mass of the top quark, the preponderance of the cross-section at 1.8 TeV proton-antiproton collisions is from $q\bar{q}$ annihilation because valence quark structure functions are required to provide sufficient energy to make such a massive object. For a top quark of mass of 90, 180, or

200 GeV/c^2, the $q\overline{q}$ diagrams contribute 50%, 80%, or 90% of the total cross section. The calculated cross section vs. m_{top} is given in Appendix I, and ranges from about 40 pb to 2 pb for top masses of 120 to 200 GeV/c^2. The error on the cross section comes mainly from the gluon fusion process due to imperfect knowledge of the gluon structure function.

b. Decay and Fragmentation:

Given that the top mass is above the threshold to decay to a W + b-quark, this decay predominates with nearly 100% branching fraction. If the top mass is 150 GeV/c^2, its lifetime is 7.8 x 10^{-25} s[34] while the typical evolution time for strong interactions is Λ_{QCD} ~ 10^{-22} s. As a result, the $t\bar{t}$ system has neither the time to bind into a meson, nor does either top quark have time to undergo fragmentation. This means we have free quarks which each quickly decay to Wb. The b fragments into a jet and the W decays promptly to $l\nu_l$ or $q'\overline{q}$. The branching ratios for W decay are based on the probability for decay to three generations of leptons and two generations of light quarks where the quarks have three color degrees of freedom. For instance, this gives a branching ratio of $BR(W \rightarrow e\nu_e)$ = 1/9. Because all quarks produced in the decay chain give rise to jets, they are to first order indistinguishable. Therefore, the W decays essentially define the distinctive $t\bar{t}$ final states. Assuming that the W decays are uncorrelated with each other, and accounting for flipped combinations (eg. *'$e\mu$' vs. 'μe'*), the $t\bar{t}$ branching ratios for various final states are given in Table 2.3. It should be noted that at a lower level, the tau decays of the W contribute to each of the channels mentioned in Table 2.3. For instance, the dielectron channel benefits from $e\tau$ and τe events in which the tau itself decays to an electron. Another aspect of top events to keep in mind is that the b-jets can sometimes be distinguished from light quark jets due to the presence of soft muons in the jet due to the semileptonic decay of the b-quark. Approximately 35% to 40% of top events possess at least one such muon.

Table 2.3. Branching ratios for selected $t\bar{t}$ states

W_1	W_2	BR
qq'	$e\nu$	14.8%
qq'	$\mu\nu$	14.8%
$e\nu$	$\mu\nu$	2.4%
$e\nu$	$e\nu$	1.2%
$\mu\nu$	$\mu\nu$	1.2%

6. Monte Carlo Event Generators:

In order to understand the properties of top in $p\bar{p}$ collisions, we must resort to detailed modelling of the physics processes based on the expected characteristics of top and of some types of background. The evolution of a high energy physics event has several components all of which need to be part of this model. First there are the incoming proton and antiproton, each of which is composed of several partons with varying momentum fractions of their parent. A collision occurs between some pair of partons from these hadrons and produces initial outgoing particles. Massive bosons, or a heavy top quark, decay rapidly into final state leptons or quarks. Some method of fragmenting the colored partons in the event must be employed. Additionally, the beam hadrons are disrupted in a hard scatter and their remnants may leave some energy in the event. Lastly, many of the hadrons produced throughout the event evolution will decay into lighter more stable particles.

The models we use are implemented in standardized Monte Carlo packages which include a simulation of each of the main stages in the evolution of an event at the collider. These programs randomly generate event kinematic parameters weighted by known or expected distributions. ISAJET is one event generator in which jets are fragmented independently of one another according to the Field-Feynman approach. HERWIG calculates angular ordering effects in the strong interaction evolution in the perturbative region although it resorts to the cluster model to fragment jets. PYTHIA also allows calculation of angular ordering effects. In addition, this event generator employs string fragmentation for jets.

7. Signatures for Top:

Before proceeding to a discussion of our experiment, we should consider the signatures for top which motivate the particular kind of search we performed for this dissertation.

a. Backgrounds and High p_T Lepton Signatures:

In moderate energy hadron collisions ($\sqrt{s}$ ~ a few GeV) the typical secondary particle transverse momentum ('p_T') is about 350 MeV[35] and the single hadron cross section falls off approximately exponentially with increasing transverse momentum, p_T. While at higher energies the general behavior is retained, the total number of particles in any p_T region has increased. In addition, the cross section of jets decreases as $\sim \frac{1}{p_T^4}$ due to the larger number of head-on parton-parton collisions. In these events, the final state particles are typically hadrons, leptons or photons embedded in high p_T jets. When a charm or beauty quark is produced, it can decay directly to a soft lepton (electron or muon only for charm), which is fairly close to the jet. The observation of muons within jets from strange quark decay is effectively eliminated by the DØ experimental geometry and notably small inner radius of the calorimeter. K mesons do not have time to decay before hitting the inner wall of this detector. By requiring high p_T leptons which are isolated with respect to hadronic activity, we are able to effectively remove all background due to $b\bar{b}$ and $c\bar{c}$ production. What remains are those processes which produce high mass states such as a W or Z, or high mass virtual photons in Drell-Yan production.

Another leptonic aspect of $t\bar{t}$ events also provides a valuable signature -- high p_T neutrinos -- which are produced when each W decays. Since neutrinos only interact weakly, they deposit no energy in the detector. Any component of the neutrino momentum therefore results in 'missing' energy in the event. Because of the composite nature of the proton and variability of the constituents' momentum fraction, we are never sure of the total longitudinal momentum in an event. Therefore, only the components of this missing energy which are transverse to the beam direction are significant. This missing E_T ($\not{E}_T$) is large in events with high p_T neutrinos, like top, while it is zero in events without neutrinos like $Z \rightarrow ee$.

Although the cross section and branching fraction is small for the signal channel of this analysis, $t\bar{t} \rightarrow ee$, a dielectron analysis exploits the strengths of the detector. The specific experimental signature is two high p_T electrons, large $\not{E}_T$ from neutrinos, and high transverse energy jets from the b quarks as in Figure 2.4. Because of the high mass of top, the opening angle of the W and b is large even in the lab frame. Therefore, the leptons from the W's will be isolated from hadronic activity. In addition, the W bosons, by virtue of their large mass, are relatively slow-moving resulting in very large $\not{E}_T$ and the presence of two electrons means this $\not{E}_T$ has good resolution. The principal backgrounds for such a signature arise from several high p_T processes:

- WW: small cross-section but very top-like in the leptonic quantities.

- Z to ee: large cross-section with high p_T dielectrons but no significant $\not{E}_T$. The dielectron invariant mass = 91 GeV/c^2 to within the natural width of the Z and the detector energy resolution for electrons.

- Z to $\tau\tau$: small branching ratio to *ee* but large Z cross section. Electron p_T and $\not{E}_T$ are moderate.

- Drell Yan to ee: significant cross-section with high p_T dielectrons but no significant $\not{E}_T$.

- QCD $c\bar{c}$ and $b\bar{b}$: huge cross section but soft, non-isolated electrons and small values of $\not{E}_T$.

- W + *jets*: large cross section but require one jet to fake an electron.

- QCD multijet: huge cross-section but no significant $\not{E}_T$ and requires two jets to fake electrons.

In the first four cases the background processes physically resemble our $t\bar{t}$ signature since they have two isolated high p_T electrons in the final state. For the first three, several kinematic properties of the leptons are shown in Figures 2.6 through 2.9. In each of the figures, the distributions for Z $\rightarrow$ ee, WW, and Z $\rightarrow \tau\tau$ are shown left-to-right and top-to-bottom. The bottom right hand plot gives the distribution expected for $t\bar{t}$ events when m_{top} = 140 GeV/c^2 (dashed histogram) and 180 GeV/c^2 (solid). In general, the lepton aspects of $t\bar{t}$ events (electron E_T, $\not{E}_T$) are fairly insensitive to a change in top mass. The W pair production and Z to $\tau\tau$ have neutrinos. In the latter case, however, the neutrinos tend to cancel each other so that the $\not{E}_T$ is not large. All events have also been processed with a detailed detector simulation using the GEANT software library.

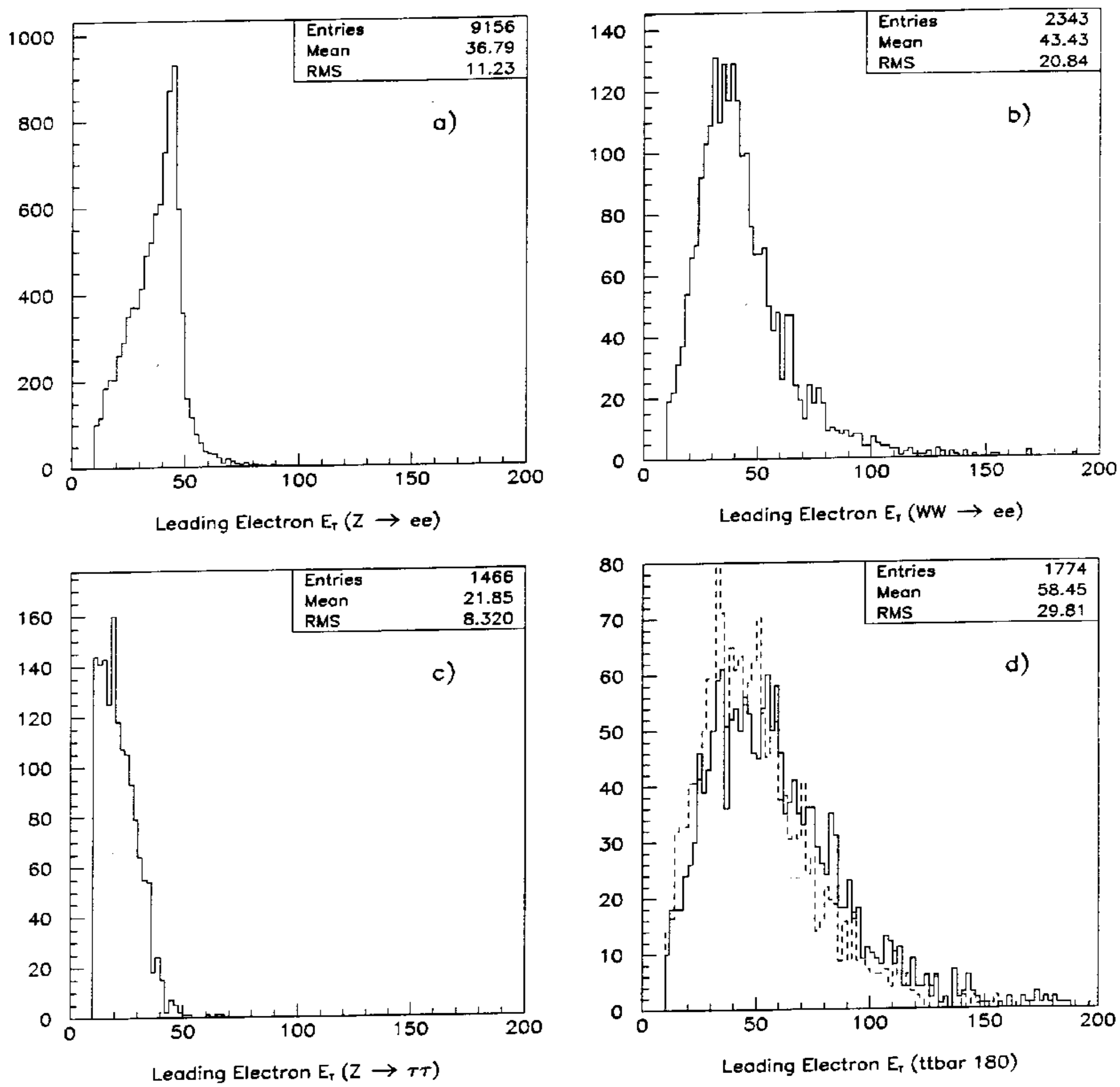

Figure 2.6: Leading electron E_T for (a) $Z \longrightarrow ee$, (b) $WW \longrightarrow ee$, (c) $Z \longrightarrow \tau\tau$, and (d) top of mass 140 GeV/c^2 (dashed) and 180 GeV/c^2 (solid).

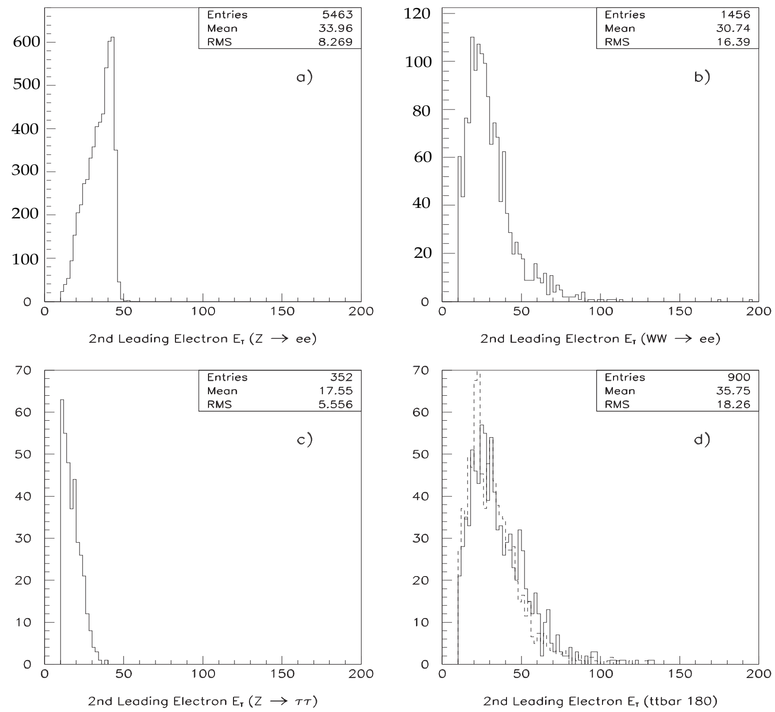

Figure 2.7: Second leading electron E_T after requiring a leading electron E_T > 20 GeV and a second leading electron E_T > 0 GeV for (a) $Z \longrightarrow ee$, (b) $WW \longrightarrow ee$, (c) $Z \longrightarrow \tau\tau$, and (d) top of mass 140 GeV/c^2 (dashed) and 180 GeV/c^2 (solid).

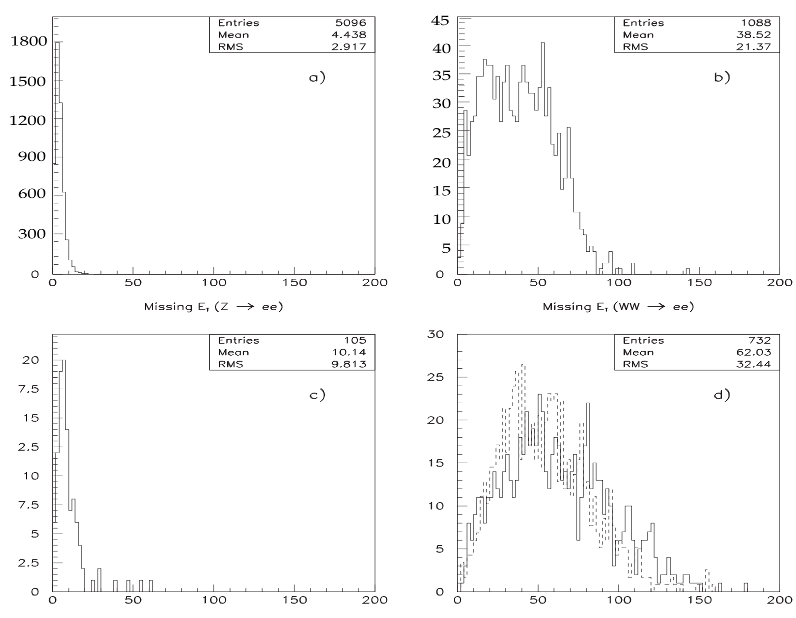

Figure 2.8: $\not{E}_T^{cal}$ after requiring two electrons with E_T > 20 GeV for (a) $Z \longrightarrow ee$, (b) $WW \longrightarrow ee$, (c) $Z \longrightarrow \tau\tau$, and (d) top of mass 140 GeV/c^2 (dashed) and 180 GeV/c^2 (solid).

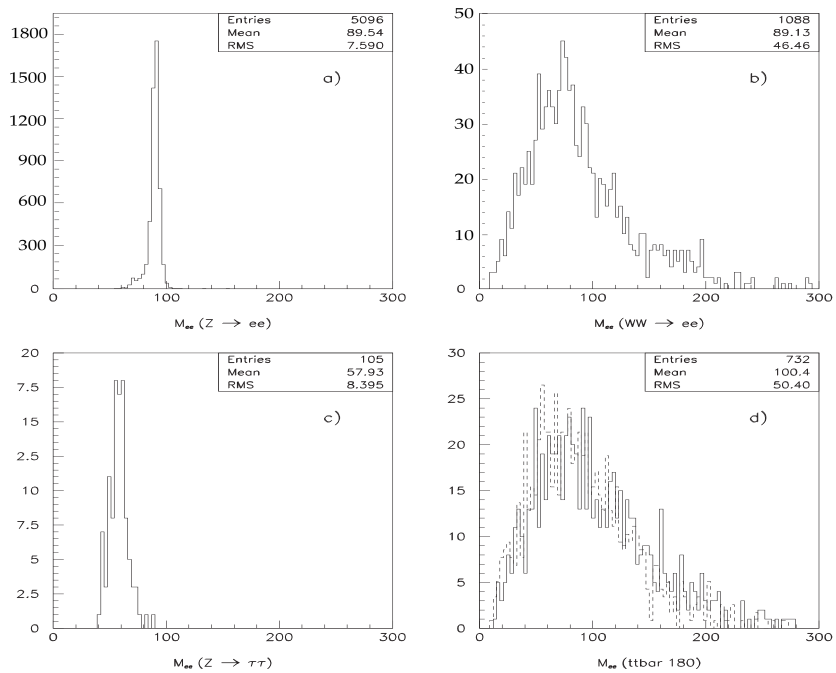

Figure 2.9: Dielectron invariant mass after requiring two electrons with $E_T >$ 20 GeV for (a) $Z \rightarrow ee$, (b) $WW \rightarrow ee$, (c) $Z \rightarrow \tau\tau$, and (d) top of mass 140 GeV/c^2 (dashed) and 180 GeV/c^2 (solid).

b. High p_T Jets in Heavy Top Production:

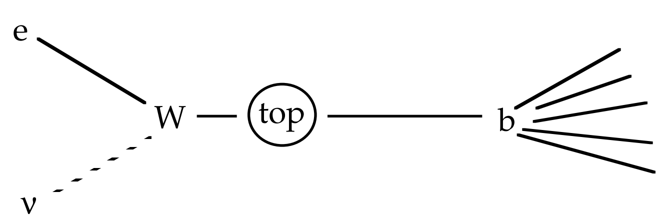

Figure 2.10: Schematic of top decay in center-of-momentum frame.

For top masses near the $W + b$ threshold, there is only enough energy to produce the b quark without giving it much momentum (Figure 2.10). As m_{top} climbs above 120 GeV/c^2, however, the percentage of events in which both b-quarks give rise to identifiable jets above 10 GeV is large. For even higher masses, these jets become a good discriminator against backgrounds in addition to cuts on the leptonic quantities. The reason for this is that we have removed the QCD heavy flavor background using our lepton isolation and E_T cuts. What is left, W and Z production mostly, contains isolated leptons but with steeply falling associated jet production due to initial state radiation.

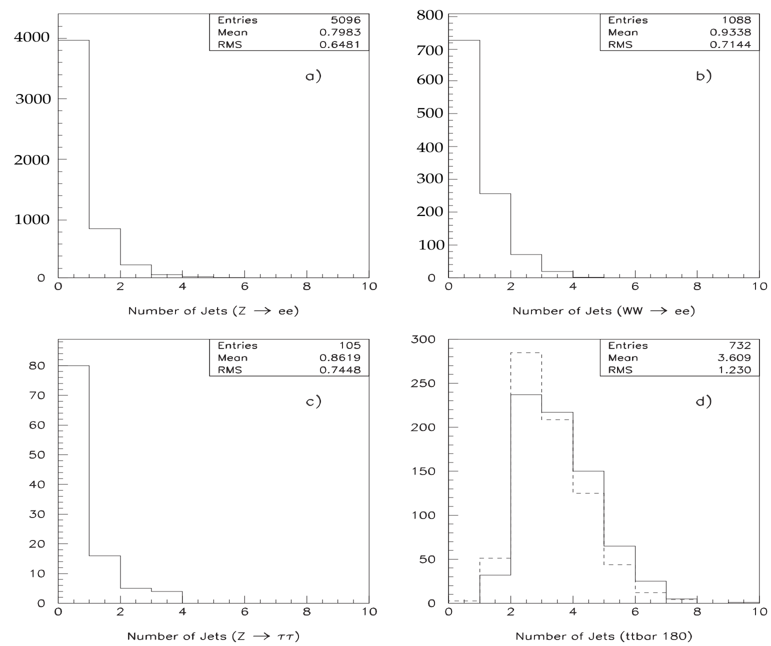

Figure 2.11: Number of reconstructed jets after requiring two electrons with $E_T > 20$ GeV for (a) $Z \longrightarrow ee$, (b) $WW \longrightarrow ee$, (c) $Z \longrightarrow \tau\tau$, and (d) top of mass 140 GeV/c^2 (dashed) and 180 GeV/c^2 (solid).

In Figures 2.11 through 2.13, the jet kinematic properties of a $t\bar{t}$ event are compared to those of the physics backgrounds as before. For the top quark plots, a histogram for a mass of 200 GeV/c^2 is added in Figures 2.12 to 2.13. Since their production mechanisms are the same, the jet multiplicity between Z to ee and Z to $\tau\tau$ is very similar as are the jet spectra. Of those backgrounds which have at least one jet in the final state, only ~20% have a second jet (see Figure 2.13a-c). As shown in Figure 2.11d, for top with a mass of 180 GeV/c^2, approximately 95% have a second jet.

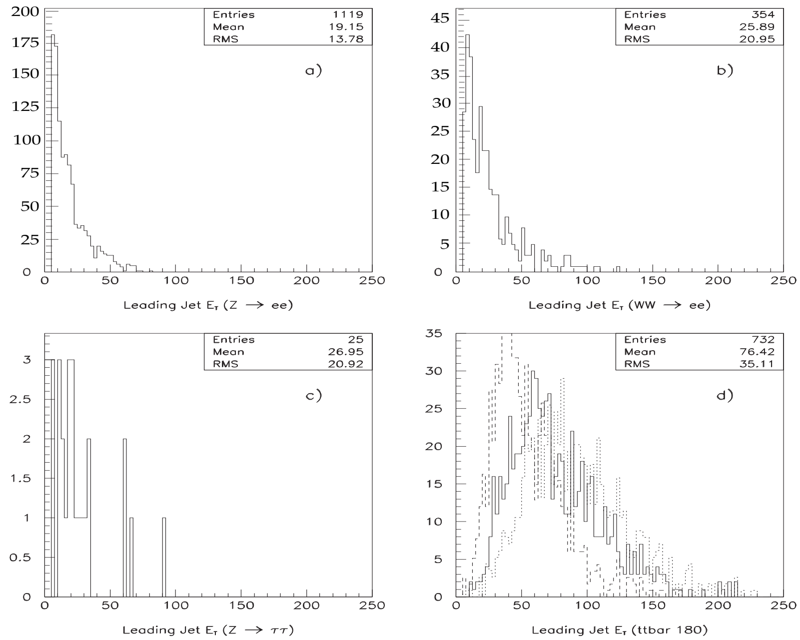

Figure 2.12: Leading jet E_T after requiring two electrons with $E_T > 20$ GeV and 1 jet with $E_T > 5$ GeV for (a) $Z \longrightarrow ee$, (b) $WW \longrightarrow ee$, (c) $Z \longrightarrow \tau\tau$, and (d) top of mass 140 GeV/c^2 (dashed), top of mass 180 GeV/c^2 (solid), and 200 GeV/c^2 (dotted).

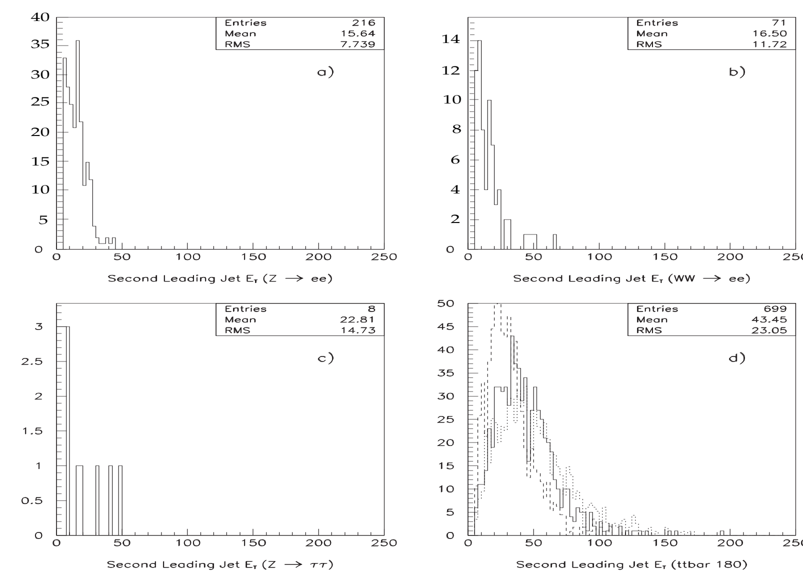

Figure 2.13: Second leading jet E_T after requiring two electrons with $E_T > 20$ GeV, 1 jet with $E_T > 15$ GeV and a second jet with $E_T > 5$ GeV for (a) $Z \longrightarrow ee$, (b) $WW \longrightarrow ee$, (c) $Z \longrightarrow \tau\tau$, and (d) top of mass 140 GeV/c^2 (dashed), 180 GeV/c^2 (solid), and 200 GeV/c^2(dotted).

c. Strategy

Given the nature of the backgrounds we face, a general strategy can be developed. In order to reduce the QCD background with two electromagnetic jets and to reduce the heavy flavor background, we will require two high E_T good electron candidates which are isolated from hadronic activity. From Figure 6, we see that $\not\!\!E_T$ is a good way to remove Z backgrounds and the dielectron invariant mass may be useful there as well. Lastly, to reject all backgrounds by another large factor, we can resort to a requirement ot two high E_T jets as shown in Figures 2.11 through 2.13.

CHAPTER 3

EXPERIMENTAL APPARATUS

1. Fermilab $p\bar{p}$ Collider -

The superconducting proton-antiproton synchrotron at Fermilab, named the Tevatron, is currently the highest energy particle accelerator in the world, delivering protons and antiprotons at 900 GeV. The combination of highest energy in the center-of-momentum system and highest instantaneous luminosity has allowed us to glean important clues concerning the fundamental interactions of particles at short distances. This feat requires seven stages of acceleration and particle production[36] (see Figure 3.1).

a. Proton Production

In the first stage, H^- ions from a plasma source are accelerated to 750 kV in a Cockroft-Walton generator. A linear accelerator ('linac') stage then brings these ions to 400 MeV (was 200 MeV in Run 1a). The beam is also focused in this stage by quadrupole magnets which are an integral part of the drift tube structure of the linac.

To accelerate to high energies with high efficiency requires an additional accelerator stage called the Booster. The H^- ions come into the Booster and are brought into parallel paths with protons already in the machine (from previous fills) in a straight section of the accelerator. These two beams are then merged and passed through a carbon foil to remove the electrons from the H^- ions. There are 84 potential RF buckets in the Booster, of which a maximum of 83 are filled. This occurs when the Booster is being used as a source of protons for antiproton stacking (see below). Otherwise, when producing protons for Tevatron collisions the Booster runs with 11, 13, or 15 bunches.

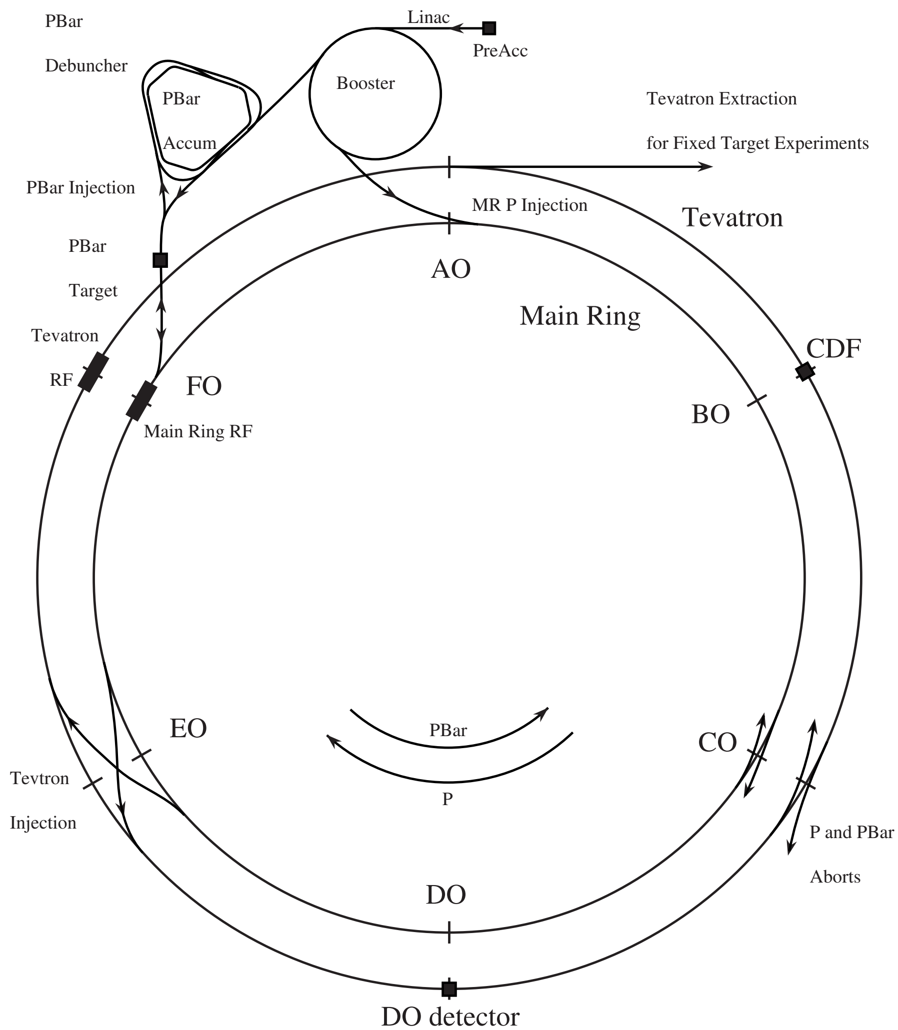

Figure 3.1: Schematic view of accelerator showing Main Ring and Tevatron and various acceleration stages.

b. The Main Ring

Next is the 'Main Ring' which was the world's highest energy accelerator before the Tevatron came online in 1983. It was used in Run 1 to bring protons and antiprotons to 150 GeV for injection into the Tevatron, and to accelerate protons to 120 GeV for antiproton production. Several aspects of the Main Ring, its interface with other accelerators, and its behavior in the vicinity of DØ are important for this analysis. This accelerator accepts protons from the Booster but there are losses because of phase space mismatches between bunches in the two. Also, the Main Ring does not operate with a well controlled magnetic field at the initial injection momentum of 8 GeV/c and this results in losses. Once in the Main Ring, the energy of the beam is increased to 150 GeV (120 GeV if stacking) and held constant. During this increase in energy a transition point occurs in the beam in which the RF phase must be changed because the particles are becoming increasingly relativistic. During this change, the beam is unstable (transition at 17.6 GeV in Main Ring or ~ 0.3 seconds after injection) and beam losses are again large. Next, different Booster bunches are coalesced into larger bunches -- about 1.5×10^{11} protons or 0.8×10^{10} antiprotons per bunch. Before these bunches can be injected into the Tevatron, the two accelerators must be 'cogged'. Timing markers, called Main Ring Beam Sync (MRBS) and Tevatron Beam Sync (TVBS), are aligned so injection can occur into a Tevatron RF bucket. During antiproton stacking, the protons are sent into the Antiproton Source while collisons are occuring in the Tevatron. The cycle for this process requires 2.4 seconds and then can begin again.

c. Antiproton Production

The Antiproton Source consists of a target, a Debuncher, and an Accumulator and in several ways it mimics the optics of the proton Booster so the interface with the Main Ring is similar. Eighty three proton bunches from the Main Ring are directed onto a nickel target from which 10^7

antiprotons are produced for every 10^{12} incident protons. The antiprotons then pass through a lithium lens which focuses them to parallel paths. Those with momenta of about 8 GeV/c are retained with an initial momentum spread of about 4% which is reduced to 0.2% in the Debuncher by stochastic cooling. In the Accumulator, further cooling occurs and a subset of the antiprotons may be extracted to make single bunches for the Tevatron via the Main Ring.

d. Collisions and the Tevatron

The final stage in the life of a proton or antiproton comes when it is annihilated in a collision with its antiparticle at 1.8 TeV. The Tevatron consists of superconducting magnets cooled to 4.6^{o}K. Because the Tevatron is very similar in structure to the Main Ring, nearly 100% of the beam is successfully transfered from one to the other (more like 85% to go from Booster or Accumulator to Main Ring). First 6 proton bunches are injected into the Tevatron, then 6 antiproton bunches are injected, and all are ramped up from 150 GeV to 900 GeV. The beam structure within the Tevatron after both protons and antiprotons are present is very complex. The bunches have significant tails transverse to the beam which can harm tracking detectors if these are operating at full voltage, and additionally can produce unwanted background interactions. Scraping is performed to remove these tails and then the beams are focused down to initiate collisions. The orbits of protons and antiprotons are kept separate by electrostatic separators which operate in the horizontal (x) and vertical (y) directions. The bunches trace helical paths around the Tevatron separated by more than 5σ of their RMS width but within 15 mm of each other. These paths intersect only at the DØ and BØ interaction regions.

The beams can be focused down at the two interaction regions, DØ and BØ, with a transverse size of the beam being about 40μm. Quadrupole magnets inserted at each end of the collider detectors focus the bunches to the interaction region at the center of the detectors. To keep the collision regions small, the beams do not exactly collide head-on, and hence there is a diamond shaped region in which the two beams actually intercept each other. The point at which the beams have a maximum transverse overlap is approximately at the center of the detector. It is also at the center of the detector that the quadrupoles are tuned to minimize the transverse width of each beam. The resulting longitudinal vertex distribution obtained in Run 1 data was centered on $z \sim 0$ cm with $\sigma_z \sim 30$ cm.

e. Main Ring Losses During Collisions

Ideally, only the Tevatron beams would be directed toward and pass through the DØ detector. However, spatial separation of the Main Ring and Tevatron is only about 1m. Unless a bypass is constructed to bring the Main Ring away from the experiment, it too will pass through the detector. Losses from the Main Ring will then leave energy or hits in the various detectors through which it passes. In the DØ case, funds were not available at the laboratory during the era of detector construction to build a full bypass. Instead, a partial overpass was constructed to bring the Main Ring through less crucial regions of the calorimeter (the coarse hadronic sections) and muon systems. This has consequences for detector operation, data taking, and impacts directly the total integrated luminosity or experimental 'live' time available for effective data analysis.

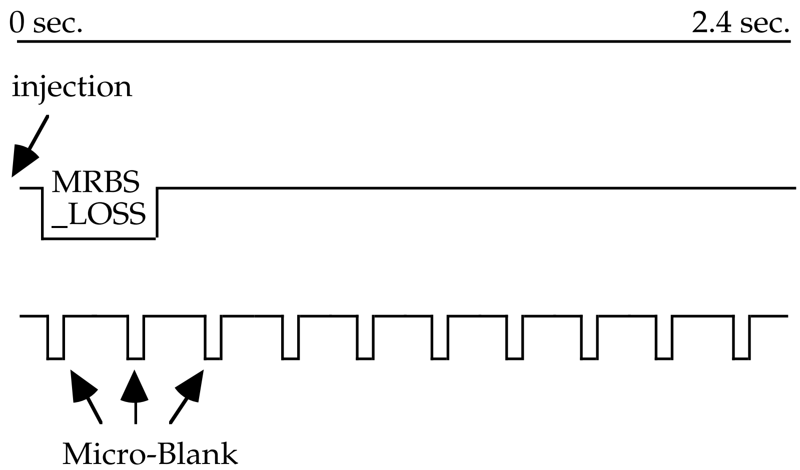

Figure 3.2: Gating structure of Main Ring cycle with respect to Tevatron timing. Neither the width of the gates nor the frequency of μBLANK gates is shown to scale.

The worst losses occur when protons are injected into the Main Ring. We flag events that are taken between 0.1 seconds and 0.5 seconds after proton injection with the 'MRBS_LOSS' designation. This flag is set for about 17% of all Tevatron crossings when stacking is occurring. We also flag events taken within 800 nsec of the passage of a Main Ring bunch through DØ. This 'micro-blank' ('μBLANK') flag is set for 8% of all Tevatron beam crossings when the Main Ring is stacking. The timing of Main Ring states is shown schematically in Figure 3.2.

Most analyses use only events for which the GOOD_BEAM term is set, which requires that neither the MRBS_LOSS nor the μBLANK flags are set. However, partly because of corrective actions developed as a part of this dissertation work, we will use all data in this analysis except for those events in which *both* the MRBS_LOSS and μBLANK flags are set, which is about 2% of all data. Special care must be taken in interpreting data reconstructed when a particle flux is present in the Main Ring. The dielectron analysis in this thesis is the first published analysis at DØ to include MRBS_LOSS data[37].

2. General Overview of the DØ Detector:

In general, a collider detector consists of inner tracking detectors which allow for vertex measurement and charged particle direction measurement. Outside of this is typically a thick calorimeter which measures the energies of all particles. If the calorimeter is hermetic, it can be used to identify missing energy resulting from escaping neutrinos. Charged particles which penetrate the calorimetry are detected in surrounding muon detectors.

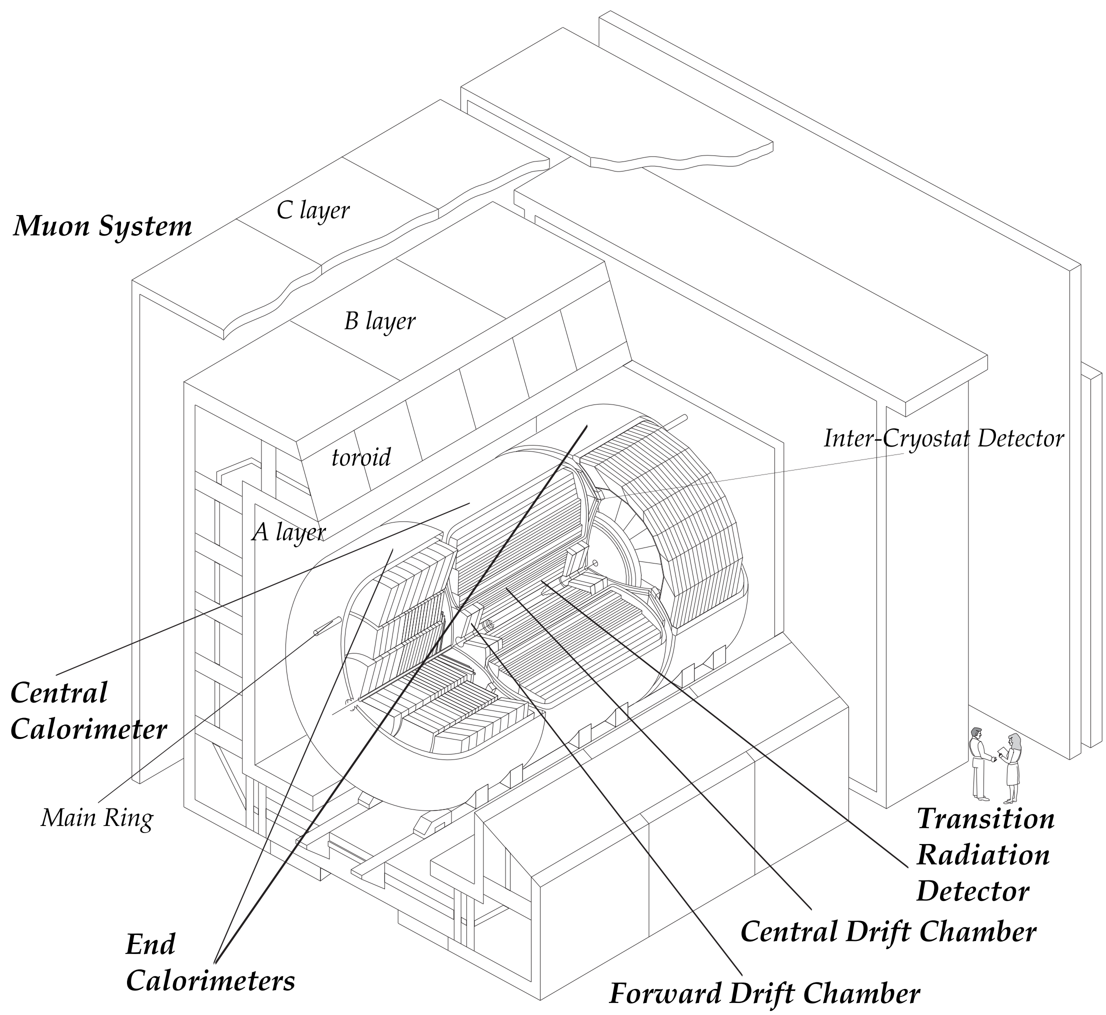

Figure 3.3: Isometric view of DØ detector.

The DØ detector, shown in Figure 3.3, includes each of these subsystems but emphasizes those aspects which will allow good measurement of high p_T objects over a substantial solid angle. In particular, strong emphasis has been placed on calorimetry which has the characteristic that the fractional resolution improves with increasing particle energy. This is in contrast to momentum measurements from tracking in a magnetic field which gives a resolution which degrades with increasing energy. The detector is compact since there is no central magnetic field, has approximately 4π coverage, and emphasizes hermetic coverage. This design is inspired by the phenomena we most want to identify, which require energy or momentum vector measurements of jets, electrons, photons, muons, and neutrinos (via good $\not{E}_T$ measurement).

The detector itself consists of inner tracking detectors, electromagnetic and hadronic U/LAr calorimeters, and outer muon detectors. The inner detectors are all drift chambers and have good spatial resolution for tracking and provide transition radiation and dE/dx measurements for electron identification. There is no magnetic field within the inner detector region so that momentum is not measured there. The calorimetry has good energy resolution and is used for electron, photon, and jet identification. A design goal of the calorimetry is to provide for good single electron energy resolution, and full detector coverage and hermeticity allows for good $\not{E}_T$ resolution. The muon detectors, which are a series of planes of drift tubes placed before and after an iron toroid magnet, measure the momentum and charge of muons as these particles emerge from the inner detectors and calorimetry.

The coordinate system we use has its origin at the center of the detector where (r,z) = (0,0). The azimuthal angle, ϕ, sweeps through the plane perpendicular to the incoming beams, and the polar angle, θ, passes from 0 to π when going from the proton beam to the antiproton beam. A more useful angular variable which we use often is the *pseudorapidity*, $\eta = -\ln(\tan(\frac{\theta}{2}))$.

3. Tracking:

The inner tracker is composed of 5.7 thousand channels and is used for reconstruction of charged tracks and particle identification. It is composed of central and forward drift chambers (CDC and FDC), and a vertex detector (VTX) which are shown in Figure 3.4. Each detector possesses the ability to measure both track-match quality (to a reconstructed electromagnetic cluster), and ionization along the track. Both quantities aid in rejection of fake electrons. The position resolutions for these devices are given in Table 3.1.

Table 3.1. Position resolutions of various tracking detectors.

Detector	**z resol.**	**rdϕ**	**rϕ*** **
CDC	3mm**	160μm*	3mm
FDC	3mm	200μm	3mm
VTX	4 - 15mm**	30 - 80μm*	~1mm

* drift direction
** wire direction
*** two track resolving power

a. CDC/FDC

The central and forward drift chambers achieve 3-dimensional tracking coverage over the interval $0 \leq |\eta| \leq 3.5$. They are therefore used to determine the positions, especially in z, of the primary vertices in an event. In each drift chamber cell, there are sense-wires which measure the track coordinate perpendicular to the wire, and there is one delay line which uses timing of the hits to determine the position along the sense-wire. Overall, these give good spatial resolution for tracking of electrons and muons.

The CDC provides track measurement in the $|\eta| < 1.0$ region and consists of four layers of drift cells staggered by half the cell width for two-track resolution. Each cell possesses seven sense wires. The radius of the inner layer is 40.5 cm while that of the outer layer is 68.0 cm. The length of the active region is 148 cm. The drift distance is less than 7 cm in CDC cells.

The FDCs cover the region $1.0 \leq |\eta| \leq 3.5$ and are composed of 16 radial cells for measurements of ϕ, and drift tubes for azimuthal (θ) measurements. The θ tubes have 8 sense wires and are divided into two sections before and after the radial tubes. These two sections are staggered by 45° in ϕ to avoid inefficiency due to cracks and to provide redundancy.

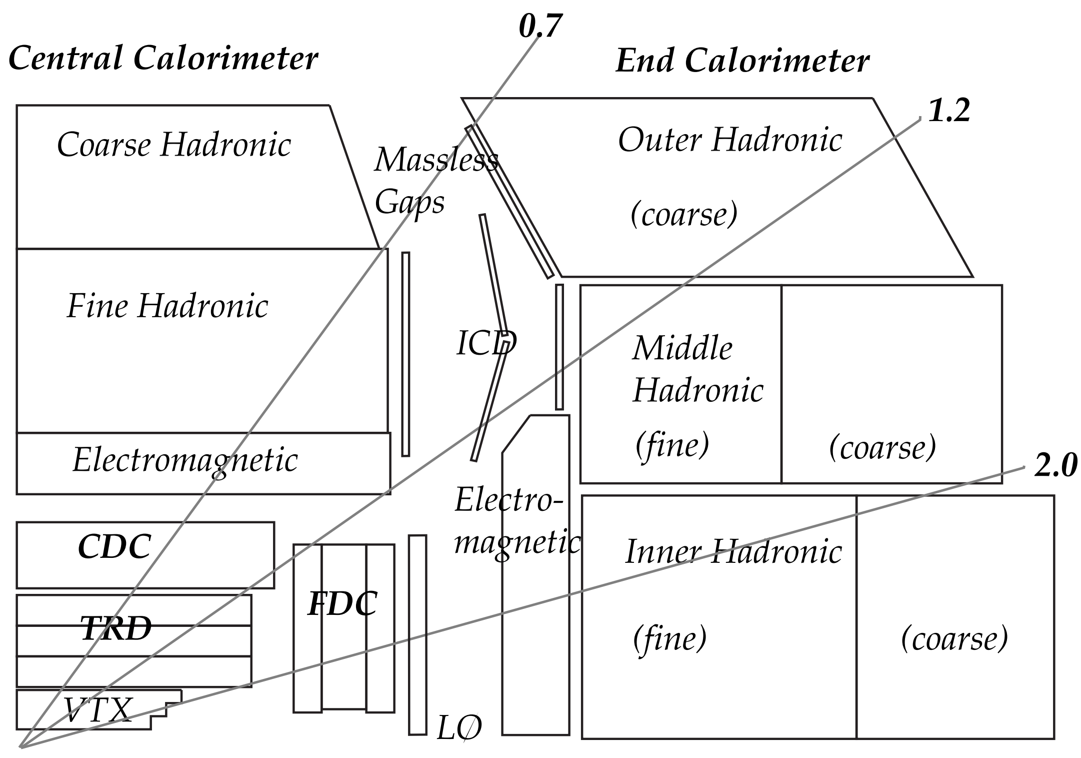

Figure 3.4: Cross sectional view of quadrant of tracking and calorimeter systems.

b. VTX

The vertex drift chamber is composed of three axial supercells which provide track segments. The supercells have 8 sense wires and use a low drift velocity gas. The longitudinal coordinate (z) is measured by timing comparison of electronic signals from both ends of the sense wires. Unfortunately, the observed resolution in z for this detector is poor, hence it cannot be reliably used to determine this coordinate for the primary vertex position of an event. Also, the 3-dimensional tracking efficiency is low. As a result, we limit our use of the VTX in this analysis to the region $1.0 \leq |\eta| \leq 1.7$ which has little or no drift chamber coverage. Outside of this region the VTX augments the CDC and FDC tracking measurements.

4. Transition Radiation Detector

a. Design

The transition radiation detector (TRD) is positioned radially between the CDC and VTX as in Figure 3.4. As the only detector built explicitly to be sensitive to the velocity of a charged particle, it is used for e-π discrimination. The way it accomplishes this is by producing transition radiation X-rays for particles with $\gamma > 800$. The structure of the detector is dictated by the need to be sufficiently dense to generate intense X-rays (intensity $\propto Z^{1/2}$ where Z is the atomic number) while still being sufficiently thin to allow the propagation of this radiation through the radiator material to a detection medium (absorption $\propto Z^5$).

To accomplish the design goals efficiently, there are three structurally identical layers each consisting of radiators, Xe gas converters, and drift chambers. A particle first passes through each layer intersecting a series of concentric sets of thin polypropylene foils. The constantly changing dielectric constant in this region (foil-gap-foil-gap) results in transition radiation being generated for high γ particles. Produced X-rays that traverse the region containing the radiator stacks and through an aluminized mylar window emerge into an X-ray conversion region filled with gaseous Xe (high Z) which is the initial part of a proportional wire chamber (PWC) for each layer. The ionization produced drifts out to the anodes and cathodes of the PWC. The primary information used is the total ionization collected on the anodes which discriminates between electrons and pions. These anode planes are segmented in azimuth into 256 *sectors* for the inner two layers and 512 sectors for the outer layer. Because of low gain (small signal) at the cathodes, they are only used as a cross-check in this analysis.

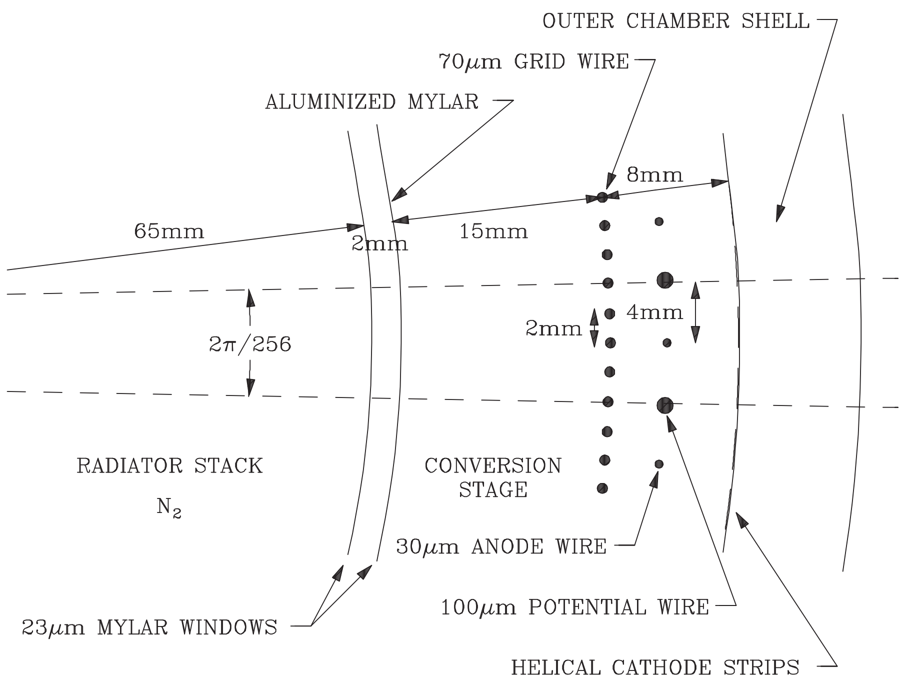

Figure 3.5: Cross section view of TRD layer 1.

b. Calibration and Monitoring

The gain of a particular chamber depends on the high voltage, temperature and pressure of the Xe gas mixture, and the electronics gain. Of these, the gas quality has a tendency to vary significantly thereby worsening the resolution. This variation is monitored with a signal produced by radiation from the decay of uranium in the calorimeter absorber. This radiation causes a fluorescence in the TRD Xe with an energy of 30 keV which leaves ionization in the drift chamber portion of the device. Since the energy of this photon is known, monitoring it indicates the quality of the gas. Dedicated 'uranium runs' are then taken when no beam is in the accelerator to monitor the gas quality.

c. Forward Coverage

Although the TRD was designed to cover only electrons found in the Central Cryostat (CC) and CDC, it turns out that significant coverage in the forward region exists for this detector albeit with fewer layers. We have noted that there are considerable nonuniformities in the tracking coverage in the region $1.0 < |\eta| < 2.0$. The addition of TRD information can assist in strengthening the identification of electrons in this region. If one considers the TRD acceptance, we find that nearly all CDC/CC electrons are within the acceptance of 3 TRD layers (by design). Nearly all VTX-only tracks are covered by at least 2 TRD layers. Lastly, a large portion of FDC electrons are covered by at least layer 1 of the TRD. Overall, the TRD covers nearly all of the CC, and additionally covers ~50% of all EC electromagnetic clusters depending on physics sample. This issue of the proper functioning of the TRD in the forward region is explored at length in Appendix III.

In addition to the difficulty in performing tracking in the forward region, it should be noted that the TRD has qualities which uniquely qualify it for forward electron identification. Electron backgrounds from hadrons increase in the forward region and it is just these backgrounds the TRD was designed to distinguish. Also, test beam studies have clearly indicated improved e-π separation for high-η tracks compared with central ones[38].

5. Calorimetry:

a. Central and End Calorimeters

The heart of the DØ detector consists of the three 'sampling' calorimeters (see Figures 3.3 and 3.4) which provide good energy measurement for e, γ, jets, and ν's (via missing E_T), and at least partial particle identification for all of these plus muons. Each calorimeter is a large stainless steel cryogenic vessel containing alternating layers of absorber and signal boards immersed in liquid Argon (see Figure 3.6). These detectors are each divided into an inner electromagnetic (EM) compartment, followed by a fine hadronic (FH) compartment, and lastly an outer coarse hadronic (CH) compartment.

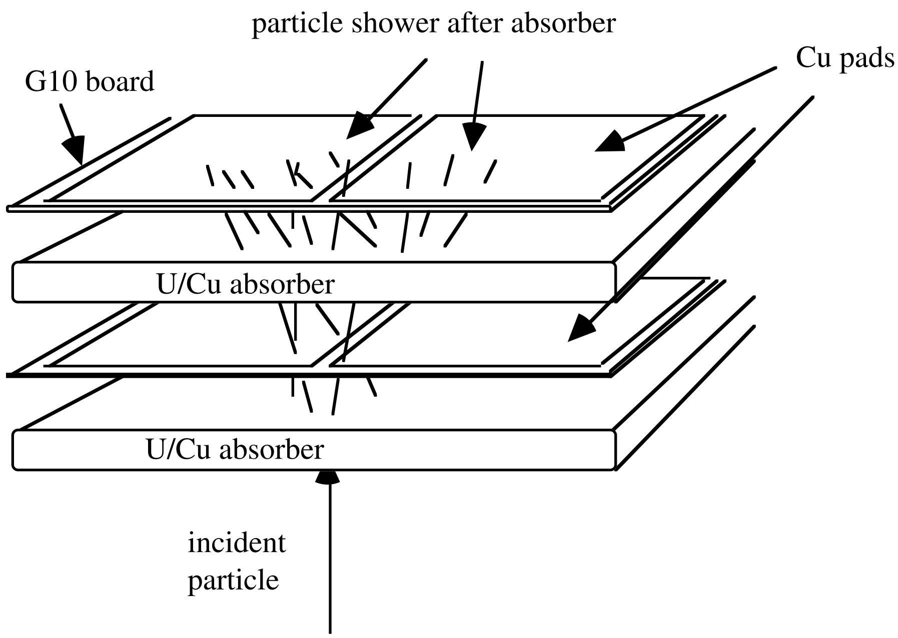

Figure 3.6: Single layer of absorber and readout board.

Uranium has been used as the absorber for most of the layers in part because it was shown to give better E_T resolution than Fe[39]. In addition, the high density of U allows a compactness of design which has aided in reducing cost as well as backgrounds in the muon system, although it adds significantly to the noise distribution in the calorimeter. The EM compartments contain four readout layers with 3 mm thick U plates. The fine hadronic compartments are composed of 3 layers of 6 mm thick U or Cu plates. The coarse hadronic compartment has one [three] layer of 46.5 mm thick Cu or steel plates in the Central [End] Calorimeter. The total depth of the EM absorber is 20.5 [21] X_0 in the Central [End] Calorimeter, while the total depth of the calorimeter in absorption lengths is 6.93 λ_0 at $\theta = 90^{\circ}$ and 8.9 λ_0 at $\theta = 11^{\circ}$.

After each plate of absorber is a liquid Argon gap containing a sheet of G10 which is 0.022 inch thick and has a thin layer of Cu etched in pads which are 0.1 x 0.1 in η and ϕ. The third EM layer corresponds with electron shower maximum so it is more finely segmented in $\eta-\phi$ to 0.05 x 0.05. This helps in position resolution and shower shape discrimination for electron and photon identification. Particle showers in the absorber produce ionization in the liquid Argon gaps which is readout on the Cu pads. Pads from consecutive layers then register the shower development in a projective tower geometry. A schematic of the η index ('IETA') and layer of the cells in the calorimeter is given in Figure 3.7. The Central Calorimeter (CC) covers the region $|\eta| < 1.1$ while the two End Calorimeters (ECs), which are of similar construction, cover the region $0.7 < |\eta| < 4.4$ (see Figure 3.4, 3.7).

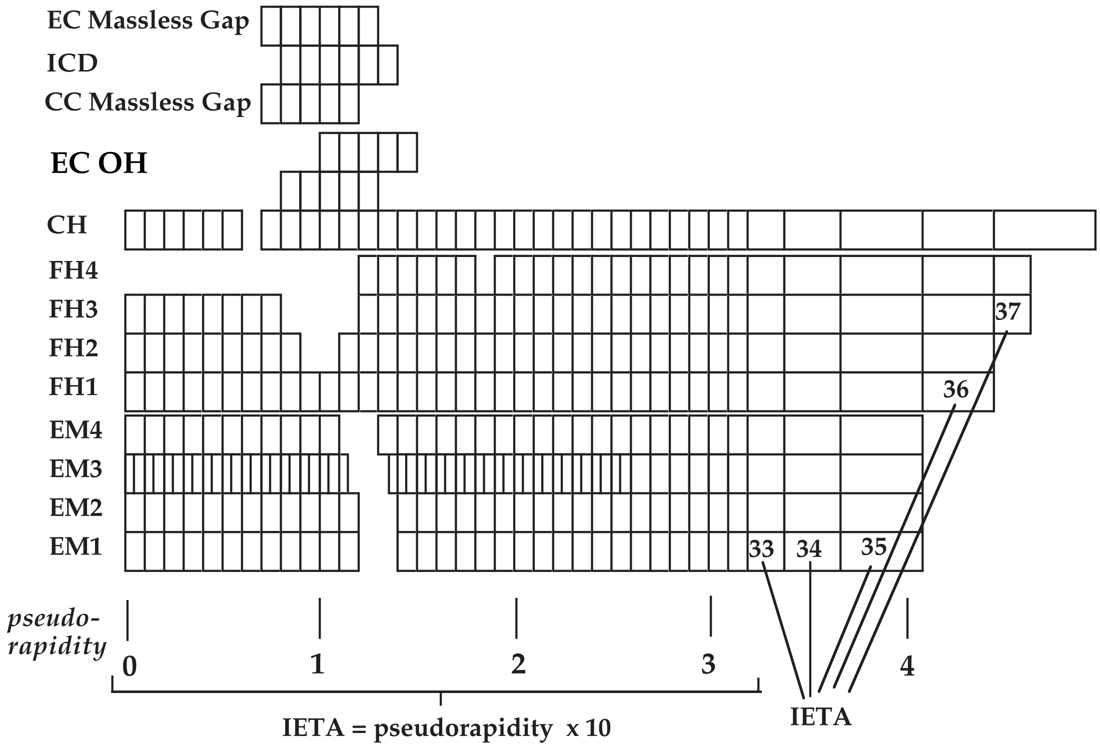

Figure 3.7: Schematic of η index, IETA, for various calorimeter cells. IETA $=10 \times \eta$ until $|\eta| < 3.2$.

Each cell in the calorimeter is sampled ten times just prior to a Tevatron crossing. The mean charge of these measurements is referred to as the 'baseline' and is subtracted from the charge measured during the crossing by 'baseline subtractors' (BLS). The remaining charge is readout only if it is further from zero than 2σ of the noise for that particular cell.

b. Energy Response and Resolution

Given that there is no central magnetic field in the tracking volume to allow us to measure the momenta of particles hitting the calorimeter, significant attention has been spent on calibrating the detector based on test beam studies. Although most of the charge produced by a particle's interaction with the absorber does not make it out of the absorber, some fraction does pass into the liquid Argon gap and is read out. The process of reading out only some of the charge at discreet points along the particle trajectory is termed 'sampling' and affects the way we calibrate the detector. The registered charge in each of the readout layers must be corrected by 'sampling weights' which allow one to estimate the total signal produced from the charge measured. As an approximation, one could envision these weights being equal to the fraction of material in the Argon gaps *vs*. the material in the absorber plus gaps ('dE/dx weights').

The determination of the sampling weights was performed using test beam data. For electrons the layer-to-layer weights were tuned in such a way as to give the best combination of resolution and linearity of response. In the process, the overall ADC-to-GeV conversion for all cells was determined. The layer-to-layer sampling weights in the hadronic sections are dE/dx weights.

Although there is no amplification or 'gain' in the calorimeter signal, time-dependence of the calorimeter response could occur due to changing purity of the liquid Argon and due to high voltage supplies which do not maintain their calibration. Given that the calorimeter is so important to the physics at DØ, these issues have been monitored throughout the collider Run.

The high voltage setting for the 136 power supplies of the CC and EC was 2kV and was set for each power supply at the beginning of the run. Each power supply internally regulates its voltage but this internal calibration can wander. Therefore, the calibration was periodically checked throughout the run with an electrostatic voltmeter. Nearly all modules were within 5 V of the nominal 2.0 kV but were recalibrated to within 0.3 V. Those that were outside of this range were rare but in a couple of cases during the run, shifts of 100 V to 200 V were noted. Rarely, a power supply did not hold voltage again after it had been brought to 0 V. These were replaced. Because even the largest changes correspond to very small changes in particle response[38] there is essentially no time dependence to the detector calibration for these variations.

The purity of the LAr is essential for the good performance of the calorimeter. For the duration of the data run, the response of the calorimeter has been monitored by α and β radioactive sources which create ionization in several gaps in each of the three cryostats. The response has been measured to be very stable and the purity is better than 0.7 ppm.

Overall, the energy response has been measured in test beams to be linear to 0.5% as shown in Figure 3.8. Furthermore, the ratio of electron to pion response has been measured to be within 10% of unity for momenta greater than 10 GeV/c as shown in Figure 3.9. For comparison, Figure 3.9 also indicates the predicted ratio of electron and pion response using the GEANT library of detector simulation software. The GEANT simulation accurately models the detector. To understand the qualitative behavior, we consider that e/π has a dependence on particle energy given by the parametrization,

$$\frac{e}{\pi} = \frac{1}{\left[F_{EM} + (1 - F_{EM})R_h\right]} \qquad \textbf{Eq. 3.1.}$$

where $F_{EM} = a_0 \ln(E_\pi)$ (see Appendix IV)[40]. Here R_h is the fundamental response of the calorimeter to purely hadronic energy relative to electromagnetic energy, or, stated differently, the response to particles interacting with the calorimeter only via nuclear absorption *vs.* that to particles interacting only electromagnetically. Plugging F_{EM} in gives

$$R_{\pi^{\pm}} = \left[\frac{e}{\pi}\right]^{-1} = \alpha + \beta \ln E_{\pi^{\pm}} \qquad \textbf{Eq. 3.2.}$$

which is the behavior shown in Figure 3.9.

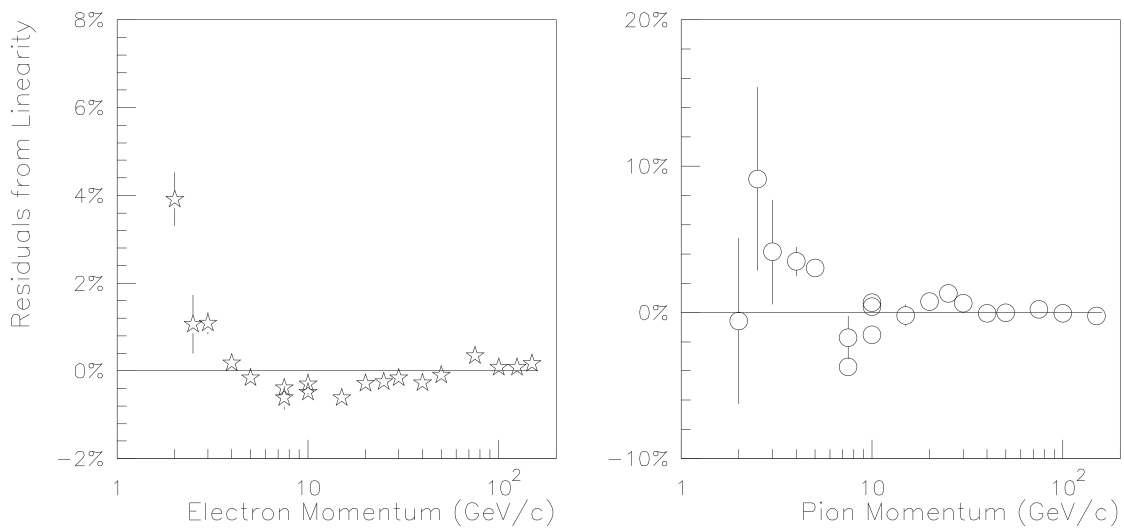

Figure 3.8: Linearity of response for electrons and pions in Central Calorimeter test beam.

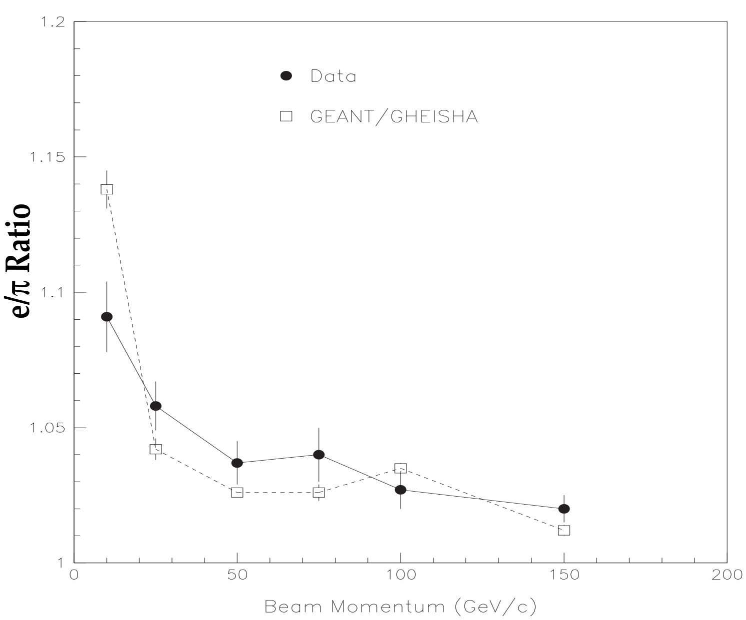

Figure 3.9: e/π response ratio *vs*. beam momentum for EC test beam.

As mentioned, the sampling weights were designed to optimize the energy resolution of the calorimeter for electrons and pions. The energy resolution of the CC from a calibration measurement[41] using the electron test beam was found to be

$$\sigma_{EM} = 0.003 + 0.13/\sqrt{E} + 0.42/E$$

where E is the particle energy in GeV. The energy resolution as measured from the pion test beam is:

$$\sigma_{had} = 0.04 + 0.48/\sqrt{E} + 2.0/E$$

d. Inter-Cryostat Region

Although the CC and EC coverages overlap, there is a region, $0.8 < |\eta| < 1.5$, which is not thoroughly instrumented to detect charge from showering in the edges of absorber plates and cryostat walls. This causes a degradation in $\not{E}_T$ resolution and jet E_T measurements. To compensate for this, boards, called 'Massless Gaps' (MG), are installed at the inner walls of both CC and EC facing the gap. In addition, a series of scintillator tiles comprising the Inter-Cryostat Detector (ICD) have been mounted on the inward facing wall of the EC. Together, the ICD and MG help greatly in recovering a potential loss in energy resolution and in avoiding compromise of $\not{E}_T$ measurements.

e. Effect of Main Ring

Losses from the Main Ring can occur which are either in the form of large positive signals if they coincide with a Tevatron beam crossing or in the form of negative signals for Tevatron beam crossings which were preceded by Main Ring losses. In the former case, positive energy deposition results in fake $\not{E}_T$ which is π radians away from the Main Ring and can create fake jet backgrounds in the calorimeter. Negative energy results when the output of the calorimeter preamps slowly decreases toward zero so that the difference between the peak and baseline sample is negative. This gives rise to fake $\not{E}_T$ in the direction of the Main Ring and can result in an inefficiency for jet reconstruction by nullifying positive energy from real jets.

6. Muon Detection:

At DØ, muon tracking and identification employ a series of inner Proportional Drift Tube (PDT) planes, magnetized iron toroids, and outer PDT planes covering $|\eta| < 3.2$ (see Figure 3.3). The wide angle muon system (WAMUS) covers the area of $|\eta| < 2.4$ while the small angle muon system modules (SAMUS) are used to track muons in the region $1.7 < |\eta| < 3.2$. In WAMUS, the inner PDT's are arranged in four wire planes while the outer drift tubes are divided up into two layers of three wire planes each and separated by about 136 cm. WAMUS is also divided into central (CF) and forward (EF) regions which have a boundary approximately at $|\eta| = 1.1$.

Toroidal iron magnets provide a magnetic field of 1.9T which allows momentum determination for muons which penetrate the muon system steel. The field is contained within the toroids; the residual field is essentially zero at the beampipe $(r,z) = (0,0)$. The material thickness of the toroids in absorption lengths is $6.4\ \lambda_o$ at $\theta = 90^o$ and $9.1\ \lambda_o$ at $\theta = 11^o$. The total depth of material in the calorimeters plus the toroids is always over 12 absorption lengths so that there is little leakage of non-muon signals into the outer drift tubes. Rejection of instrumental backgrounds from hadrons faking muons exceeds 10^4 for $p > 10$ GeV/c thus allowing us to identify muons in the cores of jets. Limitations on $\delta p_\mu / p_\mu$ are multiple scattering in the calorimeter and toroid (~20%), and measurement error for the chamber hits on the track.

7. Hardware Trigger and Data Acquisition System:

The collision rates at the Tevatron are very high and require a data acquisition system which can pare the rate of writing good events to tape down to a manageable level. To accomplish this task, we first use a token ring setup to transfer data from the detectors. Data passes through a hardware trigger framework and farm of μVAXs for software filtering, and finally to the host computer cluster which then writes the passed data to tape. DØ employs a multilevel triggering scheme composed of 2 hardware triggers and one software trigger. The final rate out of this last level is about 3 events per second or approximately 1.2 megabyte/sec.

a. Level Ø

At the primal level are the 'Level Ø' scintillation counters which are arranged in arrays near the beampipe and mounted on the inside face of each endcap calorimeter (see Figure 3.4). These detectors determine that an inelastic scatter has occurred by requiring hits at both ends of the detector, and provide quick information on the primary event vertex by using timing differences of signal pulses in North and South scintillator arrays. The detector also serves as a luminosity monitor and is used to quickly distinguish multiple interactions from single interactions.

b. Level 1 Framework

Subsequent to Level Ø is the Level 1 trigger framework which houses hardware to process special fast readouts of the calorimeters and muon systems. There are 32 available trigger bits and basic decisions concerning η and E_T of muons, electrons and jets can be performed according to several programmed thresholds. Before every run, these trigger instructions and the detector hardware constants must be downloaded. In muon triggers, crude tracks are found in wide roads and events are selected based on the number of muons and their rapidity. A fast sampling of calorimeter energy in 0.2 x 0.2 'trigger' towers to $|\eta| < 3.2$ is available so that electrons and jets can be defined and identified as EM or EM+FH trigger towers. The input rate is approximately 280 kHz with a rate reduction of about 2000 to Level 2.

c. Level 2 Processor Farm:

After the hardware triggers have been applied, a μVAX Supervisor which has overall hardware control of the data acquisition system sends a 4 bit word to the Sequencer to ensure that both are synchronous on the same event. This Supervisor looks for a free Level 2 node, and when one is found it tells the Sequencer to begin the data transfer.

Level 2 has the event assembled from the signals of the different detectors, and some basic reconstruction is available via an executable downloaded before the beginning of data-taking. Software filters are defined and executed on several Level 2 microprocessor (μVAX) nodes which decide whether the digitized data is to be sent to the host computer cluster. Fast versions of reconstruction algorithms can be used to identify electrons, jets, and muons, as well as calculate $\not{E}_T$. Quality cuts on electrons such as the requirement of a track matching the EM cluster, isolation, and EM shower shape are available. With processing times varying between 200 msec and 5 sec, the input rate Level 2 can handle is about 180 Hz and the output rate to tape is approximately 3 Hz, as previously stated.

8. Dielectron Physics at DØ

A search for top in the dielectron channel exploits fully the detector's capabilities. Electrons are well measured in the Central and End Calorimeters and can be identified to very high $|\eta|$ using inner and forward tracking.

Tracking and calorimeter information are able to give low instrumental backgrounds with reasonable efficiency. The use of uranium and copper as calorimeter absorber has also allowed full longitudinal containment of hadronic showers. The hermiticity of the calorimetry provides good jet and $\not{E}_T$ resolution, and its linearity over a broad range of particle energies, particularly to low energies, aids in our control of the uncertainty in the energy scale in the absence of a magnetic central tracker.

CHAPTER 4

DATA COLLECTION AND REDUCTION

There are several issues with regard to the obtaining and handling of data which affect the physics study reported in this dissertation. A trigger has to be designed which has both high efficiency for top and significant rejection against the background processes which occur in $p\bar{p}$ collisions. The various run conditions must be understood, and the raw information must be reconstructed into the more meaningful objects like jets, $\not{E}_T$, etc. The effect of our reconstruction algorithms on our final physics must also be understood.

1. Data Quality and Stability

Table 4.1. Runs at which detector operating conditions changed along with percent integrated luminosity obtained prior to them.

run #	**%L**	**comment**
50226	0.000	first DØ run after comissioning
52470	0.001	calorimeter high-voltage reduced from 2.5 kV to 2.0 kV
54650	0.004	TRD properly functioning, MICRO_BLANK data recorded
~72000	0.125	first 1b collisions -- modifications to triggers, TRD outermost layer segmentation doubled
~80000	0.20	MRBS_LOSS data recorded
94000	0.912	first 1c collisions, -- ICD outer photomultiplier tubes failed

a. Run Stability

The DØ detector has been in operation for data taking at the Tevatron from August 1992 through February 1996 in what is termed 'Collider Run 1'. This run is actually divided into three different periods of accelerator running: 1a, 1b, and 1c. By far the majority of the integrated luminosity was obtained in the 1b period from January of 1994 through the summer of 1995. There are a handful of points in the collider run which mark a difference in detector status or whether Main Ring data was recorded. Table 4.1 lists those demarcation points (in terms of run number) during the run that are relevant for this analysis and gives the estimated amount of integrated luminosity in the run which occurred before them.

The alteration of the calorimeter high voltage and the loss of the outer ICD channels were both minor effects and treatable with suitable adjustments to the sampling weights applied to respective cell energies in the reconstruction. The TRD suffered from problems in its gas system during the very early part of the run and cannot be used for that data. The beginning of Run 1b is when somewhat tighter triggers were instituted.

b. Bad Runs

Although the detector and data acquisition systems performed remarkably well during the entire run, there were occasions in which data were corrupted or there was a detector malfunction. In some cases the problem was minor or irrelevant, in others the data quality or luminosity measurement was compromised. As a result, a list of suspect runs had to be generated and the runs classified. The overriding concerns for this list were: whether the relevant detectors were operating, whether the data was corrupted, and whether the luminosity measurement was accurate.

In many cases, a run which was flagged online to have some problem turned out to be recoverable offline. This occurs, for instance, when there were cells in the calorimeter which fired abnormally often ('noisy cells') and/or fired consistently with an unusually high amount of energy ('hot cells'). Often, a simple algorithm or offline selection is able to either correct for these cells or remove them. Another non-fatal situation occurs when a particular problem results in deadtime for the detector. For instance, when one detector's high voltage trips, data-taking and the integration of luminosity stops for the experiment until the problem is fixed. In this case, no compromised data is recorded and the luminosity is properly calculated. Thus, runs which seem fine but have data acquisition problems or overall high trigger rates, etc. are kept.

If the data quality is compromised in a non-trivial way, however, the run is rejected as bad. For instance, runs with seemingly hot cells are rejected if a calorimeter BLS card is suspected which caused a large change in some trigger rate. In such a case, the data written to tape is biased and difficult to evaluate on the same footing as normal data. Also, the run is rejected if the deadtime is believed to have been improperly dealt with in the luminosity.

Lastly, certain detectors are not rigorously required to function. For instance, a bad SAMUS, VTX, or TRD is not enough to reject a run. The first two are either not used or minimally used in this analysis, and the third is taken care of by internal bookkeeping in the determination of the acceptance for the standard TRD variable. For this analysis, we do not require the Muon system to be functioning but the inner tracking, calorimeter and data acquisition systems must be operating properly (see Appendix II).

2. Triggering

a. Tools

At the most fundamental level, the Level 1 framework has fast analog information about the electromagnetic and fine hadronic sections of the calorimeters. The calorimeter towers are summed into 'trigger towers' 0.2 x 0.2 in $\Delta\eta$ x $\Delta\phi$ which are segmented into EM and FH components. (The coarse hadronic and ICD cells are not included in the hadronic sums.) As a result, one can select events based on 'electrons' or 'jets' at this level. We are mainly concerned with choosing the proper electron and jet thresholds for top dielectron events. The Level 1 trigger 'tools' of interest are therefore,

- **L1EM(*n*,*c*):** enables user to select an event if it has at least a number, *'n'*, EM trigger towers with E_T greater than some threshold, *'c'*.
- **L1JT(*n*,*c*):** enables user to select an event if it has at least a number, *'n'*, EM+FH trigger towers with E_T greater than some threshold, *'c'*.

At Level 2, more sophisticated techniques can be brought to bear. For every Level 1 trigger there is at least one Level 2 filter which is used to further select events. While multiple Level 2 filters may depend on (or 'hang off of') a given Level 1 trigger, the opposite is not true. A Level 2 filter cannot pass data to the host cluster which failed the Level 1 trigger it depends on. In the case of jets or electrons, the Level 2 code performs a basic reconstruction on the event using the Level 1 trigger towers as seeds. From there, various filter tools are used to indicate what algorithms or thresholds to perform. Among these tools are:

- **L2EM(*n*,*e*,*s*,η):** enables user to cut on the number, *'n'*, and E_T > *'e'* of electrons or photons. One can also specify quality cuts *'s'*, and pseudorapidity with *'η'*. The quality cuts, *'s'* include the following: *'ele'* is electron shower shape cuts, *'iso'* specifies transverse isolation from hadronic energy, *'gam'* is photon shower shape cuts, and *'esc'* is no cut. *'eis'* is *'ele'* and *'iso'*, while *'gis'* is *'gam'* and *'iso'*.

- **L2JT(n,e,r,η):** enables user to cut on number, 'n', and E_T > 'e' of jets. One can specify the algorithm parameters such as cone size 'r', and also the pseudorapidity, 'η', of the jet.

- **L2MS(e):** calculates event $\not{E}_T$ and allows one to request it to be above some threshold, 'e'.

b. General Considerations

Since this analysis occurs within the context of a wider collaboration and due to the finite bandwidth available at each triggering stage, our particular filter must not exceed a rate at each trigger stage which is allotted to it. This corresponds to a maximum rate at Level 1 of about 20 events per second, and a maximum rate out of Level 2 of about 0.3 events per second. Therefore, the trigger must be designed to accept most top dielectron events and have high rejection for background processes. We used the Monte Carlo package ISAJET to simulate the behavior of top events produced at the Tevatron. The generated events were then processed with a detector simulation employing the GEANT library routines for this purpose, followed by processing with another Monte Carlo program which simulates the Level 1 trigger framework and Level 2 algorithms. Since we did not know the top mass *a priori*, a wide range of top masses was considered. For the dielectron channel we have considered the following characteristics for top which come out of these Monte Carlo studies:

- almost all dielectron events contain at least one highly electromagnetic high p_T cluster in the calorimeter which can be identified as early as Level 1.

- there will almost always be at least one additional high p_T cluster in the calorimeter found as early as Level 1. This may correspond to the other electron, one of the b jets, or any jets from initial or final state radiation.

- there is very large $\not{E}_T$ which can be effectively used at Level 2.

- Most top dielectron events contain two electromagnetic clusters which can be found as EM towers at Level 1.

Two potential avenues could be pursued based on these findings. One requires an electron and jet at Level 1, then tightens their requirements at Level 2 and adds a $\not{E}_T$ cut. This was called 'EM_JET' at Level 1 and 'ELE_JET' at Level 2. It should be noted that one circumstance which affects the design of the ELE_JET filter is that it is an important filter for the $e\mu$ and $e{+}jets$ channels as well. The other option is to require two electrons at Level 1 and tighten their criteria at Level 2. This was called EM_2_MED at Level 1 and ELE_2_HIGH at Level 2. The first and third entries in Table 4.2 give the characteristics for these triggers as designed for Run 1a along with their estimated efficiencies for top of mass 140 GeV/c^2.

Table 4.2. Elements of dielectron triggers including filter efficiencies for a top mass of 140 GeV/c^2 using Run 1a and 1b filter versions.

trigger name	Level 1	Level 2	efficiency
1a: EM_JET/ELE_JET	L1EM(1,10)L1JT(2,5)	L2EM(1,15,*ele*) L2JT(2,10,0.3) L2MS(10)	88.2%
1b: EM_JET/ ELE_JET_HIGH	L1EM(1,12)L1JT(2,5)	L2EM(1,15,*ele*,<2.5) L2JT(2,10,0.3,<2.5) L2MS(14)	87.5%
1a: EM_2_MED/ ELE_2_HIGH	L1EM(2,7)	L2EM(2,10,*iso*)	53.9%
1b: EM_2_MED/ EM2_EIS_ESC	L1EM(2,7)	L2EM(1,20,*eis*) L2EM(2,16,*esc*)	-----

Because the second electron in top events is not always very high in p_T, the requirement of two electrons is not very efficient. Also, a dielectron trigger tends to increase our instrumental background as will be discussed in Chapter 7. As a result, the ELE_JET filter will be considered the main trigger for this analysis. Since many of the events selected by the Z filter (ELE_2_HIGH) are also selected by the ELE_JET filter, in Table 4.3 we give the efficiency for accepting events which pass either trigger for various top masses. Two conclusions can be drawn from Table 4.3. First, comparison of the efficiency when m_{top} = 140 GeV/c^2 with that found for the ELE_JET filter alone in Table 4.2 shows the Z filter adds about 6% efficiency. Second, our trigger efficiency is essentially independent of top mass.

Table 4.3. Overall trigger efficiencies for various top masses including those for a top mass of 140 GeV/c^2 using the exact same events with Run 1a and 1b filter versions.

m_{top}	**version**	**total**
120		91.0% ± 2.5%
140	Run 1a	93.7% ± 3.2%
"	Run 1b	93.0% ± 3.2%
160		92.9% ± 2.3%
180		94.4% ± 2.2%

c. Optimization for High Luminosity

As the instantaneous luminosity increased in the early part of Run 1, the rate of events passing ELE_JET dictated reconsideration of the various thresholds. In particular, to keep the Level 1 rate for this trigger less than 20 Hz and Level 2 less than 0.3 Hz a 20% reduction in rate out of Level 1 and a factor of 2 to 3 in rate reduction out of Level 2 was required. The effect of changing various thresholds was studied for samples with top mass from 100 GeV/c^2 to 180 GeV/c^2. Considered globally over all the channels using this filter, it was noted that the EM tower threshold is the most effective variable to obtain improved rejection. This is because in all cases, this is triggering on a real electron which has good resolution. Increasing the jet cut is okay for the dielectron channel but hurts the others because this is a jet with poor resolution. Adding another jet penalizes the dilepton channels since they have fewer jets. Increasing the Level 1 EM threshold to 12 GeV was found to accomplish our objective.

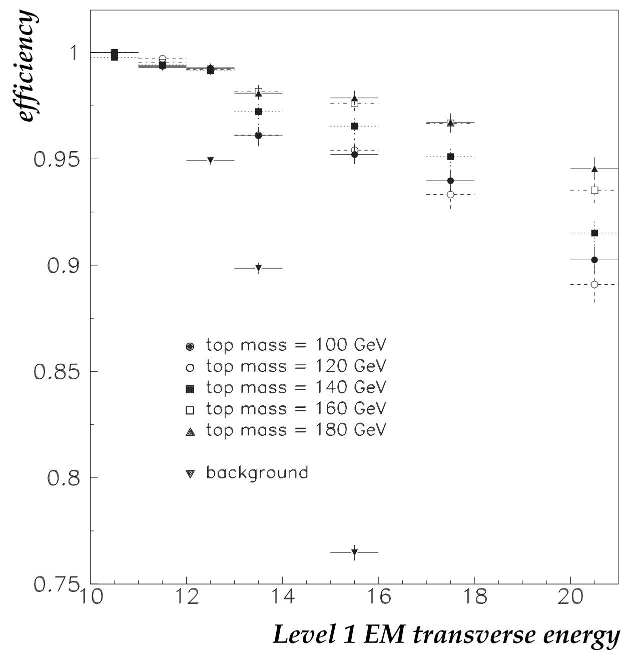

Figure 4.1: Effect of varying Level 1 EM tower E_T threshold beyond initial ELE_JET filter. Efficiencies are given relative to ELE_JET. Modest improvements in background rate can be accomplished for cuts with good efficiency.

In order to see the effect of a change in Level 1 EM threshold on events passing ELE_JET, in Figure 4.1 we plot efficiency relative to the Run 1a configuration (see Table 4.2) for various top masses and background. One can see from this that the total rejection gained from a change in this threshold is modest (ie. most of the new events we are throwing out at Level 1 were being rejected by Level 2 anyway). We have effectively transferred some rejection from Level 2 to Level 1.

A more severe problem presents itself at Level 2 where the bandwidth for the filter to the host cluster needs to be reduced by a factor of 2 to 3. It is undesirable to increase the electron E_T threshold because it would be above the offline cut for the $e\mu$ channel. A similar problem occurs for the jet cut. In all cases, however, the Level 2 $\not{E}_T$ is well away from any off-line cut these channels contemplate making (20 GeV at a minimum).

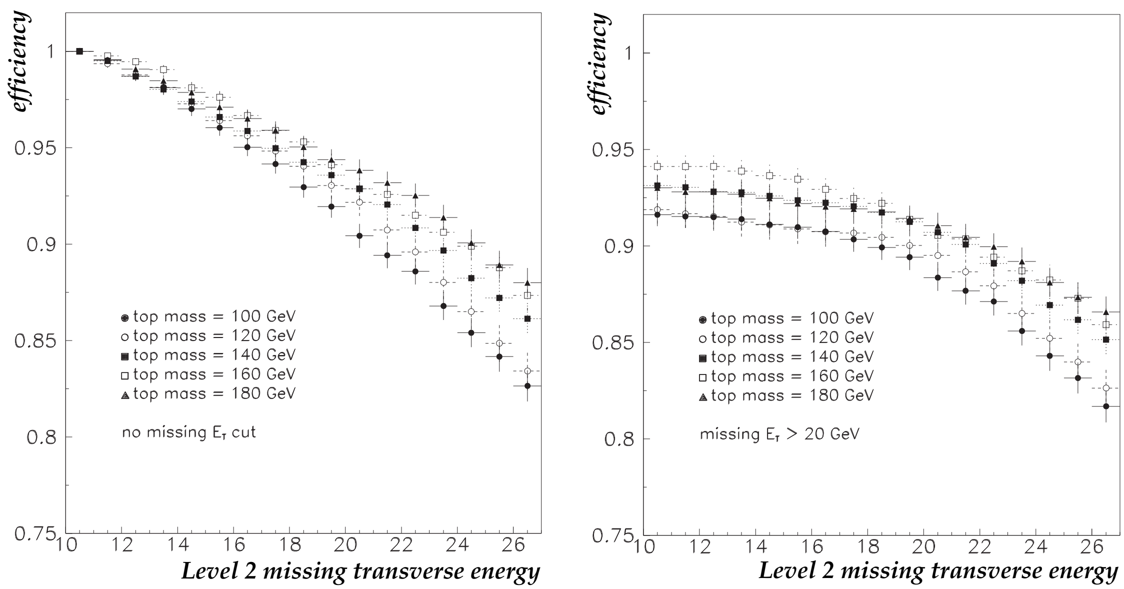

Figure 4.2: Effect of varying Level 2 $\not{E}_T$ cut. (a) raw efficiency for dielectron events for various top masses. (b) efficiency for a subset of events which pass a 20 GeV $\not{E}_T$ cut offline.

Therefore, shown in Figure 4.2 are efficiency curves for top events after various cuts on Level 2 $\not{E}_T$. These efficiencies are with respect to those from the original ELE_JET filter which had a 10 GeV threshold. Figure 4.2b shows the same thing but for those events which pass an offline cut on the $\not{E}_T$ of 20 GeV. The effect on background passing ELE_JET is shown in Figure 4.3. To obtain the required reduction in rate, we chose a 14 GeV threshold for the Level 2 $\not\!\!E_T$ which is still very efficient for top events of all masses. The new filter, termed ELE_JET_HIGH, is thus the ELE_JET trigger with the Level 1 electron threshold raised to 12 GeV and the Level 2 $\not\!\!E_T$ threshold raised to 14 GeV (see Table 4.2). The potential differences in efficiency for the final filter parameters in Run 1b and 1c (as compared to Run 1a) were studied for top mass of 140 GeV/c^2. The efficiency given in Tables 4.2 and 4.3 is essentially independent of trigger version.

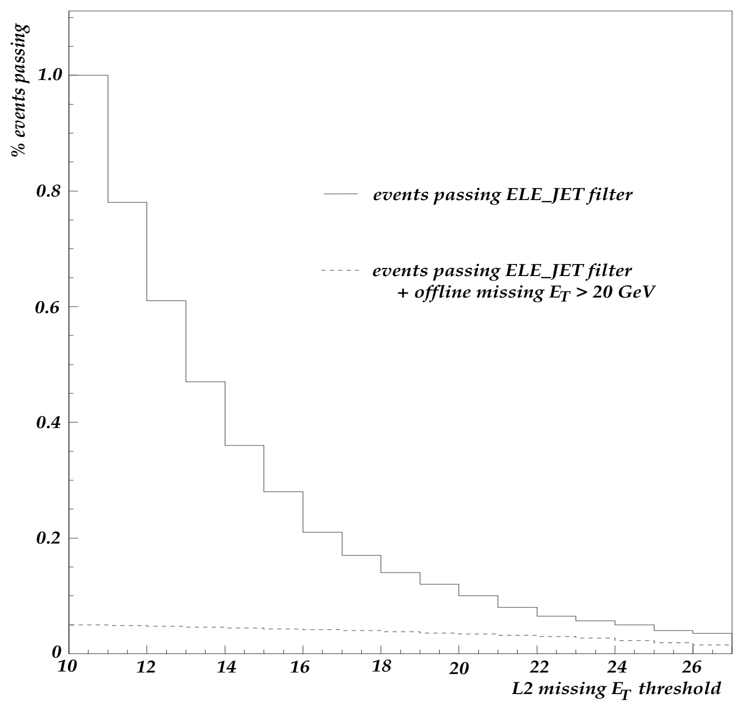

Figure 4.3: The effect of tightening Level 2 $\not\!\!E_T$ cut on the total rate of background events to the host cluster relative to the initial ELE_JET filter is shown.

One could worry that these triggers have a significantly different behavior in events taken when the Main Ring is active. We do not, however, incur a systematic efficiency problem in Main Ring events because neither the CH nor the ICD are in the trigger. Thus $\check{E}_T$ is not affected. Also, what is called a 'Jet' at Level 2 is usually one of the electrons for this analysis which are immune from Main Ring effects.

In conclusion, the triggering changes made were slightly altered after about 13% of the data was taken (ie. transition to Run 1b) and not changed thereafter. The change in efficiency from this is negligible. From the triggering point of view, then, there is no dependence on efficiency or even final background on run number.

3. Tracking and Electromagnetic Cluster Reconstruction

a. Tracking

One of the first tasks of the reconstruction of events from the raw hit information is to find charged particle tracks. These are reconstructed in the CDC and VTX in a two step process. First, within each module of these detectors, 3-dimensional hits are found and fit to a straight track segment hypothesis. These track segments for each module are then matched to obtain a 3-dimensional track in either the CDC or VTX. If tracks in the two detectors match, the fit is redone a last time. For the FDC, 3-dimensional tracking is performed first in $r\phi$ and then in θ due to the structure of the detector. If this track has a 3-dimensional VTX track which matches within the VTX track's error they are refit together.

The reconstruction of hits in the TRD involves a calibration for the response variations of the detector. Constants determined from monitoring with uranium runs are used to compensate for gas quality. The resulting energy measurement is stored for each cell in terms of the charge that would be deposited by a minimum ionizing particle ('mip').

b. Vertexing

A quantity fundamentally important to the understanding of the kinematics of any event is the primary vertex. Because it was known before the beginning of the experimental run that the VTX would be unable to find the vertex, the DØ vertexing algorithm was designed to rely heavily on the CDC. Initially CDC tracks are used to find the primary vertices in the event. If there is an insufficient number of tracks, FDC hits are unpacked, tracking performed and vertices found. The FDC is not consulted if the CDC finds enough tracks because FDC tracking requires large amounts of computing time to perform the trackfinding. Once the primary vertex is found, it is used on the final track fits. If there are more than one vertex is reconstructed, the one with the most tracks pointing to it is termed the event vertex and is what is used on the final track fits.

c. Electromagnetic Cluster Reconstruction

Once a primary vertex is found, the E_T of calorimeter towers can be ascertained. A nearest neighbor algorithm is run on all EM towers to find potential electrons and photons. This algorithm has three main steps. First, a list of calorimeter towers with significant E_T is constructed. Second, each tower in the list is considered to be a cluster. For each tower, A, a search is conducted for the highest E_T tower which is adjacent and add it (and its associated cluster if it has one) to A. Thirdly, calculate energies and positions for each cluster of towers. For the electron and photon algorithm, the clustering is confined to the EM layers plus the innermost FH layer.

When clustering is finished, the fraction of energy in the EM modules is calculated as

$$f_{EM} = \frac{\sum_{i=1}^{4} E_i}{\sum_{i=1}^{5} E_i}$$

where the sum in the denominator runs over the EM and innermost FH layer, and the sum in the numerator only runs over the EM layers in the cluster. An electron is generally contained within the EM portion of the CC or EC calorimeter. Therefore, those clusters with EM fraction > 0.9 are kept by the reconstruction as electron and photon candidates.

EM clusters are matched with any 3-dimensional tracks within a window in θ and ϕ. Those clusters which have a matching track are called "PELC's" for short, those without tracks are labelled "PPHO's". It should be noted that these are not necessarily 'electrons' and 'photons' since tracking inefficiencies, accidental charged hadron overlaps with photons, and photon conversions cloud the issue significantly. The terms PELC and PPHO should then be considered to be general terms for electromagnetic jets with or without a track in a wide road to the primary event vertex. In the PELC case, we project the track into the TRD and determine which layers are crossed. The TRD information for that layer and ϕ cell is then associated with the track. For PPHO's, the later versions of the reconstruction allow TRD information to be associated directly with the cluster by drawing a 'missing track' from the cluster centroid to the vertex.

4. Luminosity and Data Sample

The data taken with the detector is passed from Level 2 to buffer disks on a host computer cluster and then stored on 8mm magnetic tapes. This 'raw' data is eventually copied from tape to computer disks to have the hit information reconstructed into physics objects of interest. The output from the reconstruction is stored in two different formats: 'STA' which contains all raw hit information and reconstructed information, and 'DST' which lacks most raw hit information. The DST is subsequently processed with a filter which stores the data in a compact format called μDST. All of the formats are copied to additional tapes and only the μDSTs are left on disk for relatively easy access.

a. Event Streaming

There are, however, many advantages to performing a loose selection of this data and storing it on local analysis disks that one works from. As a result, we 'stream' the subset of the data with a loose selection of two moderately high E_T electromagnetic clusters. This sample then is what is used for the dielectron analysis.

We streamed the entire data set from Run 1 by requiring that the events have at least two electromagnetic clusters in the calorimeter with uncorrected $E_T > 15$ GeV. No tracking cuts were applied at this stage. In Run 1a we required that the EM clusters pass loose selection cuts based on calorimeter quantities only; these cuts were dropped for the Run 1b and 1c streaming. Furthermore, we kept all events which have two clusters with $E_T > 15$ GeV with respect to any of the reconstructed primary vertices. This was only done for Run 1b and 1c to accept events which were misreconstructed due to improper vertex-finding in high luminosity conditions. The total number of events streamed is approximately 22,000, 630,000, and 70,000 for Runs 1a, 1b, and 1c, respectively.

In addition, we had performed two earlier streams of the Run 1b data. Because some data were reprocessed with a slightly newer version of the reconstruction, approximately 0.2% extra luminosity did not make it into the newest, third, stream.

b. Integrated Luminosity

After the above selections, the total integrated luminosity breaks down according to Table 4.4 (in pb^{-1}) after bad runs were removed.

Table 4.4. Integrated luminosity in pb^{-1} for various run ranges and Main Ring states.

	GOOD_BEAM	μBLANK	MRBS_LOSS
Run 1a	13.9	0.9	0.0
Run 1b	80.92	4.74	8.94
Run 1c	9.21	0.45	0.94
totals	104.03	6.09	9.88

The Run 1b data from the older streams which did not reappear in the final stream are added to this analysis giving a final luminosity of

$$\boxed{120.2\ pb^{-1} \pm 6.5\ pb^{-1}}$$

where the 5.4% systematic error is incurred from the degree of uncertainty in the calibration of the LØ detector[42].

5. Electron and Photon Identification:

It is crucial to the success of the dielectron analysis that we are able to efficiently identify real electrons in the data and reject highly electromagnetic jets faking electrons. A significant background in electron identification consists of jets which contain leading neutral pions and which simultaneously have an associated low p_T charged pion supplying a track positionally matching the electromagnetic cluster. Additional backgrounds arise from photons associated with jets which convert to e^+e^- pairs and cannot be resolved into two tracks by the tracking chambers.

Once an electron or photon candidate has been clustered, there are several tracking and calorimeter properties which aid us in identification. These include isolation variables which quantify hadronic energy near the candidate, shape of the shower in the calorimeter, transition radiation and ionization measurements along the candidate track, and the quality of the match of the track with the cluster centroid. In this section, we describe each variable and what cuts, if any, we make on them. For PELC's we require $f_{iso} < 0.1$ and construct a likelihood, $\mathcal{L}_5$, from the other five variables and require $\mathcal{L}_5 < 0.5$. Approximately 30% of events with two electrons in the final state are reconstructed such that one of the electrons does not have a track in the drift chambers. This loss of efficiency occurs due to tracking inefficiency and bad vertexing in a high luminosity environment. These electrons will be reconstructed as PPHO's and we allow such electrons by selecting candidates which pass cuts on calorimeter quantities ($f_{iso} < 0.1$, $\chi^2 < 100$) and transition radiation ($\varepsilon_t < 0.9$). We do not allow PPHO-PPHO pairs in this analysis because the percent of real dielectron events which are classified in this category goes as the square of the tracking inefficiency -- $0.15^2 \sim 2\%$.

a. Transverse Isolation

Because our electrons are coming from a massive object, we expect them to be far from jets or other hadronic activity. On the other hand, electrons from heavy flavor decay are generally embedded within jets. Therefore, cutting on transverse isolation can reduce this background (see Chapter VII). We calculate isolation as

$$f_{iso} = \frac{E_{tot}(\Delta R = 0.4) - E_{EM}(\Delta R = 0.2)}{E_{EM}(\Delta R = 0.2)}$$

We require f_{iso} < 0.1 for the dielectron analysis.

Although this quantity works very well for high E_T electron candidates, it is inefficient for those with E_T < 15 GeV or so because there is a constant level of hadronic energy in the calorimeter regardless of whether a jet is nearby. This extra energy has to do with the underlying spectator interactions which accompany the hard scatter, and also comes from the significant energy deposited in EM and FH layers from uranium decays. As a result, for the direct photon analysis presented in Chapter VI, we use the isolation parameter,

$$iso_4 = E_{tot}(\Delta R = 0.4) - E_{EM}(\Delta R = 0.2)$$

when a photon candidate has E_T < 20 GeV.

b. Longitudinal Isolation

The longitudinal isolation is merely the fraction of energy in the EM modules as defined in Section 3c. Including this variable in the electron likelihood calculation can significantly reduce jet backgrounds to electrons. Figure 4.4 shows the fraction of cluster energy in the electromagnetic layers for the three populations in the PELC sample (electrons, hadron overlaps and conversions). Electrons tend to have values around 0.99 and most are above 0.97. Conversion backgrounds have somewhat lower values. The distribution from the hadronic overlap sample is the most distinct from the electron distribution. A significant fraction of the candidates have values below 0.97.

c. Longitudinal and Transverse Shower Shape

Electron quality is determined by using a covariance matrix χ^2 test of the transverse and longitudinal shower shape of the cluster where

$$\chi^2 = \sum_{ij} (x_i - \langle x_i \rangle) H_{ij} (x_j - \langle x_j \rangle)$$

and

$$H_{ij}^{-1} = \langle (x_i - \langle x_i \rangle)(x_j - \langle x_j \rangle) \rangle$$

The x_i are energy deposits in cells occupied by the shower and the $<x_i>$ are the mean values measured in test beam. This test was used to require cluster shape to conform with that of an electron shower from test beam.

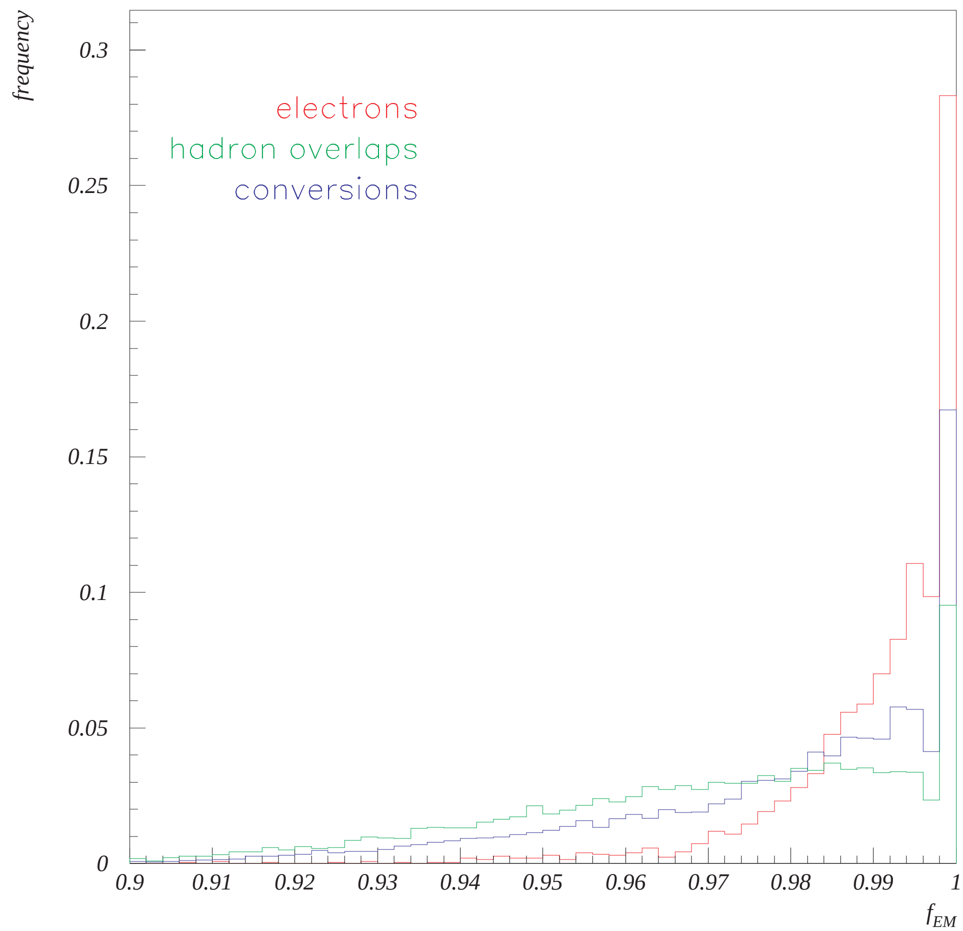

Figure 4.4: Fraction of cluster energy in electromagnetic layers for 3 populations from PELC sample: electrons (dashed), hadron overlaps (dotted) and conversions (solid).

Figure 4.5 shows the χ^2 distribution for the three populations in the PELC sample. Electrons peak strongly around values of 10 and are mostly below 100. The conversions tend to have higher values with a long tail which extends well above 100. Hadronic overlaps have the highest mean χ^2 and a long tail above 100. Approximately 25% of these have values above 500.

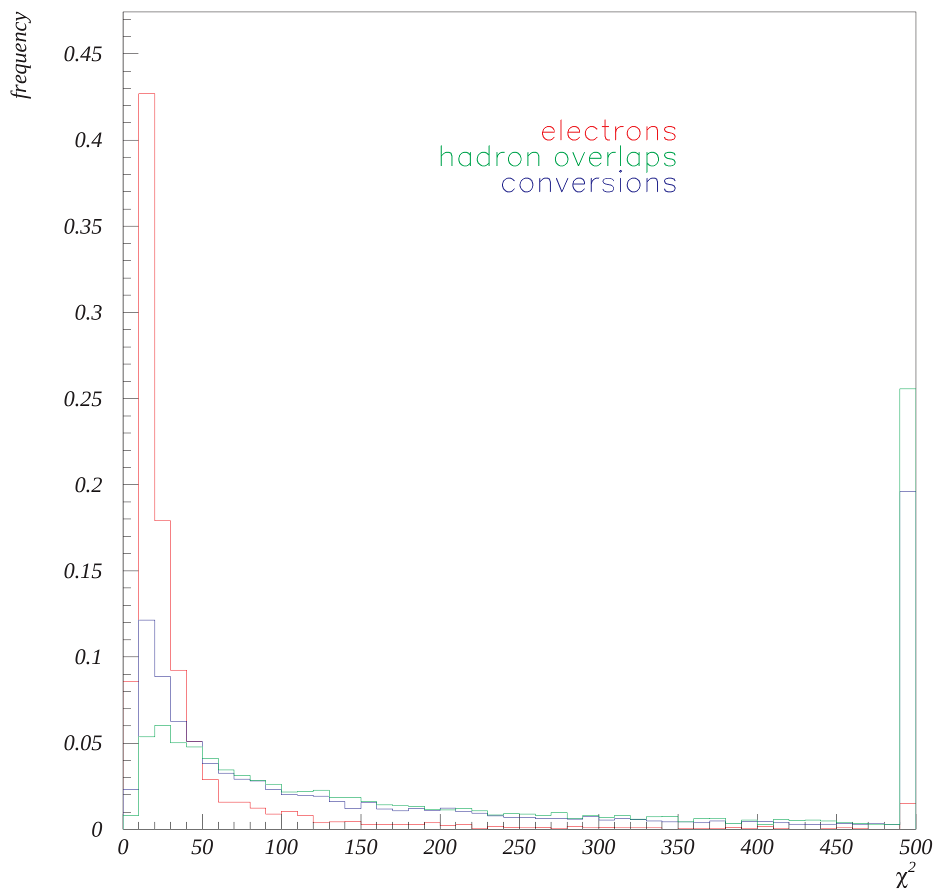

Figure 4.5: H-matrix χ^2 for 3 populations in PELC sample: electrons (dashed), hadron overlaps (dotted) and conversions (solid).

d. Transition Radiation

The momenta of the electrons in this analysis are well above the threshold to generate transition radiation in the TRD radiator stacks, whereas the backgrounds are predominantly either too low in momentum (hadron overlaps in jets) or have no charge such as photons which convert to unresolved e^+e^- after the TRD. Because part of each TRD layer is a drift chamber, all charged particles behave essentially as minimum ionizing particles. By virtue of their very small mass, electrons will be higher on the relativistic rise of dE/dx and produce slightly more ionization. More importantly, they will produce transition radiation. As a result, one would expect the ionization measured along a track in a particular layer to be a discriminant between electrons and their backgrounds. Electrons will deposit more charge than charged hadrons and unresolved photon conversions will deposit more than electrons.

In addition, electrons are detected significantly more efficiently than charged hadrons and conversions in a given layer. This is because the hadrons produce less charge and are undetected about 15% of the time, while conversions may convert after a TRD layer and thereby will not deposit energy in it. Another consideration in deciding on a specific variable of merit is that charged pions occasionally exhibit Landau fluctuations in one layer and deposit copious energy. These considerations motivate an optimized variable, called the *truncated sum*, to be computed in the following way[43].

$$\begin{aligned}
\Sigma_{trunc} &= \left(\sum_{i=1}^{3} E_i\right) - \max\left(E_1, E_2, E_3\right) && \textit{(3 TRD layers crossed)} \\
&= \frac{3\kappa}{2N}\sum_{i=1}^{N} E_i && \textit{(1 or 2 TRD layers crossed)} \qquad \textbf{Eq. 4.1} \\
&= 0 && \textit{(if any crossed layer has zero hit anodes)}
\end{aligned}$$

where for three layer tracks, one sums over all layers, i, and the highest energy layer is removed.

Table 4.5. Values of κ for 1 and 2 layer TRD tracks.

dependence	1-layer	2-layer
run 1a	1.16346	1.06346
run 1b	0.87243	0.92607
1 hit per anode plane	1.03134	1.05984

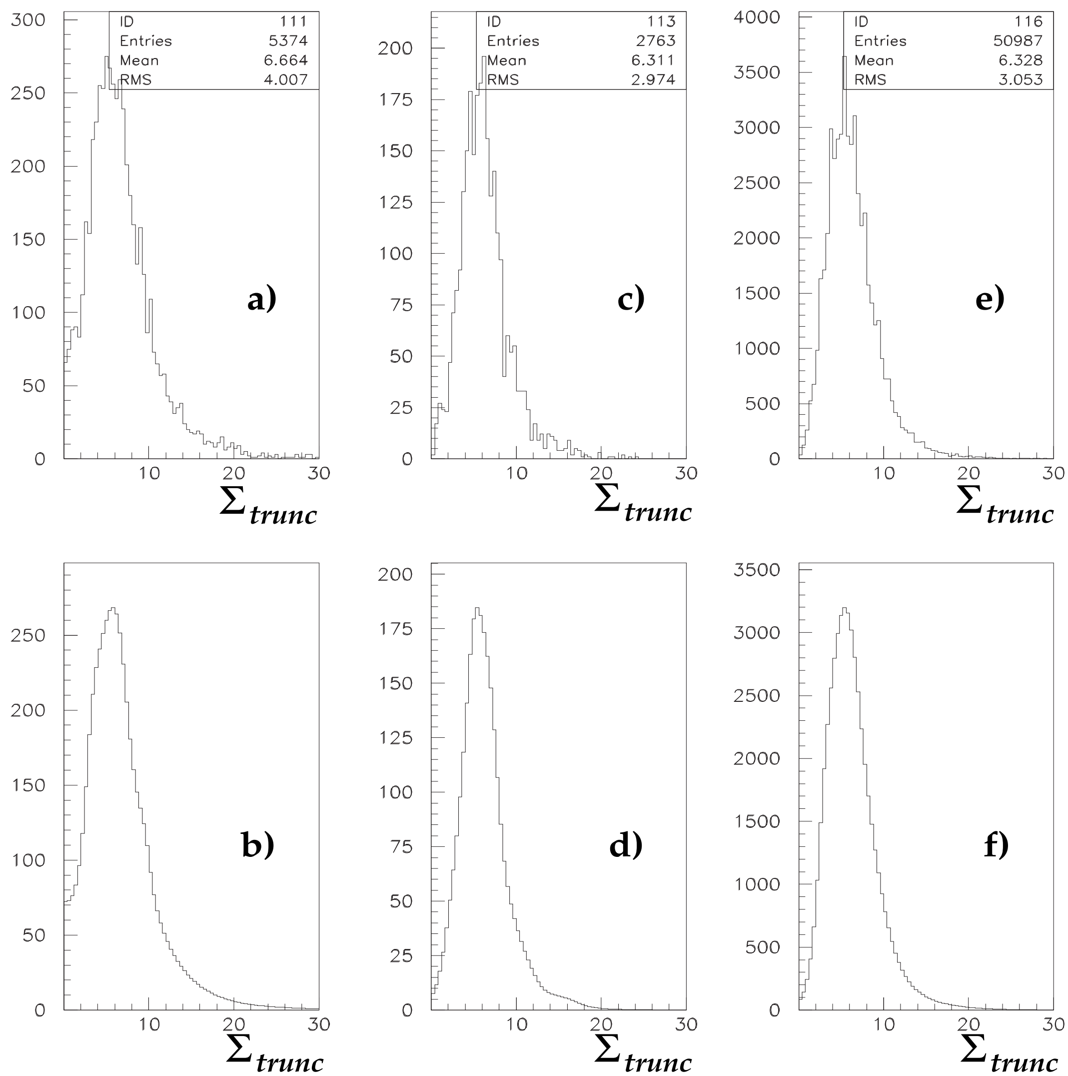

Figure 4.6: Unsmoothed and smoothed $\Sigma_{\rm trunc}$ distributions for good electrons crossing (a-b) 1 TRD layer, (c-d) 2 TRD layers, and (e-f) 3 TRD layers. The scale factors, κ, have been applied for the 1 and 2 layer tracks.

As shown in the second expression, for candidates which are within the acceptance of only 1 or 2 layers (ie. N = 1 or 2), we have modified the definition of Σ_{trunc} to be the average energy in the layers crossed. For these tracks, 3/2 is an approximate factor which makes Σ_{trunc} similar in magnitude to that in the central region and κ is a factor dependent on the hit environment. The factors given in Table 4.5 reduce a potential of 8 tables (2 runs x 4 possible # anode hits conditions) to 6 scale factors and 2 tables (one table for 1-layer tracks, one table for 2-layer tracks). Thus we gain in statistics for each table. The raw and smoothed plots for the corrected Σ_{trunc} are given in Figure 4.6.

Σ_{trunc} exhibits various dependencies which impact its resolution. In particular, the distribution is different depending on the pattern of anode hits in the layers. Indicated by the superscript *'abc'*, the pattern is given as 1-1-1, 1-1-2, 1-2-2, or 2-2-2 for central electrons. For instance, 1-1-2 means any two of the layers crossed had one anode fired in a window three anodes wide around the track and one layer had more than two anodes fired. As a result, the strategy taken has been to produce a lookup table for the different scenarios which removes these dependencies. The generalized variable ε_t is constructed from the measured truncated sum and the lookup table which is generated according to:

$$\varepsilon_t^{abc} = \frac{\int_{\Sigma'^{abc}_{trunc}}^{\infty} \Sigma^{abc} \, d\Sigma^{abc}}{\int_0^{\infty} \Sigma^{abc} \, d\Sigma^{abc}} \qquad \textbf{Eq. 4.2.}$$

Note that this variable is constructed to be a flat distribution for the sample used to generate the table which is mostly electrons. In this variable, conversions before the TRD will have low values, and hadron overlaps and conversions after or in the TRD will have high values. Electrons will be approximately flat. The conversion from Σ_{trunc} to ε_t for three layer tracks has been generated for Run 1a and 1b electrons for each environmental scenario, *'abc'*[44]. The possible combinations of # hit anodes for 2 layer tracks are 1-1, 1-2, and 2-2. For 1-layer tracks either 1 or ≥ 2 hit anodes are possible. The case where 2 or 3 anodes were hit for both layers in 2-layer tracks was rare and is included in the '1-2' case. Figures 4.7 through 4.9 show the probability distributions of ε_t for the three populations in the EC PELC sample which is within the TRD acceptance. Figure 4.7 inidates the similarity of the electron distribution for 1 and 2 layer track electrons. Figure 4.8 shows the probability distribution for the three types of background for 1 layer tracks while Figure 4.9 gives the distribution for 2 layer tracks. One can see the increased discrimination two layers gives compared to one by observing the broadness of the distribution around high values of ε_t.

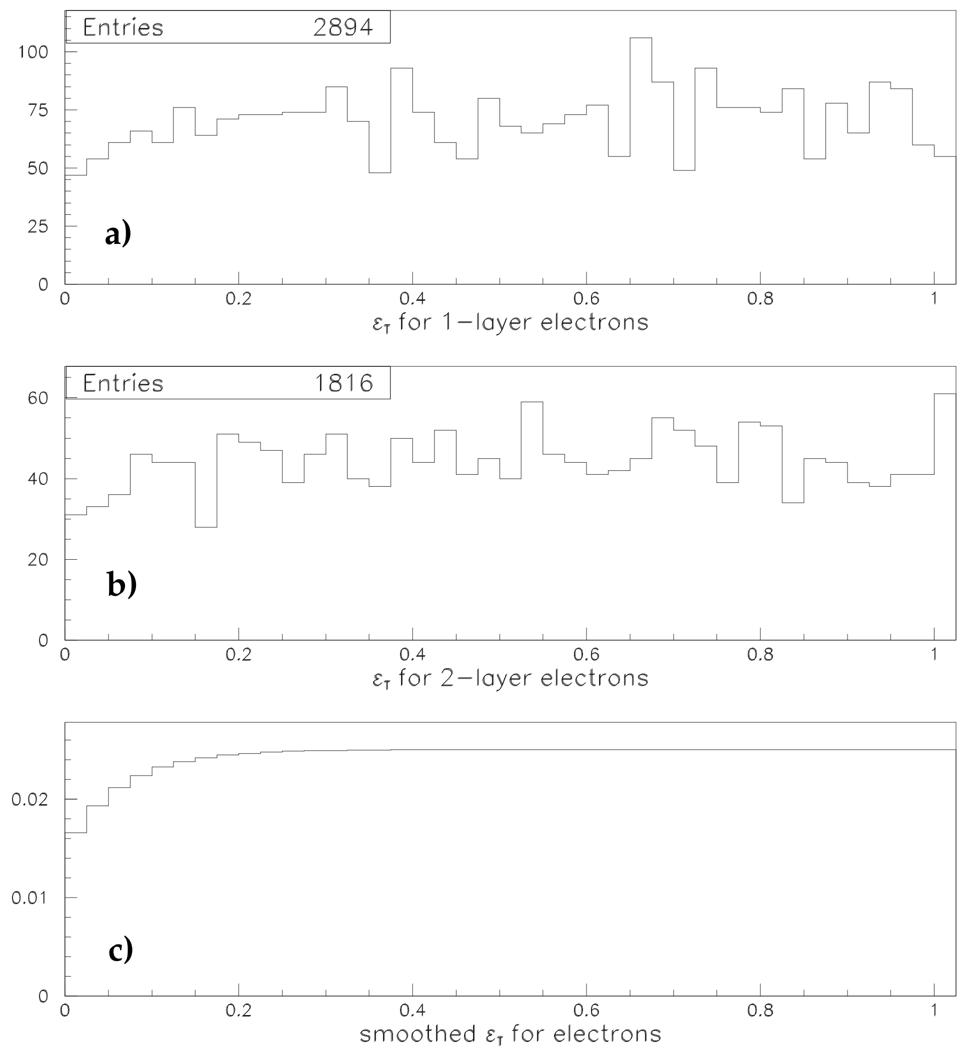

Figure 4.7: Electron distributions of ε_t for (a) 1-layer tracks, (b) 2-layer tracks, and (c) mean probability distribution from the two.

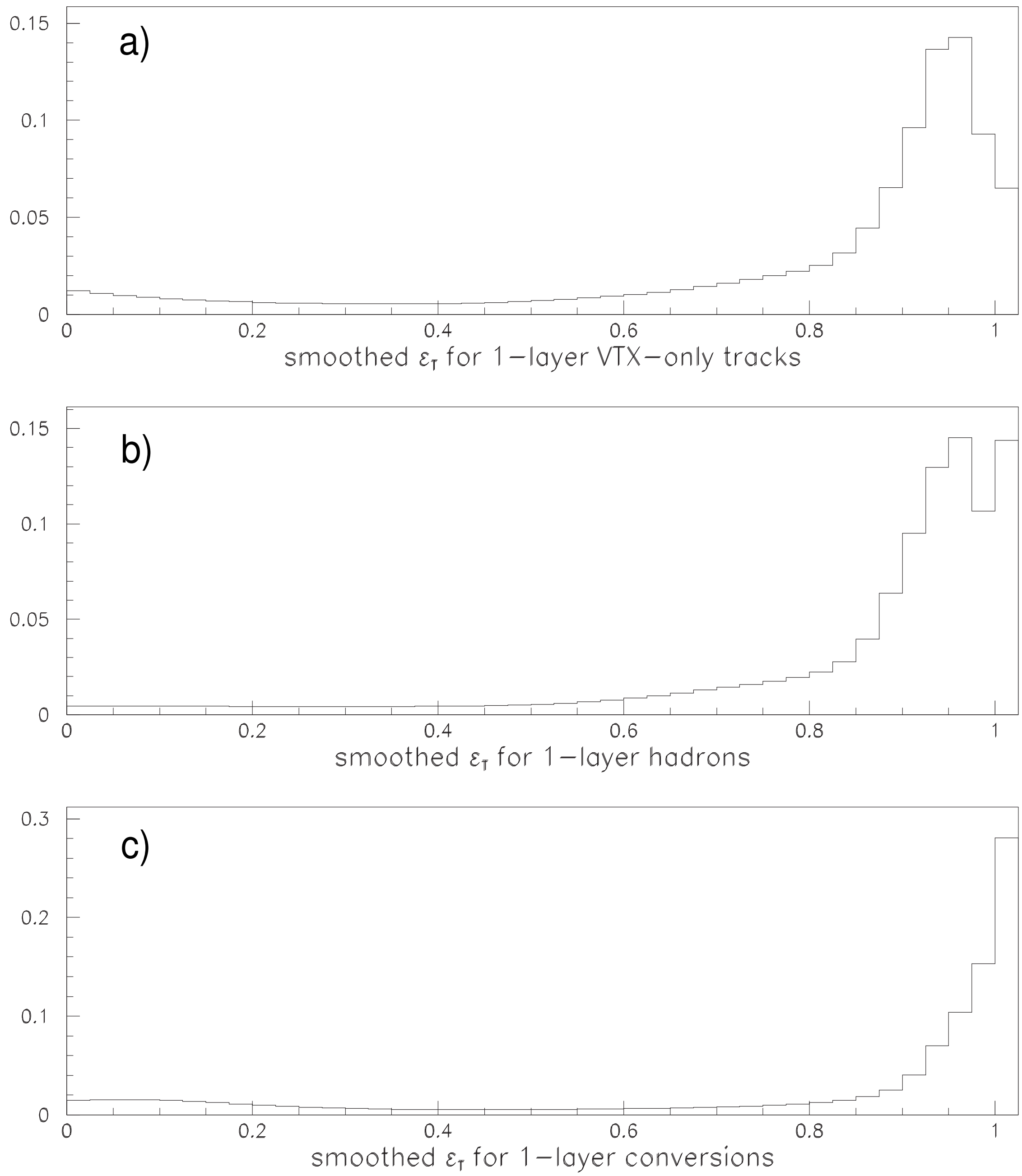

Figure 4.8. Probability distributions for backgrounds crossing one TRD layer showing (a) VTX-only tracks, (b) hadron overlaps, (c) and conversions.

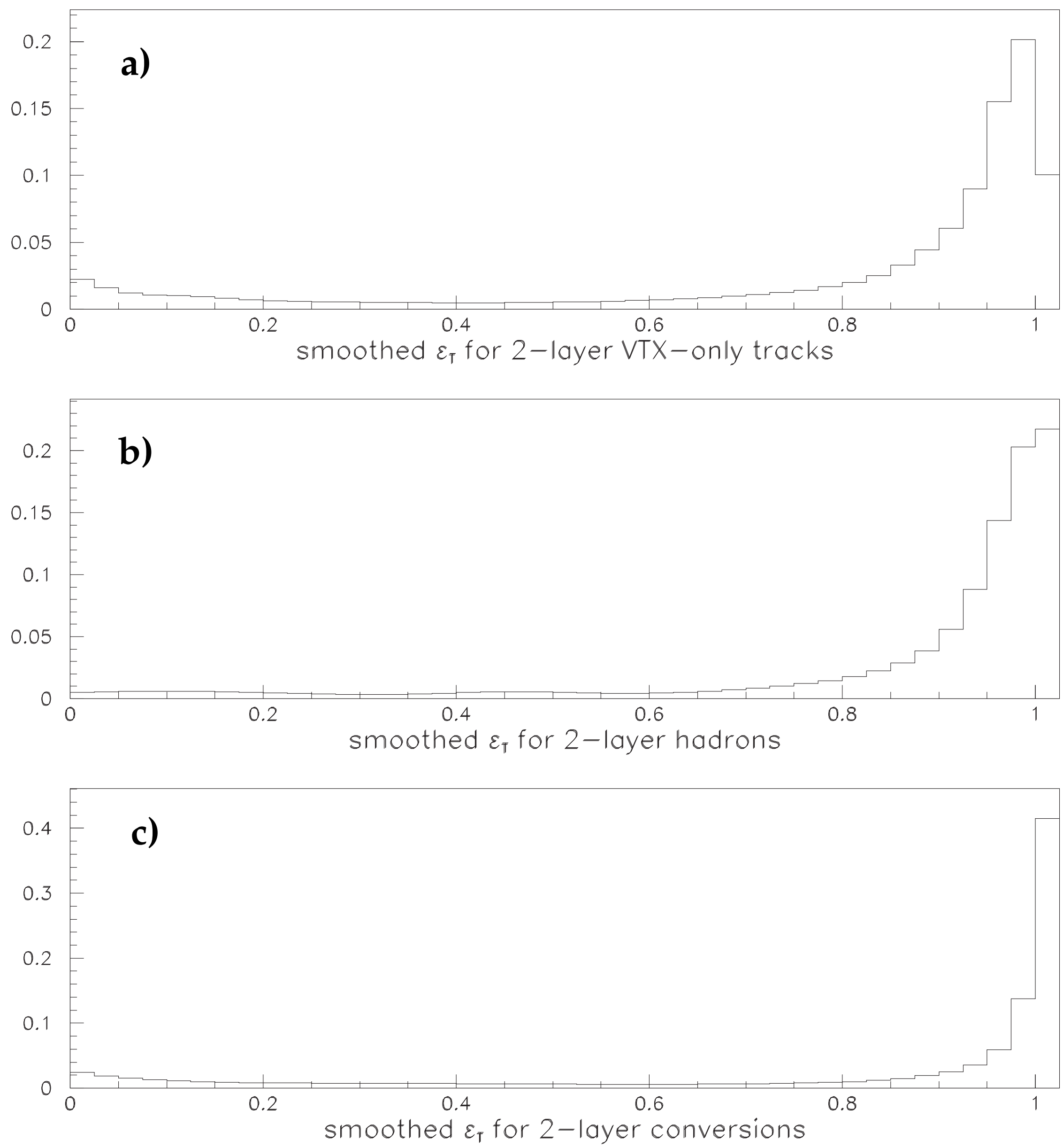

Figure 4.9: Probability distributions for backgrounds which cross two TRD layers showing (a) VTX-only tracks, (b) hadron overlaps, and (c) conversions. The distributions are sharper than for 1 layer tracks.

e. Track Match Significance

A significant background to electrons arises from low energy charged hadrons which spatially overlap high p_T photons. This pion is likely to be misaligned with the reconstructed cluster centroid and so a cut on the match of a track and cluster can discriminate against these backgrounds. This is defined in the central region as

$$\sigma_{trk}^{CC} = \sqrt{\left(\frac{\Delta\phi}{\sigma_{\Delta\phi}}\right)^2 + \left(\frac{\Delta z}{\sigma_{\Delta z}}\right)^2}$$

and in the forward region it is

$$\sigma_{trk}^{EC} = \sqrt{\left(\frac{\Delta\phi}{\sigma_{\Delta\phi}}\right)^2 + \left(\frac{\Delta R}{\sigma_{\Delta R}}\right)^2} .$$

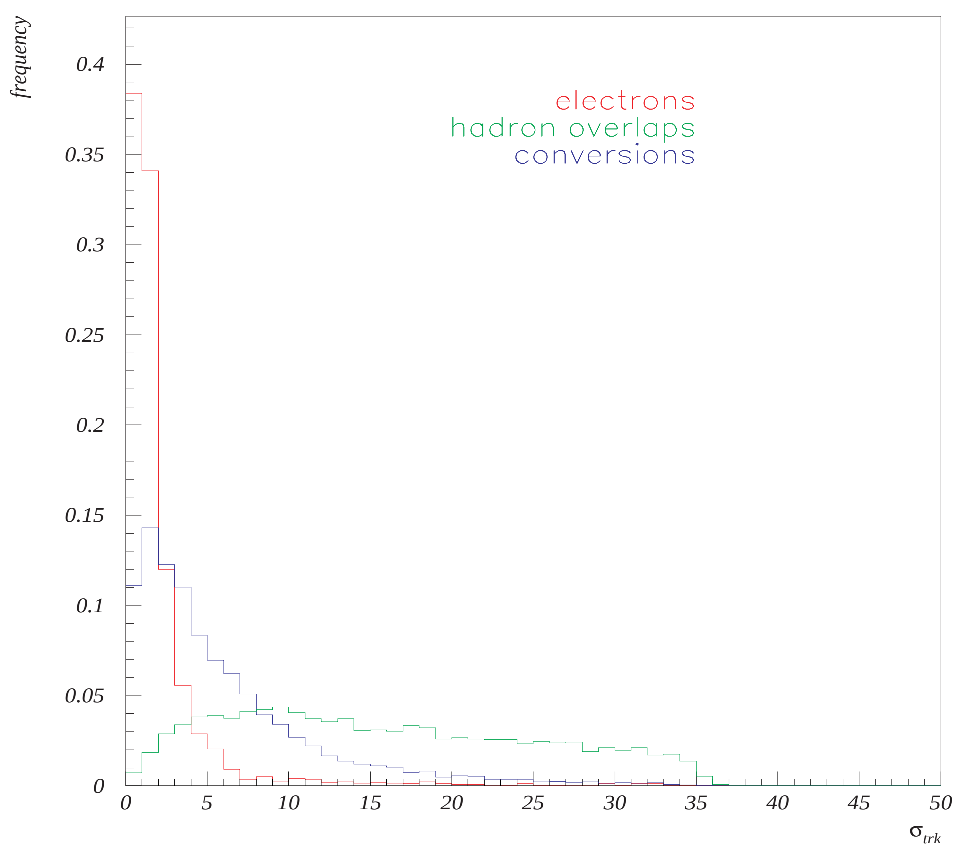

Figure 4.10: Trackmatch significance for 3 populations in PELC sample: electrons (dashed), hadron overlaps (dotted), and conversions (solid).

Figure 4.10 indicates the trackmatch significance distribution for the three populations in the PELC sample. Electrons have very low values and very few have values above 5. Conversions have higher values but a significant fraction have tracks which match the cluster centroid fairly well. The distribution from the hadronic overlap sample is the most distinct from the electron distribution. Most candidates have values above 5.

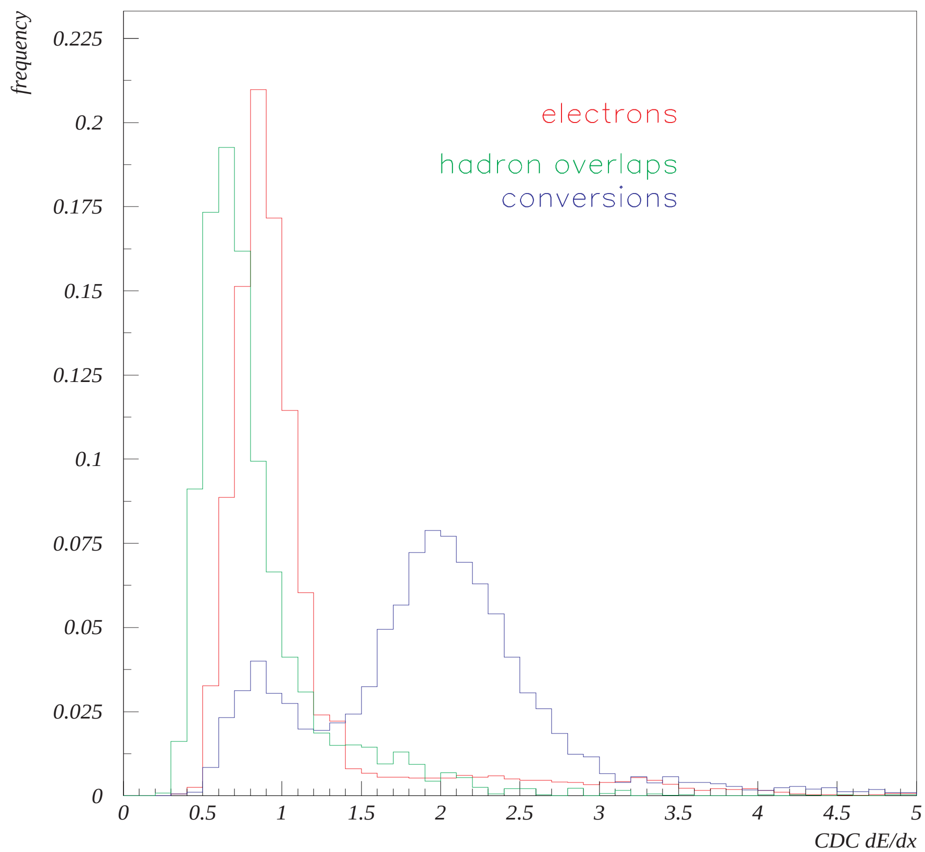

Figure 4.11: Ionization probability distribution for three populations in PELC sample: electrons (dashed), hadron overlaps (dotted), and conversions (solid).

f. Ionization

In the case of photon conversions, the recorded ionization along the merged track will amount to about twice what one expects from an electron. An electron will deposit ionization equivalent to one such particle (by design). Tracks from hadron overlaps, by virtue of being from more massive objects will tend to peak somewhat lower than electrons. These distributions are shown in Figure 4.11 for central PELC's in the Run 1b data sample.

g. Electron Likelihood

Explicit cuts on many individual variables may not make full use of all the information available. An improvement in electron efficiency relative to background rejection can be attained by calculating the probability a given candidate is an electron, hadron overlap or a conversion based on each of N quality variables. For this analysis N = 5 and the variables used are f_{EM}, χ^2, ε_t, σ_{trk} and dE/dx. One then calculates the likelihood that a given candidate is background *vs*. an electron via:

$$\mathcal{L}_N = \frac{f_{had}\,p_{had,N} + (1 - f_{had})\,p_{conv,N}}{p_{ele,N}} \qquad \textbf{Eq. 4.3.}$$

where f_{had} is the fraction of background which is hadronic overlaps, and $p_{x,N}$, the probability to be x (= hadron, conversion, electron), is the product,

$$p_{x,N} = \prod_{i=1}^{N} p_{x,i}$$

over the N variables. For clusters in the CC [EC] f_{had} = 0.52 [0.62]. Some of the distributions of $p_{x,N}$ are given in Figures 4.4 to 4.5 and 4.7 to 4.11. Such an analysis has been performed for both CC and EC electrons in the PELC sample[45]. In order to calculate these probabilities one must measure the distributions of each variable for the three contributions, x.

6. Electromagnetic Energy Scale

Sampling weights derived from test beam studies can only be expected to give back the proper energies for a detector with parameters exactly like the test beam modules. Modules can, however, have slightly different physical characteristics such as quality control of gap thicknesses, liquid Argon temperature and purity, etc. Since these can affect the energy scale, an *in situ* determination of the energy scale is necessary for the existing detector. This is typically done by comparing measured masses of well-known resonances to the world average values, and for this purpose DØ uses diphoton or dielectron decays of three different states: π^o, J/ψ, and the Z. For most analyses, the Z measurement is sufficient.

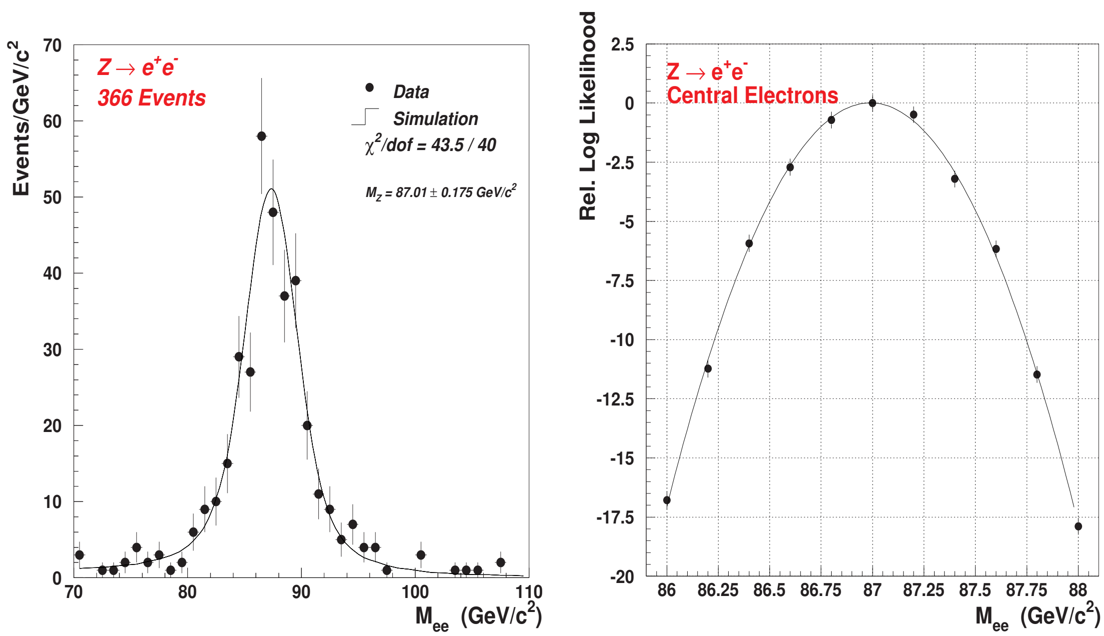

Figure 4.12: EM energy scale measurement in Z dielectron events. (a) fit to CC-CC events under assumption of a linear background, and (b) relative log(likelihood) as a function of invariant mass.

Shown in Figure 4.12 is the likelihood fit to the Run 1a Z dielectron sample with a background assumed to be exponential as a function of dielectron invariant mass. These events are those in which both electrons are central, ie. in the CC. The measured CC EM scale, determined *in situ* from the ratio of the Z mass as measured at LEP[46] to that measured at DØ[47] ($M_Z^{LEP}/M_Z^{D\varnothing}$), is about 1.05[48]. By isolating events in which at least one electron lies in one of the End Calorimeters, the scale for the EC's is similarly determined. This correction is applied to all reconstructed PELC and PPHO clusters but not to any jets or cells which are not part of reconstructed objects.

7. Electron Efficiency and Fake Rates

a. Calculation of Electron Efficiency

The track-finding efficiency for electrons is luminosity dependent because tracks fall outside the road used in reconstruction should the wrong vertex be identified as the primary vertex. We account for this effect on average by taking our single electron efficiency to be the mean in the Z sample which has the same luminosity distribution as our triggers.

To obtain the efficiency for our identification cuts, we employ a sample of events with two reconstructed electromagnetic clusters with E_T > 20 GeV. For each event we require one cluster to be a PELC which passes our quality cuts and do not apply them to the other candidate (the 'probe' electron). The probe electron will then be either a PELC or PPHO, in the CC or EC, depending on what type of object we are trying to study. If the probe electron is a PELC, we also try the combination where the former probe electron is required to be good, and remove the cuts on the other electron candidate. This is to improve statistics (a factor of two) and also to avoid biasing our sample because the leading electron and second leading electron may tend to have slightly different efficiencies.

To get the efficiency, candidates in the Z mass region were studied. To estimate the background under the Z peak from 81 to 101 GeV/c^2, we count events in sidebands from 61 to 71 GeV/c^2, and from 111 to 121 GeV/c^2 and sum them (ie. a linear background is assumed). We subtract this estimated background from the total number of dielectron events in the window around the Z. This gives us an estimate of the number of Z events (electrons) with no identification cut applied. The same process is repeated but with the identification cuts applied to the probe electron. The results are shown in Figure 4.13. The ratio of the two totals is our measurement of the electron efficiency for the cuts used. These are given in Table 4.6.

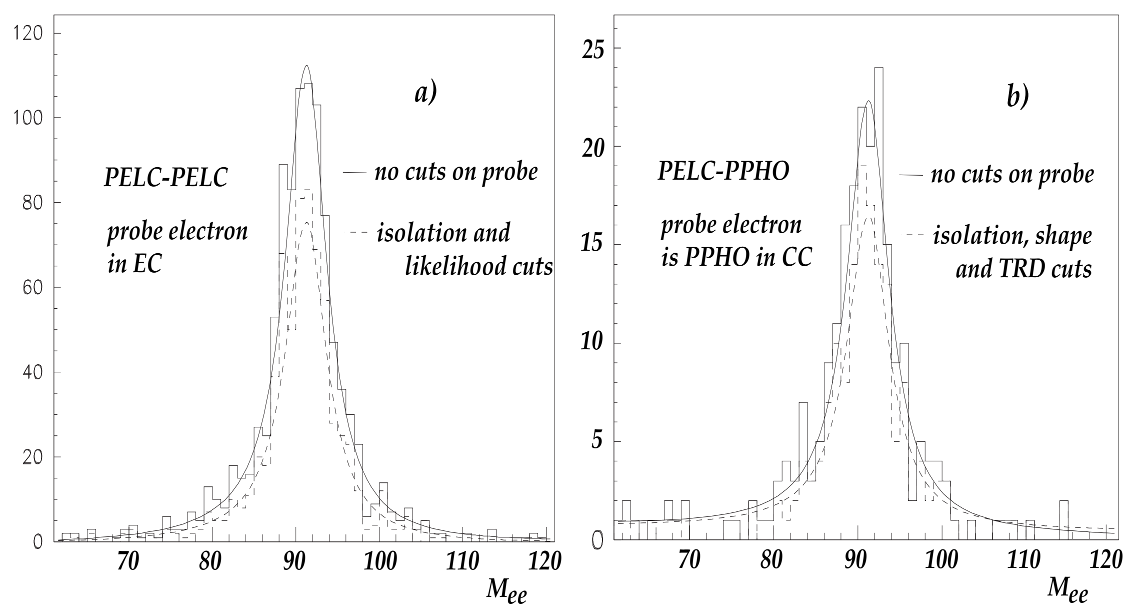

Figure 4.13: Invariant mass of two electromagnetic clusters in (a) PELC-PELC events in which the 'probe' electron is in the EC, (b) PELC-PPHO events in which the 'probe' electron is in the CC. Solid (dashed) lines are before (after) identification cuts.

In order to obtain a systematic error, we again assume a linear background but also fit the Z peak to a Breit-Wigner times a gaussian. If the resolution of the electrons is uncorrelated with the electron identification cut, then the width of the Z peak at its base is constant. This allows us to take the number of Z events to be proportional to the height of the Z peak as obtained from the fit. We fit the dielectron candidate sample with various electron identification cuts and allowed the width of the Z peak to float. We ascertained that this parameter was not strongly correlated with the electron quality within either the PELC sample or the PPHO sample. There were significant differences between these two samples, however, as we expect because the PPHO sample tends to have more events in which the primary event vertex was incorrectly chosen. The stability of the width *vs*. candidate quality lead to the conclusion that the assumption above is valid. The efficiency obtained from this method agrees with the sideband method to within about 2% [8%] for the PELCs [PPHOs].

We therefore quote the measured efficiency using the sideband method and quote a systematic error based on the difference between the sideband and fit methods. The statistical errors are binomial errors, the systematic is assumed to be gaussian.

Table 4.6. Efficiency for different definitions of electron: ε_{trk} is the efficiency to construct a track, ε_{PELC} is the efficiency of PELCs to pass the isolation and likelihood cuts, and ε_{PPHO} is the efficiency for PPHOs to pass the isolation and likelihood cuts.

region	ε_{trk}	$\varepsilon_{PELC\text{-}ID}$	$\varepsilon_{PPHO\text{-}ID}$
CC	0.827 ± 0.011	0.880 ± 0.016	0.751 ± 0.086
EC	0.852 ± 0.010	0.638 ± 0.023	0.718 ± 0.108

The efficiencies corresponding to our cuts are given in Table 4.6, and these can be used to obtain the total efficiency for electrons as

$$\begin{aligned}
\varepsilon_{PELC}^{CC} &= \varepsilon_{trk}^{CC} * \varepsilon_{PELC-ID}^{CC} = 0.728 \pm 0.016 \\
\varepsilon_{PELC}^{EC} &= \varepsilon_{trk}^{EC} * \varepsilon_{PELC-ID}^{EC} = 0.544 \pm 0.021 \\
\varepsilon_{PPHO}^{CC} &= (1-\varepsilon_{trk}^{CC}) * \varepsilon_{PPHO-ID}^{CC} = 0.130 \pm 0.015 \\
\varepsilon_{PPHO}^{EC} &= (1-\varepsilon_{trk}^{EC}) * \varepsilon_{PPHO-ID}^{EC} = 0.105 \pm 0.016
\end{aligned} \qquad \textbf{Eq. 4.4}$$

We assume these efficiencies are not dependent of energy of the electron if that energy is greater than 20 GeV. This is supported by test beam studies of the individual calorimeter and TRD variables. Likewise, since the electron is so high in energy, neither the tracking efficiency nor the dE/dx measurement should have a noticeable dependence.

The identification efficiency for EC PPHO's given in Table 4.6 was measured within the TRD acceptance. There is therefore an additional factor which reflects the fact that the TRD covers some fraction of the EC electron candidates. This fraction is obtained by looking at the fraction of electrons in the Z sample which are in the TRD acceptance and is 0.6 (0.52) for an η cut of 2.0 (2.5) (see Appendix III).

b. Electron Fake Rates:

In order to estimate the instrumental backgrounds, we must obtain a measure of the rate for jets to fake electrons. Once this probability is known, it can be folded into a sample of multijet events which satisfy all of the kinematic requirements we choose for the dielectron analysis (see Chapter VII). The fake rates must be determined such that the jet we are measuring has had the same trigger requirements as the 'fake' electron would have in our signal sample. Since we are using the ELE_JET trigger, this electron will generally be triggered as a jet at Level 1 and Level 2 (ie. no EM or other quality cuts).

The triggers which best match the requirements on the jet in this trigger are JET_MIN, JET_3_MON and JET_4_MON. We select events passing one of these filters and having at least one PELC or PPHO with $|\eta| <$ 2.5 and $E_T > 20$ GeV. To remove real sources of electrons, we apply further kinematic cuts requiring $\not{E}_T < 15$ GeV and the invariant mass of the two leading electromagnetic clusters (if there are more than one) be < 50 GeV/c^2. By measuring the fraction of all selected PELCs or PPHOs which satisfy our electron identification cuts, we determine the probability for an EM jet to fake an electron. The total fake rates are given in Table 4.7. For PELCS, all numbers are for the 5 parameter likelihood in both CC and EC. For PPHOs the numbers come from all the data for the pass rate of the calorimeter quantities. In order to estimate the pass rate of the TRD for these, we used the much smaller sample of fake triggers reconstructed with TRD information available.

Table 4.7. Probability for an EM cluster to fake an electron in percent.

cuts	Prob(EM$\rightarrow$'electron')
PELC: $f_{iso} < 0.1$, $\mathcal{L} < 0.5$ (CC)	0.569% ± 0.046%
$f_{iso} < 0.1$, $\mathcal{L} < 0.5$ (EC)	1.554% ± 0.089%
PPHO: $f_{iso} < 0.1$, $\chi^2 < 100$, $\varepsilon_t < 0.9$ (CC)	1.124% ± 0.071%
$f_{iso} < 0.1$, $\chi^2 < 100$, $\varepsilon_t < 0.9$ (EC) $\lvert\eta\rvert < 2.0$, TRD acceptance	2.130% ± 0.623%

As with our efficiency calculation, we note that we only allow EC PPHOs that are within the acceptance of the TRD. Since the fake rate given in Table 4.7 is the rate for a PPHO within this acceptance to pass our quality cuts, we must apply an additional factor which accounts for the fractional coverage of the TRD (given in Section 7a).

8. Jet Reconstruction

The theoretical models at our disposal predict parton energies in top events and backgrounds while the calorimeter measures jets after fragmentation, and calorimeter noise, response and showering. These serve to broaden jets and make them very irregular, especially for the lower energy jets (ie. 30 GeV and below) that we are often concerned with in this dissertation. As a result, jet physics is significantly dependent on the algorithm used to find them.

a. Fixed-cone Algorithm

In order to obtain observables which correspond kinematically to the partons we use a 'fixed-cone' algorithm which has three main steps. First, towers are listed and ordered by E_T if they have $E_T > 1$ GeV. In the second step, starting from the highest E_T tower, preclusters are formed around these towers by adding other towers within 0.3 in $\Delta R = (\Delta\eta^2 + \Delta\phi^2)^{1/2}$. In the third step, we find the energy weighted centroid of the cluster. This is made by adding towers with $E_T > 0.2$ GeV and inside radius ΔR, about the centroid, where for our purposes $\Delta R = 0.5$. Then a new centroid is calculated and the process is repeated. This continues until there is no change. Only jets whose $E_T > 8$ GeV are kept as jets. If a jet shares its more than 50% of its energy with a previous jet, the two are merged. Otherwise, they are split into two jets.

As a result of the high jet multiplicity in top lepton+jets final states, a large cone size tends to merge jets from distinct partons with the result that information is lost about the distribution of these objects before fragmentation. This is particularly an issue in a top mass measurement and a cone size of 0.5 has been chosen for these analyses. Although the dilepton final states do not suffer from this problem, these analyses exist within the context of the global top analysis so that we also use this cone size.

b. Jet Hot Cell Cuts

An algorithm was implemented in the reconstruction which looks for distinct calorimeter cells which are isolated from significant energy either immediately above or below in the calorimeter tower. Those cells found with this algorithm are not used in the reconstruction of jets and the calculation of $\not{E}_T$. There are, however, occasions in which one finds non-isolated energy which is not the result of a physically interesting process. The most often occurrence is when positive energy from the Main Ring is deposited in the calorimeter. Studies of jet events indicated that the most effective cut to reject such backgrounds was $f_{EM} - f_{CH} < -0.5$. In GOOD_BEAM events this mostly removes obvious Main Ring events which occur but are very rare. In the Z dielectron sample, the percentage of jets which fail this cut is less than 1%, indicating that there is no significant inefficiency for real jets. This selection does not have any effect in μBLANK and MRBS_LOSS events because we apply Main Ring jet corrections as described in Chapter 5 which have fixed these events.

9. Missing Transverse Energy:

a. Calculation of $\not{E}_T$

As noted in Chapter II, since neutrinos are weakly interacting, they deposit no energy in the calorimeter. Because the constituents of the proton and antiproton have variable momenta, we are never sure of the total longitudinal momentum in an event. However, the total transverse momentum is nearly zero because the proton and antiproton beams collide head-on and momentum is assumed to be conserved in any interaction that takes place. Therefore, we really can only consider the transverse components of this missing energy to be significant. We calculate this missing transverse energy as

$$\not{E}_x = -\sum E_i \cos\phi_i \sin\theta_i; \quad \not{E}_y = -\sum E_i \sin\phi_i \sin\theta_i$$

Figure 4.14 shows the linear dependence of the $\not{E}_T$ resolution on the total scalar E_T. This resolution was measured in events taken with a minimum bias trigger.

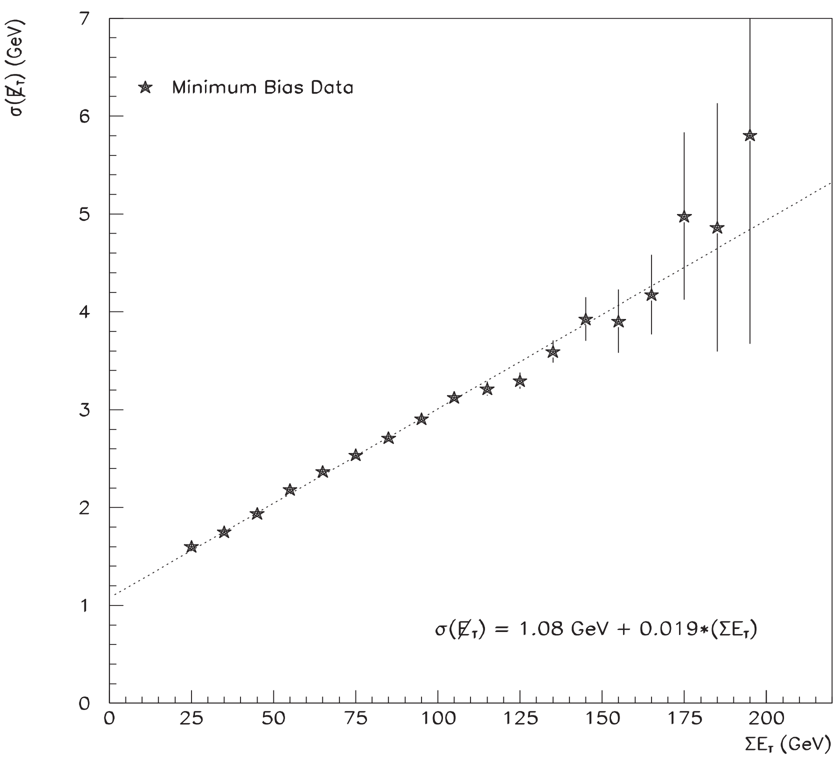

Figure 4.14: $\not{E}_T$ resolution (in GeV) *vs* . total scalar E_T in events taken with a minimum bias trigger.

b. Hot-Cell cuts on $\not{E}_T$

As we already mentioned, an algorithm was executed in the reconstruction to find and remove hot calorimeter cells. Although this algorithm generally works well, cells are occasionally removed from events incorrectly. For instance, isolated cells are sometimes produced in the course of normal particle showering in jets. A cut was employed to remove events with fake $\not{E}_T$ due to such cells. We calculate the $\check{\not{E}}_T$ by including these cells in the calorimeter and if this falls below the $\check{\not{E}}_T$ cut used by this analysis, the event is rejected. To gauge the efficiency of this cut, a sample of jet events was selected which had two jets with E_T > 20 GeV. Much less than 1% fail this cut. Therefore, this cut does not appear to incur any noticeable inefficiency in data.

10. Muons

a. Reconstruction

Muons are reconstructed in two general steps. First, 3-dimensional hits are found by using timing and charge readout of the wires and pads in the muon drift tubes outside of the calorimeter. Timing is used to obtain the distance of a hit transverse to the wire, and timing differences from readout of both ends of a wire indicate approximately where along a wire the hit is. A more precise measurement of this coordinate is then obtained by charge readout of diamond-shaped pads. The wire timing difference essentially indicates what pad is hit and the charge readout provides a 'vernier' indicating where on the pad the hit is located.

Once these hits are found, they are grouped into tracks which appear to arise from the interaction region. If a matching central track can be found, it is included on a global fit for the muon. Also, if it is consistent with the muon track, the vertex is added to the fit. These last two additions contribute a significant improvement to the momentum resolution. The final measured track momentum is obtained by correcting the fit momentum by the expected energy loss in the calorimeter and toroids.

b. Muon Quality:

The variable IFW4 is an integer variable which designates the quality of a track in the muon system. The value is zero for a perfect track and is incremented by one when the track fails one of three general criteria: 1) a module on the track has no hits, 2) the impact parameter with respect to the vertex is poor, and 3) the hit residuals on the track are poor. We require IFW4 = 0 or 1 in the central region, and IFW4 = 0 in the forward region.

For the first half of Run 1, the EF modules suffered severe radiation damage which essentially made them unusable during this time. Even after this was fixed, however, the very far forward regions were still damaged. In addition, the issues of reconstruction algorithms, triggering, and efficiency studies were never sufficiently addressed in the region in which the SAMUS and WAMUS overlap. As a result, we require muon tracks to be constrained to lie in the CF or the WAMUS-only portion of the EF. This corresponds to an effective cut of $|\eta_\mu| < 1.7$.

c. Transverse Isolation:

As in the case of electrons, muons from heavy flavor decay do not look like those from top, W or Z. In particular, there is significant hadronic activity near the muon which comes from the jet produced by the *b*-quark (or c-quark) fragmentation. In the case of the muon, we distinguish these objects by the variable $\Delta R(\mu\text{-jet})$ which is defined as the distance in $\eta-\phi$ from the muon to the nearest reconstructed jet. Because top events contain two *b*-jets, we wish to look for non-isolated muons from *b*-quark decay so we require $\Delta R(\mu\text{-jet}) < 0.5$.

d. Muon Tracking in Calorimeter

Because of its good resolution and fine granularity, the calorimeter can be used to identify muon tracks from the ionization they leave in the liquid Argon gaps. One useful selection requires that the fraction of cells along a muon track which have energy ('EFRH1') should be 1.0. If EFRH1 is not 1.0, we require the CH fraction of energy in the tower along the muon track to be significant. Jets typically deposit only a small fraction of their energy in the coarse hadronic layer. Since muons interact with the calorimeter mostly as minimum ionizing particles, however, the track they leave in the calorimeter will have a significant CH energy fraction.

CHAPTER 5

MAIN RING CORRECTIONS

"Do not go gentle into that good night."
- Dylan Thomas

1. Introduction

As mentioned in Chapter III, the Main Ring accelerator passes through the outer region of the DØ calorimeter. During collider Run 1, approximately 15% of the available Tevatron livetime is coincident with heavy losses from the Main Ring. This is less than the ~25% one would expect from the percentage of the injection cycle taken by µBLANK and MRBS_LOSS -- 8% and 17%, respectively -- because the Main Ring is not always being used for stacking while the Tevatron is running. Still, it is a substantial fraction of the total data, containing more than either Run 1a or 1c. In order to utilize this luminosity, we need to understand the impact of these losses on the objects in our sample, namely electrons, jets, and $\not{E}_T$.

Because of the thickness of the calorimeter in absorption lengths, the tracking volume, the EM portions of the calorimeter, and most of the fine hadronic portions are shielded from the main particle flux. Nevertheless, for jets we must employ corrections depending on the fraction of energy in the coarse hadronic (CH) section of the calorimeter included in the jets occuring during these periods of Main Ring activity. Fortunately, there is a clear distinction between fake jets from the Main Ring and real jets, and we find that we can correct for nearly all Main Ring activity and sacrifice very little in efficiency for normal jets.

For the $\not\!\!E_T$, we need to employ a correction which deletes the CH from the $\not\!\!E_T$ calculation for both μBLANK and MRBS_LOSS events and also subtracts out any additional negative energy in the Massless Gaps, ICD, and the outer fine hadronic layer in the CC ('CC FH3'). The corrections were optimized to have good efficiency for a spectrum of cells unbiased by the Main Ring, excellent rejection against spurious Main Ring energy, and good $\not\!\!E_T$ resolution. We find that we can achieve $\not\!\!E_T$ resolution nearly as good as that measured in data unaffected by the Main Ring (ie. GOOD_BEAM data).

All studies in this chapter begin from some form of sample with two electromagnetic clusters. There are three reasons for this: (1) these samples were readily available to us, (2) by virtue of the energy resolution of the electromagnetic jets the $\not\!\!E_T$ resolution is good, and (3) these events are triggered on with the Z filter which is unaffected by Main Ring energy deposition. We remove bad runs from our samples as described in Chapter IV.

2. Jet Correction

a. Suppression of Jets with Significant CH Energy:

Because some Main Ring particles deposit energy in the calorimeter when there is a Tevatron crossing, positive energy is registered in the calorimeter. This can sometimes cause fake jets to be reconstructed in the detector. To determine how we may discriminate against these fake jets, we first looked at a sample of events with two PELC or PPHO clusters with $E_T >$ 20 GeV. For this study we applied loose quality cuts such that the sample was largely, but not solely, Z events. Figure 5.1 shows distributions of E_T, the coarse hadronic energy fraction (f_{CH}), and ϕ for jets in μBLANK and MRBS_LOSS events in this sample. In Figure 5.1a (top left), there are clearly a large number of jets with high f_{CH} reconstructed in the direction of the Main Ring.

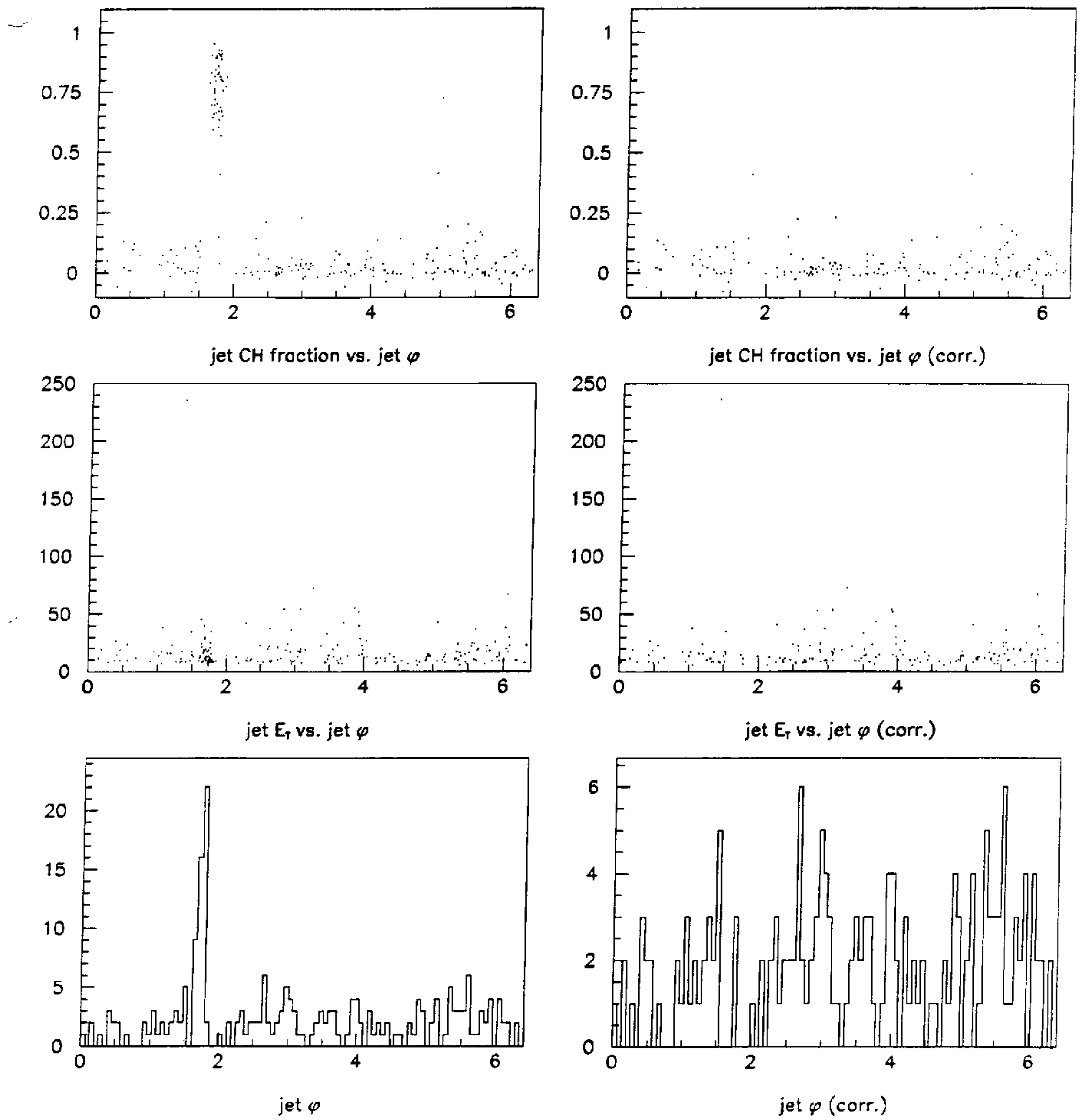

Figure 5.1: Distributions for jets in dielectron Main Ring events showing (a) jet E_T vs. ϕ (in radians) for jets before correction (left) and after (right), (b) CH energy fraction of jet vs. ϕ, and (c) ϕ of jet.

One should notice the strong dissimilarity between these jets' CH fraction and that of normal jets, which can be seen at the other values of ϕ. This distinction motivates an initial cut to correct for these jets -- $f_{CH} < 0.5$ looks reasonable. If a jet has a CH fraction > 50%, then the CH energy is removed from the jet. The average energy offset for central 0.5 cone jets is 1.5 GeV to 2.0 GeV (see Chapter VI). Any cluster of energy within 4σ of this we will consider to be consistent with the offset and not a jet. Therefore, if the sum of EM and FH E_T of the residual jet is < 5 GeV, it is removed from the event. We do not try to correct for the real CH energy we deleted from the jet if it survives our cut. These corrected jets will thus be biased slightly low in E_T but the cut affects only a small fraction (< 2%) of the jets in Main Ring events. Also, the loss in efficiency for real jets is a small fraction of this 2% because jets typically have little CH energy (of order 10%) and jets from top decays are energetic. Thus removing the CH energy from them still leaves a large amount of energy in the jet.

Figures 5.1a through 5.1f show the effect of this CH correction. The jet E_T and f_{CH} distributions have long tails in the Main Ring direction before corrections. After the corrections are applied, most of these jets are removed and the ϕ distributions become flat.

b. Study of Jets in μBLANK events:

The statistical power of our initial study was clearly limited and did not allow us to study μBLANK and MRBS_LOSS data separately. In order to look in more detail at the effect of our correction, events were chosen with two high E_T EM clusters with no electron or photon identification cuts, and at least one additional jet was required. The E_T of the EM clusters was greater than 20 GeV and their $|\eta| < 2.5$. For the different Main Ring states, various parameters of the leading jet were examined.

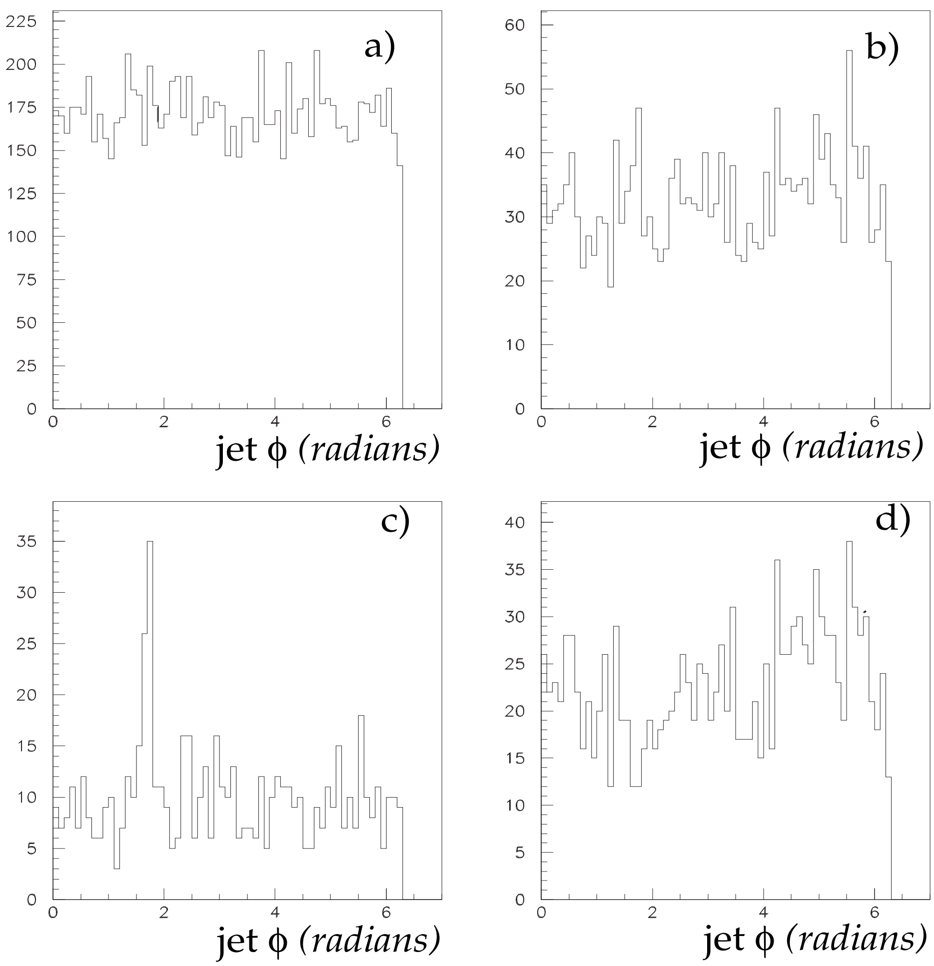

Figure 5.2: Distribution of jet ϕ (in radians) of the leading jet for (a) GOOD_BEAM, (b) .not.GOOD_BEAM, (c) μBLANK , and (d) MRBS_LOSS.

As shown in Figure 5.2, both GOOD_BEAM and the sum of all Main Ring events exhibit a distribution of jet ϕ which has a constant number of jets per radian for all ϕ.. Upon closer examination, however, we see that there is a pronounced excess of jets in the Main Ring direction (ϕ ~ 1.7) for μBLANK (Figure 5.2c), and maybe a slight dip in efficiency for MRBS_LOSS events (figure 5.2d). We would expect this relative behavior because μBLANK events often contain positive Main Ring energy which can produce spurious jets, while MRBS_LOSS events sometimes contain negative energy which could eradicate a nearby jet during clustering.

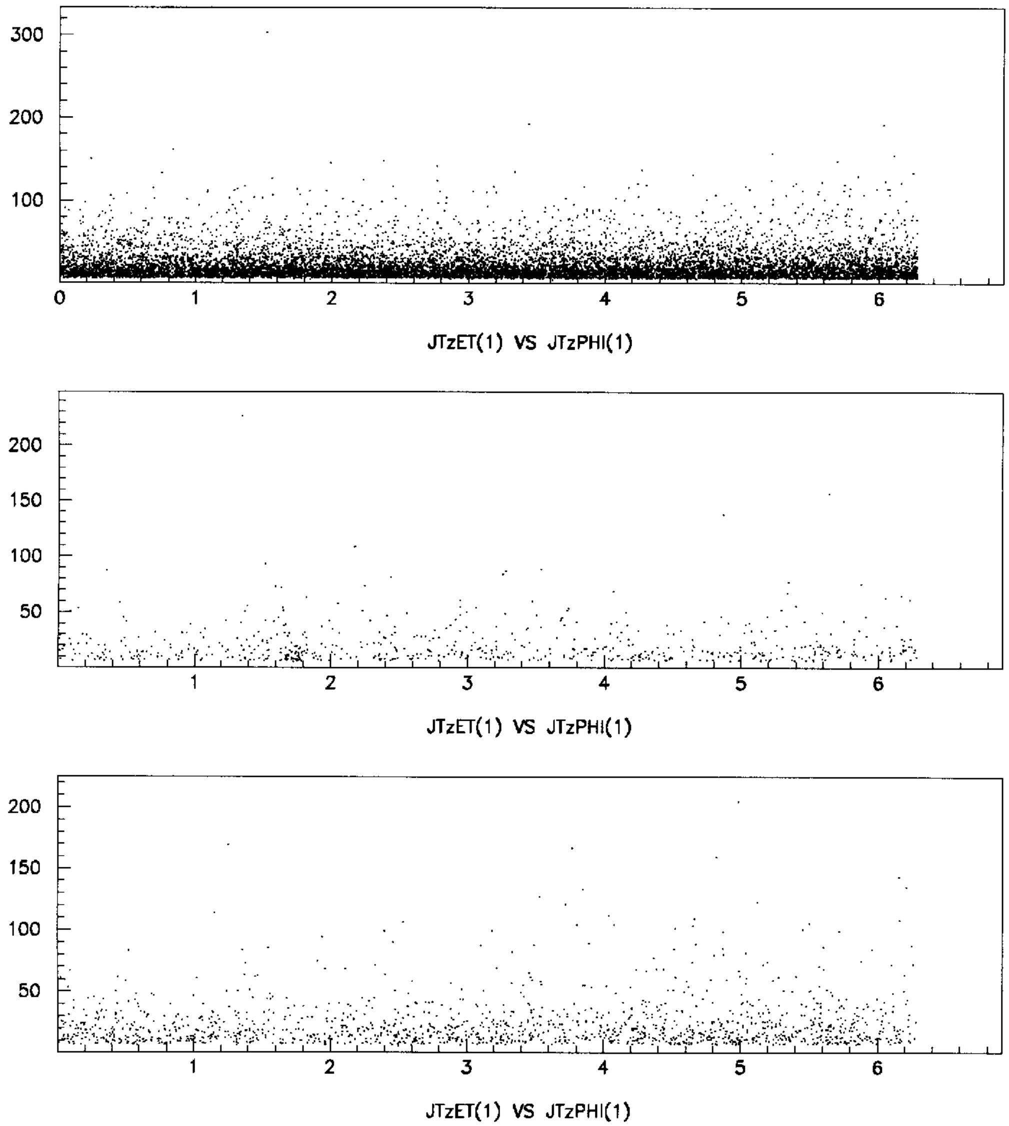

Figure 5.3: Jet E_T *vs.* jet ϕ for (a) GOOD_BEAM, (b) μBLANK, and (c) MRBS_LOSS after deleting CH from jets with $f_{CH} > 0.5$.

In trying to ascertain the properties of "jets" produced by the Main Ring which survive the selection of the previous section, we plot in Figure 5.3 the jet E_T vs. the jet ϕ for GOOD_BEAM, μBLANK, and MRBS_LOSS. Note that Figures 5.2a, 5.2c, and 5.2d are essentially projections of Figures 5.3a to 5.3c onto the ϕ axis. No enhancement of this distribution occurs except for μBLANK which possesses a cluster of low E_T jets in the Main Ring direction. Most of the jets in this clump are below 10 GeV.

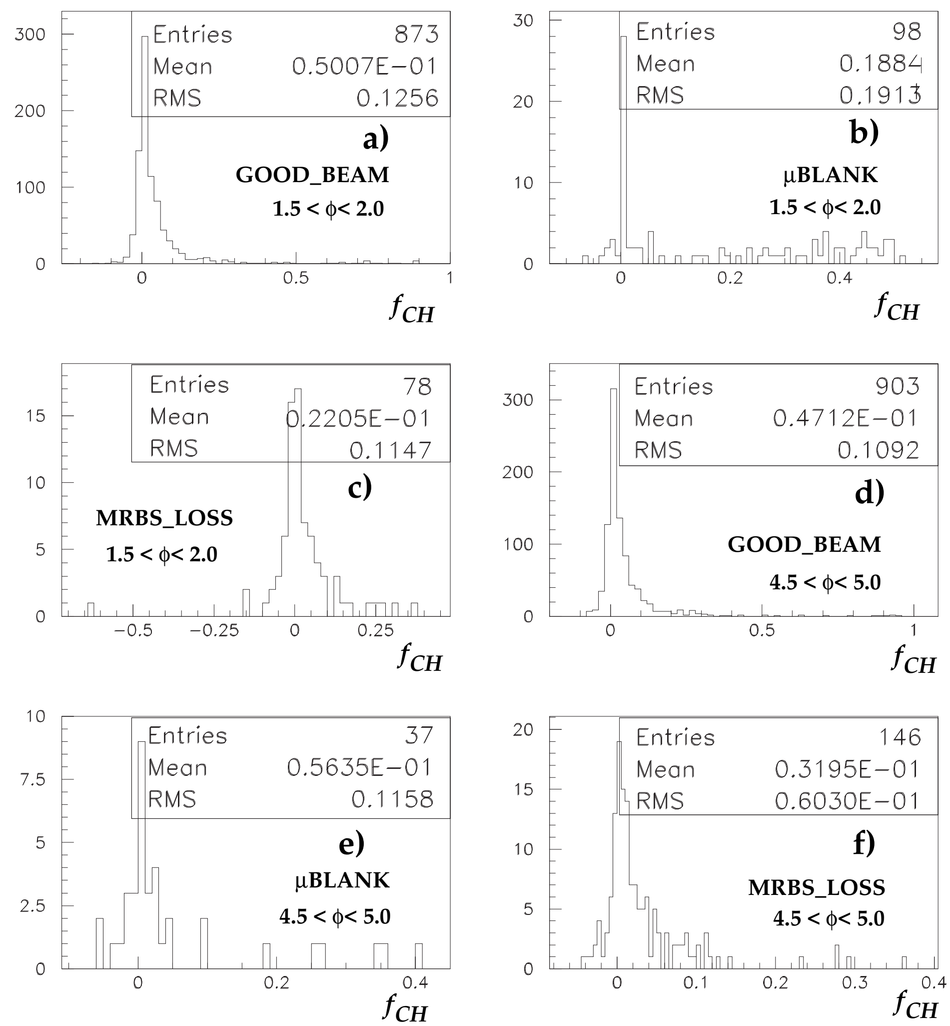

Figure 5.4: CH energy fraction for jets in two ϕ regions. (a - (c) are for jets in the Main Ring direction (ie. $1.5 < \phi < 2.0$), (d - f) are for jets approximately π away (ie. $4.5 < \phi < 5.0$). Figures are itemized according to Main Ring condition: (a) and (d) are GOOD_BEAM, (b) and (e) are μBLANK , and (c) and (f) are MRBS_LOSS.

In Figure 5.4 we plot the CH energy fraction for jets itemized according to Main Ring condition. Figures 5.4a to 5.4c show the distribution for events around the Main Ring (ie. $1.5 < \phi < 2.0$), while Figures 5.4d to 5.4f display the CH fraction for jets approximately π away (ie. $4.5 < \phi < 5.0$). Figures 5.4a, and 5.4d through 5.4f all look much the same with a mean CH fraction of about 0.05 and an RMS of this distribution of about 0.1. Figure 5.4c has one event with large negative energy. This means that the jet is actually higher in E_T than we measured. Instead of adding this energy back into the jet, we consider the effect as a source of inefficiency. In Figure 5.4b, however, many of the jets have already had their CH removed (f_{CH} = 0.0) and there is still a considerable tail of jets with high CH energy fraction out to the cutoff at 0.5. It would appear from these plots that a tighter cut than 0.5 is needed for μBLANK jets near the Main Ring.

In order to ascertain the necessary cuts for μBLANK events, we have looked at the jet E_T vs jet ϕ for different CH fraction intervals. Figure 5.5a shows this scatter plot when the CH fraction is < 0.2. Aside from a cluster of jets between 5 GeV and 10 GeV, there is no excess of jets in the direction of the Main Ring. As shown in Figures 5.5a - 5.5d, as the CH fraction increases, there is an increase in the correlation of jet ϕ with the Main Ring direction. It is evident that most of the jets in Figures 5.5c and 5.5d are associated with the Main Ring.

c. Final Corrections:

As a result of these findings, we modify our correction in the following way. Any jet with coarse hadronic energy removed must remain above 10 GeV after the correction. If a jet has > 20% CH energy, is in a μBLANK event, and is in a ϕ window around the Main Ring ($1.5 < \phi < 2.0$), the CH energy is removed. If the resultant E_T of the jet is less than 10 GeV, the jet is deleted from the list of clusters. Since this algorithm is designed to work on μDST events, no modification of the event at the cell-level occurs -- we do not re-run the jet algorithm on the event after deleting this coarse hadronic energy.

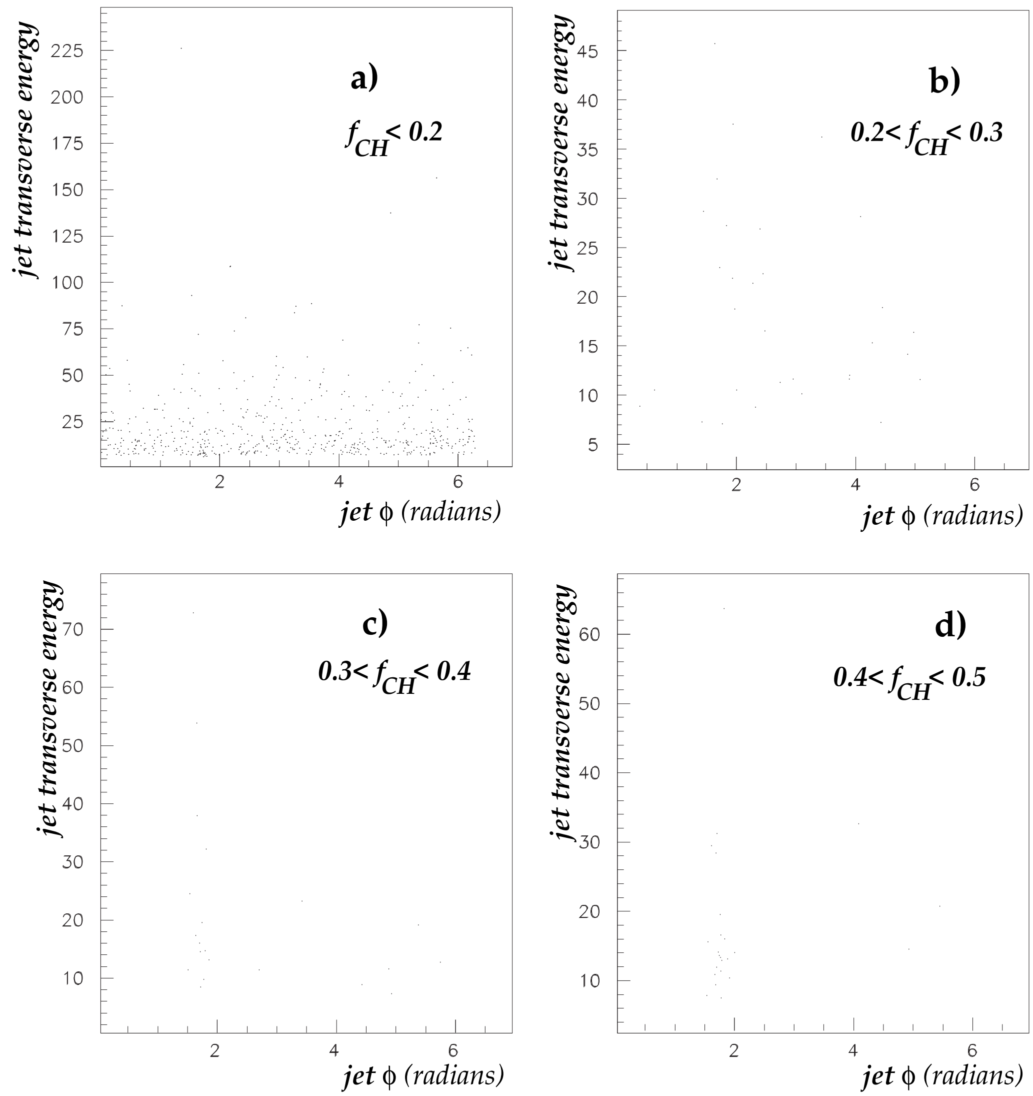

Figure 5.5: Jet E_T *vs*. jet ϕ for (a) CH fraction < 0.2, (b) 0.2 < CH fraction < 0.3, (c) 0.3 < CH fraction < 0.4, and (d) 0.4 < CH fraction < 0.5.

3. Missing E_T Corrections

Because the Main Ring passes through the CH region of the calorimeter, we will not include these layers in our determination of $\not{E}_T$. By removing this energy from the $\not{E}_T$, we correct for the vast majority of positive energy in events with the μBLANK flag set and remove the bulk of negative energy occurring in MRBS_LOSS events. Although this also discards positive jet energy which we would otherwise like to retain in a $\not{E}_T$ calculation, it does not degrade $\not{E}_T$ resolution appreciably because the CH energy fraction of jets is typically low (around 10%). This procedure is insufficient to fix MRBS_LOSS events, however, since negative Main Ring energy is not completely confined to the CH sections. Below we describe a method to remove these other negative energies to reduce the Main Ring bias to $\not{E}_T$ and improve the $\not{E}_T$ resolution in Main Ring flagged events.

a. Effects of the Main Ring

To identify when the Main Ring is a problem, we studied about 1700 events with two isolated electromagnetic clusters and tight quality cuts plus about 40 single electron events with large $\not{E}_T$ in the direction of the Main Ring.

In Figure 5.6 is shown $\not{E}_T$ $vs.$ ϕ for GOOD_BEAM and MRBS_LOSS events in this sample. The GOOD_BEAM events exhibit a distribution which is uniform in ϕ. The sample with the MRBS_LOSS flag set shows a number of events with large $\not{E}_T$ pointing in the Main Ring direction. These events generally possess cells with pronounced negative energy. Although cells with negative energy occur almost solely in events with the MRBS_LOSS flag set, there are a few events affected during GOOD_BEAM. μBLANK events lack almost any negative energy.

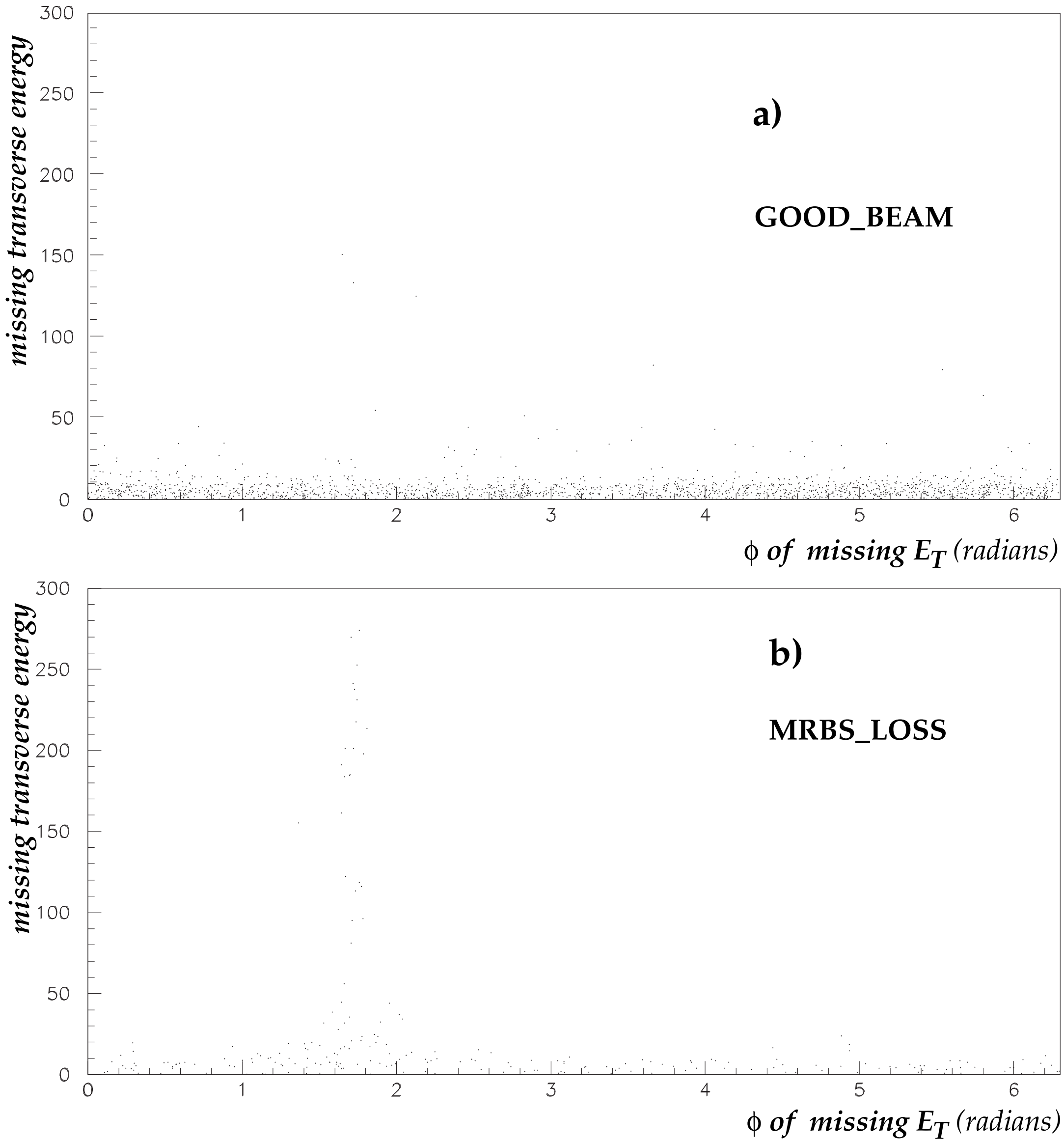

Figure 5.6: $\not\!\!E_T$ (in GeV) *vs.* ϕ for events with (a) GOOD_BEAM and (b) MRBS_LOSS flag set.

We have looked at the cell E_T spectra for all regions of the calorimeter and ICD, as a function of Main Ring state. Although we find most of the negative energy resides in the coarse layers of the calorimeter, there is still a considerable amount in the EC Massless Gaps (ECMG) and ICD (see Figures 5.7a through 7e).

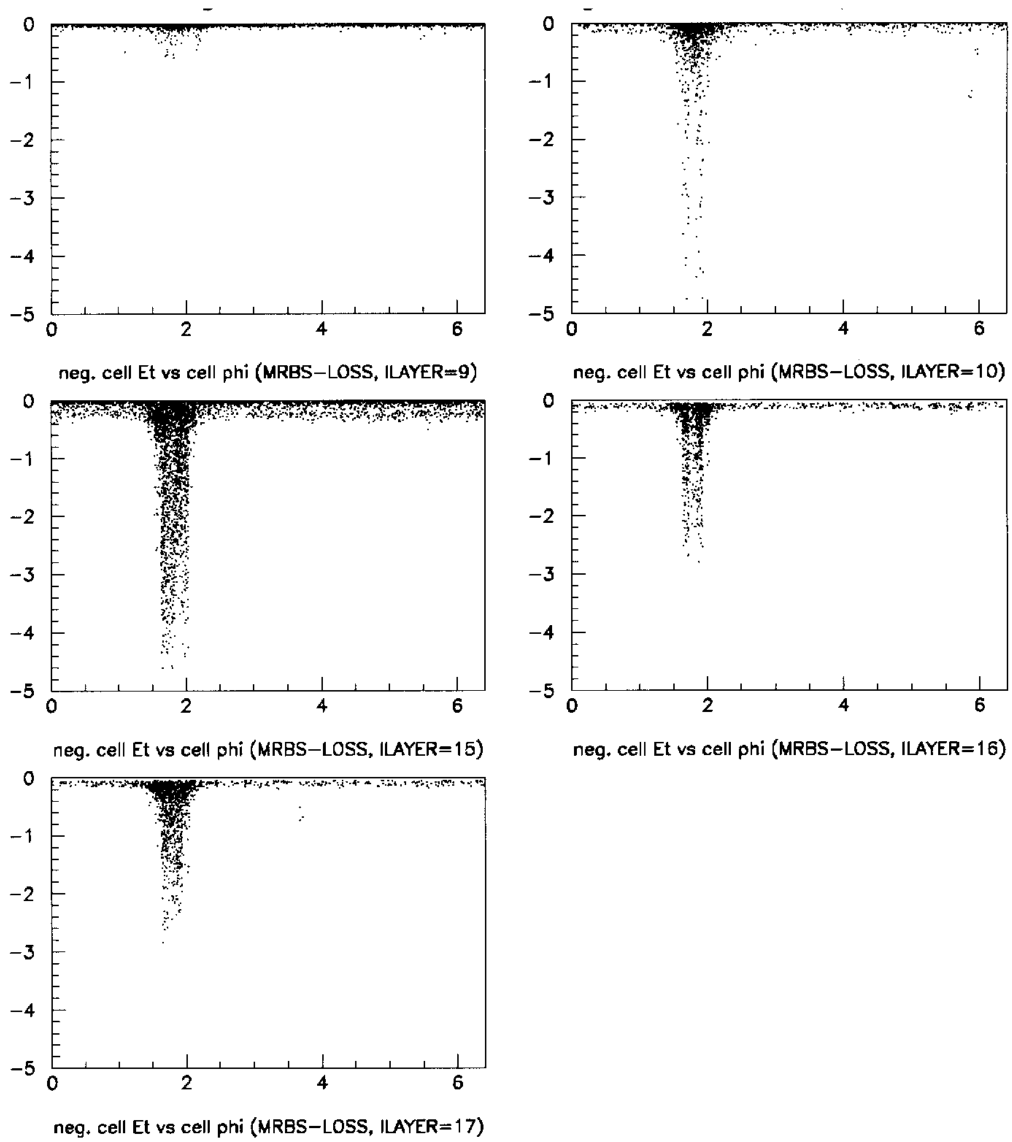

Figure 5.7: Calorimeter cell negative E_T vs. cell ϕ for events with MRBS_LOSS flag set. Figures (a) - (e) are indicated right-to-left, top-to-bottom. Distributions for (a) ICD, (b) EC Massless Gap, and (c - e) CH regions of CC and EC. There is significant negative energy in the ICD and EC Massless Gaps.

Figures 5.8a through 8f show the cell E_T spectrum near pedestal for ICD and ECMG channels with 9 < |IETA| < 15. We find that the main contribution comes from the regions of ECMG and ICD with |IETA| < 11. Occasionally we find large negative E_T (< -1 GeV) in ECMG beyond an

|IETA| of 11. We also observe such energy in CCMG, and CC FH3 and we include these regions among those from which we wish to remove negative energy. Table 5.1 itemizes the layers and IETA bins that show negative Main Ring energy.

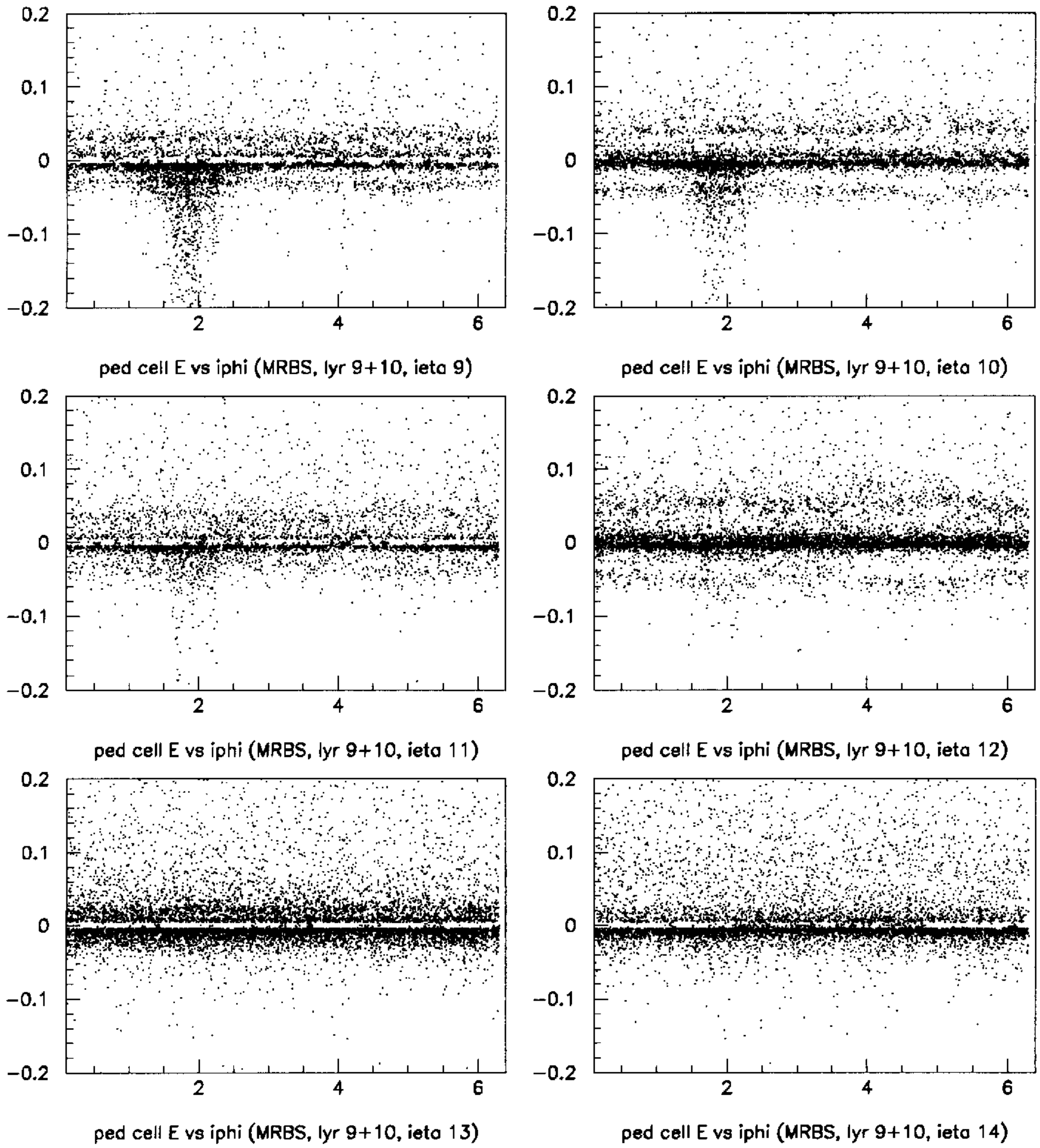

Figure 5.8: Cell E_T vs ϕ near pedestal for events with MRBS_LOSS flag set. The horizontal bands indicate different pedestal suppression cutoffs for different types of cells.

Table 5.1. IETA ranges for cells with significant negative energy.

Detector Region	Layer Index	Maximum |IETA|
CC Massless Gap	8	11
ICD	9	11
EC Massless Gap	10	13
CC FH3	13	12
CH	15	12
OH	16	13
OH	17	14

b. Optimized Vectors for Missing E_T Corrections

Figures 5.9a through 5.9e show the negative cell E_T spectra for the five regions of interest (CC and EC Massless Gaps, ICD, CC FH3, and the coarse hadronic). The dashed lines indicate the spectra for cells in events with the MRBS_LOSS flag in the Main Ring ϕ region. The solid lines indicate the spectra for cells in GOOD_BEAM events at all ϕ. We see that MRBS_LOSS events have negative energy tails which extend to larger magnitudes, and we can easily remove these tails without greatly affecting the spectra from the GOOD_BEAM events. We proceed as follows. We calculate vector sums for cells in each of the regions in Table 5.1 below some negative cell E_T threshold and remove them from the $\not{E}_T$. The following considerations guided our choice of thresholds for cell E_T:

- magnitude of energy at -3σ from pedestal
- amount of negative Main Ring energy typically seen in cell
- negative energy spectrum for the cell in data

We used the mean and RMS of x and y components of the $\not{E}_T$ to optimize these thresholds. The threshold sets explored are described in Table 5.2 while the effect on $\not{E}_T$ resolution in MRBS_LOSS events is itemized in Table 5.3.

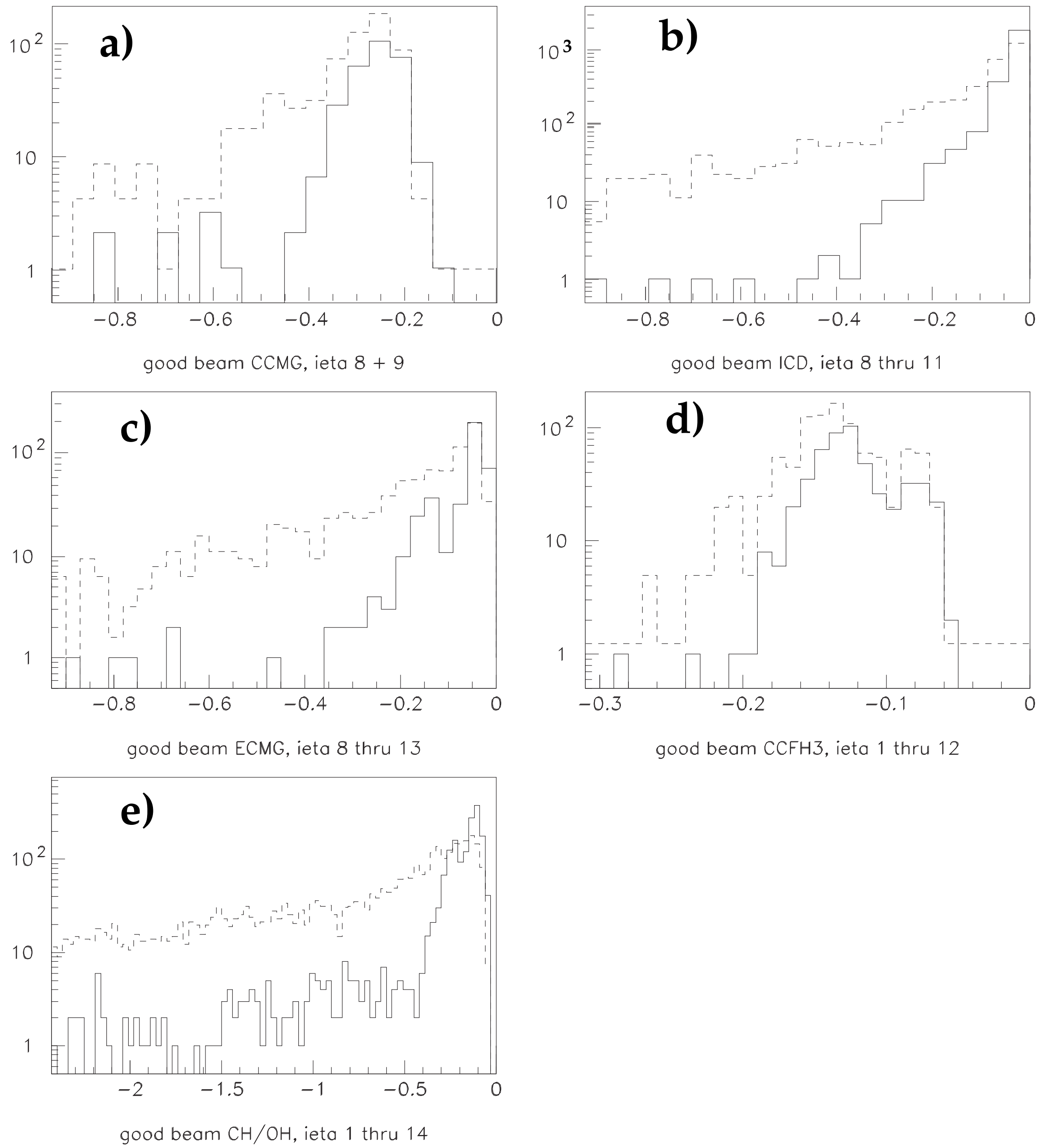

Figure 5.9: Negative cell E_T spectra for five regions of interest: (a) CCMG, (b) ICD, (c) ECMG, (d) CC FH3, and (e) CH. Solid lines are GOOD_BEAM cells from all azimuths, dashed lines are MRBS_LOSS cells in the Main Ring ϕ.

Table 5.2. Sets of negative E_T thresholds for calorimeter cells.

Vector Name	**CC MG(MeV)**	**ICD (MeV)**	**EC MG (MeV)**	**CC FH3 (MeV)**
V(1000)	-1000	-1000	-1000	-1000
V(500)	-500	-500	-500	-500
V(100)	-100	-100	-100	-100
V('OPT1')	-100	-100	-100	-400
V('OPT2')	-100	-50	-100	-200
V('OPT3')	-100	-50	0	-200
V('OPT4')	-100	-50	-100	-150

Prior to CH removal, there are large tails to the $\not\!\!E_T$ in the Main Ring direction for MRBS_LOSS events. Removal of all CH energy in the event ('V(CH)') eliminates most of the tails but the $\not\!\!E_T$ resolution is fairly poor -- the RMS of the distribution is 11 GeV in the y-direction when we normally can achieve about 6 GeV. Stated another way, the removal of all coarse hadronic energy still leaves us with an average $\not\!\!E_T$ in the direction of the Main Ring of ~4.4 GeV. Worse still, some events possess up to 100 GeV of $\not\!\!E_T$ from the Main Ring. Comparing the $\not\!\!E_T$ resolution for V(1000), V(500), and V(100) cuts indicates a steady improvement as we cut more tightly on cell E_T. Also, the remaining tail of events with large $\not\!\!E_T$ in the Main Ring direction is removed. After this, we tried four sets of variable thresholds to see if we could improve on the V(100) set. The set called V('OPT1') is looser than V(100) and shows a slightly worse resolution for the y component of the $\not\!\!E_T$. The $\not\!\!E_T$ resolution does not change much for the other threshold sets we chose.

Table 5.3. $\not\!\!E_T$ resolution in MRBS_LOSS for different threshold sets.

$\not\!\!E_T$ **calculation:**	**mean** $\not\!\!E_x$ **(GeV)**	**RMS** $\not\!\!E_x$ **(GeV)**	**mean** $\not\!\!E_y$ **(GeV)**	**RMS** $\not\!\!E_y$ **(GeV)**
$\not\!\!E_T$	-4.05 ± 0.81	12.18	32.27 ± 4.49	67.28
$\not\!\!E_T^{no-CH}$ = $\not\!\!E_T$ - V(CH)	0.53 ± 0.40	5.78	4.34 ± 0.71	10.64
$\not\!\!E_T^{no-CH}$ - V(1000)	0.70 ± 0.39	5.71	3.15 ± 0.55	8.24
$\not\!\!E_T^{no-CH}$ - V(500)	0.79 ± 0.39	5.72	2.77 ± 0.51	7.62
$\not\!\!E_T^{no-CH}$ - V(100)	0.90 ± 0.39	5.68	1.79 ± 0.43	6.52
$\not\!\!E_T^{no-CH}$ - V('OPT1')	0.91 ± 0.39	5.71	1.91 ± 0.45	6.77
$\not\!\!E_T^{no-CH}$ - V('OPT2')	0.88 ± 0.39	5.71	1.80 ± 0.44	6.65
$\not\!\!E_T^{no-CH}$ - V('OPT3')	0.85 ± 0.39	5.72	1.75 ± 0.43	6.54
$\not\!\!E_T^{no-CH}$ - V('OPT4')	0.90 ± 0.39	5.72	1.84 ± 0.43	6.57

The correction vector, V('OPT2'), best retains normal cells while eliminating appreciable Main Ring activity. Other threshold sets do not improve upon this algorithm. These cuts are approximately 3σ below pedestal while V(100), V('OPT3') and V('OPT4') are closer to pedestal for some regions. It should be noted that, as mentioned above, this sample was enriched with events having $\not\!\!E_T$ in the Main Ring direction and so the results in Table 5.3 are a worst case scenario -- results from analysis of a larger unbiased sample are given at the end of this subsection.

Throwing away large numbers of negative cells can result in a bias in the $\not\!\!E_T$. Some cells have positive energy from physics despite registering a net negative energy. Also, the pedestal width varies from cell to cell and removal of negative energy from noisy cells will incur a small $\not\!\!E_T$ vector π radians away from the cell in ϕ. As a result, we have measured our efficiency for good cells and rejection for contaminated cells. We define the efficiencies for unbiased cells in a detector region to be the number of cells in GOOD_BEAM events which survive the cuts for V(`OPT2') divided by the total number in a typical spectrum. The μBLANK and MRBS_LOSS numbers are for cells restricted to the Main Ring region (ie. $1.5 \leq \phi \leq 2.0$) and thus include both biased and unbiased cells.

Table 5.4. Cell efficiencies for GOOD_BEAM, MRBS_LOSS and μBLANK .

Detector Region	**cell ε GOOD_BEAM**	**cell ε μBLANK**	**cell ε MRBS_LOSS**
CC Massless Gap	0.98	1.00	0.80
EC Massless Gap	0.94	1.00	0.35
CC FH3	1.00	1.00	0.96
Coarse Hadronic	0.94	1.00	0.35

Table 5.4 itemizes approximate efficiencies for cells unaffected by the Main Ring (ie. GOOD_BEAM cells) and cells which are often affected by the Main Ring (ie. MRBS_LOSS cells). We find that V('OPT2') keeps excellent unbiased cell efficiency as defined by the GOOD_BEAM cells. This correction also rejects appreciable contaminated cells as seen in the MRBS_LOSS data. The GOOD_BEAM effiencies give lower limits on actual unbiased cell efficiencies as there is occasional Main Ring energy in GOOD_BEAM events. Likewise, the efficiencies from MRBS_LOSS give upper limits to efficiencies for cells with only negative energy from the Main Ring because there are good cells in the distribution.

A related statistic is the total number of cells removed in a typical unbiased event by our cuts. We have counted the mean number of cells thrown out from $\phi = 2.5$ to 6.0 (a region where the Main Ring is not affecting us) and scaled that to the total 2π. The cuts labelled V('OPT2') remove only about 3.0 unbiased cells per event out of several thousand fired per event in the calorimeter as a whole. These cells are mostly in EC Massless Gap, close to the -100 MeV threshold, and randomly distributed in ϕ. Thus the possible bias on $\not{E}_T$ is very small. The main degradation in $\not{E}_T$ occurs with the removal of positive CH energy.

As mentioned in Section II, positive energy is occasionally deposited in events with the μBLANK flag, although it can occur for MRBS_LOSS or even GOOD_BEAM events. For completeness, we attempted to determine whether this was confined to CH or spilled into the ICD and ECMG noticeably. We summed all energy in these regions into a vector and corrected the $\not{E}_T$ with this. No improvement in $\not{E}_T$ resolution was observed and no preference of this vector for the Main Ring direction was seen. We therefore consider it unnecessary to correct positive energies in any region other than CH.

Table 5.5. $\not{E}_T$ resolution in MRBS_LOSS for DST sample.

$\not{E}_T$ **calculation:**	**mean** $\not{E}_T^{\parallel}$ **(GeV)**	**RMS** $\not{E}_T^{\parallel}$ **(GeV)**	**mean** $\not{E}_T^{\perp}$ **(GeV)**	**RMS** $\not{E}_T^{\perp}$ **(GeV)**
$\not{E}_T$	10.35 ± 1.36	36.99	-0.61 ± 0.22	5.88
$\not{E}_T^{no-CH}$	1.06 ± 0.31	8.52	-0.81 ± 0.21	5.62
$\not{E}_T^{no-CH}$ - V('OPT2')	0.23 ± 0.24	6.58	-0.84 ± 0.21	5.62

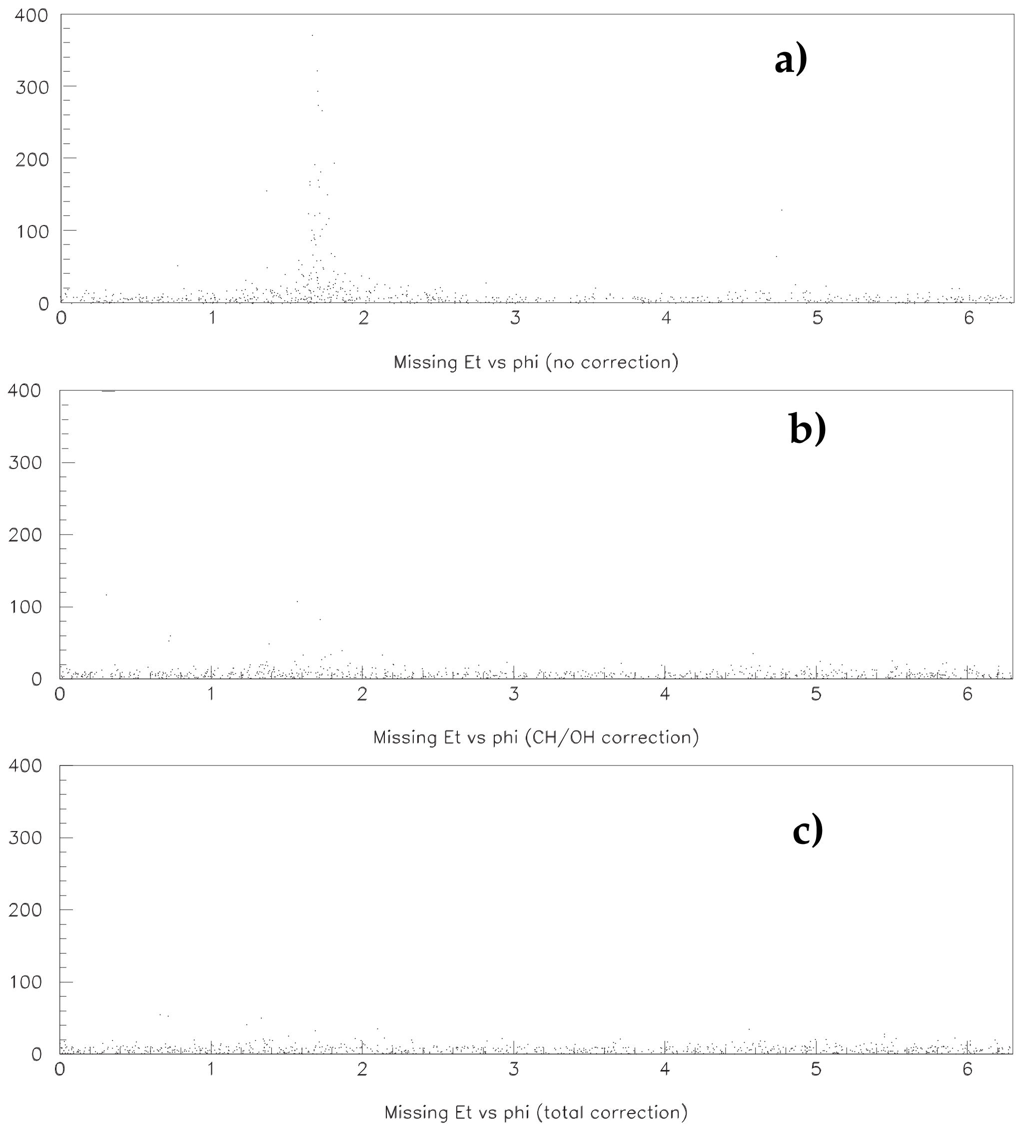

Figure 5.10: $\not{E}_T$ vs ϕ for MRBS_LOSS events in DST sample with (a) no corrections, (b) CH removal only, and (c) removal of negative energy from the ICR.

In order to check our results and determine an unbiased measure of $\not{E}_T$ resolution for these corrections, we ran on an independent sample of 7850 DST's which were selected by requiring 2 EM clusters with E_T > 15 GeV and loose quality cuts (isolation < 0.3, and χ^2 < 300). No $\not{E}_T$ or jet cuts were applied in the selection. Figures 5.10a through 5.10c show that the thresholds we have picked do well in reducing the large $\not\!\!E_T$ in the Main Ring direction. There are a few events with large $\not\!\!E_T$ after CH removal but once the full corrections are performed the distribution is flat in ϕ. In Table 5.5 we give the average $\not\!\!E_T$ projected onto an axis which points from the center of the detector to the Main Ring ($\not\!\!E_T^{\parallel}$), and onto the axis perpendicular to this direction ($\not\!\!E_T^{\perp}$). We expect Main Ring losses to bias the mean $\not\!\!E_T^{\parallel}$ but not the mean of $\not\!\!E_T^{\perp}$ since they are distributed symmetrically with respect to the $\not\!\!E_T^{\perp}$ axis. The $\not\!\!E_T^{\parallel}$ resolution is improved to nearly the level of the $\not\!\!E_T^{\perp}$ resolution and the bias in the mean value is removed by the correction.

c. Summary of Correction

The correction has two elements: the first is the threshold to be used for the Massless Gaps and ICD (-100 MeV), and the other element is the threshold for CH and CC FH cells (-300 MeV). The CH threshold was chosen in an analogous way to those chosen in Section *3b* (see Figure 5.9e). We summed this negative CH vector for different thresholds and found that a tighter cut on cell E_T adds noise and no new Main Ring energy while a significantly looser cut fails to reject all backgrounds.

Table 5.6. Two GOOD_BEAM events having large negative Main Ring energy.

Run-Event	$\not\!\!E_T$ **(GeV)**	$\phi_{\not E_T}$	$\not\!\!E_T$ **(CH) (GeV)**	$\phi_{\not E_T}$ **(CH)**	$\not\!\!E_T$ **(ECMG) (GeV)**	$\phi_{\not E_T}$ **(ECMG)**
81994-2416	153.5	1.69	142.7	1.71	6.8	1.71
82108-12569	131.2	1.71	118.9	1.71	4.9	1.71

This vector is included because of its usefulness in GOOD_BEAM events where one wants to keep the positive CH energy but may want to correct those few events that had a lot of negative CH energy. Two such events, described in Table 5.6, show large $\not{E}_T$ but if corrected with the CH alone would have little left. Use of the non-CH negative vector would provide a further improvement for these events. The cell thresholds mentioned in this section are a slightly looser set than the V('OPT2') set we optimized to in Section *2.b* but give essentially the same results.

CHAPTER 6

JET ENERGY SCALE CORRECTION

Theoretical calculations of high energy physics processes give event kinematics in terms of parton energies. Event generator Monte Carlos such as HERWIG or ISAJET go a step further by following through particle decays and the fragmentation of colored partons into jets. For physics analyses it is important to be able to treat a reconstructed calorimeter energy cluster as a more idealized object whose behavior is described by these calculations. Because one signature of top production is the presence of high p_T jets, an understanding of the jet energy scale is an important part of top physics. In particular, the uncertainty in the jet energy calibration turns out to be the limiting systematic error in the estimate of the top mass in lepton + jets candidates[37].

1. Overall Jet Corrections

It is useful to briefly note the nature of jets to help define the calibration goal. The fact that most events display a dijet structure intuitively connects the observed jets to an underlying simple parton interaction. However, it is not easy to associate the jet energy with a specific underlying parton energy -- partons radiate gluons, fragment into hadrons and interact with one another via color flow. This complexity makes jet physics very dependent on the jet definition. Figure 6.1a depicts the evolution of a typical jet. Initially, a quark parton radiates a gluon which can be considered a separate 'jet' at the parton level depending on the algorithm applied to the event. Further evolution is indicated by the energy density labelled 'particle level' which shows how this parton event migh look after averaging all possible fragmentations of the quark and gluon. Note that the distinction between the quark and gluon has been considerably blurred. In addition, energy which was not part of the original partons has been added to the jets from the underlying spectator interactions occurring coincident with the hard scatter.

In addition to these effects, at the detector level, three phenomena affect the measured jet energies: 1) response, 2) energy offset from noise or spectator interactions, and 3) showering. For the purposes of comparison with predicted event parameters in a Monte Carlo sample, we would like to compensate for any detector effects which alter the event from the final state particle level. 'Calorimeter jets' are those jets found with a given algorithm after all gluon radiation, fragmentation, and detector effects have been accounted for. We define our jet calibration to compensate only for detector effects so that we attempt to obtain the 'particle level' energy of a jet, E_{ptcl}^{jet}, from its measured calorimeter energy, E_{meas}^{jet}. This particle level energy is the energy of a jet found from final state particles with the same algorithm as the calorimeter jet. We define this energy to include only those particles arising from the partons participating in a hard scatter. Because obtaining the parton level jet energy involves physics which one would like to study, we do not attempt to implement a correction which determines this from the calorimeter jet energy.

Figure 6.1b depicts a schematic of a jet as it hits the calorimeter, in this case three charged hadrons produce wide showers and photons from π^0's and

η^o's, etc. leave narrower showers confined to the EM portion of the calorimeter. The transverse size of the lightest shower, for instance, is seen to deposit energy outside of the calorimeter jet cone from a particle inside the cone.

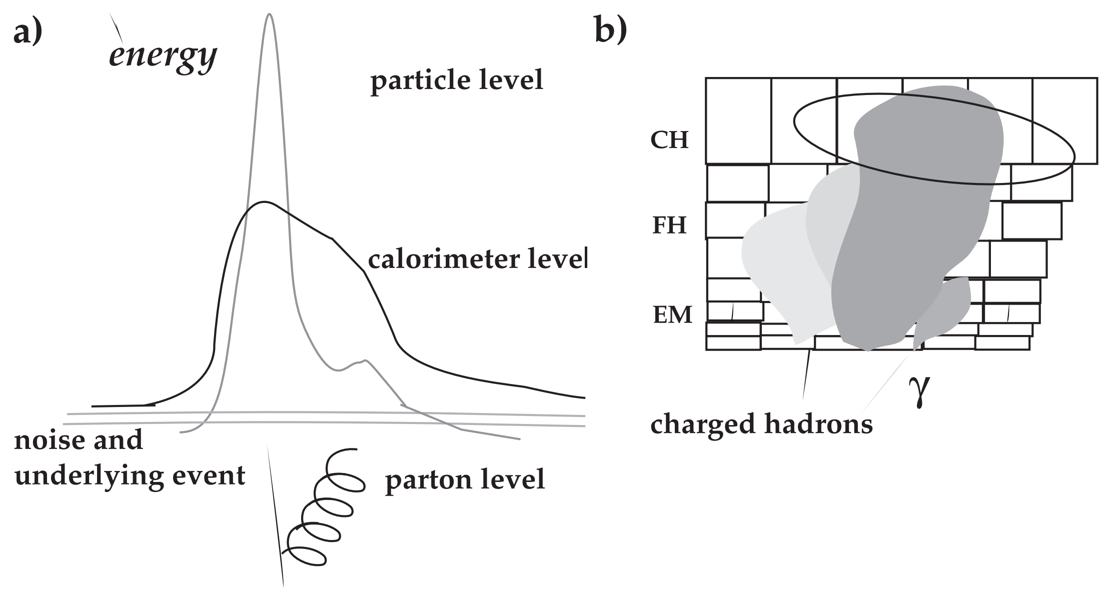

Figure 6.1: Schematic of jets. (a) Shows a section of calorimeter with individual particle showers. Charged hadrons, in particular, produce wide showers which can spill outside of a jet cone. (b) Sketch of jets at parton, particle, and calorimeter levels. At the particle level, there is not a clear association of energy to each parton. At the calorimeter level, showering and noise further alter the energy profile.

Our calibration obtains E_{ptcl}^{jet} from E_{meas}^{jet} by correcting for the following:

- An energy offset, O, which includes both detector noise and energy from the underlying event.
- A change in energy due to showering in the calorimeter, S, which is specific to each jet algorithm.
- A change of the energy scale, R (response), due to e/π ratio of the detector and energy lost in readout cracks.

Algebraically, we calculate E_{ptcl}^{jet} for a found jet by,

$$\boxed{E_{ptcl}^{jet} = \frac{E_{meas}^{jet} - O}{R(1-S)}} \qquad \textbf{Eq. 6.1}$$

2. Estimation of Offset

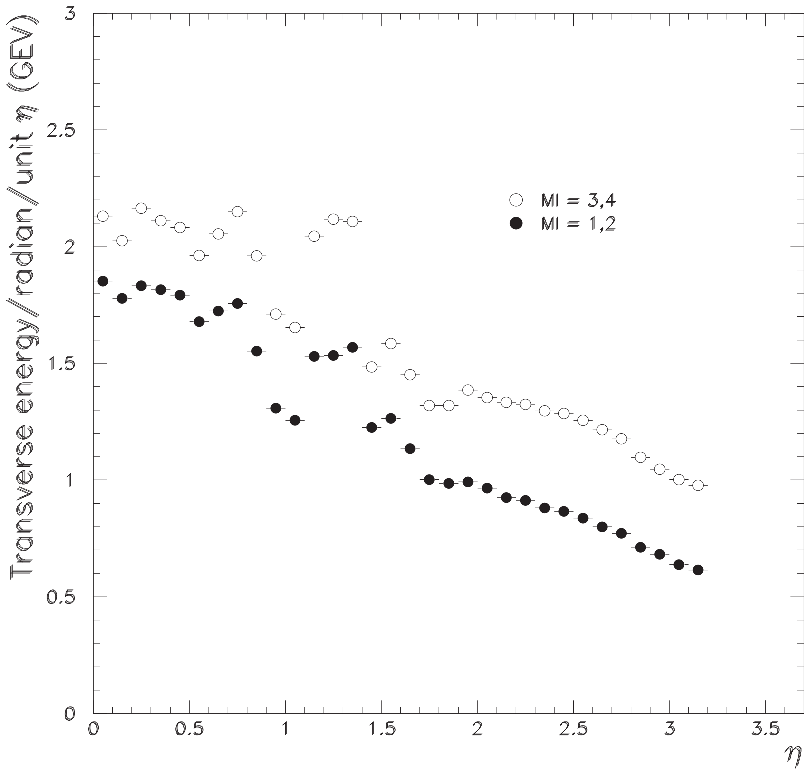

Figure 6.2: Average E_T density in GeV *vs.* calorimeter tower IETA in minimum bias events. The distribution is shown for single interaction (solid circles) and double interaction (open circles) events. These samples were selected by the status of the LØ Multiple Interaction flag (MI = 1,2 is single interaction, MI = 3,4 is multiple interaction).

Two processes contribute to the energy offset. The absorber plates in the EM and FH portions of the DØ calorimeter are made of depleted uranium whose decay results in a measurable signal. The resulting asymmetric pedestal distribution leaves a net positive energy contribution after a symmetric zero suppression cut, which we label 'noise' (N). Additional energy comes from beam remnants and additional $p\bar{p}$ interactions and is termed 'underlying event', denoted U.

Figure 6.2 shows the average E_T density as a function of calorimeter tower η from events satisfying a minimum bias trigger. The solid circles are from events where only one interaction occurred in each beam crossing as determined by the Level Ø detector. The open circles are from events where two interactions occurred. If the underlying event contribution for two interactions is twice that for single interactions, then the difference between the two histograms in Figure 6.2 is a measure of the underlying event contribution for a single interaction:

$$U = O_{MB}^{2\,\mathrm{int}} - O_{MB}^{1\,\mathrm{int}}$$

where $O_{MB}^{i\,\mathrm{int}}$ is the total E_T density in a minimum bias sample of i interaction events. The removal of the underlying event contribution from the single interaction energy density gives the noise contribution,

$$N = O_{MB}^{1\,\mathrm{int}} - U$$

The magnitude of U is approximately constant in E_T as a function of η and is about 310 MeV/rad/unit-η. We use the measure of the instantaneous luminosity for an event to tell us how many interactions occurred and the number of estimated interactions is multiplied by U to obtain the total underlying event correction for that event. The magnitude of N is approximately constant in energy as a function η and is about 1.6 GeV/rad/unit-η in the central region. The systematic error on the underlying event E_T density is 0.2 GeV/rad/unit-η, while for noise the uncertainty in the energy density is 0.1 GeV/rad/unit-η. These uncertainties reflect the different values obtained from independent minimum bias samples. Correlations between these two uncertainties are ignored.

3. Showering

According to our definition of E_{ptcl}^{jet}, no correction is needed when an algorithm is applied at the particle level. However, once the fragmentation products strike the calorimeter, the observed jet broadens due to the resultant showers and some energy can leak out of, or into, a jet cone (see Figure 6.1b). To quantify this, central jets are generated with HERWIG[49], and the energies of the fragmentation particles are deposited in the first calorimeter cells intercepted by their momentum vectors. Jet reconstruction is then performed on these cells to produce 'unshowered' jets. To produce 'showered' jets, the hadrons/photons in the jet are replaced with test beam pions/electrons of the same energy. The particle's energy is then distributed relative to the intercepted cell as observed in the test beam and jets are reconstructed from these showers. The showered and unshowered jets are matched and the ratio of showered energy to unshowered energy is calculated (= 1 - S in Equation 1). For a cone size of ΔR=0.5, S varies from 0.03 to 0.0 depending on particle jet energy as shown in Figure 6.3.

The preliminary systematic uncertainty is about 1% which is obtained from variations in the estimate of S when calculated as an E_T ratio as opposed to an energy ratio.

4. Response of the U/LAr Calorimeter to Jets

a. Origin of Response

Measured jet energies are degraded due to the response of the calorimeter to single particles which make up the jet. Prior to any correction for jet response, our energy estimate of a reconstructed jet is based solely on calibrations carried over from test beam data. The cumulative effect is to lower jet response from 100% even for higher energy jets. Several effects contribute to the response to jets of a particular detector being non-unity:

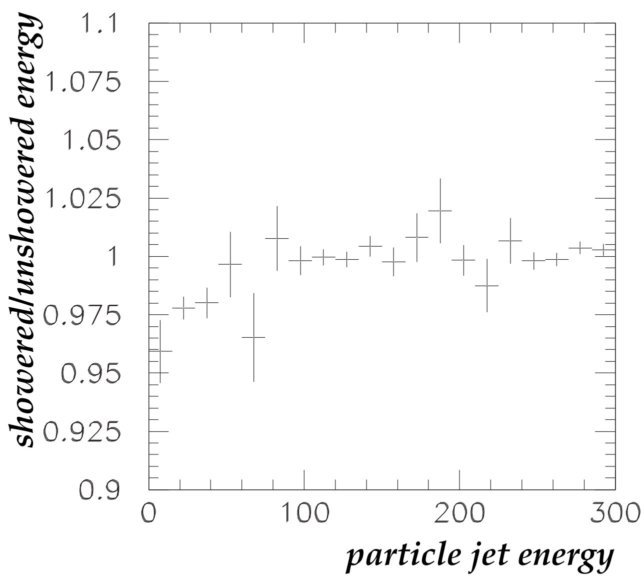

Figure 6.3: Ratio of energy in showered and unshowered jets using a fixed-cone algorithm with ΔR = 0.5 in the central region.

- Test beam analyses indicate that the calorimeter is not quite compensating (i.e. $e/\pi > 1.0$)[50].
- In general, the response of each cryostat may be somewhat different than the corresponding test-module used to obtain their sampling weights. We know from studies of Z dielectron events and other resonances that the EM-modules, at least, have a shifted scale relative to that measured in the test beam.
- Jets are extended objects which can deposit energy in poorly instrumented regions not well-represented in the test beam calibration. The most extensive such region is the region between the cryostats but there are also smaller cracks between readout boards throughout the calorimetry.
- Some jet energy is lost to the zero-suppression cut.
- An inefficiency in reconstructing low E_T jets near the 8 GeV threshold results in a biased response for the jets that are detected and reconstructed.

b. Simple Model of a Jet

It is instructive to consider a simple model of a jet to elucidate the calorimeter response to jets. Let us consider a jet which fragments into 6 particles irrespective of jet energy. From isospin considerations, consider also that the energy is distributed so that 30% is carried by electromagnetically interacting particles (eg. γ's from π^0's) and 70% is taken by charged hadrons. These percentages are roughly consistent with the ratio of neutral particle to charged particle multiplicity found in measurements of real jet fragmentation although the measured behavior is much more complex. Note that when mentioning 'EM' energy here we are not referring to the energy deposited in the electromagnetic portion of the calorimeter, but rather the energy deposited by electromagnetically interacting particles anywhere in the calorimeter. With this model in mind, we can then write the response to the jet as

$$R_j = 0.3R_{\pi^0} + 0.7R_{\pi^\pm}$$

Since we think we know the fundamental electromagnetic scale of the calorimeter as discussed in Chapter IV, we take $R_{\pi 0} = 1.0$. We discussed the behavior of the response of the charged hadron relative to this benchmark in Chapter III. If we input the parametrization for the hadron response given in Equation 3.2, we obtain

$$\boxed{R_j = a + b\ln E_j} \qquad \textbf{Eq. 6.2}$$

and the constants a and b are

$$a = 0.3 + 0.7\left(R_h + a_0(R_h - 1)\ln 6\right), b = 0.7a_0(1 - R_h)$$

If we take the values of these as $a_0 = 0.2$ and $R_h = 0.84$, which one gets from a fit to test beam data, then $a \sim 0.8$ and $b \sim 0.02$. This crude estimate is likely somewhat of an overestimate because we have neglected the effect of poorly instrumented regions whose reduced response is not represented in the e/π analysis mentioned in Chapter III. Note that the logarithmic behavior is only appropriate over some range in particle energy which happens to be the range applicable to particles in most jets at the Tevatron[40].

5. Measuring Response

Having defined response and crudely estimated its behavior, let us turn to the job of actually making a precise measurement. Without a magnetic field we cannot measure the individual charged particle response *in situ,* so instead we will use direct photon events. In these events, response differences among objects result in a measurable overall imbalance of transverse energy in the calorimeter thereby contributing to the $\not\!\!E_T$. Because little physics is involved in using the $\not\!\!E_T$ besides conservation of energy, we rely on this to measure R. Because the photon is properly calibrated in such a sample, we can use the $\not\!\!E_T$ in the event to anchor the jet to an absolute energy scale. In the following sections we will discuss

- the method and the fast Monte Carlo used to test and define it.
- systematic uncertainties due to the method.
- systematic uncertainties arising from the presence of backgrounds in our sample.
- efforts to extend the energy reach in the data.
- cross-checks of the measurement in data with other measurements of response.

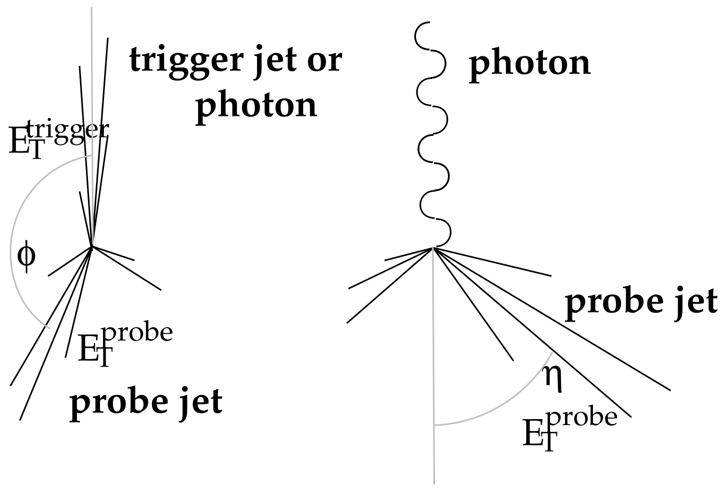

Figure 6.4: Sketch of the $\not\!\!E_T$ Projection Fraction method showing (a) the trigger jet and the recoiling hadronic system. Photon plus jets events shown in (b) are used to provide an absolute calibration of jets.

In general, we look in dijet events as shown in Figure 6.4 to determine the response relative to a trigger jet which must pass a single jet trigger. With this requirement, the other 'probe' jet is unbiased. In order to obtain the response of the probe jet in terms of the $\vec{\not\!\!E}_T$ let us consider a general event with three vectors: $\vec{E}_T^{trigger}$, $\vec{E}_T^{had}$ (vector sum of the energy of all interacting particles in the event outside of the trigger jet), and $\vec{E}_T^{\nu}$ (vector sum of the energy of all non-interacting particles in the event such as neutrinos). In the transverse plane at the particle level we have

$$\vec{E}_T^{trigger} + \vec{E}_T^{had} + \vec{E}_T^{\nu} = 0$$

At the calorimeter level, this reduces to

$$R^{trigger}\vec{E}_T^{trigger} + R^{had}\vec{E}_T^{had} = -\vec{\not\!\!E}_T$$

where $\not\!\!E_T$ is due to $\vec{E}_T^{\nu}$ and the response differences between the trigger jet and the hadronic recoil of the event, and R^{had} is the response of the hadronic recoil. If $E_T^{\nu} = 0$, at the particle level $\vec{E}_T^{trigger} = -\vec{E}_T^{had}$ and we obtain

$$\boxed{r = 1 + \frac{\not{E}_T \bullet \hat{n}_T^{trigger}}{E_T^{trigger}}} \qquad \textbf{Eq. 6.3}$$

where $\hat{n}_T^{trigger}$ is the unit vector in the transverse direction of the trigger jet, and r is $R_{had}/R_{trigger}$. These dijet events are used to obtain the relative response as a function of pseudorapidity. In the case of the photon events, however, $R_{trigger}$ = 1.0 after the EM scale corrections so r becomes the absolute energy scale of the probe jet, R_j. This quantity only involves the $\not{E}_T$ and the photon, and in an event with only two particle level jets and no offset or showering, it becomes E_{Tmeas}/E_{Tptcl}. When more than one jet comprises the hadronic recoil (ie. $\vec{E}_T^{had}$), Equation 6.3 is an approximation of the response of the probe jet. This 'topological' issue will be taken up later. The discrepancy is small, however, and we can in theory plot R_j in terms of any property, X, of the probe jet.

6. Energy Scale in Inter-Cryostat Region

Because the sampling in the inter-cryostat region is poor, the sampling weights for the ICD and Massless Gaps are chosen to compensate for this. Since the ICD, in particular, is a different technology than the CC and EC, there may remain differences in response with respect to these detectors. We use the $\not{E}_T$ in dijet events as discussed above to determine the energy scale of probe jets as a function of detector pseudorapidity in this region. In Run 1a a significant energy correction was needed while in Run 1b, preliminary studies indicated that no adjustment was needed[51].

7. Response Dependence on Angular Width of a Jet

It has been shown that jets have greater response variations due to the area in the calorimeter they cover and their particle multiplicity than to whether they showered early in the EM section[52]. Thus one might expect jet response to depend on jet angular width. Such a dependence is observed in both collider data and Monte Carlo samples with wide jets having lower response than narrow jets. Further, the dependence of relative response on the width decreases with both probe jet pseudorapidity and E_T. As a result, jet response is measured by using the $\not{E}_T$ in dijet events, plotted *vs.* jet angular width, and fit to obtain a correction. The correction is normalized such that this correction should not change the average jet response.

8. Resolution Bias in Energy Dependence Measurement

a. Standard Event

Although R_j is calculated using transverse quantities, the resulting response measurement is strictly speaking a function of the jet energy because e/π is energy dependent. As a result, we wish to measure response as a function of this property. However, jet energies are measured with comparatively poor resolution in the detector and this causes a bias in our measurement of response such that not even simple input response functions can be determined with our method. In this section, we first describe this bias, illustrate it with examples from data and a parametric calculation, and explain a way of overcoming it. In the process, it will turn out that there are two requirements that must be satisfied for the method to work. Both are satisfied by a photon which is good indicator of the parton E_T of the event. First, the photon must have a well measured response. Second, its energy resolution must be good ($\sigma_{em} \leq 0.3/\sqrt{E_j}$).

To start with, we will consider an event with one photon and one jet back-to-back in ϕ, at η = 0. Let us assume that the photon response is 100% and R_j = 85%. Furthermore, the jet and photon fractional resolutions are:

$$\sigma_{em}/E_\gamma = 0.15/\sqrt{E_\gamma}$$

$$\sigma_j/E_j = 0.80/\sqrt{E_j}$$

For reasons that will be discussed later, we initially take the direct photon cross section to be constant in $E_{\gamma T}$.

b. Trigger Effects

First let us discuss a bias caused by the direct photon triggers by taking an ensemble of direct photon events with 40 GeV E_T partons. After passing through the calorimeter, this will result in the distributions shown in Figure 6.5. On average, we would calculate R_j to be $E_{\gamma T}/E_{jT}$ which would give a response of 85% for the mean jets having E_{jT} = 34 GeV which is what we assumed.

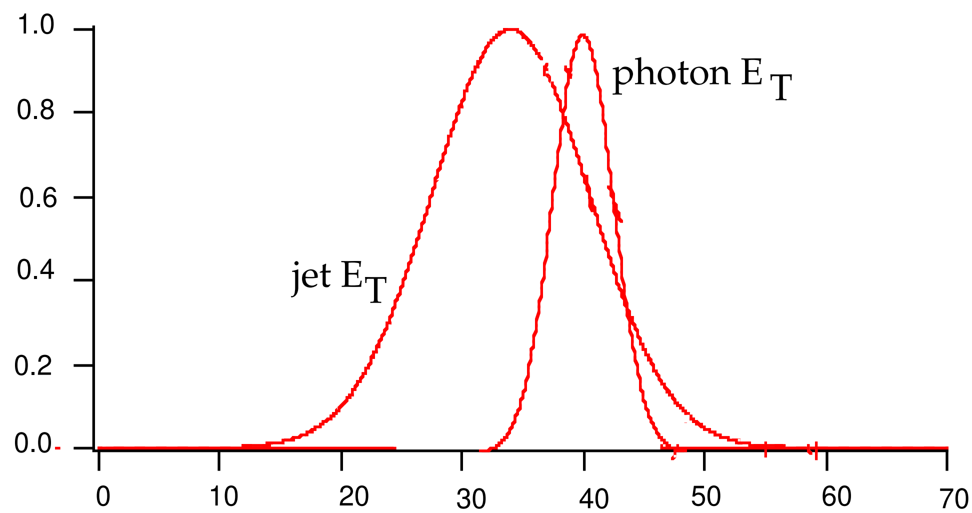

Figure 6.5: Photon and jet E_T distributions for an ensemble of 40 GeV Et parton events. The photon resolution is much better than the jet but the ratio of their means gives R correctly.

Instead of considering only 40 GeV parton events, we allow for the parton E_T to be any value and classify (ie. 'bin') events in terms of the jets as we would in the analysis. For instance, take events with a leading jet having E_T = 34 GeV. Due to the jet resolution, the parton that the jet comes from would have an energy spectrum shown as the narrower curve in Figure 6.6. The photon, because of its good resolution and response, approximates the parton E_T on an event by event basis causing its spectrum to look like the slightly wider curve in Figure 6.6.

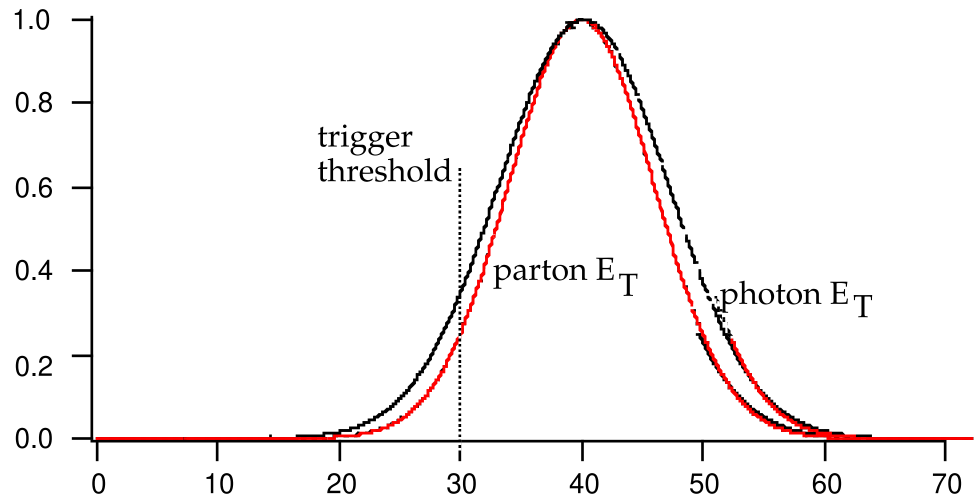

Figure 6.6: Photon and parton spectra for 34 GeV jets. The spectra are broad due to the jet resolution (ie. we do not know what parton the jet came from.)

If we apply a (trigger) E_T cut to the photons around 30 GeV, instead of $<E_{\gamma T}>$ being 40 GeV it will now be ~ 44 GeV so that $R_j = E_{jT}/E_{\gamma T}$ = 77% rather than the actual value of 85%. If we apply a lower E_T cut on the photon like 15 GeV then we have $<E_{\gamma T}>$ = 40 GeV and the jet response is measured correctly. Just such a behavior between different thresholds (triggers) is seen in the data in Figure 6.7.

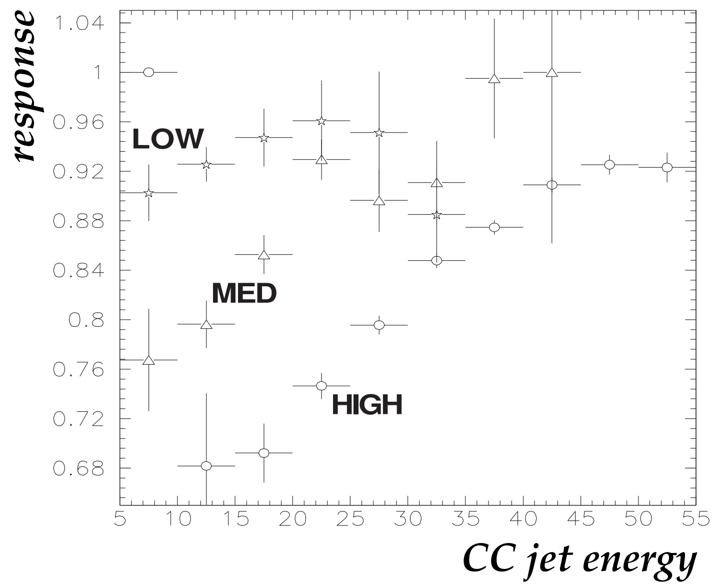

Figure 6.7: Response vs. *Ej* for direct photon triggers. 'LOW' is data passing GAM_LOW_ISO, 'MED' refers to data passing GAM_MED_ISO, and 'HIGH' is data passing GAM_HIGH_ISO.

To see explicitly what is happening in the data, we look in one jet E_T bin. Application of the GAM_MED_ISO and GAM_HIGH_ISO triggers gives the $E_{\gamma T}$ distributions in Figure 6.8. We can see that, as with Figure 6.6, the GAM_HIGH_ISO trigger has raised the mean $E_{\gamma T}$ by dropping all events below 30 GeV in $E_{\gamma T}$ Considering the approximate equality of $E_{\gamma T}$ with the parton E_T, a selection (ie. triggering) on $E_{\gamma T}$ above some threshold is essentially a selection of a higher mean parton E_T. This is therefore a selection of a lower mean R_j for a given jet energy. Looked at another way, near and below the threshold selected for the direct photon triggers we exclude events where the jet fluctuated high into the E_j region we are considering. This skews the $\not{E}_T$ high by removing part of its normal distribution and this results in measuring a lower <R_j>.

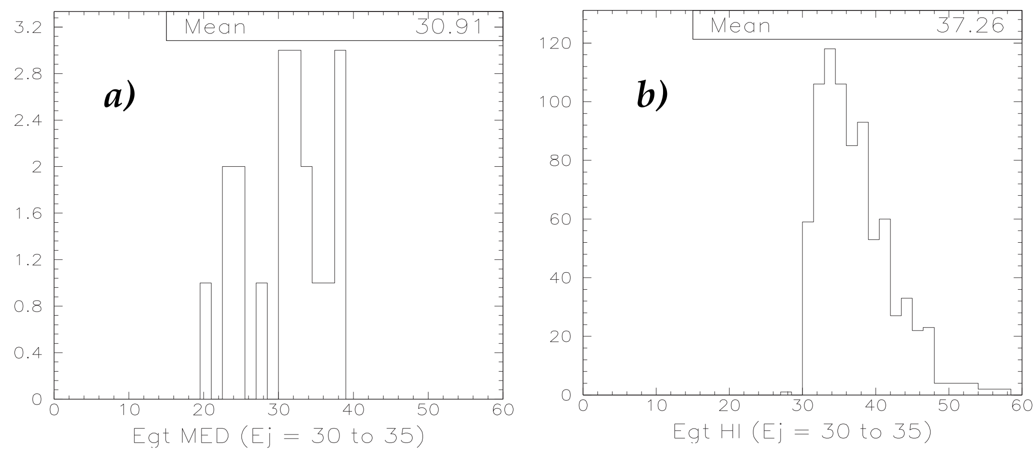

Figure 6.8: Photon spectra for GAM_MED_ISO and GAM_HIGH_ISO triggers.

A study of $E_{\gamma T}$ spectra in E_j bins indicates that trigger-dependent and cone-size dependent cuts on E_{jT} in Table 6.1 are necessary for the method to overcome this resolution bias. The cone size dependence occurs because the larger cone jets have larger fluctuations in energy due to the underlying event and other factors. When taking data from the triggers according to these cuts, the measured response for all triggers agree in the region in which they overlap.

Table 6.1. Required E_{jT} thresholds for direct photon triggers for four cone sizes

cone size	LOW	MED	HIGH
0.3	12 GeV	22 GeV	42 GeV
0.5	15	22	45
0.7	17	25	50
1.0	20	27	55

c. Effect of Photon Cross Section

The cuts produce a great loss in statistics in the E_T region in which we have triggered (ie. < 45 GeV) although we should be able to obtain the right answer for the energy dependence of response. There is, however, an additional problem which cannot be avoided with any suitable choice of cuts.

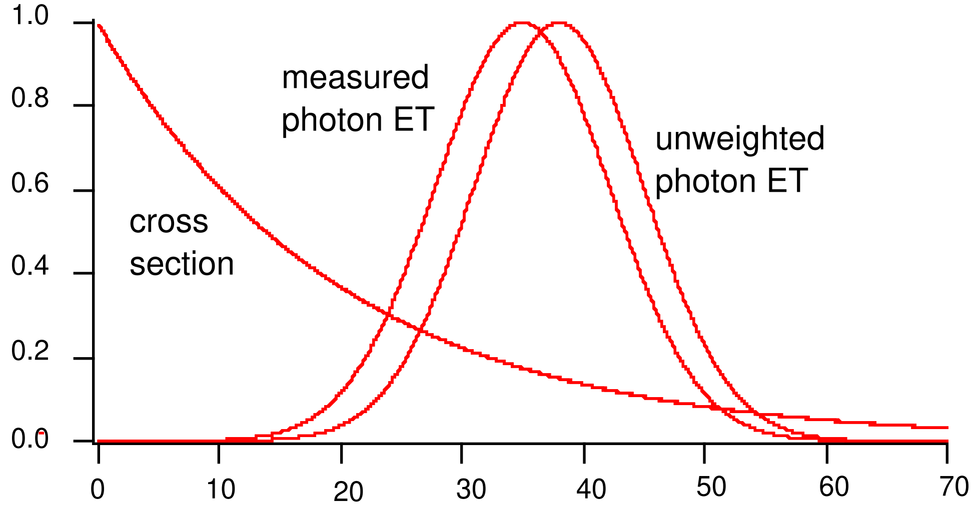

Figure 6.9: Effect of direct photon cross section on photon E_T distributions within a fixed jet E_T bin.

A bias encountered when directly binning response in terms of E_j is due to the $E_{\gamma T}$ dependence of the direct photon cross section. We now require that our standard events adhere to the direct photon cross section -- a rapidly falling distribution in $E_{\gamma T}$. As described with Figure 6.6, when we classify ("bin") events according to E_j we accept events of widely varying parton E_T scales. The lower E_T parton events are much more likely to be produced than higher E_T events in a given E_j bin. For this fixed jet E_T bin, this shifts the mean of the $E_{\gamma T}$ (ie. parton E_T) distribution to a lower value than it should be (see Figure 6.9). The degree to which this shift occurs depends on how steeply the photon cross section falls and how good the jet resolution is. The fractional jet resolution itself becomes worse as the jet energy gets lower which causes the bias to worsen as well since the $E_{\gamma T}$ spectrum extends over a larger percent drop in the photon cross section.

Before delving into estimating this bias, note that our measurement has now become strongly (and undesirably) tied to the production mechanism of direct photons. To compensate, we must know both the E_T dependence of the cross section and the resolution of jets as a function of jet energy. This introduces a variety of limitations to the analysis, both statistically and systematically, which we will attempt to circumvent.

9. Event Simulation

There are a variety of systematic effects which require a large ensemble of tests to quantify the statistical impact they have on our response measurement. Therefore, a parametric Monte Carlo has been developed which weights different parton bins by a cross-section which falls (or rises) as some power of the parton E_T. It also smears the photon and jet with their resolutions. The response of the calorimeter to a jet is an input. The simulation also accommodates the jet reconstruction threshold, and a photon trigger threshold.

An illustration of the effect of the cross section bias is shown in Figure 6.10. The response function used is $R_j = 0.85 + 0.0005*E_{jT}$ and otherwise the events conform to the standard defined in Section 8a. Figure 6.10a shows R_j vs. E_j for jets and photons with perfect resolution and a cross section falling as $1/E_T^5$. Figure 6.10b adds jet resolution and two different cross sections are shown: a cross section following $1/E_T^2$ dependence (stars), and a cross section following $1/E_T^5$ dependence (open circles). The jet resolution skews the measurement very badly and the bias is worse for steeper cross-sections. The dominant problem is the jet resolution -- smearing the photon has almost no effect.

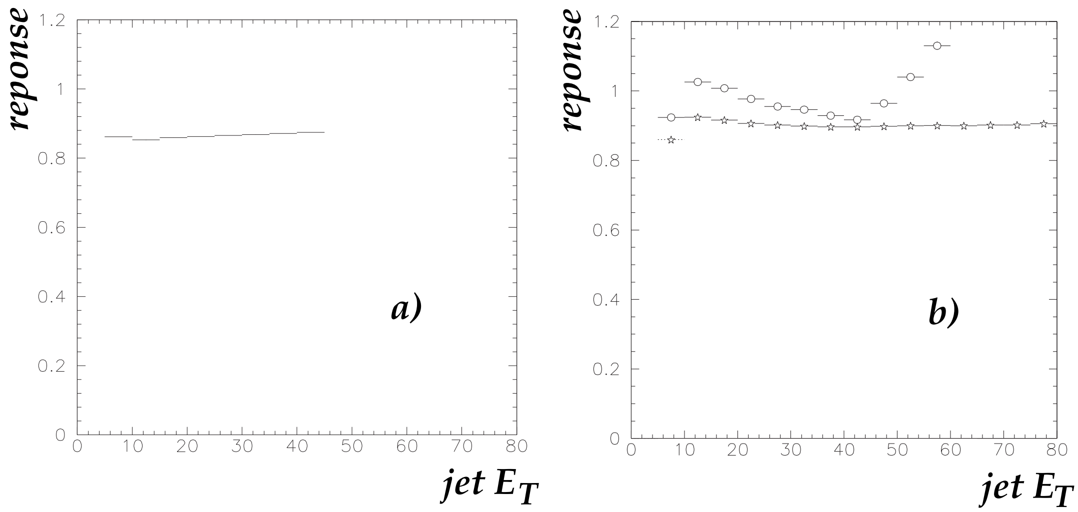

Figure 6.10: Measured response *vs*. measured jet energy for (a) perfect jet resolution, and (b) nominal detector resolution for two different behaviors of the photon spectra. The lower curve is a spectrum falling as the -2 power of E_T and the upper curve falls as -5.

The shape of the curves in Figure 6.10b can be understood. For conciseness, consider the $1/E_T{}^5$ curve. The decrease in measured response below 15 GeV is due to a lessening of the impact of the cross-section bias because there are no photons below 8 GeV. Above about 15 GeV, R_j is consistently several percent above the input value due to the cross section bias. As expected, the bias lessens as E_{jT} increases. Note that the measured response in Figure 6.10b for the case of a $1/E_T{}^5$ dependence of the cross section, the plot indicates an increase in response when E_{jT} > 40 GeV because no partons were generated above 40 GeV (ie. the jet resolution allows the jet to fluctuate much higher than the photon can in this region). Since this is unphysical, this portion of that plot should be ignored.

10. The Energy Estimator, E'

The cross section resolution bias can be eliminated by binning the response as a function of $E_{\gamma T}$ instead of E_j directly. This is because we are classifying events with a quantity which is known better and is representative of the original partonic E_T. Figure 6.11 illustrates that, for both cross sections mentioned above, we obtain a response curve which agrees much better with the input value. The close correspondence between the curves from the two cross sections indicates we also obtain a cross section independent measurement from this method. The rise in R_j at low energy is due to a jet reconstruction bias which will be discussed in a later section. Note that for this method to work on real jets, we need to also determine the measured jet E_T vs. $E_{\gamma T}$ to ultimately get R_j vs. E_{jT}.

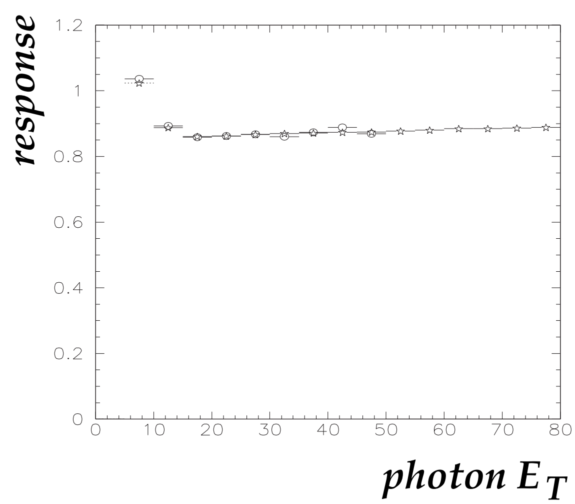

Figure 6.11: Measured response vs. photon E_T for two different cross sections. A cross section falling as the -2 (-5) power of the photon E_T is shown in the stars (circles).

For an ensemble of direct photon events with a photon in a given E_T range, the jets fluctuate in a way consistent with their resolution. We can see that no further biases are incurred by looking at these events in the following way. The photon represents the parton which gave rise to the jet before detector resolution caused its energy to vary widely. The jet represents itself -- the parton after detector resolution -- and is distributed in a symmetric gaussian unweighted by the cross section for each photon bin. In this case the mean jet E_T in each $E_{\gamma T}$ bin is unbiased and accurately indicates the response.

This method has been simulated and the corrections derived from a fit (0.848 + 0.0006*E_{jT} above 15 GeV) were applied to see how well the corrected E_{jT} matches the parton value. Figure 6.12 gives the corrected jet energy *vs.* the actual jet energy when the correction was determined (a) directly vs. the jet E_T, and (b) vs. the photon E_T. A perfect correction will give a plot with zero offset and slope of 1.0.

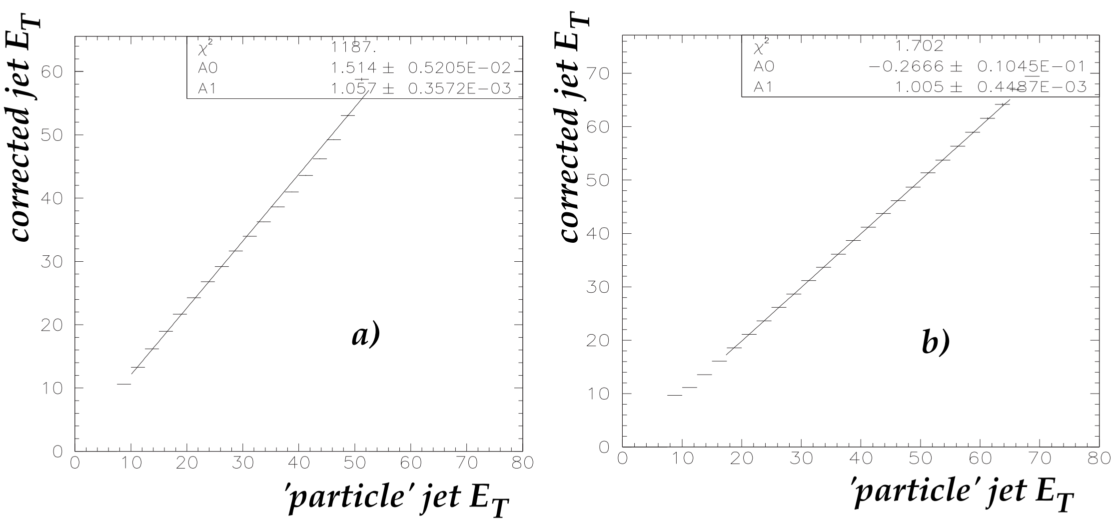

Figure 6.12: Verification of method. Shown in (a) is the calorimeter jet E_T *vs.* particle jet E_T where the calorimeter jet was corrected with response measured directly in terms of jet E_T. Shown in (b) is the calorimeter jet E_T *vs.* particle jet E_T where the calorimeter jet was corrected with response determined initially in terms of $E_{\gamma T}$.

Although indirect, Figure 6.12b has an improved slope, offset, and χ^2 compared with the old method. The large χ^2 in Figure 12a is due to forcing a straight line fit to a non-linear plot; the nonlinearity being due to applying the wrong correction to the jets. A correction derived from a fit of the low energy R_j curve slightly worsens Figure 6.12a and slightly improves Figure

6.12b.

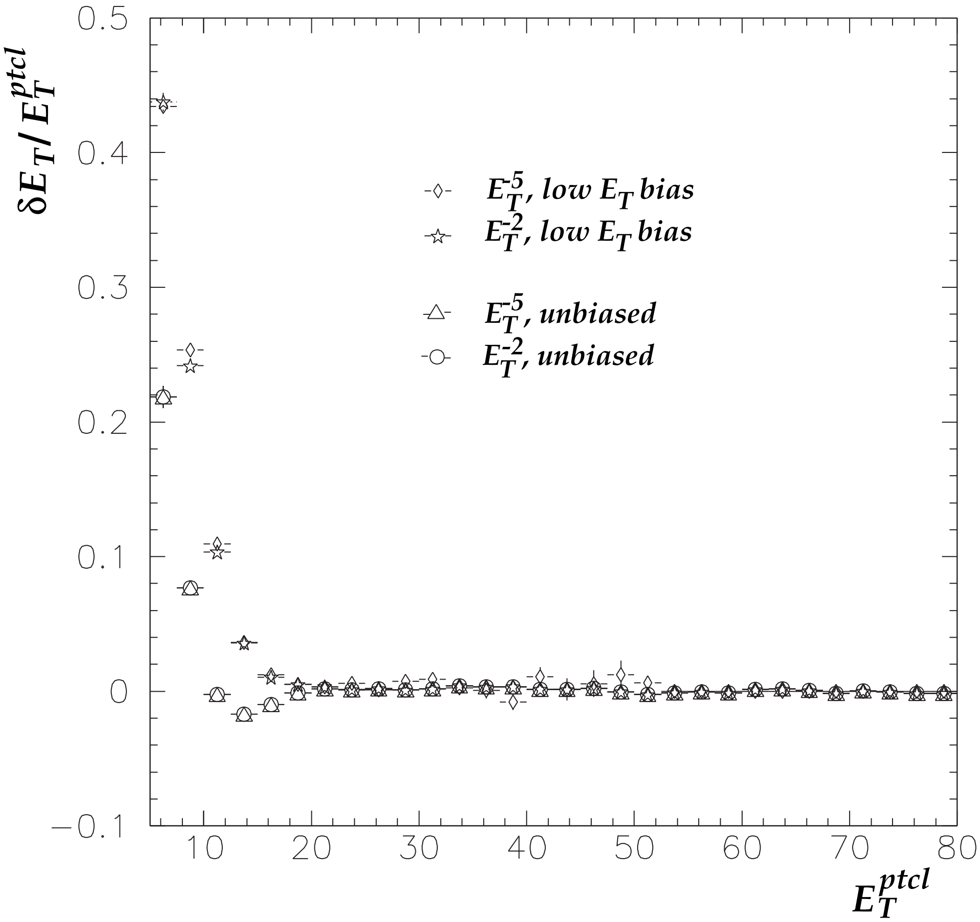

Figure 6.13: Percent descrepancy of corrected jet, $\left(E_{Tmeas}^{jet} - E_{Tptcl}^{jet}\right) / E_{Tptcl}^{jet}$, vs. E_{Tptcl}^{jet} for two different photon cross sections (E_T^{-2} and E_T^{-5}), and with or without the low E_T bias correction (*'low E_T bias'* or *'unbiased'*)

To get a better idea of how well we are doing in the low E_T region, we plot $\left(E_{Tmeas}^{jet} - E_{Tptcl}^{jet}\right) / E_{Tptcl}^{jet}$ *vs.* E_{Tptcl}^{jet} in Figure 6.13 where four curves are given. These correspond to photon cross sections falling as E_T^{-2} or E_T^{-5}, and whether or not the jet was corrected with the low E_T bias correction (discussed later). All jet energies are corrected with the curve obtained above 15 GeV and extrapolated at lower energies. If one considers the two labelled *'low E_T bias'*, we see they agree very well with one another.

The most important advantage to the new method is its immunity from resolution bias. An additional benefit is that we can retain more statistics since we do not have to cut on the jet energy as is necessary if binning in E_j. We merely need to cut on $E_{\gamma T}$ at the values given in Table 6.1 to get rid of any trigger bias from the photon's resolution. We also avoid complications due to unsmearing the correction. This also means we can study the region affected by the reconstruction bias since we do not have to explicitly require a jet.

Since we want to measure response as a function of energy, not E_T, we note that both the E_T of the photon and direction of the probe jet are well-measured. We therefore define the energy estimator of the jet, E', to be

$$E' = E_T^{\gamma} \cosh \eta_{jet} \qquad \textbf{Eq. 6.4}$$

where η_{jet} is the pseudorapidity of the jet with respect to the reconstructed primary vertex of the event. In events with two particle jets, $E' = E_{ptcl}^{jet}$ and even in multijet events it is highly correlated with jet energy. We note that E' is fairly independent of the jet algorithm because it only uses the jet direction.

We can now determine the proper dependence of response on energy by plotting R_j vs E'. This is, however, not directly applicable to determining the correction for a jet in a general event where we only know E_{meas}^{jet}. In order to relate the response to the measured jet, we measure the average jet energy also as a function of E'. This results in a second histogram which can be combined as shown in Figure 6.14 to give the average response as a function of average jet energy bin-by-bin in E'. As an example, if $R_{probe} = r_n$ when $E' = e'_n$, and $E_{meas}^{jet} = e_n$ when $E' = e'_n$, then $R_{probe} = r_n$ when $E_{meas}^{jet} = e_n$. If two separate E' bins have the same average jet energy, their response estimates are combined weighted by their statistical errors. It should be noted that this correction does not in any way force the probe jet to directly balance the photon or equal E'.

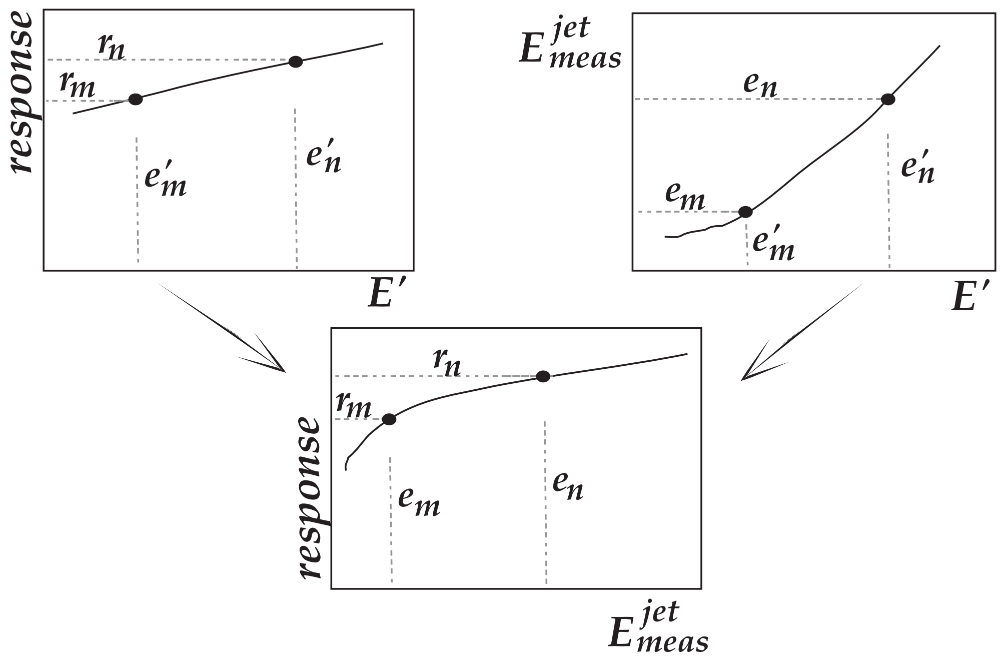

Figure 6.14: Construction of Response *vs*. jet energy using $E' = E_T^{\gamma} \cosh \eta_{jet}$. By classifying events by the well-measured variable, E', we obtain a plot of response *vs*. measured jet energy.

Response plots for jets reconstructed with 0.5 cone-size in collider data are shown in Figure 6.15 for the scheme where events are classified via jet energies and in terms of the photons using E'. The change in shape at low energies is due to the jet reconstruction bias. The overall drop in response is due to the elimination of the cross-section bias. The change between the two curves is consistent with that indicated by comparing Figures 6.10b and 6.11.

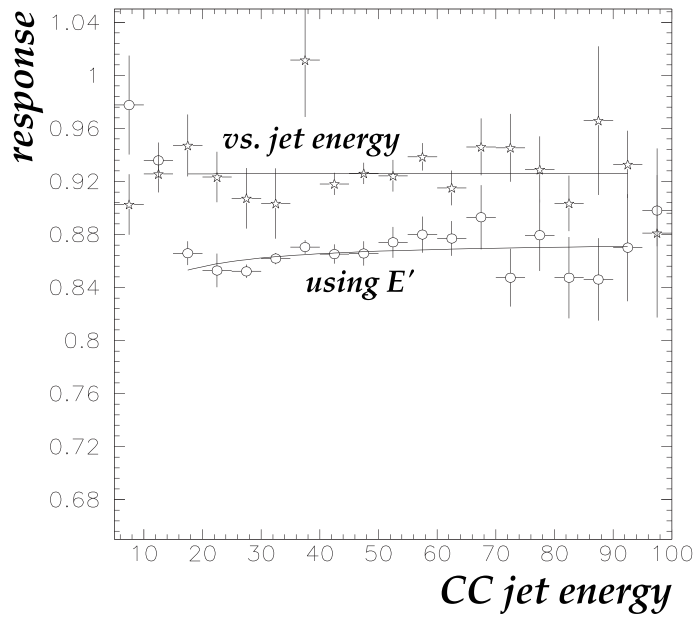

Figure 6.15: Measured jet response plot directly vs. jet energy, and plotted using E'.

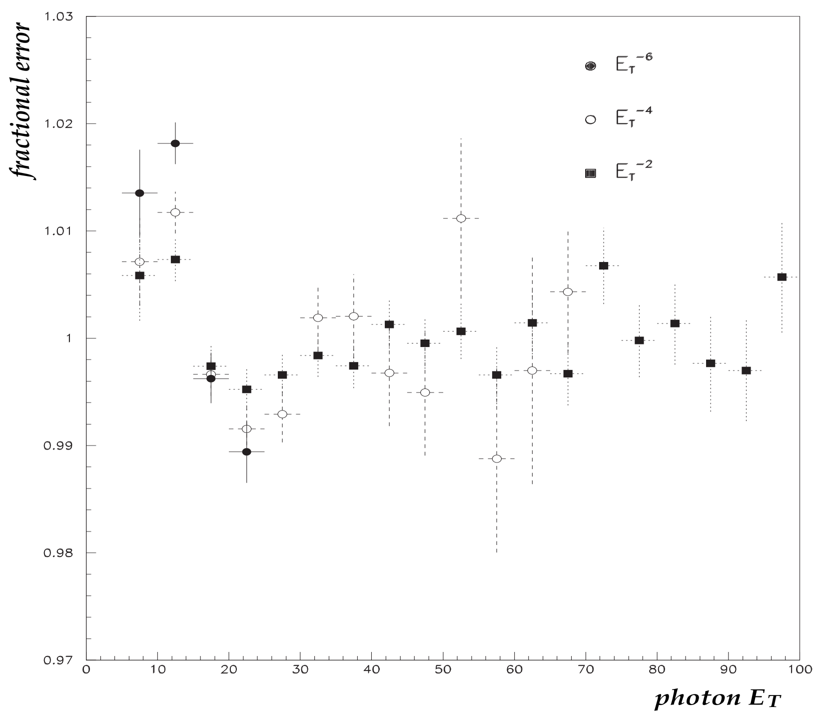

Figure 6.16: Residual bias due to finite photon resolution for two different photon cross sections.

To estimate any residual resolution bias in the E' method, we resort to the parametric calculation. Figure 6.16 shows the fractional error incurred by the method for a wide range of cross sections. For photon E_T's below about 20 GeV there is a slight shift caused by the finite photon resolution. At 10 GeV the bias is about 1% for a cross section with E_T^{-4} dependence. If one knew the sample E_T dependence accurately, a fit could be performed to the relevant points in Figure 6.16 and this could be used to correct the measured response function. Although the theoretical prediction of the direct photon cross section is fairly accurately known to have a roughly E_T^{-4} dependence, we cannot use this for our sample because our selection cuts have efficiencies which are strongly E_T dependent.

11. Further Tests of Method:

The above method for determining a jet's response is susceptible to several systematic errors which include the effects of initial or final state radiation, binning, and unbiasing low energy jets. The binning systematic comes from the finite size of bins in our final response vs. jet energy plots. This error is the change in response over the bin size in this region and for the energy dependence measurement. This error is small.

a. Initial State Radiation

Another problem is initial state radiation which is lost down the beampipe. An ongoing debate concerning the physics of direct photon production (and QCD in general) is whether the parton level theoretical calculations correctly predict the typical net transverse momentum of a QCD process at the Tevatron. As expected from the uncertainty principle, a typical momentum transfer in the transverse plane ('k_T') for photons colliding with protons is 350 MeV[53]. Both DØ and CDF, however, appear to measure significantly more than this. Using diphoton events, these experiments measure $<k_T> \sim 4$ GeV[54]. Because this seriously smears out low E_T events, we must determine the effect on the measured response.

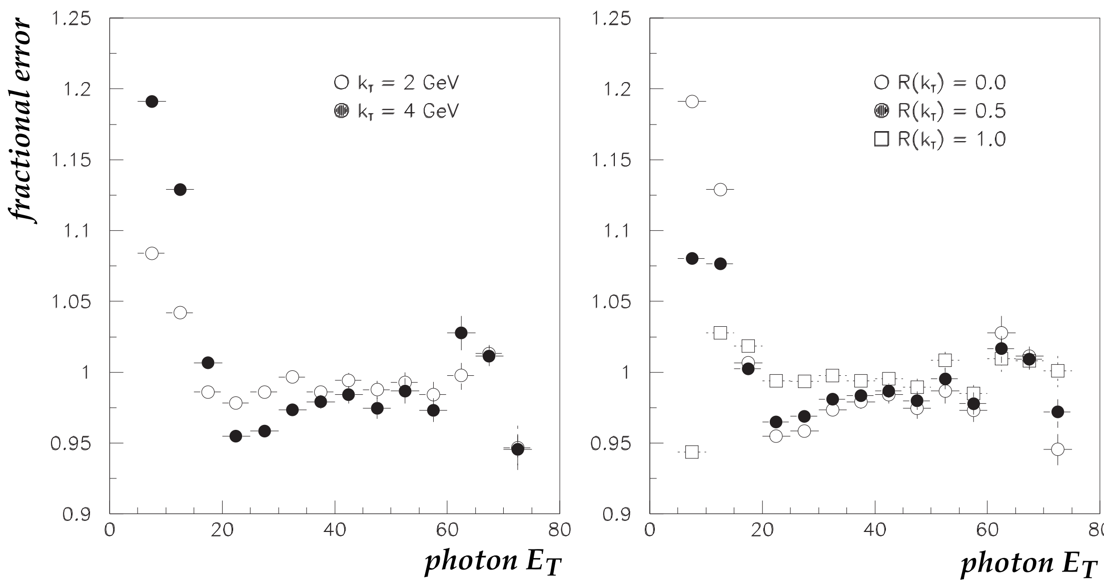

Figure 6.17: Fractional error from the effect of initial state radiation. In (a) is shown the dependence of the measured response of the magnitude of k_T, while (b) shows the dependence for $<k_T> = 4$ GeV on varying levels of containment.

Using the parametric Monte Carlo, we input various low energy jets into the event to represent this radiation and then the vectors of all the objects are readjusted. The vector transverse momentum of this jet is labelled 'k_T'. All responses and resolutions are input with the 'response' of the k_T being changed. If all of the k_T passes down the beam pipe (ie. k_T 'response' = 0), then the bias caused by initial state radiation is significant for a moderately steeply falling photon cross section (see Figure 6.17a). In that case, we investigate the dependence on the degree to which the energy is contained in the calorimeter. If 50% is contained within the calorimeter (ie. k_T 'response' = 0.5), the error is about 3% at 20 GeV and negligible above 40 GeV.

It should be noted that this systematic effect is correlated with the resolution bias error mentioned above. In fact, Figure 6.17 is the product of the two effects. Therefore, we obtain a combined 'k_T/resolution-bias' systematic error that ranges between 0% and 3% for events with photon $E_T > 15$ GeV.

b. Topological Concerns

An additional concern arises from the fact that the $\not{E}_T$ is integrated over the entire calorimeter. Thus R^{had} is affected not just by the photon and probe jet, but any other object in the event. If the hadronic recoil is not dominated by the leading jet, we may be assigning the wrong response to the jet. In cases in which there is a third jet, R^{had} really measures the average response of the two jet system. However, most of the response comes from the probe jet because, as the leading jet in the event, its E_T usually dominates the total E_T of the hadronic recoil. The approximation is best when the response difference between the leading and second leading jet is small and when the leading jet is the primary object balancing the photon.

This systematic has been studied in two ways. Systematic shifts of up to 3% were observed if we allowed the jet and photon not to be back-to-back or if we allow another jet in the event of comparable energy to the leading jet. A third jet or unreconstructed energy cluster can cause the photon and leading jet not to be back-to-back.

Another study of the topological error was also performed by measuring the response in ISAJET direct photon events processed through the particle shower library. At the generator level these events were required to have at least one photon above the generator threshold and within the CC ($|\eta| < 1.2$). Furthermore, these samples were required to have one and only one particle level jet above 5 GeV using the 0.5 cone algorithm. This jet was also required to be central and more than 90^{o} away from the photon in ϕ. The response measured in these events was compared with that measured in ISAJET shower library events in the same energy region which had no jet cuts (ie. can have any number of jets). The uncertainty ranges from 1% to 2% depending on jet energy. This error can be considered fairly uncorrelated with the resolution bias and k_T errors because these effects are present in our ISAJET samples. We are measuring the residual dependence on topology after these effects.

12. Event Selection

As described so far, we have discussed this analysis in terms of direct photon events. It is, however, a nontrivial exercise to acquire a sample of pure direct photon events in the data. In addition, the analysis calls for the largest statistical sample possible to explore the response of each calorimeter to jets. We note that, as mentioned in Chapter III, the calorimetry is linear to a high degree for electrons (and therefore photons) so that a jet composed of two 10 GeV photons will have the same response as one 20 GeV direct photon. Therefore, in order to perform this analysis in the data, we have chosen those cuts which retain the most events while limiting our systematic errors. These cuts are not tuned to give a pure sample of *direct* photon events but rather to give a sample of *isolated* photon events.

a. Triggering

We employ triggers designed for the various Run 1 direct photon analyses which span the range from 4 GeV through 60 GeV. Two less restrictive triggers, GAM_LOW in Run 1a and EM1_ESC in Run 1b at the low and high end of this range, respectively, are used to help with statistical limitations in their respective kinematic regions. Aside from these two, all

Level 2 filters used required one isolated electromagnetic cluster with shower shape consistent with a photon. They are listed in Table 6.2.

Table 6.2. Triggers used for photon event selection. For description of Level 2 photon conditions, see Chapter 4.

trigger name	*run*	*Level 2 photon condition*	*low offline E_T thresh*	*high offline E_T thresh*
GAM_LOW	1a	L2EM(1,4,*gam*)	4.5 GeV	15 GeV
GAM_LOW_ISO	1a	L2EM(1,6,*gis*)	7 GeV	50 GeV
GAM_MED_ISO	1a	L2EM(1,14,*gis*)	15 GeV	50 GeV
GAM_HIGH_ISO	1a	L2EM(1,30,*gis*)	31 GeV	900 GeV
GAM_6_ISO_GAM	1b	L2EM(1,6,*gis*)	7 GeV	15 GeV
GAM_14_ISO_GAM	1b	L2EM(1,14,*gis*)	15 GeV	50 GeV
GAM_20_ISO_GAM	1b	L2EM(1,20,*gis*)	21 GeV	900 GeV
EM1_GIS	1b	L2EM(1,25,*gis*)	26 GeV	41 GeV
EM1_GIS_HIGH	1b	L2EM(1,40,*gis*)	41 GeV	900 GeV
EM1_ESC	1b	L2EM(1,60,*esc*)	61 GeV	900 GeV

In general, we cut 1σ above the Level 2 filter E_T threshold to avoid accepting biased photon candidates. Where there is more than one trigger defined for a given trigger configuration we also have a maximum cut on the offline cluster E_T to avoid situations in which a reconstructed cluster E_T is well above a filter which we know it did not pass.

b. Offline Cuts

Aside from the events passing the GAM_LOW and EM1_ESC filters, we use events collected in the standard direct photon stream. Events are selected which pass our triggers and an offline E_T cut is applied to the leading electromagnetic cluster at the filter threshold value. A loose cut is applied which requires $\not\!\!E_T/E_{\gamma T} < 2.0$ (< 3.0 for GAM_LOW_ISO).

We select from this sample events which possess one or more PELCs and/or PPHOs which satisfy quality cuts to remove major backgrounds. For this analysis, these backgrounds are defined to be jets in which there is significant hadronic energy deposition near a leading photon (or pair of photons from a π^o). To remove this 'instrumental' background, we apply longitudinal and transverse isolation cuts. It should be noted that jets dominated by a leading π^o or γ with no nearby hadronic activity are not considered backgrounds because their responses are that of an electron. As a result, we do not use the standard direct photon analysis selection. Rather the selection presented here is an attempt to obtain the largest statistical sample (and therefore widest energy reach) with reasonable systematic errors on the response measurement. The backgrounds also include Drell-Yan, Z, and most notably $W \rightarrow e\nu$ backgrounds which are mostly removed by cuts on EM-clusters with a track in a road to the vertex. The detailed photon identification cuts are given in Table 6.3.

Table 6.3. Quality cuts on photon candidate for different E_T regions to reject backgrounds.

	0 GeV	**15 GeV**	**30 GeV**	**100 GeV**	**180 GeV**
dE/dx	< 0.8, > 1.5	< 0.6, > 1.5	< 0.6, > 1.5	< 0.6, > 1.5	no cut
ε_t	< 0.25, > 0.75	< 0.1, > 0.9	< 0.1, > 0.9	< 0.1, > 0.9	< 0.25, > 0.75
σ_{trk}	> 3.0	> 3.0	> 3.0	> 3.0	> 3.0
f_{EM}	> 0.9	> 0.96	> 0.96	> 0.96	> 0.9
f_{iso}	< 0.5	< 0.2	< 0.15	< 0.15	< 0.15
iso_4*	< 2.0 GeV	< 3.0 GeV	< 10.0 GeV	no cut	no cut

In order to ensure that the PELC or PPHO is a well-measured cluster, we also require fiducial cuts which throw away candidates near detector edges.

The distance of CC clusters from a ϕ EM crack must be greater than 0.01 *rad*. To avoid the inter-cryostat region and to avoid the region in which the granularity of the calorimeter EM3 layer coarsens, we require the detector η to satisfy $|\eta| < 1.0, 1.6 < |\eta| < 2.5$

In general, the event is rejected if the μBLANK bit is set. Events with primary vertices reconstructed in the far forward region tend to be poorly measured. As a result, we require the z coordinate of the vertex to be within 70 cm of $z = 0$. Also, the $\not{E}_T$ in events which were flagged with the hot-cell killer in the reconstruction was significantly different than the rest of the sample. These events tended to register lower response jets which implies that energy is being incorrectly removed from the probe jets. As a result, any event with a hot-cell removed by the reconstruction is rejected. These events are rare, however, and the effect on the measured response is less than 0.2%. In order to avoid events with photons due to bremsstrahlung from cosmic ray muons, we use the Muon System as a loose veto. If the leading photon E_T < 30 GeV then we require no muons to be reconstructed in the event, otherwise we require $p_T^{\mu} < 100\ \mathrm{GeV}/c$.

For the response measurement, we require at least one reconstructed jet in the event. We ignore the event if any jets fail noisy cell cuts which are defined as CH energy fraction < 0.5, ratio of energy of leading to second leading cell in the jet < 10, and $0.95 > f_{EM} > 0.05$ for that algorithm. The $|\eta|$ of the jet must be less than 0.7. We also apply a loose cut on $\Delta\phi(\gamma\text{-jet}) > 2.1$ *rad* to avoid events in which there are very many jets or in which the 'leading jet' turns out to include the photon for the large jet algorithms. Another cut had been employed to limit the error caused by multijet topologies which required the second leading jet E_T to be some small fraction of the probe jet E_T. We do not use this cut, however, because it results in events being accepted because the second leading jet has fluctuated low. We only use the angular cut mentioned above for the topological cut.

13. Studies of Backgrounds to Direct Photon Events

Having verified that this analysis can, with certain assumptions, determine jet response within a small error, we confront the practical concerns of obtaining a useful calibration sample from the data. In a real direct photon event, the $\not{E}_T = 0$ and the photon is an indicator of the actual p_T of the cumulative hadronic recoil of the event. In the calorimeter the photon possesses good resolution and a well-known response. In terms of tracking we may have no track, or a photon conversion (2 mips). The $\not{E}_T$ at the detector level is a measure of the energy not measured in the recoil. There are several processes which satisfy the signature we are looking for but which are undesireable samples from which to extract a calibration. Physics backgrounds are those which have at least one isolated electron or photon and include various Drell-Yan processes to one or two electrons and diphoton production. Instrumental backgrounds arise from QCD dijet events in which one or more jets fake a photon or electron.

a. Instrumental Background:

The signature of the QCD dijet event in which one jet fakes a photon is much like that for the direct photon. If there is a track associated with the cluster, it does not look much like an electron. By virtue of the leading π^o, the EM-jet has good response and resolution. Also, there is no real $\not{E}_T$ in the event. In some sense, the use of this sample to calibrate is superior to the photon sample because the Feynman diagrams present give more representative jets (gluons *and* quarks). Leading jets balancing high E_T photons are mostly quarks while for low E_T photon events, the recoil is mostly gluons. Also, the fraction of the recoiling jet population which comes from gluons dependends on the difference in η of the jet and photon. Integration of the QCD and direct photon samples allows us to improve our statistics and results in an analysis which is measuring the response of the calorimeter to more representative jets. The drawback is that the leading π^o will have associated hadronic activity which will have response less than the EM scale. Therefore our measured jet response will be too high.

We strive for a set of 'photon' identification cuts for which a sample with high background behaves like one with significantly lower background. We use isolated electrons from Z dielectron events to indicate the typical behavior of isolated EM-clusters which adhere to the EM-scale. The calorimeter and tracking properties used to identify electrons were compared for EM-jets in the direct photon sample and electrons from the Z sample. Each variable was studied as to whether it was significantly correlated with the measured R_j. It was noticed that little or no correlation existed between measured response and any of the tracking properties. There was also little correlation with the H-matrix χ^2. The isolation variables, on the other hand, were significantly correlated with f_{EM} being strongly so. A preliminary set of cuts were devised which minimized the differences with the electron sample and which also reduced the variability of the measured response in our EM-jet sample with respect to further cuts.

The magnitude of the remaining variability, and therefore our potential remaining systematic error, is estimated by comparing the measured response in events with photon candidates that were PELCs *vs*. PPHOs after applying quality cuts.Before these cuts were imposed $\delta R_j/R_j$ ~ 4% between these two samples, while after the cuts the fractional difference was 1.42%. This is taken as a systematic error. For photon candidates below 20 GeV there was no clear correlation of any particle identification variable with response even though we expect the background to be considerably higher. In lieu of a better idea, the above systematic error was used in this E_T region.

b Physics Backgrounds

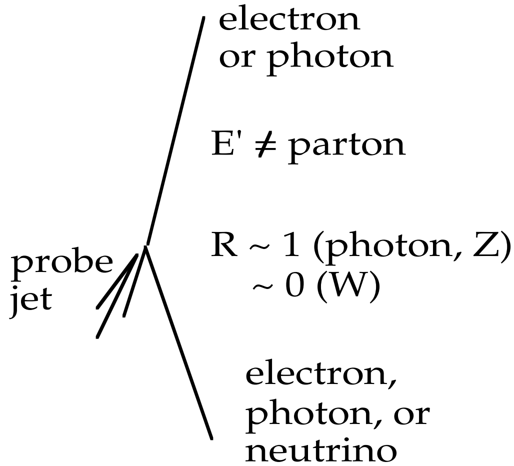

Figure 6.18: Drell Yan event topology.

The physics background consists of Drell-Yan signals (γ^* to ee), Z to ee, W to $e\nu$ and diphoton production. In collider data, the major problem comes from W plus jet events.

If there are two electromagnetic particles in the event such as in Z production, the leading one is not a measure of the parton E_T of the hadronic recoil. In these events $\vec{\not{E}}_T \bullet \hat{n}_{\gamma T} \big/ E_{\gamma T} \sim 0$ and $R_j \sim 1$. Looking at the Z dielectron ISAJET sample, we see $R_j = 0.95$. This background can be effectively removed by a cut on $E_{\gamma T2}/E_{\gamma T1} < 0.1$. For leading photons below 20 GeV, the second cluster may pass this cut but still be unreconstructed. Since we are unable to reject this background in the low energy region, we have a 0.5% systematic error for events with photon $E_T < 20$ GeV. Only a small bias is incurred from those physics backgrounds which generate two high p_T electromagnetic clusters.

We do not want events naturally having $\not{E}_T$, especially when correlated in direction with the 'photon'. Events where there is a *W* boson which decayed to an electron are just this kind of event (see Figure 6.18). In order to remove our W background, first we looked in a subset of the Run 1a direct photon stream to estimate the number of $W \to e\nu$ events. We selected events passing the GAM_HIGH_ISO filter and applied our analysis cuts described in the previous section. For the W estimation, we use a subset of 5000 PELC events passing our cuts which corresponds to a luminosity of 3.8 $pb^{-1} \pm 0.6\ pb^{-1}$.

We then estimate the efficiency of W events to pass our selection relative to the Run 1a W cross section analysis cuts by looking at a sample of ISAJET $W \to e\nu$ events. These efficiencies are shown in Table 6.4.

Table 6.4. Efficiencies of $W \to e\nu$ using ISAJET.

cut	efficiency
geometrical acceptance, $\eta_\gamma < 0.9$	0.67
EM cluster $E_T > 31$ GeV	0.79
electron ID	0.85
>= 1 jet, $\eta < 0.7$	0.3

This gives a cumulative efficiency of 0.135. In the total *W* sample in Run 1a, there were 9800 *W* events for $12.8 \pm 0.7\ pb^{-1}$. For our sample, we expect

$$\begin{aligned} N &= N^{W}_{total-1a} \times (\mathcal{L}_{subset} / \mathcal{L}_{total-1a}) \times \varepsilon \\ &= 9800 \times (3.8/12.8) \times 0.135 \\ &= 393 \text{ events} \end{aligned} \qquad \textbf{Eq. 6.5}$$

As shown in Figure 6.19, a good discriminator against W events is the cut of $\not{E}_T / E_{T\gamma} < 0.65$. We count events failing this cut to be 376 in our sample, with the number being photon events being small. Since 10% of W events will pass the $\not{E}_T / E_{T\gamma}$ cut, we estimate the total number of W events 'observed' in our sample to be 376 x 1.1 = 414 events. This agrees with the result in Equation 6.5.

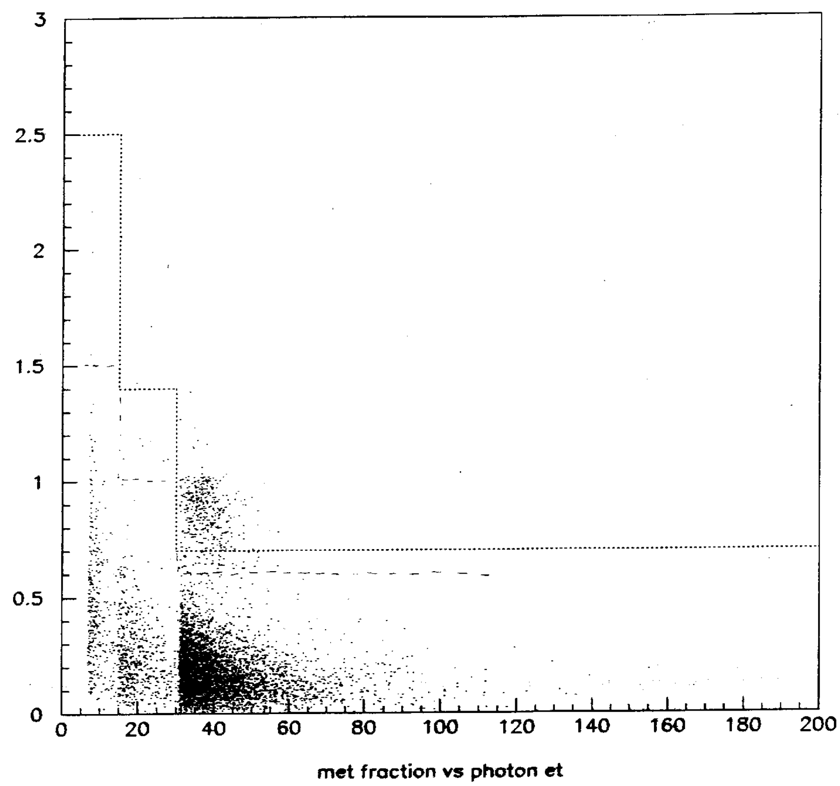

Figure 6.19: Scatterplot of $\not{E}_T / E_{T\gamma}$ vs. photon E_T in a subset of Run 1a events.

Because the neutrino in W events is opposite the electron, R_j will be very low (~ 0.1 from the ISAJET sample) while for real photons R_j is closer to 0.85. As a result, if no anti-W cut is applied, we expect

$$\Delta R = (393/5000)(0.85 - 0.1) = 0.060$$

where we have used the estimate of 393 W events from the Monte Carlo analysis because the estimate from data (which gives 414 events) has not had background subtracted. This 6% predicted shift in response is the size of the response dip seen in the PELC sample. For the PPHO sample,

$$\Delta R = (0.15/0.85)(18.5/22)(393/5000)(0.85 - 0.1) = 0.009$$

The W background is reduced by cutting on $\not{E}_T / E_{T\gamma} < 0.65$ for moderate to high p_T photon events. Because we are now cutting on the $\not{E}_T$ we can bias the $\vec{\not{E}}_T \bullet \hat{n}_{\gamma T} \big/ E_{\gamma T}$ distribution by cutting off the tail preferentially on the low side. In order to be more selective, we consider the tracking variables to remove $W's$ while keeping photons and EM jets. If the event fails the $\not{E}_T / E_{T\gamma}$ cut then the dE/dx, σ_{trk}, *and* ε_t must be inconsistent with an electron (see Table 6.3). If $\not{E}_T / E_{T\gamma} < 0.65$, then we must pass one of the tracking cuts. If we are dealing with a leading PPHO we do not have the tracking information and only have TRD information available for late versions of the reconstruction. Therefore, an event with a leading PPHO must pass the $\not{E}_T / E_{T\gamma}$ cut to enter the anlaysis sample. Because the W's are not a problem in the low E_T photon sample and because the $\not{E}_T$ resolution is a significant fraction of the photon E_T in that region, we loosen the $\not{E}_T / E_{T\gamma}$ cut to avoid biasing the response measurement. The cuts to remove the physics backgrounds are given in Table 6.5 *vs*. photon E_T. The residual amount left in the PELC sample after the $\not{E}_T / E_{T\gamma}$ cut is about 0.1*0.06 ~ 0.5% which is the systematic error ascribable to this background.

Table 6.5. Cuts to remove Drell-Yan backgrounds.

$E\gamma_T$ bin	**$\not{E}_T / E\gamma_T$**	**$E_{\gamma t2}/E_{\gamma t1}$**
< 15 GeV	2.0	0.1
15 GeV - 25 GeV	1.2	0.1
> 25 GeV	0.65	0.1

14. Multiple Interactions

There is a fairly strong dependence of the measured response on the number of interactions estimated to occur in a particular event. R_j decreased as: (1) the instantaneous luminosity increases, and (2) the Level Ø timing spread increased (ie. multiple interaction flag indicated a higher probability of multiple interactions.). Of these two, the correlation with the multiple interaction flag was much stronger. Additionally, it was noticed that the dependence was minimal when the probe jet was in the CC (~ 1% total spread) while if it was in the EC the dependence was large (~4% total spread). When the probe jet was in the far forward region ($|\eta| > 2.5$) the response was seen to actually decrease as a function of E', and the dependence on multiple interactions was at least as large as the more central portion of the EC already mentioned.

This behavior can be discerned in Figure 6.20 where response vs. E' is shown for various multiple interaction selections for Run 1b. Run 1a points are provided for reference and are a bit higher because $\langle L \rangle$ is lower than the comparable 1b curve and the definition of the multiple interaction flag ('MI') was more precise. Each curve of points represents a continuum of data where the probe jet is in the CC ($|\eta| < 0.7$, $E' < 180$ GeV), EC ($1.6 < |\eta| < 2.5$, 90 GeV $< E' < 350$ GeV), and the far forward EC ($|\eta| > 2.5$, $E' > 200$ GeV). The EC points have been adjusted for a scale factor to bring them into agreement with the CC points in the energy region in which they overlap. The determination of this scale factor is described in a later section.

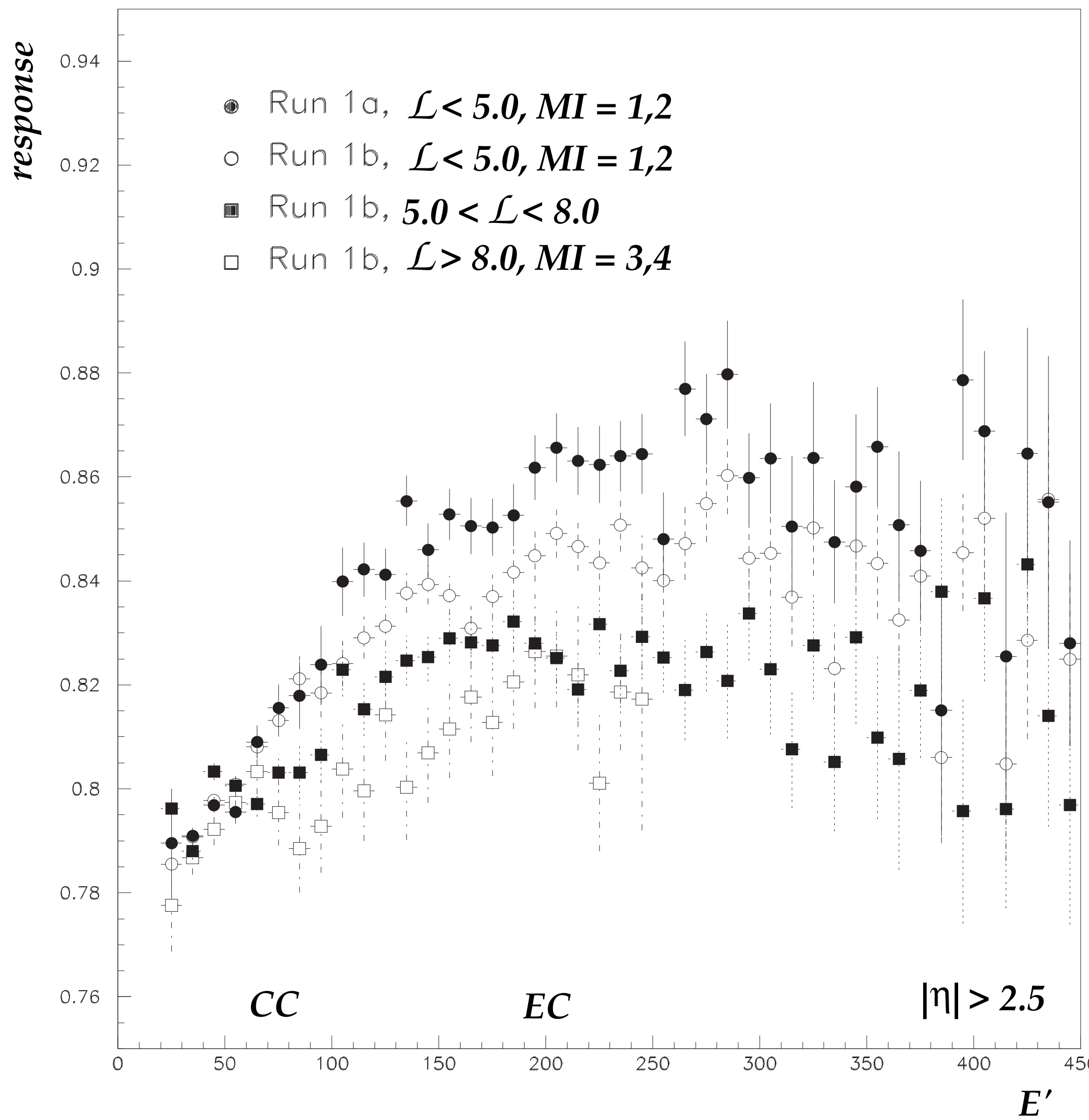

Figure 6.20: Multiple interaction dependence of response measurement.

Two mechanisms can produce this effect. First, the primary vertex could be misidentified increasingly often as the number of interactions per beam crossing increases. This would be a more severe problem for events with forward jets because the FDC is not used to do vertex finding unless insufficient numbers of tracks can be found with the CDC. For these events, as the number of interactions in a given crossing increases, the probability that enough CDC tracks will be found and permit the reconstruction of a vertex may increase. Since these tracks are central and not associated with the vertex of the photon event, the reconstructed vertex may be biased to be more central ($|z^{reco}| < |z^{\gamma}|$). This will tend to reduce the measured E_T of the probe jet. It will not have an affect on the photon on average since it can be central, in the same EC as the probe jet, or in the other EC. The net effect of this is to increase the $\not{E}_T$ in the direction of the jet and therefore underestimate the response. Little such bias should occur if the probe jet is in the CC.

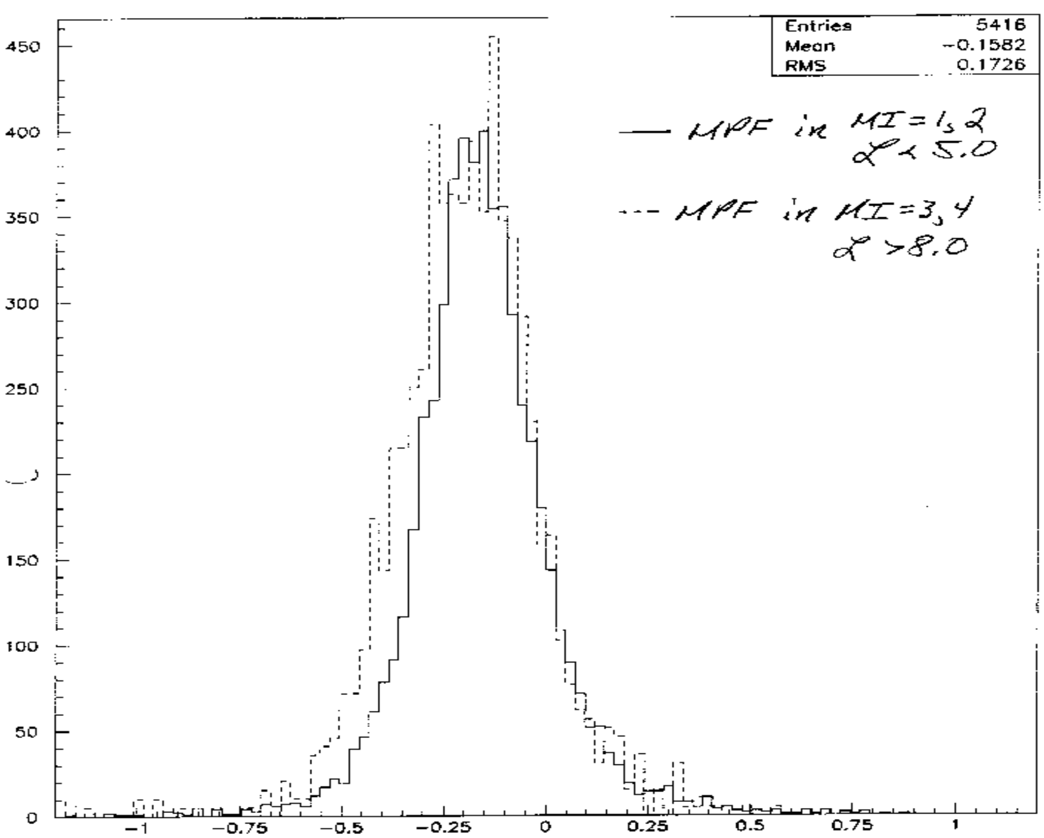

Figure 6.21: $\not{E}_T$ projection fraction in direct photon events for single interaction and multiple interaction events.

The stronger correlation of response with number of interactions rather than luminosity implies that this is exactly what is happening. Additionally, looking at the vertex distribution for events with EC probe jets, one sees a slight shift of the mean vertex distribution to become more central as the number of interactions increases. Figure 6.21 shows $\vec{\not{E}}_T \bullet \hat{n}_{\gamma T} / E_{\gamma T}$ for single interaction events and for several interaction events. We can see a broadening of the distribution to more negative values.

The other possible explanation is that pile-up is occuring which is contributing negative energy to the cells in a jet. This possibility is unlikely, however, because there is no mechanism by which pile-up should align with the objects in the event. As a result, it will not contribute to the $\not{E}_T$ on the average even though it will worsen $\not{E}_T$ resolution.

This issue is important in that, if it is a fault of the vertexing, then jet response is not in fact dependent on the number of interactions and we should not correct for it. If it is pile-up, however, we might have to correct the jet for this dependence. Because we do not have a conclusive answer as of yet, the variation is cited as a systematic error and no correction in terms of number of interactions is performed. This uncertainty is about 0.5% in the CC and 2% in the EC and is taken as the difference in Run 1b between the response plot with the tightest multiple interaction cuts and the next tightest. For instance, the difference between open cirles and filled squares in Figure 6.20 gives the 2% systematic error mentioned above. We note that, within a particular region of the detector, the variation with multiple interactions does not appear to affect the shape of the R_j vs. E' curve. A better understanding of this effect will be able to significantly reduce our error on EC jets' energy scale.

15. Unbiasing Low E_T Jets

Events produced at hadron colliders contain energy from spectator interactions and energy from connections between colored objects. Noise in the detector also contributes energy. As a result, the standard jet algorithm used in hadron colliders employs a cutoff to avoid creating jets from this energy. At DØ, this E_T cutoff (8 GeV for fixed-cones, 5 GeV for nearest neighbor) has been chosen to retain good efficiency for E_T > 20 GeV while keeping the number of jet candidates down[55]. Because we apply a threshold to jets and they have finite resolution, we create a bias in jet response for jets near this cutoff. Because this bias is a matter of resolution and not response, we do not always wish to correct for it, but we do want to 'unbias' the absolute scale measurement. We will attempt to measure the bias and use it to correct the measured response energy dependence, which is algorithm dependent for low E_T events, to an algorithm independent curve.

a. Origin of Bias

To understand the origin of this bias, consider a detector with perfect resolution. The efficiency would be a step-function with efficiency = 0 for E_T < 8 GeV and efficiency = 1.0 for E_T > 8 GeV. Finite resolutions result in a gradual increase in the reconstruction efficiency with E_T as shown in Figure 6.22. The width of the transition region, which extends up to about 15 GeV in Figure 6.22, is directly related to the resolution of the jets. There is another source of 'resolution' which involves fragmentation fluctuations in a jet. Some jets are composed of one particle and form fairly compact energy clusters, others are broadened due to fragmentation to many particles. Jets with low E_T (~< 10 GeV) are often distended objects in which clear energy clustering is absent. As a result, a given algorithm will have decreasing efficiency in this region.

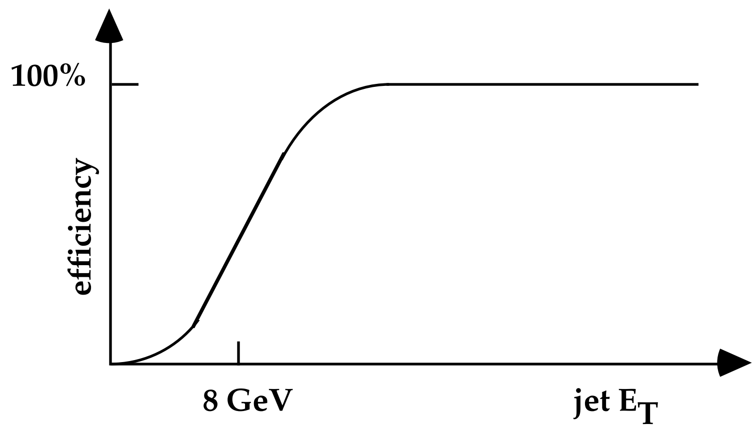

Figure 6.22: Efficiency *vs*. reconstructed jet E_T.

The inefficiencies resulting from these effects mean that those jets which are able to be reconstructed are a biased subset of the original sample. Those that survive have tended to fluctuate to higher response to be reconstructed. The extent of the bias can be estimated with the parametric Monte Carlo using our resolutions and thresholds as input. As shown in Figure 6.11, the bias is zero at 20 GeV and increases with decreasing E_T. To see if the predicted bias describes the data, one can compare Figure 6.10b and 6.11 to the two curves shown in Figure 6.15. Note, however, that the data plot is slightly distorted because for the data energy is plotted, not E_T.

The large descrepancy in Figure 6.13 at low jet energy indicates the bias incurred if we do not fit the low energy part of our response curve. The low E_T portion of the response curve in Figure 6.13 was fit to a quadratic function. The two curves which are least descrepant in Figure 6.15 are also for the two cross sections with the low energy correction applied. A large improvement in the agreement between corrected jet and parton is evident. A rapidly increasing descrepancy still occurs at the very lowest energies due to problems in binning and fitting a rapidly changing correction.

b. Measuring the Low E_T Bias:

In order to properly measure the bias in data, we use photon events and take advantage of the fact that the measured R uses no jet quantities, the photon resolution is good, and the energy scale is known. As a result, we can plot the response of the calorimeter to the hadronic recoil of the photon with no reference to a jet algorithm. Such a plot might look like Figure 6.12a. In order to obtain a measure of the bias, we plot the same but only for those events having at least one jet found with a given algorithm. Such a plot might look like Figure 6.13. The ratio of these two plots is the bias caused by the algorithm vs. the photon E_T. The final step then is to obtain a mapping of the raw jet E_T obtained with that algorithm for each photon E_T. We finish with a plot of the bias vs. reconstructed jet E_T and the inverse of this is the low E_T bias correction. The corrections obtained from data and Monte Carlo are shown in Figure 6.23. Here we see the data has more of a bias (ie. worse resolution) than Monte Carlo. This might be expected from the fact that the Monte Carlo does not have uranium noise which is a significant component of jet resolution at low E_T[56]. As mentioned, different reconstruction thresholds should produce different biases. Figure 6.24 shows a comparison of the low E_T bias measured for jets reconstructed with the fixed-cone algorithm with an 8 GeV cutoff and ΔR = 0.5, and with the nearest neighbor jet algorithm with a 5 GeV cutoff. The bias in the latter case is considerably less than for the algorithm with a higher threshold.

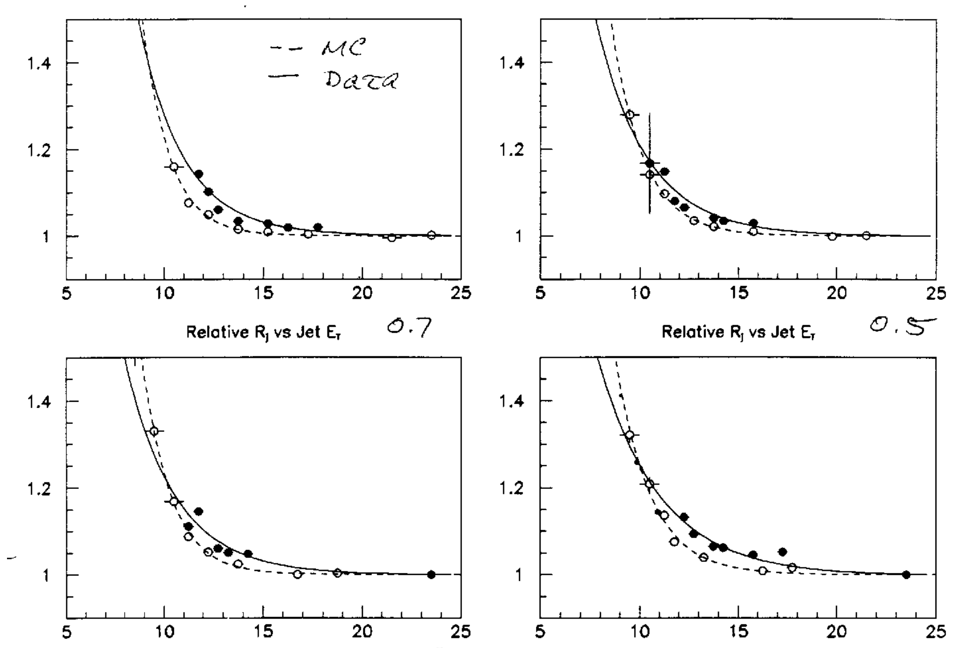

Figure 6.23: Low E_T bias for Data (solid) and Monte Carlo (dashed) showing the bias on the y-axis and the jet E_T on the x-axis. Different jet algorithms are shown: ΔR = 0.7 at top left, ΔR = 0.5 at top right, ΔR = 0.3 at bottom left, and the old Run 1a nearest neighbor jet algorithm with an 8 GeV E_T threshold at bottom right.

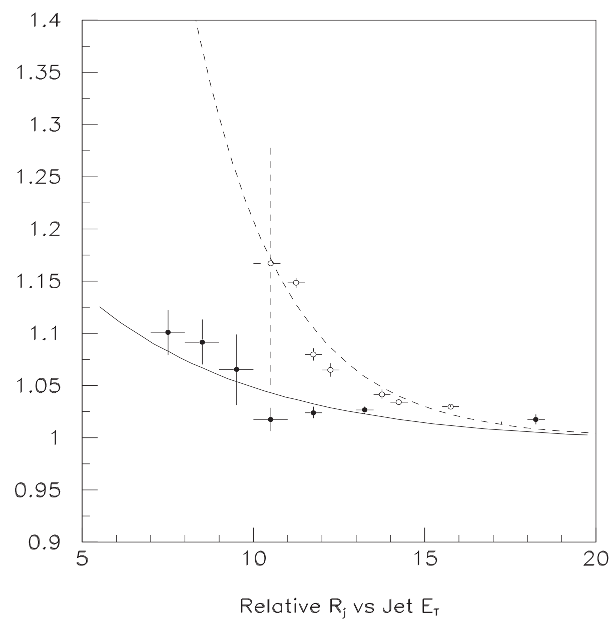

Figure 6.24: Comparison of low E_T bias measured for jets reconstructed with the fixed-cone algorithm with an 8 GeV cutoff, and with the nearest neighbor algorithm with a 5 GeV cutoff.

In Table 6.6 are given the fit parameters for the low E_T bias correction. Polynomials were tried for the fit but the best behaved was an exponential function, $R = 1.0 + \exp(a_0 + a_1 * E_T)$. The χ^2 for the data curves were poor due partly to the large number of triggers used. These triggers came from very different run periods and did not completely follow a smooth curve. Some of this can be seen in Figure 6.23 where we see that the points fluctuate by large amounts on the scale of their statistical errors. Because the correction obtained for different jet algorithms was very much alike within the data or Monte Carlo, the 0.5 cone size was chosen for all algorithms because it had the largest statistical sample.

Table 6.6. Fit parameters for low E_T bias correction. The fit function used was $R = 1.0 + \exp(a_0 + a_1 * E_T)$.

algorithm	a_0	a_1	χ^2**/df**
ΔR = 0.5 (*data*)	2.32 ± 0.36	-0.39 ± 0.03	10.1
nearest neighbor, 5 GeV threshold (*data*)	-0.94 ± 0.93	-0.20 ± 0.08	3.9
ΔR = 0.5 (*MC*)	4.64 ± 0.50	-0.62 ± 0.05	0.24

c. Systematic Uncertainties

One of the limitations of this analysis is that as one approaches the reconstruction threshold, it becomes difficult to obtain sufficient numbers of events. Because the bias grows rapidly as the E_T decreases, it is very important that we have as much data as possible. In the Monte Carlo sample, we are able to measure the bias down to jet E_T's of 9 GeV while in the data we are restricted to > 10 GeV. As a result, we cut-off the correction at about 30% which is approximately the value at about 10 GeV obtained from the fit .

There are also several difficulties which make this measurement problematic. For the most part, these mean that we make a mistake because we cannot ensure that the plot without a jet requirement is on the same footing as the one with a jet requirement. For instance, as was noted in the preceding section, events with forward probe jets tend to have undermeasured responses because of the effect of multiple interactions. This causes a problem in that it is a pseudorapidity-dependent effect. Since we do not specify a jet in the unbiased plot, we cannot specify where in the detector the hadronic recoil lies. As a result, events with forward recoil are present in this sample, while for the most part we throw these out in the sample with a jet required. Thus, even above 20 GeV, the ratio of the 2 plots may not be 1.0.

Another issue involves pseudorapidity-dependent response variations. Some of these are trivial like the fact that, for a given E_T, a jet's energy rises so that its response increases as it moves forward. Other variations can occur because each calorimeter subdetector does have a somewhat different raw energy scale. Again, the plot without a jet requirement cannot reject these events and our final ratio may not be 1.0 even above 20 GeV.

d. Application of the Correction

There are a number of issues which must be considered when deciding how to use the low E_T bias correction. First, because this bias is relative to the uncorrected E_T threshold of 8 GeV (or 5 GeV) this correction is applied before any other jet corrections.

Some jets, however, are not biased by the 8 GeV cut because of merging or splitting, or because reconstructed electromagnetic clusters were removed from them. As described in Chapter IV, the fixed-cone jet algorithm allows split jets which have two well separated energy clusters. This splitting is performed after the 8 GeV threshold is applied so that they may now have E_T < 8 GeV. The effect of the algorithm on the response of jets found in such a way is difficult to know because they are rare. Such a jet, however, is not biased with respect to 8 GeV as normal jets are. Another special case occurs when a jet shares energy with an electromagnetic cluster (PELC or PPHO). Here the electromagnetic cluster is removed from the jet and the remainder is left to be corrected as a jet. Again, the jet threshold is with regard to the combined cluster so the remaining jet stub, while it may be biased in some way, is not biased like normal jets with respect to 8 GeV. In neither case do we allow the jets to be corrected for the bias.

One implication of this bias is that for some analyses, only certain jets near the reconstruction E_T threshold should be corrected. For instance, in an analysis one might select events by requiring at least one reconstructed jet. The $\not\!\!E_T$ distribution of the events which pass is biased by this selection. The low E_T bias correction could be used to obtain the proper jet E_T and $\not\!\!E_T$ distributions. If no selection is made on the number of jets, then the $\not\!\!E_T$ is fine and no correction is necessary. In general, to get the proper $\not\!\!E_T$ and jet E_T relative to the final state particle level the bias correction must be applied to all jets required in the analysis event selection.

This has implications for a response measurement which is dependent on the $\not\!\!E_T$ such as ours. Since we are measuring the response of the calorimeter to jets, we must require a jet in the event. The response we measure will correspond to that shown in Figure 6.11 while we would like to measure the real response corresponding that shown in Figure 6.10a which is independent of jet algorithm. We use the biased sample to obtain the $\not\!\!E_T$ distribution for an unbiased sample by applying the low E_T bias correction. In our case, we only want to correct the probe jet since that is the only jet required for the analysis.

16. Extending the Reach in Jet Energy

For CC jets, we are limited to energy less than 150 GeV by the rapidly falling photon cross section. This presents problems in extrapolation to higher energies because there is insufficient information about the shape of the curve. This concern was in fact part of the motivation for using EC photons and combining PPHO and PELC samples. In addition to this limitation for high energy jets, there are large systematic errors involved in the collider data analysis at low E_T (< 20 GeV). To overcome these limitations, we first exploit the uniformity of the detector by using the EC which has higher energy jets. To further extend the energy reach, we compare jets in data and our ISAJET[57] direct photon sample with full GEANT detector simulation.

a. Combining Ia and Ib Samples:

Since we have performed the electromagnetic scale corrections we have put photons on the same footing in Runs 1a and 1b. There are a few sampling weight corrections, however, which need to be applied to jets before these runs are completely equivalent. After applying these corrections, we obtain the response curves for CC and EC as shown in Figure 6.25. Both Run 1a and Run 1b energy scales are in agreement at the 0.5% level after reconstruction-dependent corrections have been applied. We therefore combine these two samples in our analysis.

b. Using High Energy EC Jets:

We have performed the analysis where the jet is in the EC, avoiding the very far forward region due to known η-biases in the jet position and vertexing problems, and we avoid the ICD as well. We plot R vs. E' because it is algorithm independent and because it is not subject to the η-dependent changes in showering and offset which have nothing to do with response. We compared CC and EC curves for events with one interaction. Taking the ratio of these two curves where they overlap gives Figure 6.26a. The ratio is consistent with a normalization factor (χ^2 = 7.5 for 8 degrees of freedom) of 1.029 ± 0.005 and no offset. The ratio of response for ECN/ECS is about 1.011. The overall CC/EC ratio is sensitive to the number of multiple interactions in an event and this results in a 2% systematic error which is applied to EC jets. This need not be applied in the CC because the normalization of EC to CC removes any difficulty since there was no energy dependence observed. After this is done, we now can cover the region of 25 GeV through 350 GeV in energy.

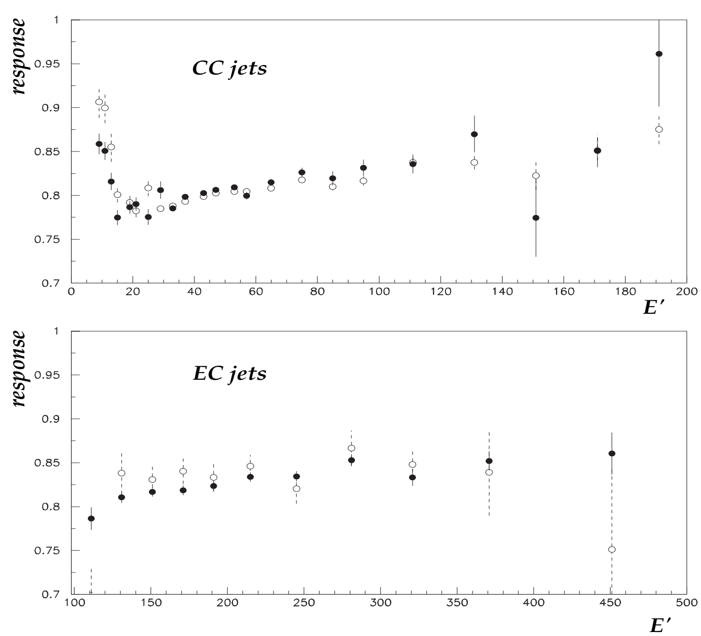

Figure 6.25: Response *vs*. E' for (a) CC probe jets and (b) EC probe jets for Run 1a (open circles) and Run 1b (closed circles). Reconstruction dependent corrections have been applied. The low E_T bias correction was not applied.

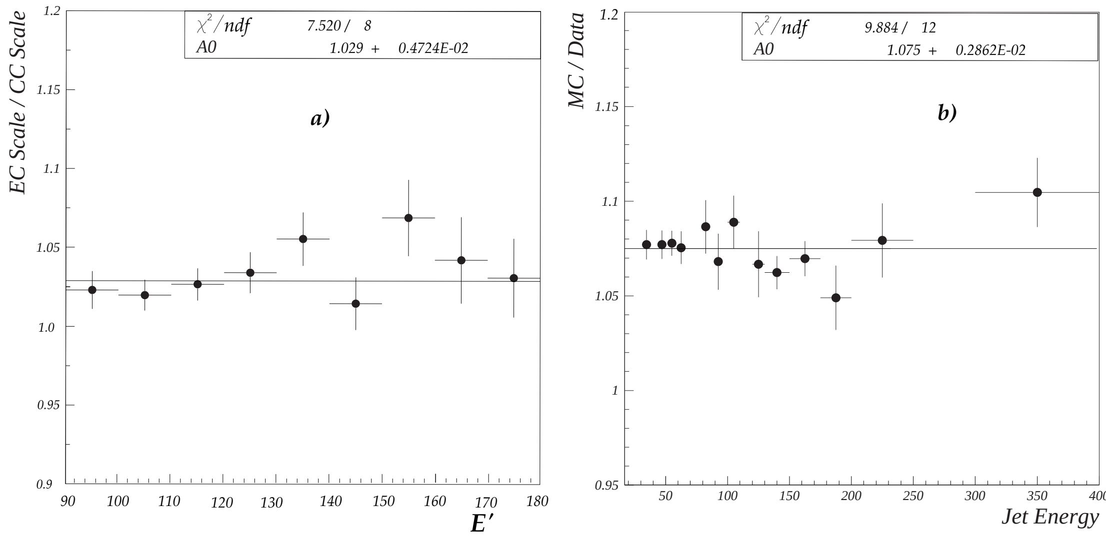

Figure 6.26: Comparison of energy dependence of response in different samples, (a) ratio of EC to CC response, and (b) ratio of CC response in data and Monte Carlo.

c. Monte Carlo Extrapolation

After the above addition to the energy reach we can measure the response of the calorimeter to jets with energies between about 10 GeV to 350 GeV. The collider data curve for jet energies below 20 GeV is not reliable, however, due to several effects. Energy scale variations between cryostats and degradation in $\not{E}_T$ resolution with increased numbers of multiple interactions means that the unbiasing correction breaks down in the data because the two histograms we are dividing have more differences than just the requirement of a jet.

Because both the low energy and high energy correction is important for various physics analyses, we would like more information on which to base our fit in these kinematic regions. An analysis of the response of the 'GEANT detector' using the same techniques results in a similar functional form as the data but the level is a few percent higher. The ratio of the two data sets is shown in Figure 6.26b. Over the range 25 to 350 GeV the ratio is flat (χ^2 = 9.9 for 12 degrees of freedom) at 1.075 ± 0.003. The Monte Carlo does not suffer from the problems in the low E_T region because the recoil was specified to be central at generation time and the sample is all single interactions. We normalize the Monte Carlo curve by 1/1.075 and use it for jets below 25 GeV and above 350 GeV.

17. Final Response Correction and Absolute Scale Uncertainty

a. Energy Dependence

After our analysis is complete, we have points constraining the energy scale of jets over the range from 10 GeV to 500 GeV. Figure 6.27 shows the measured response *vs*. jet energy for five jet algorithms from collider data direct photon candidate events. Data points from the EC and Monte Carlo have been added in after being corrected for the factors determined above. The poor χ^2 per degree of freedom results from statistically significant discontinuities in the various samples used. Figure 6.28 displays the measured response vs. jet energy in the Monte Carlo ISAJET direct photon samples. The χ^2 per degree of freedom is better than in the data due to the uniformity of the sample.

The dependence of the calorimeter response on jet energy is well described by the form of Equation 6.2. For data, a = 0.71 and b = 0.025, while for Monte Carlo, a = 0.74 and b = 0.031. The data has not had the EM scale factor applied to the jets. The shapes of the Monte Carlo and data in these two fits do not reflect the agreement in shape and the 1.075 scale factor seen in the MC/data ratio mentioned above. This is because the correction for the dependence of R_j on jet angular width, which was derived from the data and applied to the Monte Carlo, biases the Monte Carlo which has significantly narrower jets than the data. The MC/data scale factor was derived with the width correction turned off.

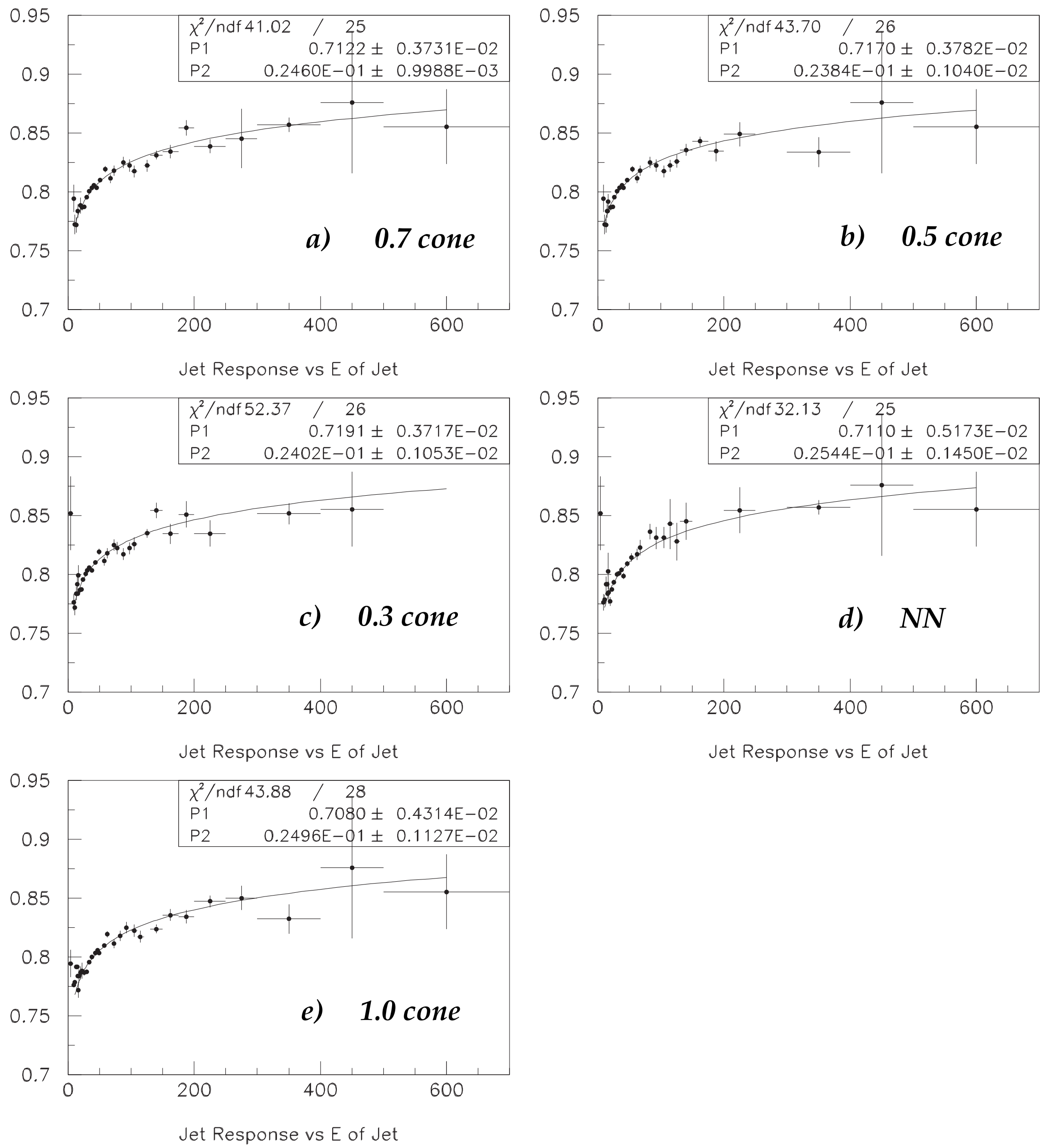

Figure 6.27: Response vs. jet energy for five jet algorithms from collider data direct photon candidate events. The poor χ^2 per degree of freedom results from statistically significant discontinuities in the various samples used.

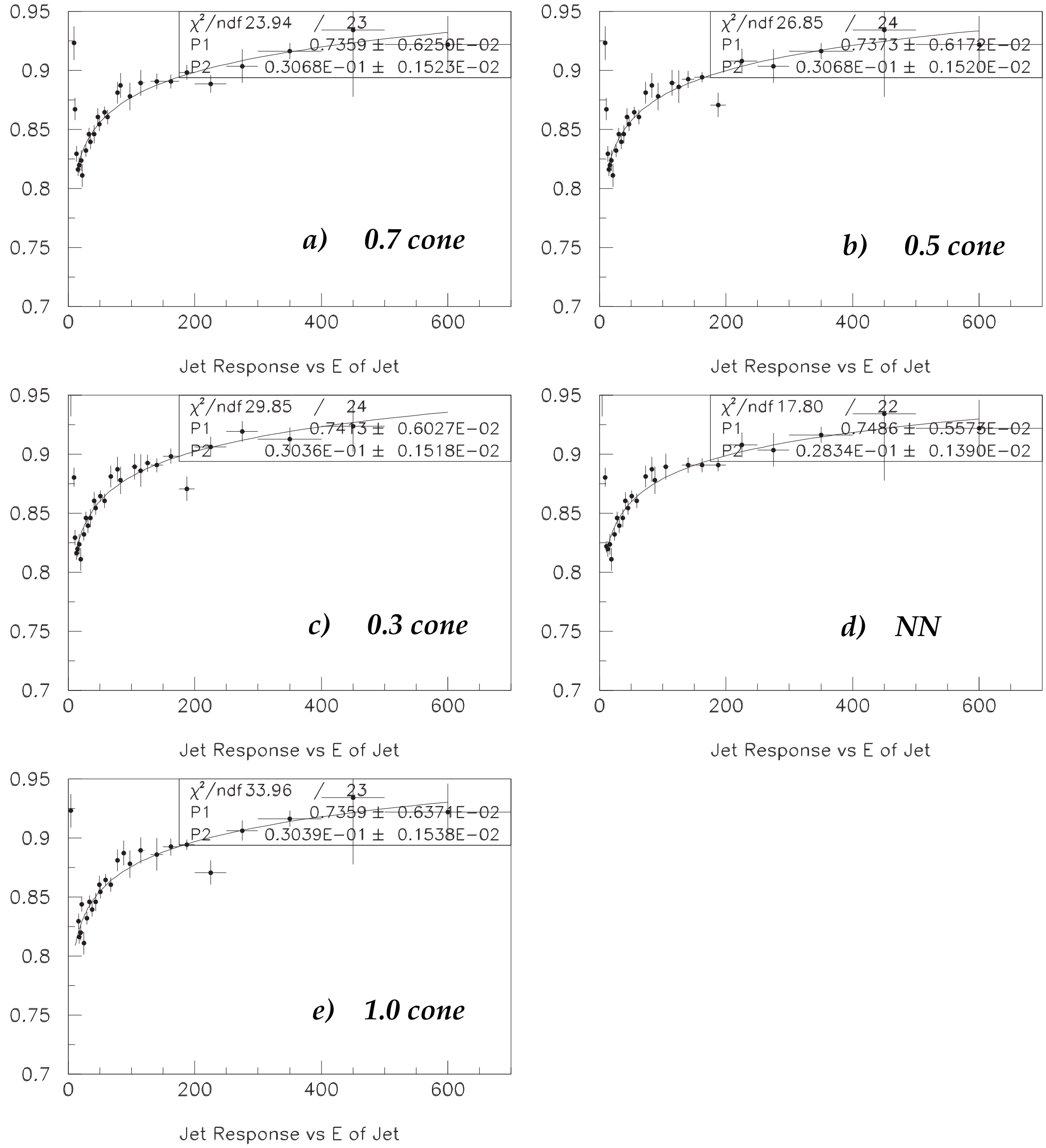

Figure 6.28: Response vs. jet energy for five jet algorithms from Monte Carlo ISAJET direct photon events. The χ^2 per degree of freedom is better than in the data due to the uniformity of the sample.

It is interesting to compare our findings to the crude model in Section I. We find that the model was not unreasonable, but our fits give a smaller value for *a* and larger for *b*. This is consistent with the jets being governed by the lower energy region of the e/π curve in Chapter III. As discussed in

Appendix IV, the models which attempt to describe the behavior of e/π actually suggest a slightly more complex behavior than $a + b\ln(E)$. This is necessary if one wants to accommodate particle energies much larger than 100 GeV while still describing low energy response accurately. Adding a $c*(\ln(E))^2$ term into the fit function does improve the agreement between our simple model and the measured response.

b. Tabulation of Systematic Fractional Uncertainties:

As discussed in previous sections, there are a number of systematic uncertainties involved in this analysis. Tables 6.7 and 6.8 indicate the breakdown of each systematic error as a function of jet energy for collider data and Monte Carlo, respectively. The unbiasing error is added separately to the others which are summed (in quadrature) at the bottom row. The unbiasing correction has a systematic error due to the fact that the final bins are finite in size and the correction is steeply changing as a function of jet E_T.

In the region where the Monte Carlo was used in the fit to the data (below 20 GeV and above 350 GeV), the errors are the differences between the data and the Monte Carlo. Since the MC/data ratio was calculated over the range 25-350 GeV, the differences in topology error is averaged over this range. The 150 GeV points and the 400 GeV points are treated as one point for this because only about 25 % of the data is in the EC. The 150 and 350 GeV points correspond to data from the EC sample. Thus, in the data these have the statistical error from the cryostat factor analysis along with the 2% systematic uncertainty from the multiple interaction dependence added in.

Table 6.7. Collider Data Errors in %.

energy (GeV)	10	15	20	30	80	150	400
Method:							
topology	1.3	1.3	2.02	1.78	1.22	0.88	1.3
k_T**/res-bias**	3.0	3.0	1.0	0	0	0	0
binning	1.0	1.0	0	0	0	0	0
unbiasing	5.0	0.5	0	0	0	0	0
multiple interactions	0.5	0.5	0.5	0.5	0.5	0.5	0.5
Background:							
instrumental	1.42	1.42	1.42	1.42	1.42	1.42	1.42
physics	0.5	0.5	0.5	0.5	0.5	0.5	0.5
Extrapolation:							
EC/CC	0.1	0.1	0	0	0	0.472	0.1
MC/data	0.286	0.286	0	0	0	0	0.286
Total =	3.781	3.781	3.949	2.585	2.001	1.874	2.073

Table 6.8. Monte Carlo Errors in %.

energy (GeV)	10	15	20	30	80	150	400
Method:							
topology	0	0	0	0	0	0.88	0.88
k_T**/res-bias**	3.0	3.0	3.0	1.0	0	0	0
binning	1.0	1.0	0	0	0	0	0
unbiasing	5.0	0.5	0	0	0	0	0
Background:							
physics	0.5	0.5	0	0	0	0	0
Total =	3.202	3.202	3.0	1.0	0	0.88	0.88

18. Comparison of Measured Response with Other Estimates:

a. Comparison of Monte Carlo and Data

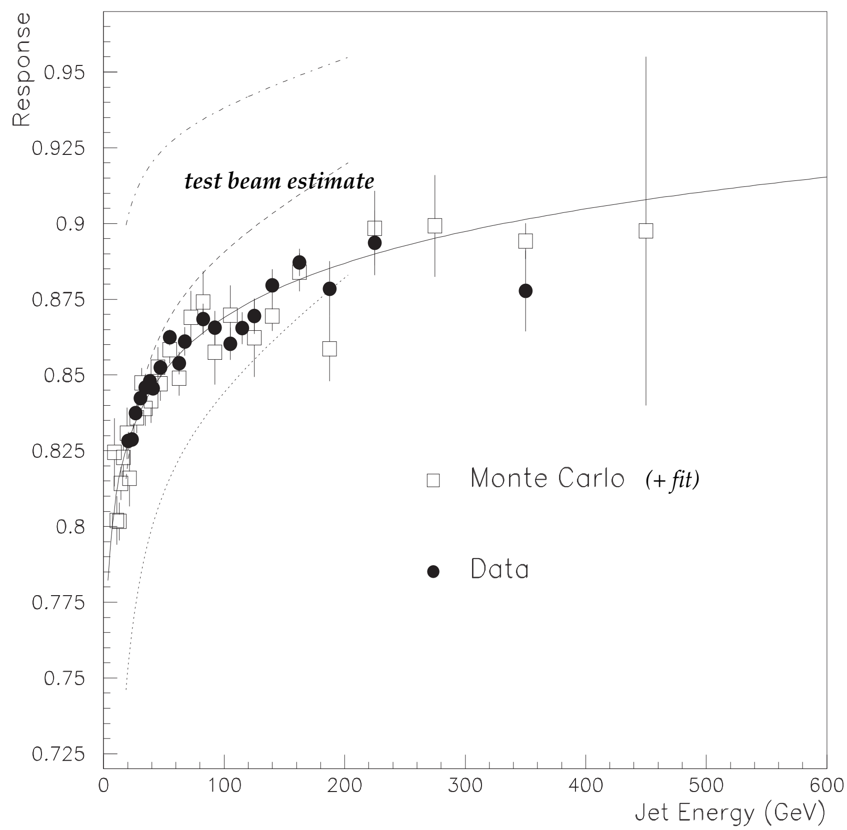

Figure 6.29: Response, r, of the probe jet relative to the photon *vs*. mean jet energy for Data (solid circles) and Monte Carlo (open squares).

As mentioned above, we have measured the ratio of Monte Carlo and DØ responses to be 1.075. This comparison is misleading, however, because we have corrected the photons in order to properly combine and compare Run 1a and Run 1b, and we have not corrected the jets by such a scale factor. What is perhaps more useful is a statement of the inherent response of the calorimeter for jets relative to photons. This is shown in Figure 6.29 for data and Monte Carlo, and it indicates that Monte Carlo has predicted our *in situ* measurement to within our systematic errors.

b. Comparison with Z events

To cross-check our result, we can compare with a similar measurement that was obtained by using the $\not{E}_T$ in Z dielectron events. Using the sampling weights for Run 1a, the response of the central calorimeter to the hadronic recoil in Z events was measured[48] to be 0.83 ±0.04. This measurement was made with no selection on jets. When looking in the isolated photon sample and removing our jet selection criteria, we obtain 0.828 ± 0.001 which is in agreement.

c. Comparison with Test beam

Interestingly, a totally different method has previously been used to predict jet response using test beam particles input into ISAJET particle jets[58]. For comparison, the nominal predicted response and upper and lower limits of the error band are superimposed on Figure 6.29. Although the errors from such an analysis are quite large, the resulting curve agrees well with the measurements from collider data and Monte Carlo presented here.

19. Jet Scale Correction and Verification

Once we have obtained the response, offset, and showering corrections, we can correct jets. The effective overall factor is shown in Figure 6.30 as a function of uncorrected E_T for central jets. The upper and lower dashed lines correspond to 1σ upward and downward excursions of the total error, calculated as the sum in quadrature of all errors. These errors are dominated by systematic errors and there are substantial correlations between errors at different energies.

We have verified that the total calibration procedure successfully obtains E_{ptcl}^{jet} from E_{meas}^{jet} using jets in the Monte Carlo sample of direct photon events. Figure 6.31 shows the ratio of calorimeter and particle jet energy *vs*. particle jet energy before corrections (open circles) and after corrections (solid circles). The ratio is consistent with unity after corrections.

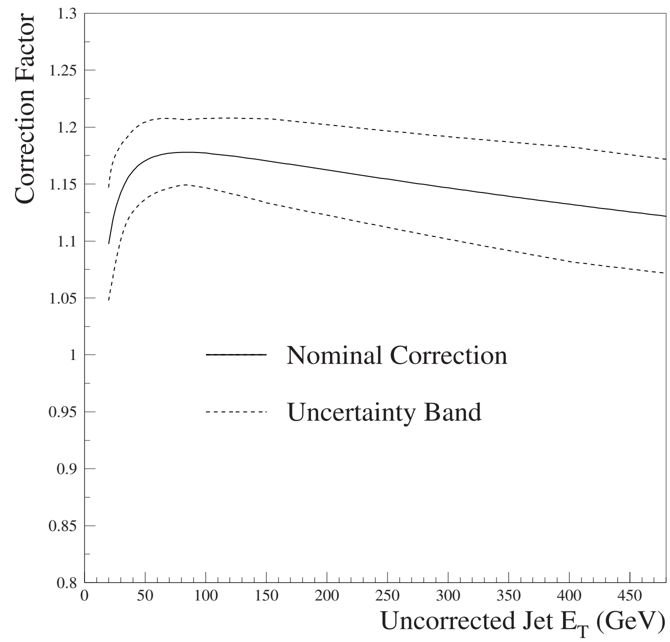

Figure 6.30. Total jet energy scale correction for central ($|\eta| < 0.5$) jets. The jet algorithm used $\Delta R = 0.7$.

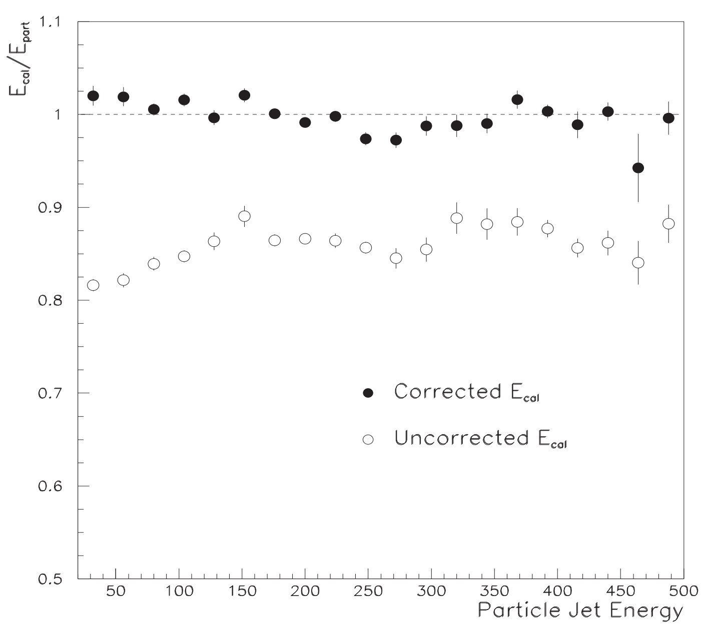

Figure 6.31. Ratio of reconstructed jet energy to particle jet energy *vs*. particle jet energy before (open circles) and after corrections (solid circles).

CHAPTER 7

ANALYSIS OF DIELECTRON + JETS EVENTS

In the previous chapters, we have produced the raw materials needed to execute a search for the top quark. These include a stable and quality data set, sophisticated reconstruction algorithms to identify the objects we are looking for, knowledge of the efficiency and biases of these algorithms, and determinations of the requisit calibrations. This allows us to compare our data to the various processes which may occur in the data and which we may model. In this Chapter we will describe the needed Monte Carlo samples, an initial event selection for the dielectron search, and some verification of the data. We can then proceed to the optimization of the analysis to search for a high mass top quark, and estimate the signal and background levels expected in the data. We finish with a calculation of the top cross section and a limit on the dielectron branching ratio from this analysis.

1. Monte Carlo Samples

Given that the cross section for top production is so small, it becomes very important that selection criteria be determined which are best able to accept top events while rejecting backgrounds. The choice of these cuts is motivated by expectations for top production at Tevatron energies, branching ratios for top decay, and our knowledge of the detector's capabilities. Much of this knowledge comes from Monte Carlo simulations of various physics processes and estimation of their behavior in the detector.

a. Top Monte Carlo

Our simulation of top events proceeds in two stages. First, we have generated moderately sized samples of events (~ 2000) with ISAJET where we have specified the top mass to be at discrete values from 100 GeV/c^2 to 200 GeV/c^2. These events were specified to have two electrons at the final state particle level from W decay. Some of the main kinematic properties of these samples have already been shown in Chapter II. These samples were used to tune the cuts for this analysis.

In order to improve our statistical sample and include contributions from tau decay chains, two additional sets of top events were generated. One set was generated with HERWIG for top masses between 100 GeV/c^2 and 230 GeV/c^2 at 10 GeV intervals. In the range 140 GeV/c^2 to 200 GeV/c^2 the samples contained 100,000 events each while outside of this range the samples contained 50,000 events. The parton structure functions used were CTEQ3M. They were generated to include all dilepton contributions including τ decay sequences (ie. ee, $e\mu$, $\mu\mu$, $\tau\tau$, $e\tau$, $\mu\tau$), such that the total branching ratio was 6.85%. A similar but smaller set of ISAJET events were generated for comparison with about 10,000 events per mass point. The HERWIG sample will be our main sample for this analysis because that generator generally reproduces QCD behavior well. The high statistics are more necessary for the top mass measurement but do help to reduce statistical errors in this analysis as well.

b. $Z \rightarrow ee$

As with the top samples, two sets of Monte Carlo were generated for each major physics background. The first sample was used to tune the cuts of the analysis while the second was either used to cross-check the data, as in the case of the $Z \to ee$ background, or was used to obtain the final background estimate with a smaller statistical uncertainty.

Although we will determine our Z background from data, we have generated two samples of events for cross checks. The first is a 10,000 event sample generated with ISAJET. To compare Z plus 2 jet states, we have also generated a sample of 4069 HERWIG events with two final state electrons with E_T > 10 GeV and two 0.5 cone particle jets with E_T > 5 GeV.

c. $Z \to \tau\tau \to ee$

Initially we have studied this background via an ISAJET sample of 1996 events, generated with cuts requiring two electrons with E_T > 5 GeV. Because this sample suffered from low statistics, a separate sample was generated to actually obtain the $Z \to \tau\tau \to ee$ background. This was a sample of ISAJET events which were generated with both tau's forced to decay to electrons, and with the requirement that the E_T of the electrons be above 14 GeV and the p_T of the Z be above 20 GeV. This was done in order to save on resources required to further process the events with the GEANT particle shower library and the reconstruction program. These cuts were determined to be > 95% efficient for events with two reconstructed electrons with E_T > 15 GeV and two reconstructed jets with E_T > 15 GeV, which were considered to be the loosest one would ever cut on these quantities for this analysis.

d. $WW \to ee$

An initial sample for this background was obtained using PYTHIA with the W's forced to decay to electrons. This sample suffers from low statistics when our cuts are made so we generated an additional sample using ISAJET. They were required to have two final state electrons with E_T > 10

GeV, and to have two 0.5 cone particle level jets with $E_T > 5$ GeV. These cuts were chosen as the tightest possible while still requiring > 95% efficiency for offline cuts of 12 GeV on two reconstructed electrons and 10 GeV cuts on two reconstructed 0.5 cone jets in the existing $WW \rightarrow ee$ sample.

e. $b\bar{b}, c\bar{c} \rightarrow ee$

In order to calculate the heavy flavor background, we have generated Monte Carlo samples using ISAJET. We retain only those events which have at least two electrons produced in the event at the final state particle level. These events were generated in parton p_T intervals of 40-60, 60-80, 80-100, 100-130, 130-160, 160-200, and 200-240 GeV/c.

f. Drell-Yan

A sample of Drell-Yan events was generated using PYTHIA with 2 electrons having p_T > 15 GeV/c and 1 jet with p_T > 10 GeV/c. The cross section for this sample, which is obtained by using the DØ measurement in the dielectron invariant mass region of 30 GeV/c^2 to 60 GeV/c^2[59] and normalizing to the Monte Carlo distribution, is 4.2 pb.

2. Choice of Cuts

Before any cuts are applied the two largest backgrounds to a dielectron search are QCD instrumental backgrounds and heavy flavor production. Reducing these backgrounds dictates our electron cuts since these are not sources of truly isolated high p_T electrons. By choosing the electron identification cuts defined in Chapter 4 plus requiring E_T > 20 GeV and moderately central pseudorapidity ($|\eta|$ < 2.5), we can remove nearly all heavy flavor background and reduce the instrumental background to be small relative to the Z. Although it depends somewhat on what the mass, and therefore the production cross section, of the top is, the ratio of expected signal to background after the electron cuts is of order 1:1000.

At this point, the main background is the Z but there are contributions from WW production and fakes. The next most useful cut is a $\not{E}_T$ cut of 40 GeV if an event is in the Z mass region defined to be 79 GeV/c^2 to 103 GeV/c^2. This has a rejection factor of about 600 for Z events. At this point, the major backgrounds are Drell-Yan and fakes and these generally have no real $\not{E}_T$. A $\not{E}_T$ cut of 25 GeV outside the Z mass region reduces these backgrounds by over a factor of 100.

The S/B after these leptonic cuts is on the order 1:10 and we cannot cut tighter on these variables without major losses in efficiency. In Chapter II, we noted, however, the softness or absence of jet activity for the background processes. For each successive requirement of a jet with E_T > 15 GeV, we get a factor of about 6 rejection of background. There is not much loss in efficiency if m_{top} > 120 GeV/c^2 from requiring two such jets for $t\bar{t}$ production.

Based upon the above observations, our event selection is as follows,

- two electrons with E_T > 20 GeV and $|\eta| < 2.5$
- $\not{E}_T > 25$
- $\not{E}_T$ > 40 GeV if 79 GeV/$c^2 < M_{ee} <$ 103 GeV/c^2
- two jets with E_T > 15 GeV and $|\eta| < 2.5$.

3. Verification of Events in Data

We have now performed all of the particle identification selections, energy corrections, and data integrity cuts and have devised our initial physics analysis cuts. Before proceeding into the search optimization for high mass top (ie. m_{top} > 140 GeV/c^2), however, it is important to try to use some criteria to verify the sensibility of our data. In particular, caution is advisable in terms of both the Main Ring data and the use of the TRD to reclaim electrons in the PPHO sample, both of which were untested in a physics setting before this analysis.

a. Verification of Main Ring Data

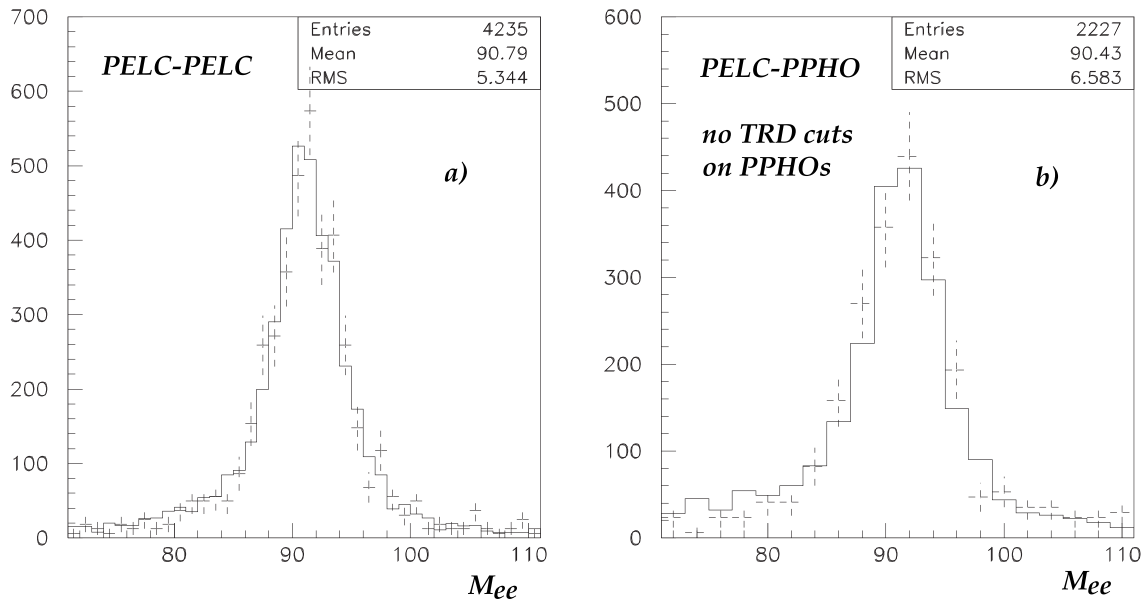

Figure 7.1: Invariant mass of two leading electromagnetic clusters for (a) PELC-PELC events in GOOD_BEAM (solid line) and Main Ring (points with errors) events, and (b) PELC-PPHO events with no TRD cuts on the PPHOs.

Although we found in Chapter 5 that the Main Ring did not affect the inner layers of the calorimeter and tracking, it is important to actually perform a physics measurement in these data that one can verify is reasonable. To do so, we examine the dielectron invariant mass distribution for GOOD_BEAM and Main Ring events. As shown in Figure 7.1, the shape of the distribution is consistent for both sets of data in both the PELC-PELC and PELC-PPHO samples. The mean and width of the distribution is 90.8 GeV/c^2 and 5.3 GeV/c^2, repectively for the PELC-PELC sample, which are slightly lower and higher than what one should get for Z events alone due to the presence of backgrounds. The effect of these backgrounds is amplified in the PELC-PPHO sample distributions. Figure 7.2 shows the $\not{E}_T$ versus M_{ee} for events having two electrons and two jets for GOOD_BEAM events and for Main Ring events before and after corrections. The corrected population of Main Ring events (Figure 7.2c) are topologically similar to GOOD_BEAM events.

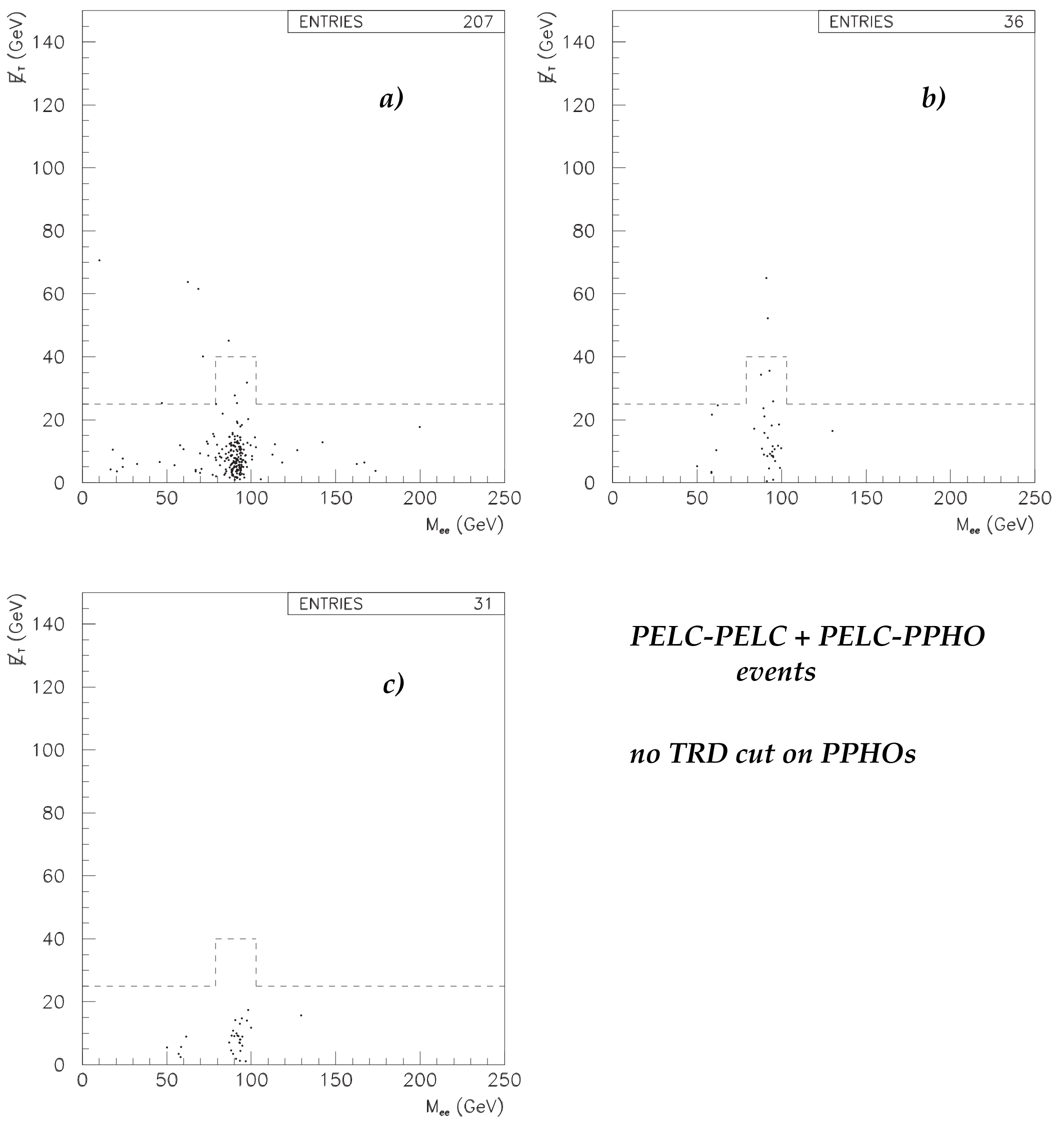

Figure 7.2: $\not{E}_T$ vs. invariant mass in events with two electron candidates with E_T > 20 GeV and two jets with E_T> 15 GeV for (a) GOOD_BEAM data, (b) Main Ring data without corrections, and (c) Main Ring events with corrections.

b. Jet Multiplicity in Dielectron Events

In most of our backgrounds, jets are produced due to initial state radiation which is reconstructed as a high p_T jet. This radiation couples directly to one of the incoming partons with strength α_s and the rate to produce each additional jet is reduced by approximately this factor. This scaling of jet multiplicity is not exactly α_s (~ 0.13 for $q^2 \sim m_Z$) but is expected to occur for W and Z events and is seen in the DØ W sample[60] to have a value of 0.17.

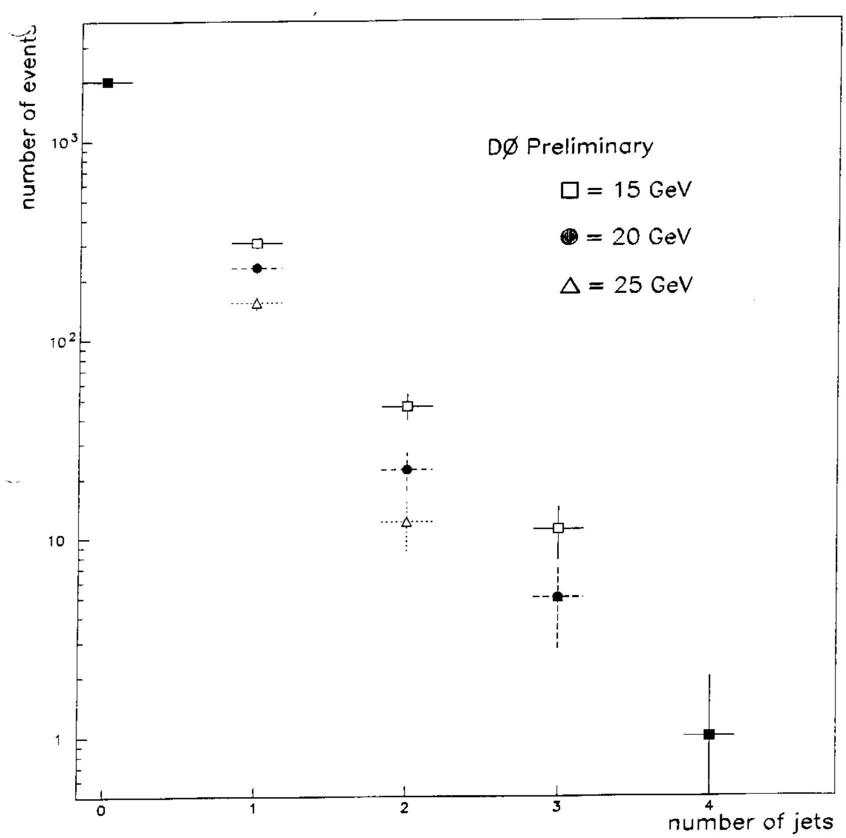

Figure 7.3: Scaling of jet multiplicity in Z dielectron events for three different jet E_T thresholds. The sample is the first 48 pb^{-1} of GOOD_BEAM Run 1a + Run 1b data. The slope of a linear fit to the points corresponding to a 15 GeV jet E_T cut was 0.16 in this sample.

In Figure 7.3, we show the observed scaling of jet multiplicity in Z candidates for 15, 20, 25 jet E_T thresholds. Although the statistics are poor for multiplicities above two jets, the scaling is observed and is roughly consistent with that observed in the W sample.

A further cross check of Main Ring data is comparing the breakdown of events for different jet multiplicities. Events were selected to be in the Z mass region 81 GeV/c^2 to 101 GeV/c^2 and all electron identification cuts were imposed except the TRD cut on the PPHO's. The fraction of events in each Main Ring state is given in Table 7.1 for various jet multiplicities. For comparison, Table 7.1 includes the actual fraction of the luminosity that each state constitutes according to the Level Ø estimate. Within their statistical errors, the share of the data which is in each Main Ring state is not dependent on the jet multiplicity.

Table 7.1. Fraction of events in three Main Ring states for various jet multiplicities for dielectron candidates in the Z mass region.

	GOOD_BEAM	µBLANK	MRBS_LOSS
Z + ≥ 0 jets	0.859 ± 0.014	0.049 ± 0.003	0.092 ± 0.005
Z + ≥ 1 jet	0.871 ± 0.035	0.047 ± 0.008	0.082 ± 0.011
Z + ≥ 2 jets	0.854 + 0.083	0.033 ± 0.017	0.114 ± 0.030
Z + ≥ 3 jets	0.88 ± 0.23	0	0.12 ± 0.08
Level Ø	0.865	0.051	0.082

4. Optimization for High Mass Top

The mass analysis of lepton+jets events in Run 1a indicated the possibility of a high top quark mass (about 200 GeV/c^2)[61]. In addition, if the top quark were much lighter we should have seen a signal in Run 1a with our cuts described above. Therefore, for analysis of the full Run 1 sample we re-optimized our selection cuts to be sensitive to a top quark mass in excess of 140 GeV/c^2.

a. Choice of Variables

We examined many different variables such as jet E_T, event shape variables like aplanarity and sphericity, $\not{E}_T$, and the scalar sum of all clustered hadronic (ie. 'jet') transverse energy, 'H_T', of the event. We found individual jet E_T's and the H_T in an event to be the best remaining discriminator between signal and background. Our optimization proceeded by first studying different cuts on jet E_T and then optimizing on an H_T cut. We define H_T in three different ways:

$$
\begin{aligned}
H_T^{(1)} &= E_T^{e1} + E_T^{j1} \\
H_T^{(2)} &= E_T^{j1} + E_T^{j2} \\
H_T^{(3)} &= E_T^{e1} + E_T^{j1} + E_T^{j2}
\end{aligned}
$$

where E_T^{e1} is the E_T of the leading electron, E_T^{j1} is the E_T of the leading jet, and E_T^{j2} is the E_T of the second leading jet.

These choices of definition were the best among a wide range of choices which could be used. For instance, one could add in the $\not{E}_T$ or the second leading electron E_T. For the dielectron channel, however, these two variables do not give very good discrimination between signal and background after our initial cuts. As a result, including them into the H_T calculation merely dilutes its effectiveness. Therefore, we rejected these options. Figure 7.4 shows the distribution of $H_T^{(3)}$ for three main backgrounds and for $t\bar{t}$ for masses from 140 to 200 GeV/c^2.

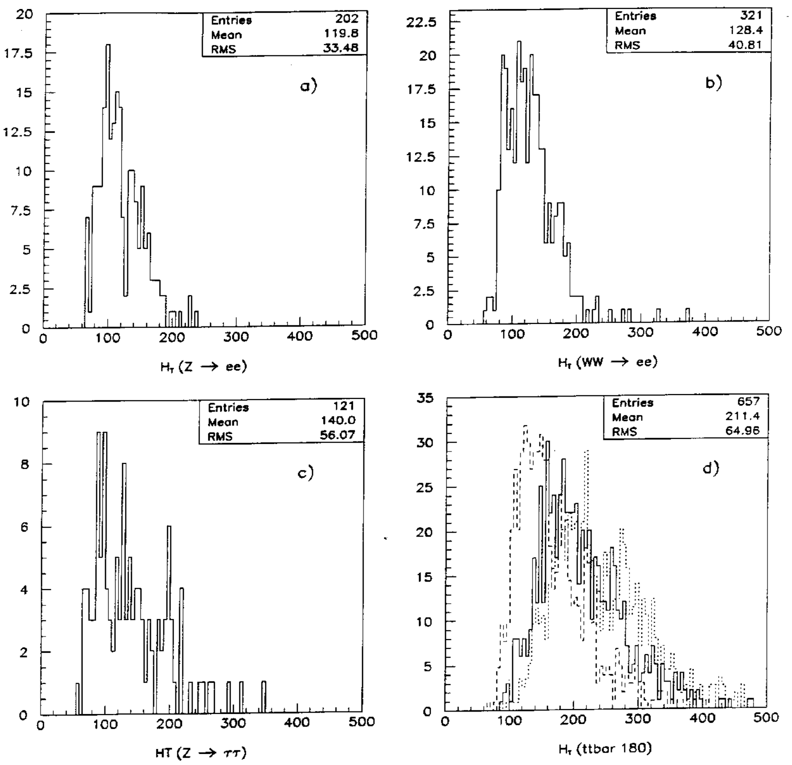

Figure 7.4: Total hadronic transverse energy, $H_T^{(3)}$, after requiring two electrons with E_T > 20 GeV and two jets with E_T > 15 GeV for (a) $Z \longrightarrow ee$, (b) $WW \longrightarrow ee$, (c) $Z \longrightarrow \tau\tau$, and (d) top of mass 140 GeV/c^2 (dashed), 180 GeV/c^2 (solid) and 200 GeV/c^2 (dotted).

b. Grid Search of Jet E_T and H_T

In order to carry out the cut optimization, we used the initial sample of ISAJET Monte Carlo $t\bar{t} \longrightarrow ee$ events with m_{top} = 180 GeV/c^2 generated using ISAJET as the signal sample. For particular choices of cuts, we computed both the physics backgrounds using Monte Carlo samples and fake electron backgrounds using 'electron'+ ≥ 3 jet data. The results of this 'grid search' on jet E_T are given in Appendix V, Table A5-1 and were obtained assuming a data set corresponding to an integrated luminosity of 32 pb^{-1}. The results for the optimization for two different jet cuts in terms of H_T are given in Appendix V, Tables A5-2 and A5-3. The results are shown in Figure 7.5. In addition to retaining the maximum efficiency for $t\bar{t}$ production, we chose cuts which maximized two different measures of significance,

$$\sigma_1 = S / B$$
$$\sigma_2 = S / \sqrt{B}$$

where S is the number of events expected for signal, and B is the number expected for background.

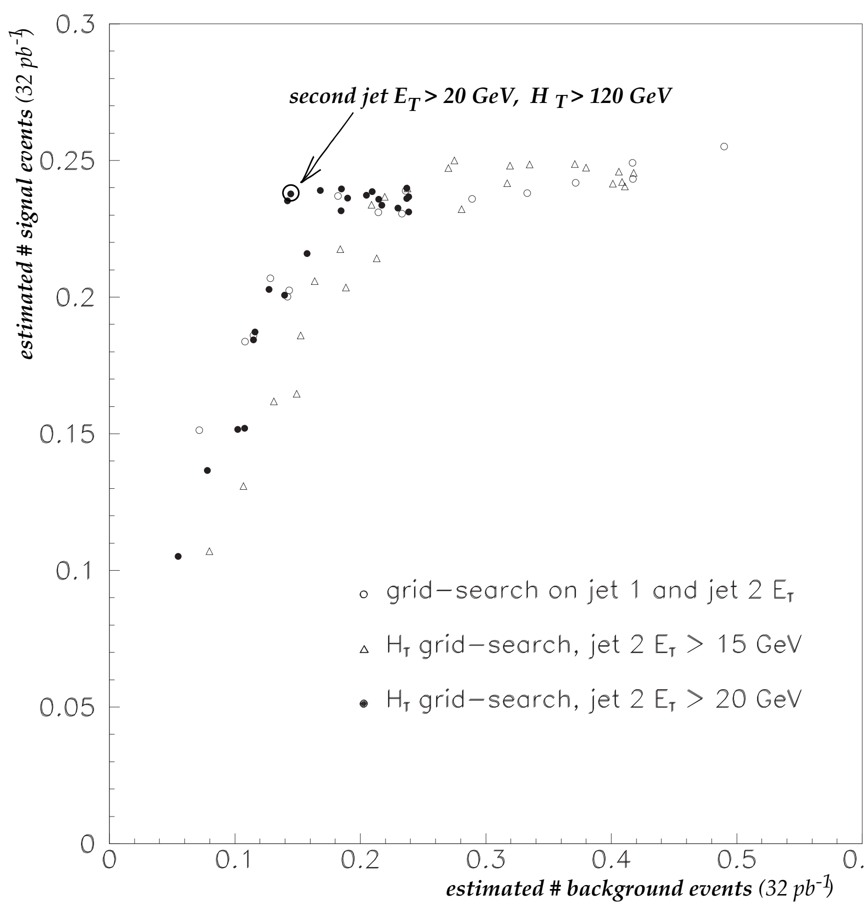

Figure 7.5: Estimated Signal vs. Background in 32 pb^{-1} for various choices of hadronic cuts. Shown are possible cut choices for different combinations of leading and second leading jet E_T's (open circles), various H_T cuts with a 15 GeV second jet cut (open triangles) and 20 GeV cut (closed circles).

We find that we get the best significance by moderately increasing the jet E_T cuts and adding a loose lower limit requirement on the value of H_T for the event. Increasing the jet E_T from 15 to 20 GeV generally reduces the backgrounds by around 40%. The H_T variable provides another similar factor of rejection. Both cuts are about 95% efficient for high mass top events. We use a combination of H_T and increase in jet E_T cuts to balance the background rejection with signal efficiency across the range of masses we are interested in. We find that $H_T^{(3)}$ is the most powerful discriminator of the three H_T variables. Including the E_T of the leading electron in the definition of H_T helps discriminate against the major backgrounds (fake backgrounds and $Z \to \tau\tau \to ee$) for the dielectron channel. For these backgrounds, the E_T spectrum of the leading electron is softer than for top events with dielectrons in the final state.

After the optimization had been performed, Monte Carlo studies showed that inclusion of all jets above 15 GeV gave a further mild improvement in signal to background. This arises from the large amount of gluon radiation which is seen as a substantial number of three and four jet events in our top Monte Carlo samples as compared to the backgrounds (see Figure 2.11). Also, depending on the way top is evolved by each event generator and depending on the effect of the jet algorithm, the average number of jets and their E_T can vary. Using all of the reconstructed jets can reduce our susceptibility to Monte Carlo differences. We therefore define

$$H_T^e \equiv E_T^{e1} + \sum_{i=1}^{\# jets} E_T^{j_i} (|\eta| < 2.5, E_T > 15 GeV) \qquad \textbf{Eq. 7.1}$$

where E_T^{e1} is the transverse energy of the leading electron.

As a result of the optimization we define a new set of cuts for the analysis. The electron and $\not{E}_T$ cuts are the same as before while our standard cuts will include a 20 GeV cut on two jets and a cut on H_T^e of 120 GeV.

5. Expected Signal and Errors

We have calculated the offline cut efficiencies for selecting $t\bar{t} \rightarrow ee$ decays using the HERWIG samples described above. In Figure 7.6 are shown the efficiency x branching ratio for various top masses (see Appendix 6 for numbers). The systematic error on these efficiencies includes contributions from the Monte Carlo generator, jet energy scale, the effect of multiple interactions, and trigger simulation uncertainty.

The Monte Carlo generator error is estimated from a comparison of ISAJET and PYTHIA top samples with our standard HERWIG samples. As shown in Figure 7.6, the other generators are contained within about a 10% band around the HERWIG curve. In the PELC-PELC sample, for instance, ISAJET tends to give a slightly higher efficiency than HERWIG for low top masses while PYTHIA appears to be significantly lower at m_{top} = 160 GeV/c^2. This discrepancy occurs after the 20 GeV jet cut and is worsened by the H_T^e cut. For m_{top} = 130 GeV/c^2, the ISAJET and HERWIG samples give a 2%, 8%, and 14% difference in efficiency after the $\not{E}_T$, jet E_T cuts of 20 GeV, and H_T^e cut at 120 GeV, respectively.

The error due to the jet energy scale is estimated by toggling jet scale corrections 1σ high and low. This results in a ±5% shift in efficiency for top events. The effect of multiple interactions in a single beam crossing was examined with about 5000 of the HERWIG top events from the 170 GeV/c^2 mass sample. These events were passed through simulation software which adds minimum bias data events on top of normal Monte Carlo events to simulate extra interactions. Addition of one extra interaction resulted in 2.8% loss in efficiency while addition of two extra interactions gave little efficiency loss compared to the case of zero additional interactions.

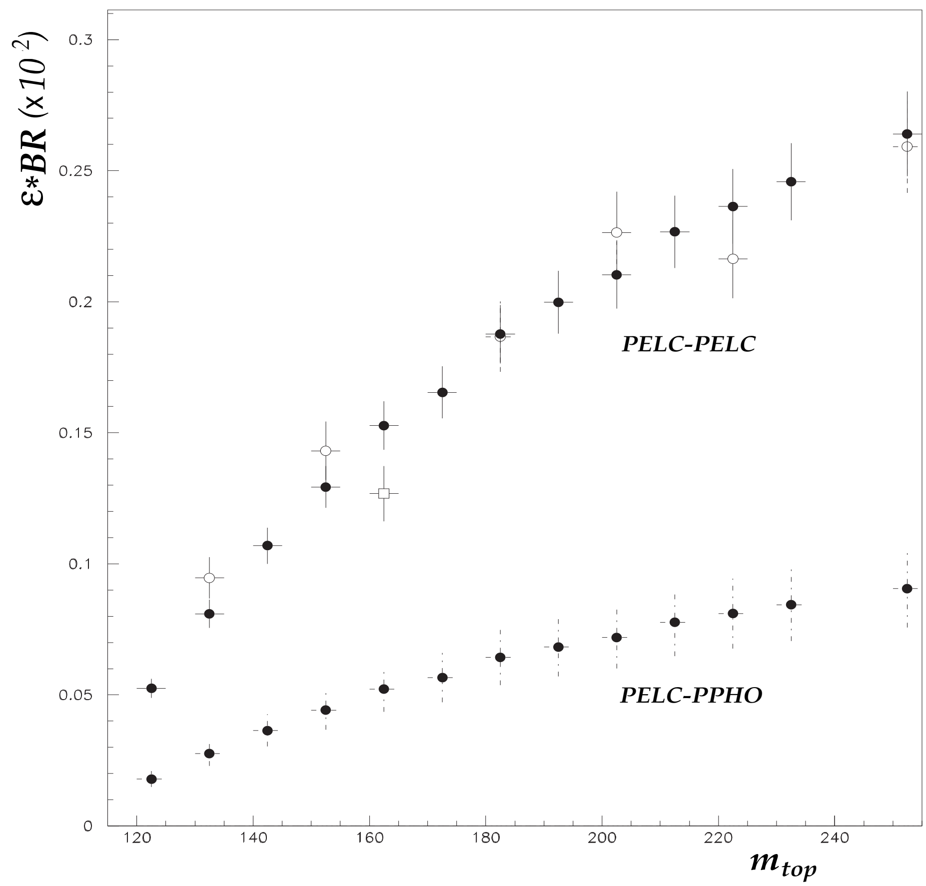

Figure 7.6: ε∗BR for top showing HERWIG (solid circles), ISAJET (open circles) and PYTHIA (open box).

As discussed in Chapter IV, our trigger efficiency for the ELE_JET filter is about 88% and addition of the Z filter brings this up to 93%. This efficiency is, however, not the efficiency we should apply to our Monte Carlo samples because cuts executed at the trigger level are looser than our cuts in the analysis. In other words, although 88% of top events pass the trigger, it is likely that a higher percentage of those top events passing our offline cuts also pass the filter. We have estimated this trigger efficiency using the top Monte Carlo samples at various masses, and we obtain 99.5% ± 0.2% for the ELE_JET filter for top masses throughout the range 100 to 250 GeV/c^2. The Z filter has about 99.0% ± 0.2% efficiency after our cuts. The reason these efficiencies are so high and independent of top mass arises from the fact that the offline cuts are much tighter than the trigger cuts. The chances of an event being able to pass our offline cuts but fluctuating to fail the trigger at Level 1 or Level 2 is negligibly small. For instance, that portion of the backgrounds which pass the offline kinematic selection also have a very high trigger efficiency -- for the $Z \rightarrow \tau\tau \rightarrow ee$ background it is about 98%. As a result, we consider all of our samples to be 99% efficient and assign a 1% systematic uncertainty to this number.

When calculating event yields, we also need to include a 5.4% systematic error from the luminosity calibration[42] and an error due to the uncertainty in the theoretical calculation of the top cross section which varies from 21% when the top mass is about 100 GeV/c^2 to 12%[62] above 200 GeV/c^2. We must also propagate in the electron identification error according to the distribution of CC and EC electrons there are. The systematic errors are itemized in Table 7.2. We display the expected number of top events into dielectron final states in Table 7.3, as a function of the top mass.

Table 7.2. Systematic errors in top efficiency and event yield determination.

source of uncertainty	**fractional error**
Monte Carlo generator	10%
jet energy scale	5%
multiple interactions	2.8%
trigger simulation	1%
theoretical cross section uncertainty	21% to 12%
luminosity calibration	5.4%

Table 7.3. Number expected top events for various top masses.

m_{top} (GeV/c^2)	N_{evt}(PELC-PELC)	N_{evt}(PELC-PPHO)
140	2.17	0.74
160	1.50	0.51
170	1.23	0.42
180	0.95	0.32
200	0.57	0.19

6. Estimated Background and Errors

Physics backgrounds are defined as those processes which lead to dielectron final states. For example, such backgrounds arise from $Z \to ee$, $Z \to \tau\tau \to ee$, $WW \to ee$, $b\bar{b}, c\bar{c} \to ee$, and $\gamma^* \to ee$. We use Monte Carlo samples generated using ISAJET, PYTHIA, and HERWIG as well as data to estimate the contribution from such processes. The Monte Carlo generator used is somewhat arbitrary although HERWIG could not at the time generate WW events. For the most part, ISAJET is used in this analysis for the backgrounds. Instrumental backgrounds arise from events in which one or both the electrons in the event are actually misidentified jets. For the dielectron analysis, there are three sources of instrumental backgrounds: (1) W (to $e\nu$) + ≥ 3 jets, (2) direct photon + ≥ 3 jets in which at least one jet is misidentified as an electron, and (3) QCD multijet events where at least two jets are misidentified as electrons.

a. $Z \to ee$

Due to the tremendous rejection power of the $\not{E}_T$ cut, it is impractical to generate a Z dielectron sample of sufficient size that the number of events which pass the final cuts give a reasonable statistical error (say 10%). Also, there are other complications. For example, the $\not{E}_T$ resolution from GEANT Monte Carlo is better than that attained in the actual data. First of all, the energy deposited by uranium decay is not simulated in the Monte Carlo and this significantly smears out the $\not{E}_T$ distribution in the data. Also, the Main Ring and hot cells contribute a tail of large $\not{E}_T$ events in the data and these are not simulated. As a result, we determine our $Z \rightarrow ee$ background from data.

In our estimation of the Z background below we need to know the rate at which events with jets passing our cuts will have sufficient $\not{E}_T$ to pass our Z window cut. We have estimated this by looking at events passing jet triggers. Ideally, we would want such a sample to have the same jet multiplicity distribution as our Z sample. However, the trigger rate of the low E_T jet trigger was very high and was heavily prescaled. As a result, this trigger does not yield a very good statistical sample for events with 2 jets and is much worse for higher jet multiplicities. Therefore, for the three and four jet multiplicities, at least, we also use three and four jet triggers for which the prescale was comparatively small. If the event has one 'good' electron (ie. PELC with f_{iso} < 0.1 and L_5 (electron likelihood) < 2.0, and E_T > 20 GeV) then the event is thrown out as a potential W event. In Figure 7.7 is shown the $\not{E}_T$ distribution in two, three and four jet events in Run 1b data. The histograms are plotted on a logarithmic scale to show the shape of the high $\not{E}_T$ tail. The distribution before the hot cell cuts is shown for comparison (dashed histogram), The hot cell cuts remove a significant fraction of the events with $\not{E}_T > 40$ GeV.

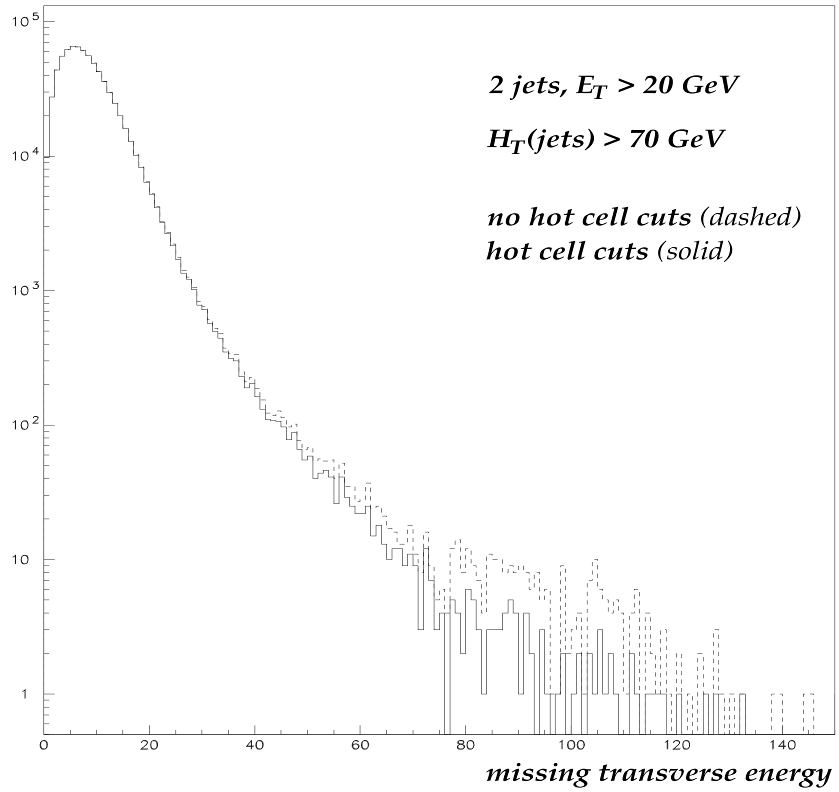

Figure 7.7: $\not\!\!E_T$ distribution in 2, 3, and 4 jet events in Run 1b data. The histograms are plotted on a logarithmic scale to show the shape of the high $\not\!\!E_T$ tail. The distribution before the hot cell cuts is shown for comparison (dashed histogram)

The fake rate is given in Table 7.4 as the percent of dijet events having $\not\!\!E_T$ above some value. Note that the fake rate for three jet events is somewhat lower than for two jet or four jet events. This may reflect two conflicting effects. As the jet multiplicity increases, the number of tracks also increases which will help in finding the proper primary vertex for the event. This in turn will improve the $\not\!\!E_T$ resolution. On the other hand, larger jet multiplicities mean more jets to worsen the $\not\!\!E_T$ resolution. There is a mild dependence of the $\not\!\!E_T$ fake rate on jet multiplicity. As a result, we re-weight by the Z jet multiplicity given below.

Table 7.4. $\not\!\!E_T$ fake rates for various jet cuts.

cut	**25 GeV cut(%)**	**40 GeV cut(%)**
2 jets > 15 GeV	1.350 ± 0.011	0.234 ± 0.004
2 jets > 20 GeV	1.567 ± 0.014	0.277 ± 0.006
2 jets > 20 GeV, + H_T^e > 120 GeV*	1.728 ± 0.015	0.308 ± 0.006
"", clean event**	1.579 ± 0.015	0.226 ± 0.006
"", 2 jets in event***	1.023 ± 0.089	0.203 ± 0.040
"", 3 jets in event***	0.858 ± 0.021	0.142 ± 0.008
"", 4 jets in event***	1.119 ± 0.021	0.165 ± 0.008

*The H_T^e is cut on 70 GeV because for Z events the electron supplies 50 GeV of E_T itself to H_T^e so the jets only need to make up 70 GeV.
**'clean event' refers to the hot cell cuts described in Chapter IV.
*** $\not\!\!E_T$ hot cell cut performed here.

Table 7.5. Number dielectron candidates in invariant mass bands after requiring 2 electrons with E_T > 20 GeV, 2 jets with E_T > 20 GeV and H_T^e > 120 GeV. The number of events for three different jet multiplicities is given for PELC-PELC and PELC-PPHO events. The estimated number of Z events for each jet multiplicity is given in the last row.

mass region	**PELC-PELC** (# events)			**PELC-PPHO** (# events)		
	2 jets	3 jets	≥ 4 jets	2 jets	3 jets	≥ 4 jets
low mass sideband	3	0	0	0	0	0
Z mass window	18	9	11	12	3	2
high mass sideband	0	0	2	0	0	0
# Z's	15	9	9	12	3	2

We must first do a background subtraction under the Z peak which is performed by first counting events in sidebands from 61 GeV/c^2 to 73 GeV/c^2, and 109 GeV/c^2 to 121 GeV/c^2. The sum of these two is assumed to be the background under the Z peak where the signal region is defined to be 79 GeV/$c^2 \leq M_{ee} \leq$ 103 GeV/c^2. After electron, jet, and H_T^e cuts we have the breakdown in Table 7.5. Therefore, our Run 1 Z sample is 33 (17) PELC-PELC (PELC-PPHO) events using both the Z trigger and ELE_JET_(HIGH). The jet multiplicity of the 33 (17) events in the Z window is given in the last row in Table 7.5. Weighting the $\not{E}_T$ fake rates from the $\not{E}_T$ section by the fractions falling in these jet multiplicities, we obtain:

$$f_{\not{E}_T}^{Z\,\mathrm{sample}} = \frac{\left(N_{2jet} * f_{\not{E}_T}^{2jet} + N_{3jet} * f_{\not{E}_T}^{3jet} + N_{\geq 4jet} * f_{\not{E}_T}^{\geq 4jet}\right)}{N_{2jet} + N_{3jet} + N_{\geq 4jet}}$$

$$= \frac{(15*0.203 + 9*0.142 + 9*0.165)}{33} = 0.176\% \pm 0.028\%$$

$$= \frac{(12*0.203 + 3*0.142 + 2*0.165)}{17} = 0.188\% \pm 0.034\%$$

where $N_{i\mathrm{jet}}$ is the number of Z events with i jets and $f_{\not{E}_T}^{i\mathrm{jet}}$ is the rate at which an event with that jet multiplicity will have $\not{E}_T$ > 40 GeV. The second line is the calculation for the PELC-PELC analysis while the third line is for the PELC-PPHO analysis. Using these rates, we obtain a Z background of

	PELC-PELC	PELC-PPHO
# events	0.05868 ± 0.01375	0.03193 ± 0.00800

b. $Z \rightarrow \tau\tau \rightarrow ee$

After accounting for branching ratios of the Z to two τ's and each τ to an electron, the cross-section of $Z \rightarrow \tau\tau \rightarrow ee$ is 5.2 pb. From the DØ measurement of the Z p_T distribution[63], the fraction of Z bosons having p_T > 20 GeV/c at the Tevatron is 0.164 ± 0.010. Further, in the sample with such a Z p_T cut described earlier, the fraction which passed the cut of two electrons with p_T > 14 GeV/c was 9612 out of a total 64994 generated or 0.1479 ± 0.0014.

Therefore the cross-section of this sample is:

$$\sigma(Z \to \tau\tau \to ee)_{p_T^Z > 20}^{p_T^{e2} > 14} = 5.2 * 0.164 * 0.147$$
$$= 0.1254 \pm 0.00774\, pb$$

where the error does not include the error on 5.2 pb.

From this sample, after applying our electron efficiencies, we obtain an efficiency and event yield of

	PELC-PELC	**PELC-PPHO**
efficiency	0.00496 ± 0.00058	0.00167 ± 0.00033
# events	0.07476 ± 0.00990	0.02517 ± 0.00521

c. WW to ee

The WW cross section is 9.5 pb. The dielectron branching ratio is the same as for $t\bar{t}$, namely 1.24%. There is also the factor to accommodate the particle level cuts. This was measured to be 0.4178 ± 0.0049 at generation time thereby giving a cross-section of (0.04922 ± 0.00058) pb. The efficiencies and expected event yields from this sample are the following:

	PELC-PELC	**PELC-PPHO**
efficiency	0.01353 ± 0.00153	0.00446 ± 0.00092
# events	0.08005 ± 0.00905	0.02639 ± 0.00544

d. $b\bar{b}, c\bar{c} \to ee$

In the heavy flavor sample, very few events have at least one isolated electron. Table 7.6 gives the number of events for each p_T bin for this study as a function of cuts. We find no events surviving in any interval. The few dielectron events in the sample fail the $\not{E}_T$ cut. Because no events survive and because they are rejected early in the cut chain, we consider this background to be negligible ans assign the value 0. If we had taken the 1 sigma upward statistical bound as our number we would obtain 0.06 events.

Table 7.6. Events passing per E_T interval in heavy flavor events.

	40-60	60-80	80-100	100-130	130-160	160-200	200-240
total	3288	4956	2695	4417	3348	2822	2100
2 electrons	1	0	2	0	0	1	0
1 jet	1	0	2	0	0	1	0
2 jets	0	0	1	0	0	1	0
$\not{E}_T$	0	0	0	0	0	0	0
second jet E_T **> 20 GeV**	0	0	0	0	0	0	0
H_T^e **> 120**	0	0	0	0	0	0	0

e. Drell-Yan (γ*) to ee

The Drell Yan dielectron production cross section is 90 ± 9 pb if the dielectron invariant mass is > 25 GeV. Given the particle level selection cuts mentioned in Section 1, there is a further reduction factor for our Monte Carlo sample. This factor was measured to be 0.0467 ± 0.0021 at generation time thereby giving a cross-section of (4.20 ± 0.19) pb. The efficiencies and expected event yields from this sample are the following:

	PELC-PELC	PELC-PPHO
efficiency	0.000103 ± 0.000024	0.000035 ± 0.000010
# events	0.0520 ± 0.0127	0.0177 ± 0.0051

f. Instrumental Background Estimation

We do not itemize the different subprocesses which make up the instrumental background but rather sum them together. We consider the PELC (or PPHO) nearest neighbor algorithm as merely a high EM fraction jet algorithm. We determine the probability that a PELC (or PPHO) in the multijet sample will be selected as a good electron as described in Chapter IV. Once we have these probabilities, we select events in which there are two EM jets (PELC or PPHO clusters), one of them passing our electron identification criteria. We apply all of the kinematic cuts of the analysis: two electron candidates with E_T > 20 GeV; two jets with E_T > 20 GeV; $\not{E}_T$ > 25 GeV; and H_T^e > 120 GeV. Since we allow both PELC-PELC and PELC-PPHO events, we require the 'trigger electron' to be a PELC.

Because Main Ring events occasionally have biased $\not{E}_T$ which cannot be corrected at the μDST level, we leave these out of this sample. We will normalize back to 120.2 pb^{-1} in the end. Also, the Run 1a stream had loose electron identification cuts performed so that the EM cluster we select to fake is biased for this calculation. Therefore, we restrict ourselves to the 90.13 pb^{-1} of GOOD_BEAM 1b and 1c data. In addition, examination of this background provides another motivation, as mentioned in Chapter IV, to utilize only the ELE_JET(_HIGH) trigger for this analysis. The number of events which pass the above offline cuts but which pass the Z trigger and not the ELE_JET(_HIGH) trigger) is about 5% to 7% of the total. Since the electron fake rate for these is about a factor of 5 higher (see Appendix III), this contributes approximately 30% to the instrumental background and there is no increase in efficiency for top.

The final numbers for tries for PELC or PPHO jet fakes in CC and EC. are listed in Table 7.7.

Table 7.7. Number of tries for EM cluster to pass electron identification criteria.

	# PELC candidates	# PPHO candidates
CC	15	17
EC	4	0

We multiply these 'tries' by the fake rates for the different regions and normalize the expected event yield to 120.2 pb^{-1}. This gives,

	PELC-PELC	**PELC-PPHO**
# events	0.1967 ± 0.0077	0.2548 ± 0.0121

g. Analysis of Errors on Backgrounds

For each background listed above, there are systematic errors which must be considered. Some of these errors are uncorrelated from background to background and can be added in quadrature. Examples are $\not\!\!E_T$ fake rate, electron fake rate, etc. There are also correlated systematic uncertainties as listed in Table 7.8. Although these processes are well understood compared to $t\bar{t}$ production, some of the errors in Table 7.8 are larger than corresponding errors for top. For the Monte Carlo generator error and the jet energy scale error this is partly due to variations in calculation of jet processes in the Monte Carlo and the fact that the backgrounds tend to congregate near the jet E_T cut. Similarly, the multiple interaction error is larger for backgrounds than for top production because various kinematic quantities we cut on tend to be near thresholds and mismeasurement of the vertex results in a larger change in efficiency. The total background and error is tabulated in Table 7.9.

Table 7.8. Systematic errors for Monte Carlo backgrounds.

source of error	$Z \rightarrow \tau\tau \rightarrow ee$	$\gamma^* \rightarrow ee$	$WW \rightarrow ee$
input cross-section	8.1%	10%	10%
Monte Carlo generator	14%	14%	14%
multiple interactions	10%	10%	10%
trigger simulation	1%	1%	1%
luminosity calibration	5.4%	5.4%	5.4%
jet energy scale	10%	10%	10%

Table 7.9. Total background and errors.

	PELC-PELC	**PELC-PPHO**
total background	0.462	0.356
uncorrelated stat. + sys.	0.021	0.015
correlated sys.	0.049	0.021

7. Observed Event Yield

We have verified the integrity of our data in terms of GOOD_BEAM and Main Ring data, and we have chosen our cuts and estimated their efficiency for signal and background. We now return to the data to see what the event breakdown is.

Although it makes sense in terms of the backgrounds to perform the electron cuts first, the $\not{E}_T$ cuts second, and the jet cuts last, the nature of our Main Ring corrections necessitates a different order. As mentioned in Chapter IV, the initial data we streamed consists of 750,000 events in μDST format. Because this format lacks raw hit information, the Main Ring $\not{E}_T$ corrections are not calculable. We require a sample of STAs which contain the calorimeter cell hit information. Also, the TRD PPHO information is not available in most reconstruction versions.

For these reasons, we have analyzed data via an alternative approach as shown in Table 7.10. The first part of this analysis is performed from the μDST sample and most of the electron and jet cuts are applied. The electron identification cuts on PELCs and Main Ring corrections to jets are performed. Also, the electron identification cuts on PPHOs are performed with the exception of the TRD ε_t cut. These events are required to pass the analysis trigger [ELE_JET(_HIGH)] or the dielectron diagnostic trigger (see Chapter IV). The event breakdown for each level of cuts is given in Table 7.10. The cuts are listed in the left column with the middle column showing the progression for PELC-PELC events and the right column gives PELC-PPHO events.

We then reprocess our events after some selection with the latest version of the reconstruction. After re-reconstructing the data, we select only the events passing ELE_JET(_HIGH) and apply $\not{E}_T$ Main Ring corrections, and cut on ε_t for PPHOs. The event yields after each cut are given in Table 7.10 under the heading 'STA sample'. For both the PELC-PELC and PELC-PPHO samples, two columns are given which show the observed number of events (left column) and the expected number of background events (right column). The observed number is consistent with background at each level of cuts for both samples. After all of the cuts, one event survives our selection. The total estimated background is 0.82 events ± 0.08 events. It should be noted that the PELC-PPHO column has one event noted in parentheses which does not pass the selection but is a very interesting event nevertheless. This event will be discussed in the next section and in Appendix VII. The candidate event is 88295-30317 and the PELC-PPHO event is 95653-10822.

Table 7.10. Run 1 dielectron data. Shown is the breakdown in number of events seen after each cut.

	PELC-PELC		**PELC-PPHO**	
μDST sample: Main-Ring jet corrections: 2 electrons > 20 GeV	5342		2821	
≥ 1 jet, E_T > 15 GeV	869		576	
≥ 2 jets, E_T > 15 GeV	147		103	
STA sample: Main-Ring $\not\!\!E_T$ corrections TRD on PPHOs: ELE_JET only	52		6 (7)	
$\not\!\!E_T$ > 25 GeV	3	1.65	1 (2)	1.05
Z-window cut	2	1.18	0 (1)	0.87
≥ 2 jets, E_T > 15 GeV	2	0.74	0 (1)	0.54
H_T^e > 120 GeV	1	0.46	0 (1)	0.36

Four important kinematic distributions are given in Figures 7.8 through 7.11. The first three figures display these for (a) $t\bar{t}$ for a top with mass 180 GeV/c^2, (b) Z dielectron background from the HERWIG sample, (c) the PELC-PELC sample, and (d) the PELC-PPHO sample. In Figure 7.8 is shown the distribution of the second leading jet E_T after the cuts on the two electrons and one jet in the μDST sample. Figure 7.9 shows the $\not\!\!E_T$ after requiring the final electron and jet cuts in the STA sample. Figure 7.10 displays the distribution of $\not\!\!E_T$ *vs.* M_{ee} after requiring the final electron and jet cuts in the STA sample. Figure 7.11 indicates the distribution of H_T^e for the three events before the H_T^e cut along with the distribution for top and background.

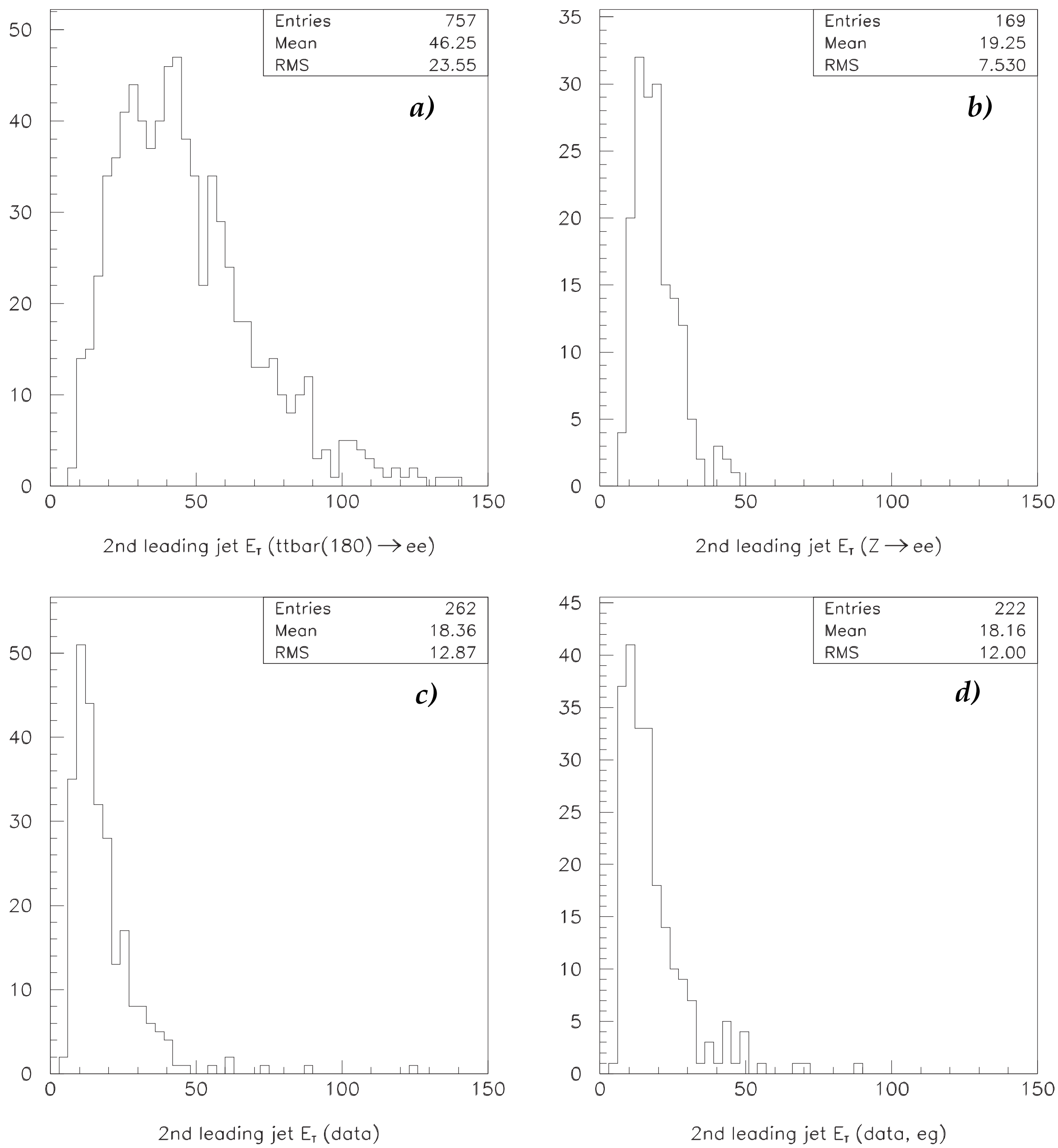

Figure 7.8: Second leading jet E_T for (a) top of mass 180 GeV/c^2, (b) Z dielectron background, (c) Run 1 PELC-PELC events, and (d) Run 1 PELC-PPHO events. No ε_t cut was applied to the PPHO clusters.

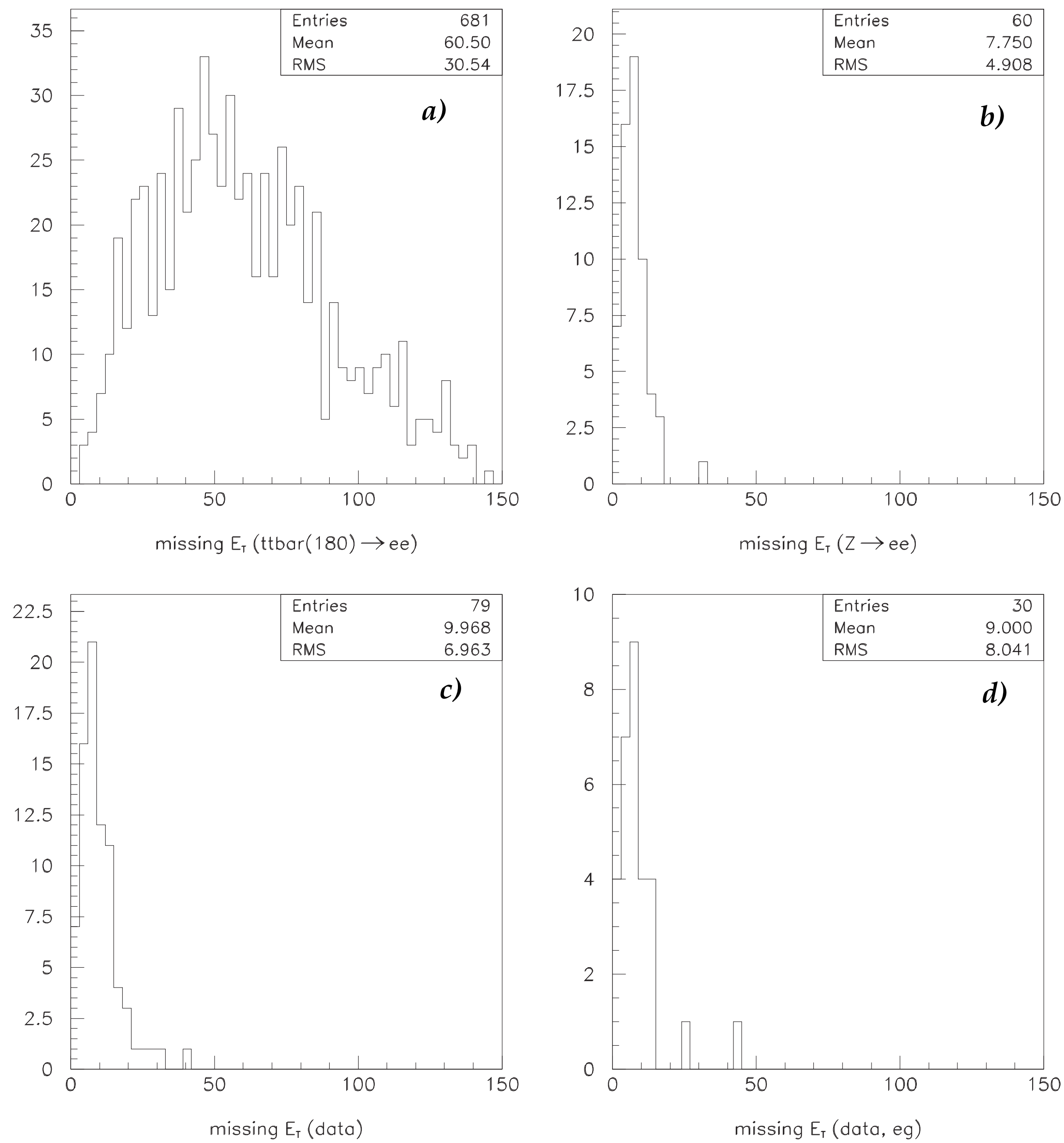

Figure 7.9: $\not{E}_T$ after $E_T^{e2} > 20 GeV, E_T^{j2} > 20 GeV$ in (a) $t\bar{t} \rightarrow ee$ for m_{top} = 180 GeV/c^2, (b) $Z \rightarrow ee$ from ISAJET, (c) PELC-PELC events in Run 1, and (d) PELC-PPHO events.

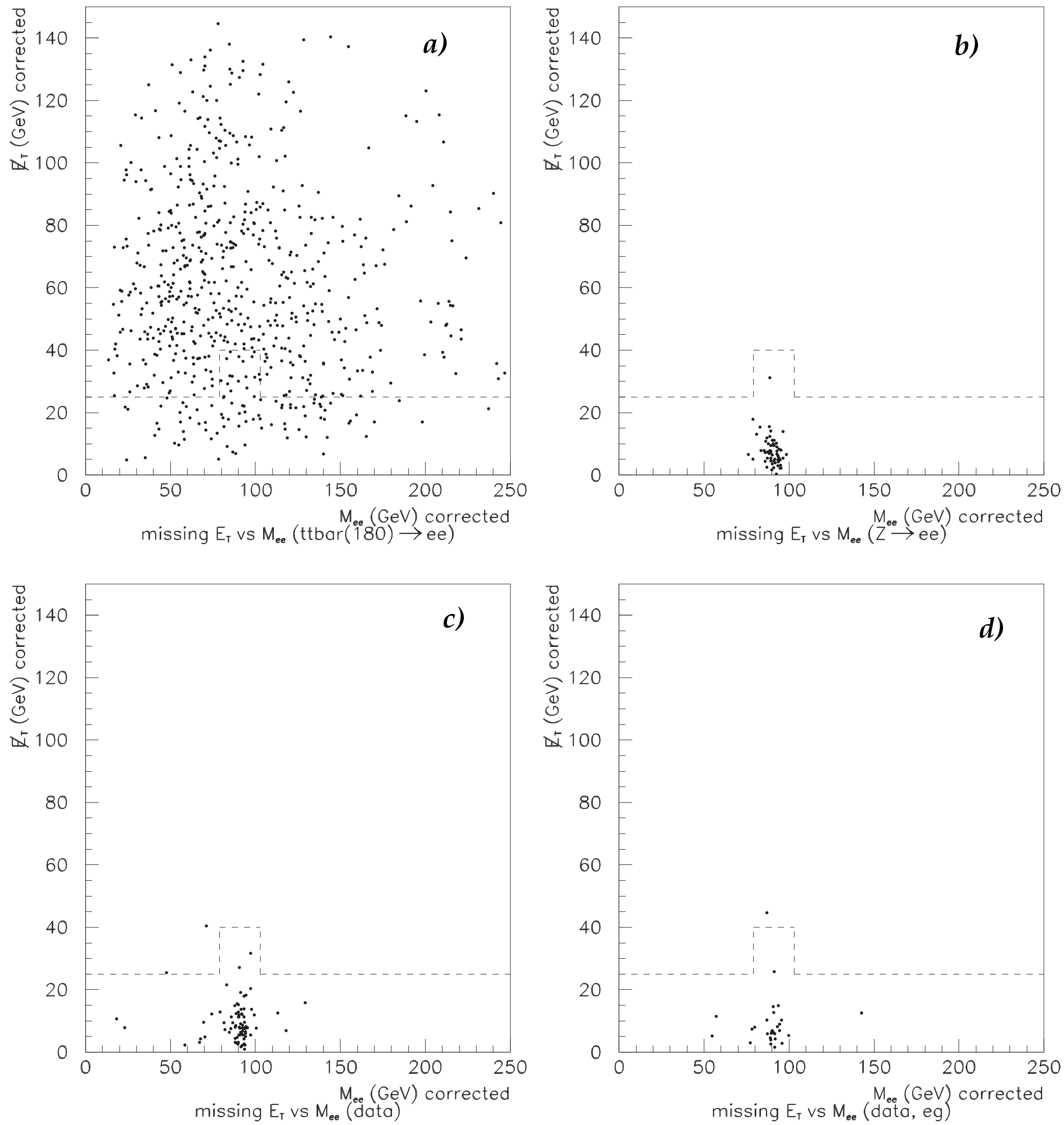

Figure 7.10: $\not\!\!E_T$ $vs.$ M_{ee} after $E_T^{e2} > 20GeV, E_T^{j2} > 20GeV$ in (a) $t\bar{t} \to ee$ for m_{top} = 180 GeV/c^2, (b) $Z \to ee$ from ISAJET, (c) PELC-PELC events in Run 1, and (d) PELC-PPHO events.

8. Dielectron Top Candidates

The H_T^e distribution of the three events which survive all but the H_T^e cut are shown in Figure 7.10 along with the summed distribution for background and for top of mass 170 GeV/c^2. The two events which pass this cut are kinematically described in this section.

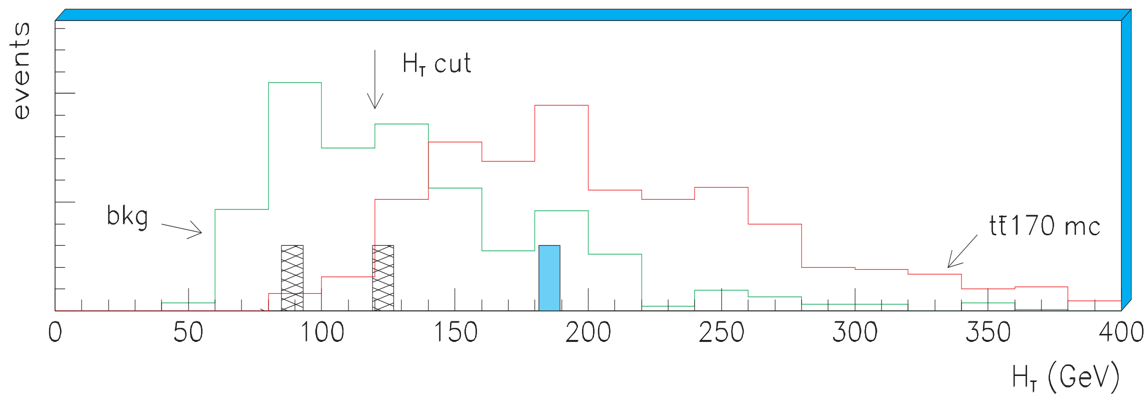

Figure 7.11: H_T^e distribution for dielectron events.

a. Event 30317

88295-30317		η	ϕ
Event Quantities M_{ee}	71.4 GeV/c^2		
H_T^e	123.0 GeV		
$\not{E}_T$	40.9 GeV	---	6.22
Electrons leading	50.6 GeV	0.33	1.52
second leading	22.6 GeV	-1.49	1.91
Jets leading	45.7 GeV	-0.72	4.04
second leading	26.7 GeV	-0.92	4.84

b. Event 10822

This event was found while studying muon tagging in Z events. Because of the way this event was found (see Appendix 7 for details), the background and signal expectations are somewhat difficult to assess. As a result, we will not include it in the standard dielectron analysis. Nevertheless, based on information in the TRD, inner CDC layers, and calorimeter, it is a likely dielectron event. Based on the event kinematics and the fact that it is a trilepton event, it is interesting to consider as a possible top event.

95653-10822		η	ϕ
Event Quantities M_{ee}	86.0 GeV/c^2		
H_T^e	182.6 GeV (196.5 GeV *with muon*)		
$\not{E}_T$	44.2 GeV (56.2 GeV *with muon*)	---	6.02
Electrons leading	52.8GeV	-0.60	6.20
second leading	27.7 GeV	0.87	4.40
Jets			
leading	69.7 GeV (83.5 GeV *with muon*)	-0.59	3.42
second leading	33.7 GeV	-0.86	2.32
third leading	26.5 GeV	0.63	1.57
Muon leading	13.8 GeV/c	-0.60	3.47

The lepton identification qualities of these events are discussed in Appendix VII.

9. Top Cross-Section and Dielectron Branching Ratio

In order to determine our total measured cross section we count the number of events passing the above cuts. The cross section is then calculated as

$$\sigma_{t\bar{t}} = \frac{S-B}{\sum \varepsilon_i * BR_i * \mathcal{L}_i} = \frac{S-B}{\mathcal{L} * BR * (\varepsilon_{ee'} + \varepsilon_{e\gamma'})} \qquad \textbf{Eq. 7.2}$$

where S is the number of events seen, B is the background expected, BR is the branching ratio of the signal channel, and $\mathcal{L}$ is the luminosity for the analysis. The denominator is summed over all channels. Since BR_i and $\mathcal{L}_i$ are the same for the PELC-PELC and PELC-PPHO analyses, we get the second part of the expression. The error can be calculated as

$$\delta\sigma_{t\bar{t}} = \sigma_{tt}\sqrt{\frac{S+\sum \delta B_i^2}{(S-B)^2} + \left(\frac{BR_i * \mathcal{L}_i * \delta\varepsilon_i}{\sum BR_i * \mathcal{L}_i * \varepsilon_i}\right)^2 + \left(\frac{\delta\mathcal{L}}{\mathcal{L}}\right)^2}$$
$$= \sigma_{tt}\sqrt{\frac{S+\delta B^2}{(S-B)^2} + \left(\frac{\delta\varepsilon}{\varepsilon}\right)^2 + \left(\frac{\delta\mathcal{L}}{\mathcal{L}}\right)^2}$$

where again the second part comes from BR and $\mathcal{L}$ being the same for the two channels in this dissertation.

Because our efficiency varies with m_{top}, we must assume a top mass to calculate its cross section. If we assume m_{top} =170 GeV/c^2, and taking only event 30317 as a candidate, we obtain

$$\boxed{\sigma_{t\bar{t}} = 0.9 \pm 5.0\,pb}$$

If we include event 10822 in the calculation and consider the effect on the efficiency and background to be negligible, we obtain

$$\sigma_{t\bar{t}} = 5.9 \pm 7.1\,pb$$

The cross section varies as the excess over background so that with one event we have a 0.18 event excess while with two events the excess is 1.18 events.

Another more general way of looking at the data is to use the observed number of events to determine a limit to the dielectron branching ratio. We do this by calculating a limit to a measured cross section, and then using the theoretically calculated cross section to determine instead an equivalent branching ratio limit. In Figure 7.12a is shown the cross section limit along with the theoretically predicted cross section. The contour of the branching ratio limit as a function of top mass is shown in Figure 7.12b.

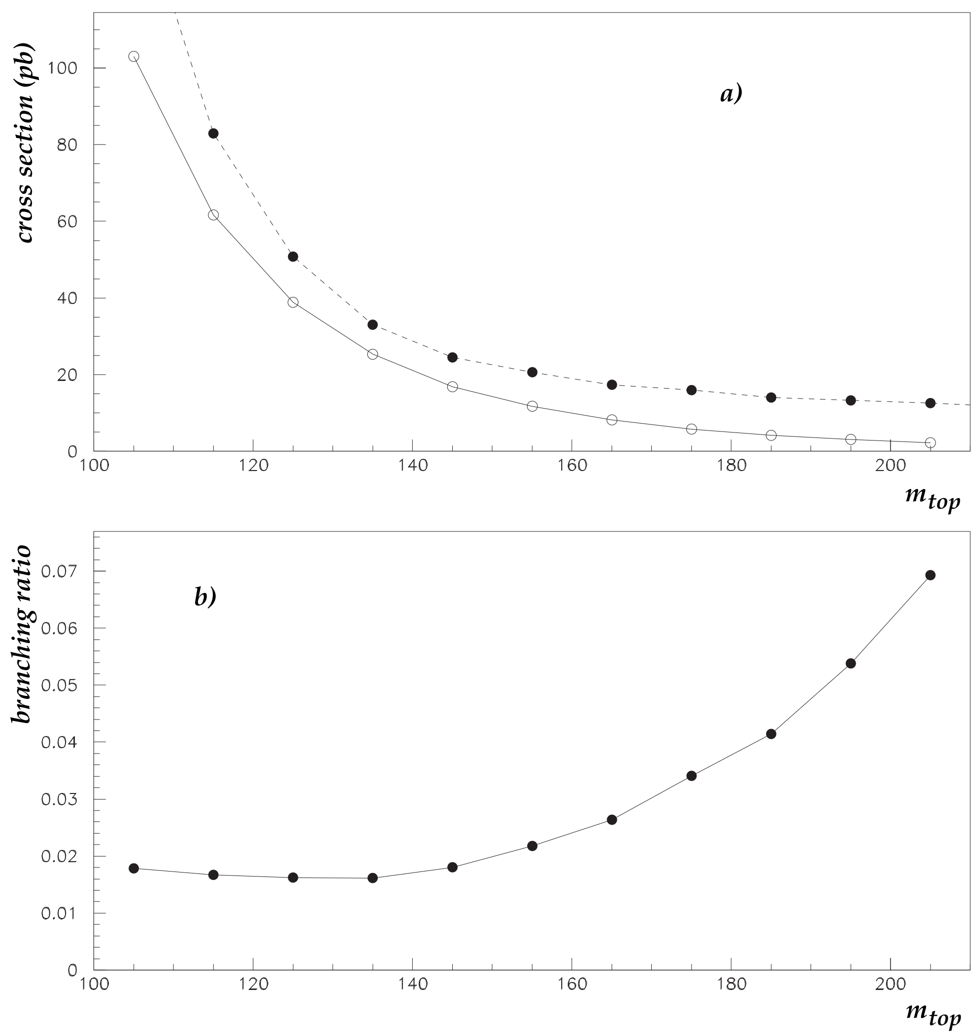

Figure 7.12: Top mass dependence of (a) top cross section limit at 95% c. l. where the limit is the solid circles and the theoretical cross section is given as the open circles, or (b) branching ratio limit at 95% c. l.

Lastly, given that top has been discovered and its mass and cross section measured, we can use these values to set a limit on the dielectron branching ratio of the observed top. It should be noted that, while this channel is part of the cross section measurement, it is a fairly minor contribution. Thus, for the sake of simplicity we assume that the cross section measurement is uncorrelated with this measurement. For a top of mass 170 GeV/c^2, we calculate an upper limit to the cross section to be 16 *pb* and the measured value is 5.2 *pb*. Therefore, the limit on the branching ratio is

$$\boxed{BR(t\bar{t} \rightarrow ee) < 3.8\% \text{ @ } 95\% \text{ c.l.}}$$

CHAPTER 8

CONCLUSIONS

'Don't look at the finger! Look at the moon, in all it's heavenly glory.'
B. Lee, *Enter the Dragon*

1. Dielectron Analysis Summary

We have undertaken an analysis of dielectron events to search for the top quark. We have attained a ratio of the estimated signal to background of about 2:1 for a top quark with mass 170 GeV/c^2 while retaining a high level of efficiency. In 120.2 pb^{-1} of collider data we see 1 candidate event in this channel. Our estimated top event yields vary from 2.9 events at m_{top} = 140 GeV/c^2 to 0.8 events for m_{top} = 200 GeV/c^2 for our cuts. For the backgrounds we expect about 0.82 ± 0.08 events. This gives a cross section of 0.9 ± 5.0 pb. We have also determined the upper limit of the branching ratio of $t\bar{t}$ into dielectron final states. If the top mass is 170 GeV/c^2, the branching ratio is < 3.8% at 95% c.l.

2. Jet Energy Scale Analysis Summary

We have utilized direct photon candidates in Run 1 to obtain the absolute energy scale of jets in the DØ calorimeter. By using these events, we were able to determine the energy dependence of this response *in situ,* and find it to be in agreement with expectations from test beam and Monte Carlo analyses. The mean response of jets is approximately 80%-85% in the data, a level which is about 5% below that predicted by Monte Carlo and test beam. If this 5% is equated with the known electromagnetic energy scale then there is agreement.

3. Prognosis for Future

Before closing this dissertation, we will try to make a few notes about how this analysis can be optimized to do the best physics in the future. Let us first consider the current status.

a. Immediate Future

Both analyses presented in this thesis can be significantly improved even with the Run 1 data samples. In the case of the dielectron search, the most significant issue has to do with the choice of the $\not{E}_T$ and H_T^e cuts. Given that most backgrounds (instrumental and Z to $\tau\tau$) have a dielectron mass less than the Z mass and also have $\not{E}_T$ which is not very large, a $\not{E}_T$ cut > 30 GeV below the Z mass, and 20 GeV above the Z mass will have superior efficiency and rejection. Also, given the magnitude of the instrumental background, it should be reduced. The TRD cut on PPHO candidates was chosen to give a fake background which totalled about 50% of the total background. A minor improvement in the analysis would be to tighten the cut on ε_t to 0.8 rather than 0.9 for these clusters. Such a modification would cost about 2% in efficiency for processes with two real electrons and reduce the instrumental background by about 25%. If top were 170 GeV, we would expect 1.60 events with about 0.68 events background.

For the jet energy scale, the main issues relate to a reduction in the systematic error at low and high energy. For jets around about 15 GeV, the dominant systematics are the instrumental background, and the error due to initial state radiation and secondary jets. The instrumental background can be significantly reduced by merely cutting tighter on the isolation of the photon. It is likely that a systematic uncertainty of about 0.5% can be achieved without too much loss in statistical size of the analysis sample. More importantly than this, the affect of gluon radiation producing more jets should be dealt with in a more systematic way, especially since there are likely correlations between the two effects studied and since the amount of energy which passes down the beampipe has likely been grossly overestimated. Implementation of a more realistic description of initial and final state radiation into the parametric Monte Carlo would allow untangling of these effects. To account for correlations between systematic errors, and to reduce the overall error, an accurate parametric simulation of these errors on the method should be performed. This would include: initial state radiation, topological effects, resolution biases (including low E_T bias) and binning. A correction function could be obtained and applied to the measured response function to acquire the actual response. For high energy jets, the largest systematic uncertainty is due to multiple interactions. By normalizing the EC to the CC again after the cryostat factor corrections have been applied should allow a large reduction in error at high energy. It is likely that the error in both the low and high energy regime can be reduced to the order of 2.5% to 3.0% after these improvements with an error of better than 2% occurring for 100 GeV jets.

b. Run II Analyses

The top analysis presented in this dissertation was part of the top quark discovery analysis which was announced in March of 1995. With this discovery, the physics of the top quark has changed such that the cross section and branching ratios must be measured accurately. In terms of the cross section measurement, the dielectron channel can particularly benefit by garnering the utmost efficiency in Run II to attempt a measurement of the branching ratio of the $t\bar{t}$ system to two electrons. Any anomaly from 1.2% would suggest new physics. If in fact it is lower, the top decay chain may include a Higgs boson instead of a *W*.

The current central tracking detectors generally provide good coverage over the available electromagnetic portions of the calorimeter. However, this coverage is very uneven near the edges of the cryostats and the more central regions of the EC EM sections. More importantly, they do not measure the axial coordinate of the vertex well, particularly in high luminosity environments. This latter effect is further worsened by the fact that the tracking efficiency is poor (~85%) even at low luminosity. In a dielectron analysis this is particularly hurtful because the dielectron efficiency goes as the square of the single electron efficiency. Recent studies have also shown that loss of tracks due to misreconstructed vertices significantly reduces signal efficiency and background rejection.

In addition to the tracking efficiency problem for this analysis, a significant issue revolves around the determination of the response of the calorimeter to jets. Currently, we have no redundancy which allows us to check this scale for hadrons. Since the test beam measurements have been shown to be of limited applicability to DØ energy scale determinations, and since *in situ* measurement is fraught with peril, we could benefit from another measure of these effects.

The above issues will be addressed either in whole or in part with the DØ upgrade for Run II. Approximately 10 to 20 times more data is expected in the next run of the Tevatron. On the issue of tracking uniformity, the scintillating fiber upgrade will accomplish this task with coverage extending out to $|\eta| < 2.0$. In addition, the tracking efficiency in cosmic ray tests has been seen to be quite high[64] which will be a significant improvement. The measurement of both primary and secondary event vertices using a silicon inner tracker will allow better efficiency and resolution in high luminosity environments and background rejection via use of *b*-tagging with detached vertices.

Also, any estimate of the *in situ* single pion response for the DØ detector will help us ascertain our jet energy scale with better precision. Magnetic/momentum analysis will aid in this measurement. Given the current energy scale analysis and an augmentation with momentum measurement of charged tracks, it is reasonable to think a 1% to 1.5% systematic error can be attained for jets with $E_T > 20$ GeV.

Lastly, the instrumental backgrounds to electrons will be greatly reduced by comparing the energy of the calorimeter cluster with the momentum determined from the tracker. If we estimate the efficiency of this channel to be the same as the current PELC-PELC and PELC-PPHO analysis due to improved tracking efficiency, and we estimate the instrumental background to be negligible, then for 2 fb^{-1} we would expect 27 top dielectron events with about 6 events background.

[1] Hamilton, E., Mythology. New American Library, New York, 1969.

[2] Popol Vuh, transl. D. Tedlock, Simon and Schuster, Inc. New York, 1985.

[3] Lucretius, De Rerum Natura, transl. R. Latham, Penguin Books, New York, 1982.

[4] Whorf, B., Language, Though and Reality, ed. J. Carroll, The M. I. T. Press, Cambridge, Mass, 1956.

[5] Kuhn, T. S., Structure of Scientific Revolutions, University of Chicago Press, Chicago, IL, 1970.

[6] M. Gell-Mann, Phys. Lett. 8, 214 (1964); G. Zweig, CERN Report 8182/Th.401 (1964).

[7] R. D. Field and R. P. Feynman, Nucl. Phys. B136 (1978) 1.

[8] R. D. Field and S. Wolfram, Nucl. Phys. **B213** (1983) 65.

[9] X. Artru and G. Mennessier, Nucl. Phys. **B70** (1974) 93; B. Andersson, G. Gustafson, and T. Sjöstrand, Z. Phys. **C6** (1980) 235; B. Andersson et al., Phys. Rep. **97** (1983) 31.

[10] S. Glashow, J. Iliopolous, and L. Maiani. Physical Review, D2, 1285, (1970).

[11] J. Augustin et al, Phys. Rev. Lett., 33, 1406, (1974).

[12] J. Aubert et al., Phys. Rev. Lett., 33, 1404, (1974).

[13] LEP # light neutrino estimate

[14] M. Perl et al., Phys. Rev. Lett. 35, 1489, (1975).

[15] S. Herb et al., Phys. Rev. Lett., 39, 252, (1977).

[16] Wolfenstein, PRL 51, 1945 (1983).

[17] J. Christenson, J. Cronin, V. Fitch, and R. Turlay, Phys. Rev. Lett. 13, 138, (1964)

[18] Grotz, K., Klapdor, H., The Weak Interaction in Nuclear, Particle and Astrophysics, Adam Hilger, New York, 1990.

[19] G. L. Kane, M. Peskin, *Nucl. Phys*. B **195**, 29 (1982).

[20] UA1; A. Bean et al., Phys. Rev. D 35, 3533 (1987).

[21] Albrecht, H. et al. (ARGUS) Phys. Lett. 192B. p. 245. 1987

[22] P. Franzini, Phys. Rep. 173:1-62, 1989.

[23] G. Kane, Top quark topics, In J. Hawthorne, ed., Gauge Bosons and Heavy Quarks: Proceedings of 18th SLAC Summer Institute on Particle Physics, p123-142. SLAC-Report-378, July 1990.

[24] E. Ma, Phys. Rev. Lett. **57**, 535, (1986)

[25] E. Elsen et al. (JADE), Z. Physik, C46:349-359, 1990; H. Behrend et al. (CELLO), Z Physik, C47:333-342, 1990; A. Shimonaka et al. (TOPAZ). Phys. Lett., B268:457-464, 1991.

[26] L3,OPAL

[27] Barger, V., Hewett, J. and Rizzo, T. Phys. Rev. Lett. 65. p. 1313. 1990; Ellis, J. and Fogli, G. Phys. Lett. 249B. p.543. 1990.

[28] D. Schaile, CERN-PPE/94-162, presented at 27th Int. Conf. on High Energy Physics, Glasgo, July 1994.

[29] Abe et al. (CDF), Phys. Rev. D 45, 3921 (1992).

[30] G. Abrams et al. (Mark II), Phys. Rev. Lett. 63, 2447 (1989).

[31] D. Decamp et al. (ALEPH), Phys. Lett. B 235, 399 (1990).

[32] CDF Collaboration, *Proceedings of the 9th Topical Workshop in pp Collider Phsyics,* Tsukuba, edited by K. Kondo.

[33] E. Laenen, J. Smith and W van Neerven, Phys. Lett. B **321**, 254 (1994).

[34] R. Dalitz, G. Goldstein, Phys. Rev. D 45, 1531 (1992).

[35] fermi momentum reference

[36] J. Thompson, *Introduction to Colliding Beams at Fermilab,* Fermi National Accelerator Lab internal report, TM-1909, October 1994.

[37] S. Abachi et al., 'Observation of the Top Quark', Phys. Rev. Lett. 74:2632

(1995).

[38] S. Abachi et al. (DØ), Nucl. Instr. and Meth., A 338, 185-253, (1994).

[39] P. Grannis, 'D0 Design Report', 1984.

[40] D. Green, Fermilab Report No. FERMILAB-TM-1958, 1996; C. Fabjan, Calorimetry in High Energy Physics, in Experimental Techniques in High Energy Physics, ed. T. Ferbel, Addison-Wesley, 1987.

[41] S. Aronson et al., Nucl. Instr. and Meth., A269 (1988) 492.

[42] J. Bantly et al., Improvement to the D0 Luminosity Monitor Constant, FERMILAB-TM-1930 (1995).

[43] TRD reference

[44] A. Pluquet, 'The TRD_ANALYSIS Package', D0 internal note 1899, September 1993; L. T. Goss, 'The Layperson's Guide to the TRD', D0 internal note 2522, April 1995.

[45] M. Narain and U. Heintz, 'Electron ID with Transition Radiation Detector and Central Drift Chamber'. D0 internal note 2355, 1994; U. Heintz, M. Narain, S. Chopra, I. Adam, 'A Likelihood Test for Electron ID', D0 internal note (in progress), October 1995.

[46] P. Renton, "Precision Tests of Electroweak Theories", Lepton-Photon Conference, Beijing, China (1995), OUNP-95-20.

[47] J. Kotcher, Proc. of the 1994 Beijing Calor. Symp., IHEP - Chinese Acad. of Sci., Beijing, China, Oct. 25-27, 1994, pp. 144-158.

[48] S. Abachi et al., (D0 Collab.) 'Measurement of the W Boson Mass', Phys. Rev. Lett. 77:3309 (1996).

[49] G. Marchesini and B. R. Webber, Nucl. Phys. B310 (1988) 461, vers. 5.7.

[50] H. Aihara et al., (D0 Collab.), Nucl. Instr. and Meth., A325 (1993) 393.

[51] R. Kehoe, R. Astur, Determination of the Hadronic Energy Scale of D0 Calorimetry, D0 internal note #2908, 1996.

[52] R. Astur, 'On Correcting Jets by Correcting the Electromagnetic and Hadronic Calorimeters Separately', D0 internal note 2575, 1995.

[53] F. Halzen and A. Martin, "Quarks and Leptons: An Introductory Course in

Modern Particle Physics", John Wiley and Sons, Inc., p.214. 1984.

[54] D0, CDF kt measurement

[55] N. Hadley, 'Cone Algorithm for Jet Finding', D0 Note 904, Nov. 1989.

[56] Daniel Elvira, Private communication.

[57] F. Paige and S. Protopopescu, Brookhaven Report No. BNL38034, 1886 (unpub.), vers. 6.49, 7.20.

[58] A. Milder, R. Astur, 'Jet Energy Scale Using Test Beam Data". D0 internal note 1595. 1992.

[59] J. McKinley, Private communication.

[60] S. Abachi et al., 'A Study of the Strong Coupling Constant Using W + jets Processes', Phys. Rev. Lett. 75:3226 (1995).

[61] S. Abachi et al., 'Top Quark Search with the D0 1992-1993 Data Sample', Phys. Rev. D52:4877 (1995).

[62] top cross section error

[63] Danilo Puselic, Private communication.

[64] B. Baumbaugh et al., Performance of a Large Scale Scintillating Fiber Tracker using VLPC Readout. IEEE Transactions of Nuclear Science, vol 43, pp. 1146 - 1152, June 1996.